Synthesis and characterisation of new multi-component compounds containing the non-steroidal anti-inflammatory drugs fenbufen and S-(+)-ibuprofen

By Hannah Maggie Frösler

Dissertation Presented for the Degree of Master of Science

In the Department of Chemistry

University of Cape Town

March 2024

Supervisor: Professor Mino R. Caira

Plagiarism declaration

I know the meaning of plagiarism and declare that all of the work in the dissertation, save for that which is properly acknowledged, is my own.

Signed by candidate

Signature: Signed by candidate

Date: March 2024

Acknowledgements

I would like to especially thank:

My supervisor Professor Mino Caira for the guidance and knowledge.

I am grateful for the endless support, love, and encouragement from my sister Esther and parents Julriech and Verna throughout my academic career.

My friends for their kindness, laughter and advice.

Dr Hong Su for single-crystal X-ray data-collection and Professor Clive Oliver for offering me advice when needed.

Dr Alexios Ivan Vicatos for his willingness to assist me.

Dr Cesarina Edmonds-Smith for her assistance with HPLC analysis.

The ICP-MS & XRF unit at Stellenbosch University for elemental analysis results.

Everyone in the Centre for Supramolecular Chemistry Research for their advice when needed.

Postgraduate funding office for providing financial support during my studies.

Ada and Bertie Levenstein award for funding the outstanding costs of my study.

Abbreviations

Solvents:

EtOH	Ethanol
MeOH	Methanol
MeCN	Acetonitrile
DMSO-d_6	Deuterated dimethyl sulfoxide

Chemical compounds:

S-IBU	S-(+)-ibuprofen
ACA	6-aminocaproic acid
TXA	Tranexamic acid
FEN	Fenbufen
ISN	Isonicotinamide
DMB	Heptakis(2,6-di-*O*-methyl)-β-cyclodextrin
HPBCD	Hydroxypropyl β-cyclodextrin
TRIMEA	Hexakis-(2,3,6-tri-*O*-methyl)-α-cyclodextrin
TRIMEB	Heptakis (2,3,6-tri-*O*-methyl)-β-cyclodextrin
SBEBCD	Sulfobutyl ether β-cyclodextrin sodium
ACD	α-Cyclodextrin
BCD	β-Cyclodextrin
GCD	γ-Cyclodextrin
RAMEB	Randomly methylated β-cyclodextrin

Instruments and programs:

HPLC	High-performance liquid chromatography
FT-IR	Fourier transform infrared
SCXRD	Single-crystal X-ray diffraction
PXRD	Powder X-ray diffraction
VT-PXRD	Variable temperature powder X-ray diffraction
DSC	Differential scanning calorimetry
TGA	Thermal gravimetric analysis
HSM	Hot stage microscopy
^{1}H NMR	Proton nuclear magnetic resonance

Co-crystals, salts and cyclodextrin inclusion complexes:

$Fen^{-}Na^{+}$	Fenbufen sodium salt - $[C_{16}H_{13}O_3]^{-}Na^{+}\cdot 4.16H_2O$
$Fen^{-}K^{+}$	Fenbufen potassium salt - $[C_{16}H_{13}O_3]^{-}K^{+}\cdot 4H_2O$
$BCD\cdot Fen^{-}Na^{+}$	Fenbufen sodium salt and β-cyclodextrin inclusion complex
$GCD\cdot Fen^{-}Na^{+}$	Fenbufen sodium salt and γ-cyclodextrin inclusion complex
FEN-ISN	Fenbufen and isonicotinamide ionic co-crystal
GCD·FEN	Fenbufen and γ-cyclodextrin inclusion complex
$(S\text{-}IBU)^{-}(ACA)^{+}$	S-(+)-ibuprofen and 6-aminocaproic acid salt
$(S\text{-}IBU)^{-}(TXA)^{+}$	S-(+)-ibuprofen and tranexamic acid salt
DMB·S-IBU	S-(+)-ibuprofen and DMB inclusion complex

General:

API	Active pharmaceutical ingredient
CD	Cyclodextrin
LAG	Liquid-assisted grinding
GRAS	Generally recognized as safe
FaSSIF	Fasted State Simulated Intestinal Fluid

Crystallographic terms

ASU	Asymmetric unit
U_{iso}	Isotropic atomic displacement parameter
RMSD	Root-mean-square deviation
s.o.f.	Site-occupancy factor
CSD	Cambridge Structural Database

Conferences and publications

Conferences:

Poster presentations:

- *Co-crystal and salt forms of the NSAID Fenbufen*, Frösler, H.M.; Mancapa, R.; Caira, M.R., Southern Africa Powder Diffraction Conference 2023, Midgard, Namibia, 16 - 21 April **2023**.

- *Salts of S-(+)-Ibuprofen Formed via Its Reaction with the Antifibrinolytic Agents Aminocaproic Acid and Tranexamic Acid: Synthesis and Characterization*, Frösler, H. M., Ramulumo, H. S.; Edmonds-Smith, C.; Caira, M. R., The Annual SACI and RSC Western Cape Young Chemists Symposium 2023, Cape Town, South Africa, **2023**.

Publications:

- Frösler, H. M.; Ramulumo, H. S.; Edmonds-Smith, C.; Caira, M. R., Salts of S-(+)-Ibuprofen Formed via Its Reaction with the Antifibrinolytic Agents Aminocaproic Acid and Tranexamic Acid: Synthesis and Characterization. *Crystals* **2023,** *13* (8), 1222.

Abstract

Fenbufen and S-(+)-ibuprofen are non-steroidal anti-inflammatory drugs with poor aqueous solubility. In attempts to improve their solubility and bioavailability, crystal engineering techniques were employed to synthesise salts, co-crystals and cyclodextrin inclusion complexes containing these drugs. All newly discovered phases were characterised using single-crystal X-ray diffraction (SCXRD), powder X-ray diffraction (PXRD), hot stage microscopy (HSM), Fourier transform infrared (FT-IR) spectroscopy, differential scanning calorimetry (DSC), thermal gravimetric analysis (TGA) and proton nuclear magnetic resonance (^{1}H NMR) spectroscopy.

The synthesis of metal salts of fenbufen containing sodium, potassium, calcium and magnesium ions was attempted. Sodium (Fen^-Na^+) and potassium (Fen^-K^+) salts were successfully synthesised and characterised, the former also being successfully characterised by SCXRD. Using Fen^-Na^+ as a potential 'guest', the syntheses of inclusion complexes with β-cyclodextrin (BCD) and γ-cyclodextrin (GCD) were attempted. The resulting complexes, BCD·Fen^-Na^+, and GCD·Fen^-Na^+, were successfully synthesised and characterised and were shown to have 1:1 cyclodextrin-salt compositions.

Solubility studies of all salts and cyclodextrin inclusion complexes reported in this dissertation were performed in both aqueous and Fasted State Simulated Intestinal Fluid (pH 6.5) media. Phase solubility studies of fenbufen were carried out using hydroxypropyl β-cyclodextrin (HPBCD), randomly methylated β-cyclodextrin (RAMEB), γ-cyclodextrin (GCD) and sulfobutyl ether β-cyclodextrin sodium (SBEBCD). RAMEB effected the greatest solubility enhancement of fenbufen by a factor of ~200 at the highest CD concentration employed.

Liquid-assisted grinding (LAG) and co-precipitation experiments involving fenbufen and water-soluble coformers resulted in the successful synthesis and full characterisation of an ionic co-crystal consisting of fenbufen and isonicotinamide (FEN-ISN) with 2:3 stoichiometry.

Salts of S-(+)-ibuprofen with the antifibrinolytic agents 6-aminocaproic acid [$(S\text{-IBU})^-(ACA)^+$] and tranexamic acid [$(S\text{-IBU})^-(TXA)^+$] were successfully synthesised and comprehensively characterised. A second crystalline form of a cyclodextrin inclusion complex between S-IBU and heptakis(2,6-di-*O*-methyl)-β-cyclodextrin (DMB·S-IBU) was discovered. All new phases, $(S\text{-IBU})^-(ACA)^+$, $(S\text{-IBU})^-(TXA)^+$ and DMB·S-IBU, were found to occur with 1:1 stoichiometry.

Given the paucity of different structural forms of fenbufen and S-(+)-ibuprofen reported in the Cambridge Structural Database, this study resulted in a significant extension of the structural landscapes of these active pharmaceutical ingredients.

Table of Contents

Chapter 1: Introduction

1.1. Overview

The most prominent challenge in the pharmaceutical industry is the poor water-solubility of newly synthesised active pharmaceutical ingredients (APIs) which has an effect on both their oral absorption and bioavailability. Drugs are designed based on their target enzymes, hence the factor of solubility is not always considered.[1] Other challenges with drug design include unwanted side effects, instability, and poor taste. Drugs that are administrated orally are divided into one of four classes, described in Table 1.1, that categorises them based on their aqueous solubility and permeability for absorption in the gastrointestinal tract.[2]

Table 1.1: The four classes of drugs that are administered orally.

Class	Classification
Class I	Good solubility and permeability.
Class II	Poor solubility and good permeability therefore making absorption dissolution dependent.
Class III	Adequate solubility and poor permeability.
Class IV	Poor solubility and permeability.

The synthesis of new drugs, which is a very time-consuming process, has shown a decrease over time as the regulations for approval of new drugs have become stricter over the years.[3] Crystal engineering has therefore become a useful approach to improve the properties of existing drugs. By modifying APIs via the generation of polymorphs, co-crystals, drug-drug co-crystals, cyclodextrin inclusion complexes, salts, and solvates, their dissolution rate as well as their permeability may be enhanced. This enables drugs in the classes II, III and IV to be upgraded to a better class, preferably Class I.

1.2. Crystal engineering

Pharmaceutical ingredients can either be amorphous or crystalline solids. Amorphous materials do not exhibit long-range order and are often desired due to their enhanced solubility. However, they are not widely used in the pharmaceutical industry as they have lower stability in comparison to their crystalline counterparts, which possess a repeating pattern of molecules arranged in the crystal.[4] There

are also advantages of lower hygroscopicity and reproducibility of crystalline material compared to amorphous material.[5]

Numerous factors influence the formation of crystals, including supersaturation, solvent temperature, presence of impurities, rate of cooling as well as the degree to which the solvent is agitated during the crystal formation. Therefore, it is important that the solution is not disturbed during the crystallisation process and the rate of cooling is lower than that of the rate of nuclei formation.[6] Various packing arrangements, as seen in Figure 1.1, are possible when molecules crystallise. The packing is influenced by many bonds varying in strength, but all contribute to the overall packing arrangement of the molecules in the crystal, with hydrogen bonds and coordination bonds both being strong contributors. When forming crystal structures, the functional group combinations of the different components will influence how molecules are bonded together. The resulting bonding patterns found between the molecules are referred to as supramolecular synthons.[7] These will be discussed in greater detail in subsection 1.3.2. Co-crystals. Other attractive interactions such as C-H···N, C-H···O and C-H···π may also be present.[8]

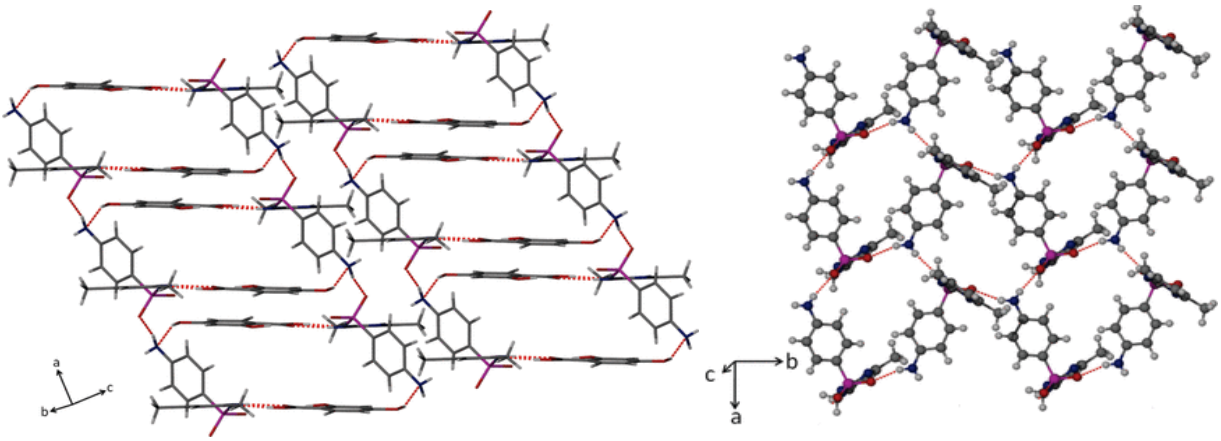

Figure 1.1: Different packing arrangements of co-crystals due to hydrogen bonding present.[9]

1.3. Drug modification

As previously mentioned, APIs can be modified via their formation of polymorphs, co-crystals, salts, cyclodextrin inclusion complexes, and hydrates, as illustrated in Figure 1.2.

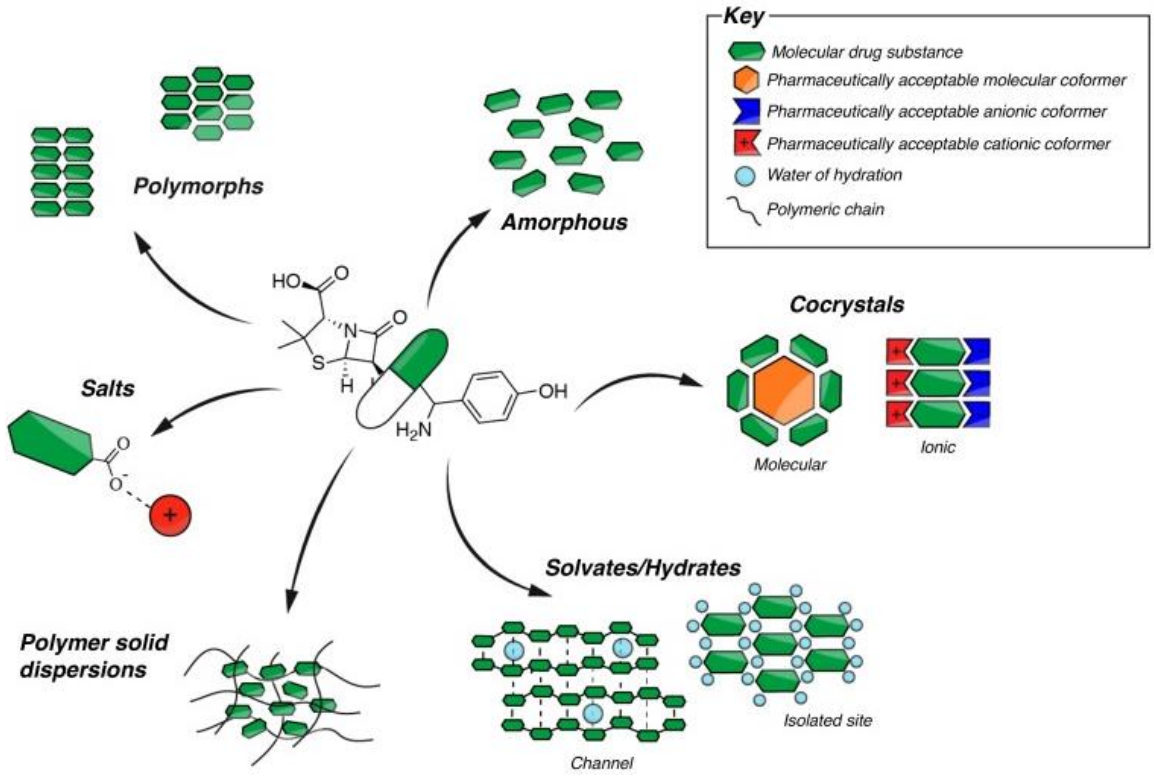

Figure 1.2: Schematic of the methods to optimise solid drug bioavailability.[10]

The manner in which the diverse solid forms of a drug illustrated above can improve drug bioavailability is discussed below.

1.3.1. Polymorphs

The first method that will be discussed to enhance the properties of APIs is the synthesis of different polymorphic forms. Polymorphs are defined as crystal structures made from the same molecule(s), but the latter are arranged differently in their respective crystals.[11] Each polymorph will have different physicochemical properties, e.g., each will have a unique melting point, thermal stability and dissolution rate. Carbamazepine is an anticonvulsant and analgesic API that has different polymorphic forms (Figure 1.3).[12]

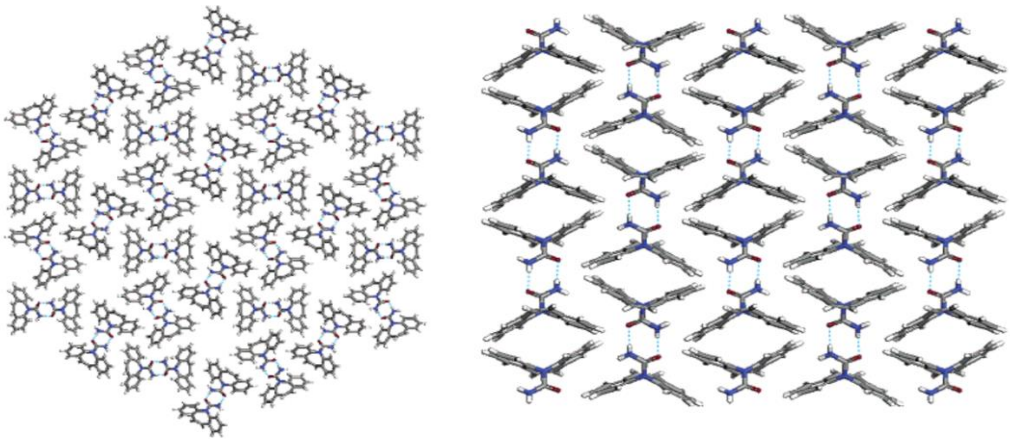

Figure 1.3: Forms II (left) and III (right) of the API carbamazepine.[12]

1.3.2. Co-crystals

Pharmaceutical co-crystals are neutral crystalline solids that consist of an API and a biocompatible coformer, which may be another API. The first co-crystal synthesised goes back to 1844 when quinone and hydroquinone were combined by Friedrich Wöhler using a 1:1 stoichiometry.[13] A century later, when single-crystal X-ray diffraction (SCXRD) became available, the structure was confirmed. Over time, as the benefits of co-crystals have been better understood, there has been an increase in their study in the pharmaceutical industry. When forming co-crystals, as well as any pharmaceutical product, it is important that all components are not toxic and are safe for consumption. These coformers are classified as 'generally recognized as safe' (GRAS) substances.[14] The co-crystal lattice energy and the solvation energies of the components in the co-crystal will determine the overall effect that the coformer has on the API.[15] The interactions found in a co-crystal may be hydrogen bonding, van der Waal forces, π-stacking and halogen bonding.[6,16] Although the most common co-crystal ratio is 1:1, different stoichiometric ratios are possible. Li *et al.,* using co-crystals of carbamazepine and 4-aminobenzoic acid, concluded that increasing the ratio of coformer, or using a highly soluble coformer, does not guarantee an increase in the solubility of the API.[15]

Computational methods are available to predict the likelihood of co-crystal formation between an API and a given coformer. The Molecular Complementarity Screening tool of the program Mercury[17] screens the API against a list of GRAS coformers and generates a list stating the probability of co-crystal formation. This prediction is based on the hydrogen bonding rules, graph sets and the possibility of synthon formation. Although the prediction may indicate that a co-crystal is likely to form, there is no guarantee of such an outcome. Factors such as the solvent employed, temperatures, solubilities, functional groups and solution concentration, all influence co-crystal synthesis. The

solvent choice is especially important as the molecule with a lower solubility (usually the API) may crash out while the more soluble component (coformer) will remain in solution. Functional groups such as alcohol, carboxylic acids and amides are favourable due to the possibility of their engaging in hydrogen bonding. Examples of the strong ('classical') and weaker hydrogen bonds are O-H···O, N-H···N, N-H···O, O-H···N, and C-H···O/C-H···N and C-H···O=C respectively.[6] Figure 1.4 shows typical synthons found in co-crystals.

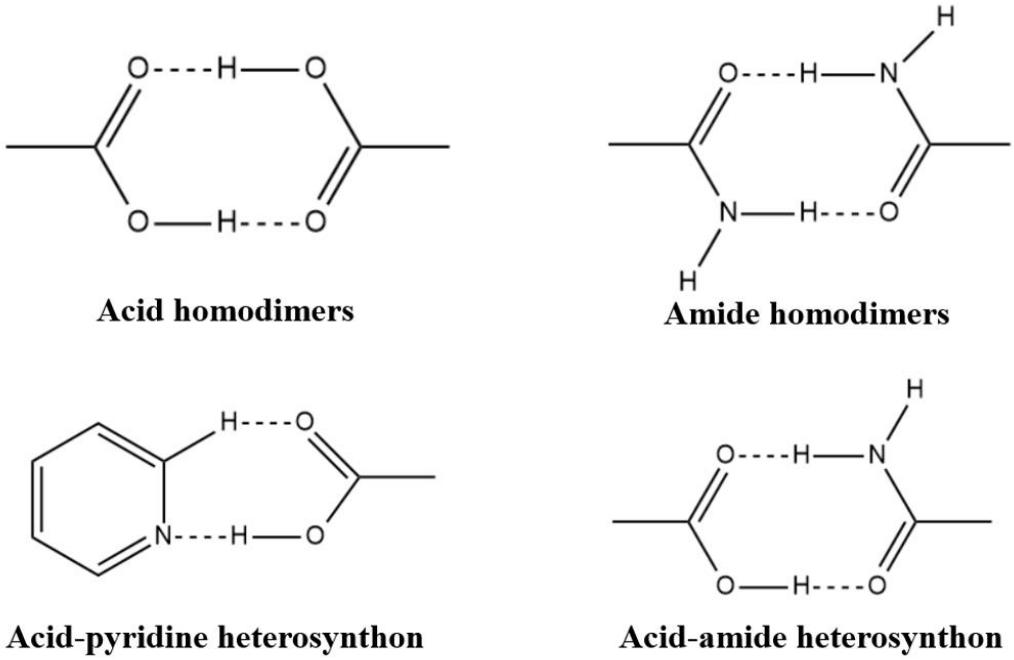

Figure 1.4: Commonly occurring synthons in co-crystal formation.[18]

Another approach in the synthesis of co-crystals is the preparation of an API-API co-crystal. Examples of these are paracetamol-indomethacin, ibuprofen-paracetamol, tramadol-naproxen and ethenzamide-gentisic acid.[19] By administering API-API co-crystals, more than one ailment may be treated at a time, thereby decreasing the number of tablets a patient is required to ingest. API-API co-crystals can also be advantageous for paediatric patients who cannot take a large number of tablets or medication in liquid form.[20]

1.3.3. Salts

One of the most common and effective ways to improve the solubility, physicochemical properties, pharmacokinetic profile and dissolution rate of a drug is through salt formation ('salification').[21] This

involves acid-base chemistry in which proton transfer takes place. For this to occur the API and coformer should both have an ionizable functional group.[22] Salt formation can either occur between the coformer and the API, or between the API and a common base (e.g., NaOH or KOH) to form organic or inorganic salts respectively.[23] Just as the requirement of any coformer, the metal used should likewise be classified as a GRAS substance. As shown in Figure 1.5, counterions are divided into three classes. GRAS substances are arranged in classes I, II and III. Compounds in Class I are safe for consumption with no limitations for pharmaceutical use. Class II materials have a low toxicity and do not occur naturally in the human body. Compounds in Class III have limited pharmaceutical use and are reserved for specialised uses.[24] Although salt forms are desirable to increase solubility, there is a potential negative effect due to hydrophobicity of the salts. This is especially the case for salts that consist of both an organic anion and cation.[25]

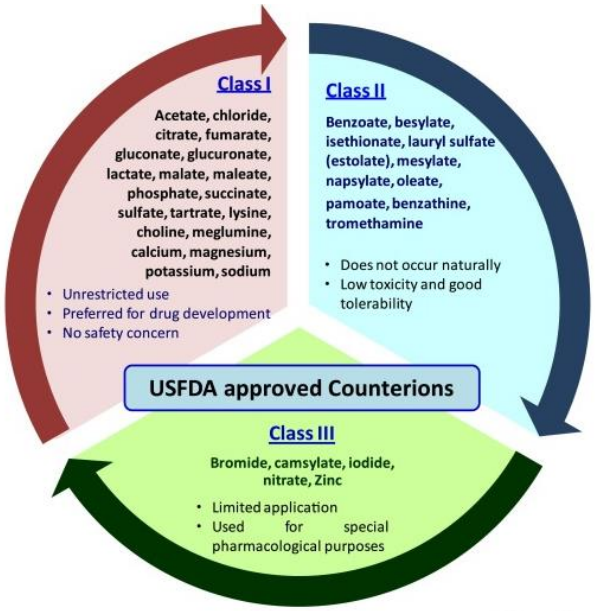

Figure 1.5: Classification of counterions used in the synthesis of pharmaceutical salts.[24]

As previously stated, the first factor to consider when forming pharmaceutical salts is the nature of the functional groups of the API. The presence of a -COOH or -NH_2 (acidic or basic respectively) functional group will determine which counterion (Na^+, K^+, Cl^-) is appropriate.[22] There are a few salt screening guidelines one can use to determine the probability that a salt will form. One of these is known as the "rule of three" which states that a pKa difference of at least 3 between the acid and base is required. This value indicates the likelihood that proton transfer will take place, and hence whether the product will be a co-crystal or a salt.[26]

Although, it is expected that an API in the salt form will result in an increase in its solubility, many factors such as the pH, size, lipophilicity, polarity and ionization potential of the salt all have an effect on the outcome. Factors that should be considered when selecting salt forms are the degree of crystallinity of the salt and its solubility at different pH levels, and it should have a low hygroscopicity,[22] and scalability.[27] Another important factor is the common-ion effect.[28] When there is a common ion found in both the salt and the digestive tract, this could decrease the solubility of the salt in the body. This is a common occurrence with chloride salts, as chloride ions are present in the gastrointestinal (GI) tract and may also be the case for Na^+ salts.[29]

The first sodium salt of an API was synthesised in 1939 (Figure 1.6). It was from this point in time that many salt forms of existing drugs were approved. Pitavastatin a drug containing a -COOH group, is used to lower cholesterol. Inorganic salt forms of pitavastatin containing the counterions Na^+, Mn^{2+} and Ca^{2+} were successfully synthesised. The Ca^{2+} and Na^+ salt forms were approved by the Food and Drug Administration (FDA) in 2009 and 2018 respectively. The two forms were found to be bioequivalent and increased the solubility of the lipophilic drug.[23]

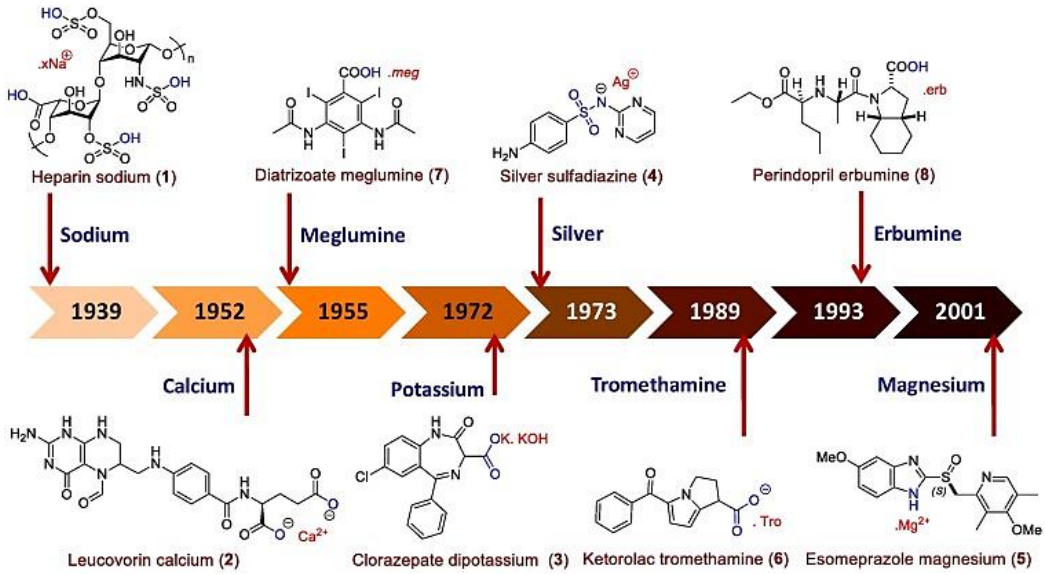

Figure 1.6: Approval timeline for pharmaceutical salts, highlighting the cationic counterions.[23]

Since the first carboxylate salt, hydrocodone tartrate, was synthesised in 1943, there has been a large increase in FDA-approved salts with various coformers (Figure 1.7).[27] Verdugo-Escamilla *et al.* synthesised a new molecular salt of metformin and citric acid (MTF-CIT).[30] Metformin is an antihyperglycemic agent that is widely used in its hydrochloride form. At physiological pH metformin has poor stability, which is a motivating factor to discover new co-crystal and salt forms of the drug.

The MFT-CIT salt showed an increase in the aqueous solubility of MFT relative to that of pure metformin. There was also an increase in the solubility at pH values 3.0 and 6.8.

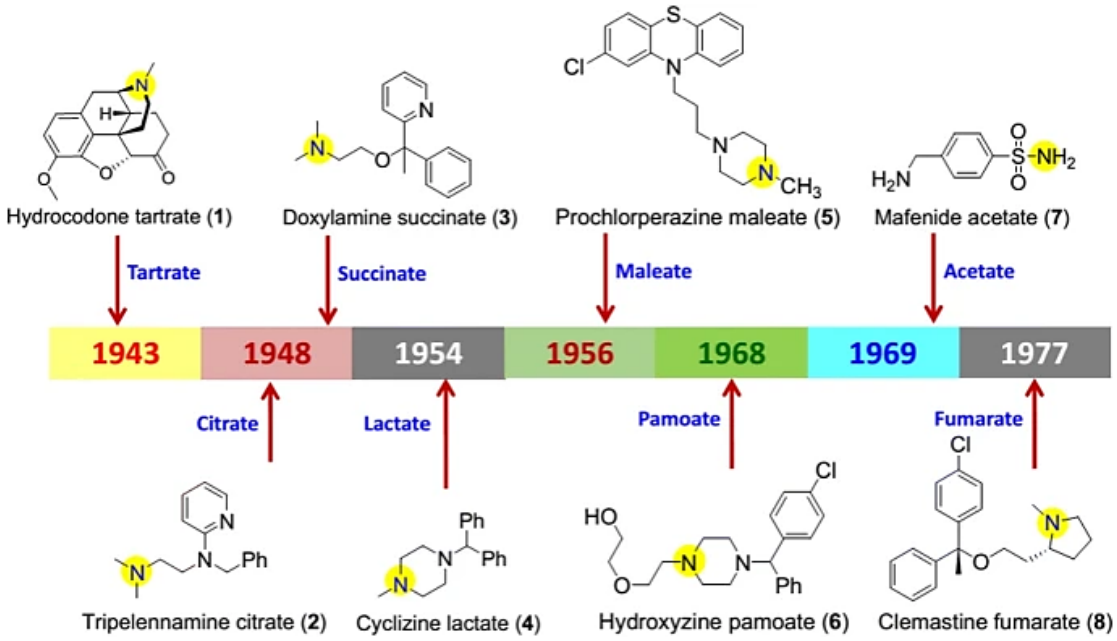

Figure 1.7: Approval timeline of salts, highlighting the organic anionic counterions.[27]

1.3.4. Cyclodextrin inclusion complexes

Cyclodextrins (CDs) are macrocyclic oligomers derived from glucose oligomers through the enzymatic degradation of starch.[2] They are very soluble in alkaline conditions and show stability in water. The native cyclodextrins are designated α-cyclodextrin (ACD), β-cyclodextrin (BCD) and γ-cyclodextrin (GCD). These consist of 6, 7 and 8 glucose subunits respectively (Figure 1.8).[31] The difference in the number of glucose subunits allows for differences in the cyclodextrin diameter, volume, and aqueous solubility. The size of the internal hydrophobic cavity will influence which compounds can be included within that micro-environment. The multiple hydroxyl groups on the periphery of the CD molecules render them soluble in aqueous media while they can accommodate lipophilic API molecules in their cavities. CDs also offer a wide variety of drug delivery systems and routes of administration, such as oral, rectal, nasal, transdermal and ocular.[32] In a CD-API complex, the API molecule located in the hydrophobic cavity is stabilised, but since it is not covalently bonded to the CD, it can partition into a more favourable environment e.g. the gastrointestinal membrane, on administration of the complex, while the CD molecules, being too large to diffuse through the membrane are degraded via human intestinal flora or amylases.[33,34]

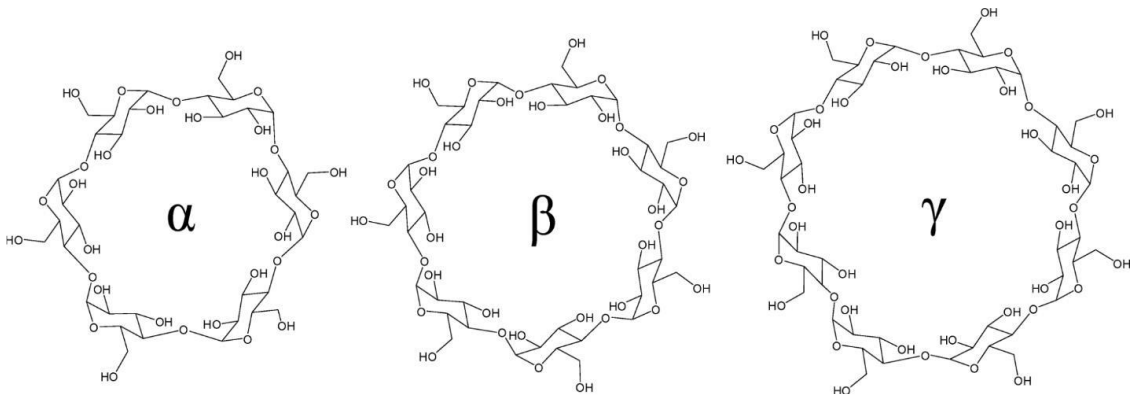

Figure 1.8: The chemical structures of three native cyclodextrins.[31]

Table 1.2 shows the physical properties of the native cyclodextrins ACD, BCD and GCD. GCD has the greatest solubility of the native species as well as the largest diameter and cavity size, which allows it to encapsulate larger molecules in comparison with ACD and BCD.

Table 1.2: Major physical features of native cyclodextrins.[35]

	α	**β**	**γ**
Number of glucose molecules	6	7	8
Molecular weight	972	1135	1297
Aqueous solubility (g/L, 25 °C)	145	18.5	232
Cavity diameter (Å)	4.7 - 5.3	6.0 - 6.5	7.5 - 8.3
Cavity volume (Å^3)	176	346	510

One might expect these structures to have a cylindrical shape, but instead a truncated cone conformation is adopted, with hydroxyl groups lining the exterior (Figure 1.9).

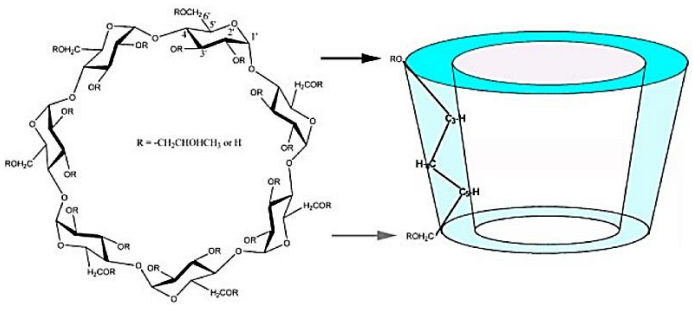

Figure 1.9: Truncated cone structure adopted by CDs (left) and peripheral hydroxyl groups.[36]

This makes it possible for intramolecular O-H···O hydrogen bonding between contiguous glucose rings, reinforcing the circular shape of the macrocycle on the secondary (wider) side. With a hydrophilic exterior and hydrophobic interior it is possible for lipophilic, poorly soluble molecules to be accommodated within the hydrophobic cavity (Figure 1.10), while the hydrophilic exterior allows for an increase in the solubility of the resulting complex. The interior is composed of ether-like and aliphatic groups. Each glucose unit in a CD molecule is a D-(+)-glucopyranose ring with a $^4C_1$ conformation and it is linked to the neighbouring unit via an α-1,4-glycosidic bond. Cyclodextrins are found in a large variety of sizes and conformations. The native structures are relatively rigid and the larger structures tend to have an increased flexibility with a decreased stability. Cyclodextrins can increase the rate of release of a drug by increasing the aqueous solubility and concentration of the diffusible species.[37]

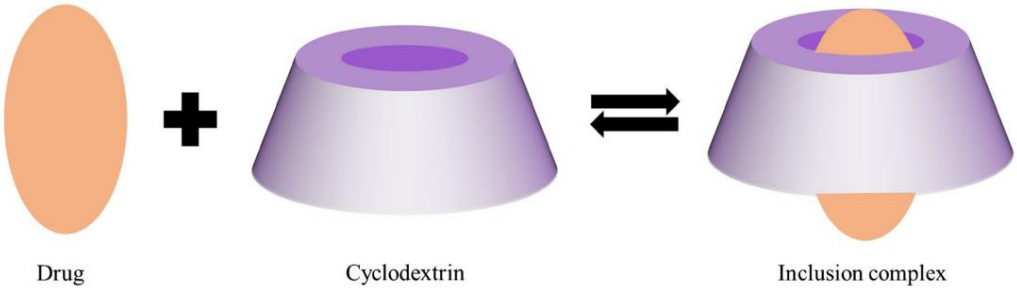

Figure 1.10: Illustration of an API within the hydrophobic cavity of a CD.[33]

There are cyclodextrin derivatives available for pharmaceutical use which in some cases have superior properties to those of the native species. It is important that the cyclodextrins used are not toxic, i.e., they will not cause harm when applied to human skin or are ingested. Well-known examples are sulfobutyl ether β-cyclodextrin (SBEBCD) and hydroxypropyl β-cyclodextrin (HPBCD) (Figure 1.11) which, when compared with BCD (aqueous solubility 18.5 g/L at 25 °C), have much greater aqueous solubilities, viz., >1200 g/ml.[38] Derivatives of ACD and GCD are not commonly used, but the BCD derivatives mentioned above are approved for pharmaceutical use. Cyclodextrins such as permethylated ACD (TRIMEA) and permethylated BCD (TRIMEB) are not used in the pharmaceutical industry due to their haemolytic properties, but they serve as useful models of inclusion phenomena for comparison with those of other CDs.[39]

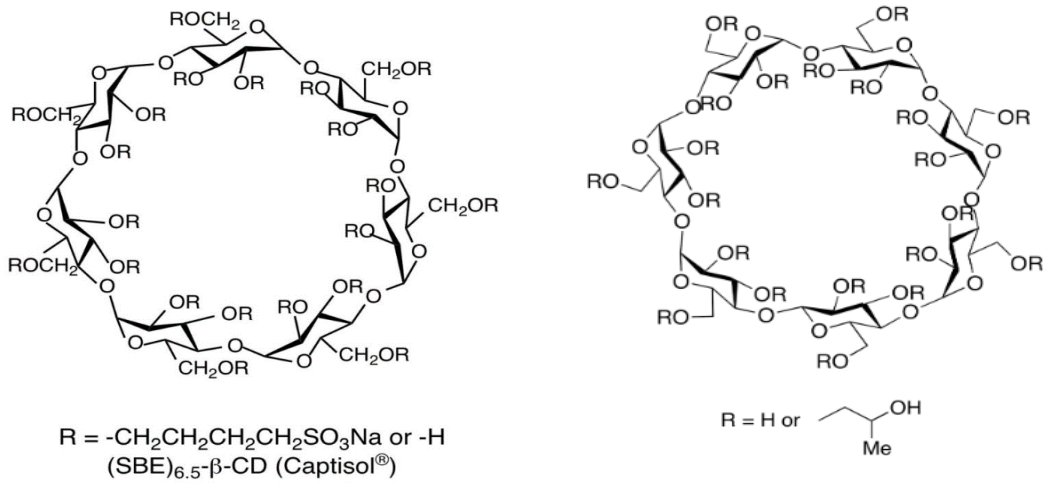

Figure 1.11: Chemical structures of SBEBCD (left)[40] and HPBCD (right).

Due to their ability to form host-guest complexes there is a wide variety of applications of cyclodextrins. They may decrease the unpleasant tastes and odours of products manufactured in both the food and the pharmaceutical industries. In the cosmetic industry they may decrease local irritation of the skin and increase the moisturising and healing properties of lotions.[41] Another beneficial result of CD-mediated API delivery is the reduction of gastrointestinal ulceration that would otherwise result with the uncomplexed API. APIs with acidic functional groups (for example, -COOH) are known to cause ulcers and irritation of the stomach lining, but when they are encapsulated by a CD, such adverse effects are generally mitigated[42] as was evident when meloxicam and prednisolone were encapsulated in CDs.[32] Paczkowka-Walendowska *et al.* showed that there is an increase in both the dissolution rate and membrane permeability of the antibiotic tedizolid, a Class II drug, when complexed with HPBCD.[43] In view of the ongoing concern regarding bacterial resistance, this is an important discovery as it results in enhanced antibacterial potency of tedizolid.

Cyclodextrins as hosts may be used in the extraction and separation of compounds. A combination of CDs has been used in the separation of enantiomers. This can either be achieved with a single CD system or with a dual CD system.[44] The separation of enantiomers using charged and neutral CDs has been extensively studied. Fillet *et al*. investigated the separation of non-steroidal anti-inflammatory drugs (NSAIDs) using capillary electrophoresis (CE).[45] Separation can also be performed with HPLC by having stationary phases that are based on chiral CDs, while CE has the chiral selector in the run buffer.[46] In the food industry cyclodextrins are also used to remove caffeine from coffee and tea to produce caffeine-free beverages. They are also used for the extraction of the active ingredients found in spice plants, and can serve as a coating of the internal surfaces of cans to form a protective barrier

between the food and the can to prevent metal contamination.[47] Cyclodextrins are also used in the synthesis of supramolecular hydrogels through formation of pseudopolyrotaxanes (PPRXs). A PPXR consists of a polymeric chain and a cyclodextrin through which the chain is threaded.[48] Solubility of the polymer as well as the cavity size are important factors to consider in this case.

1.4. General aims and objectives

The overall aim of the present study was to generate new solid forms of the NSAIDs fenbufen and S-(+)-ibuprofen (Figure 1.12). Such new forms might demonstrate improvements in e.g., the aqueous solubility of these APIs.

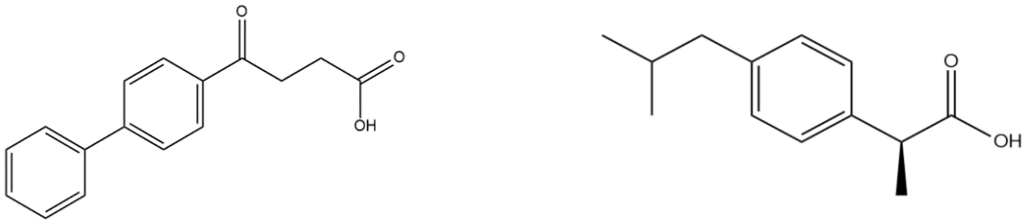

Figure 1.12: Molecular structure of fenbufen (left) and S-(+)-ibuprofen (right).

Anti-inflammatory drugs are well known causes of myocardial infarction, gastrointestinal bleeding and strokes.[49] They are administered world-wide for conditions such as osteoarthritis, rheumatoid arthritis, fever and pain.[50, 51] Hence, it is necessary to mitigate the side effects mentioned above to decrease the negative impact in the body and increase the effectiveness of the treatment.

The mechanism of action of the NSAIDs depends on the drug being used. There are different ways in which NSAIDs act to decrease inflammation. The most common mechanism, and the way in which fenbufen and S-(+)-ibuprofen act, is through the inhibition of cyclooxygenase (COX). Cyclooxygenase is an enzyme used in the synthesis of prostaglandins. These hormone-like lipid compounds are responsible for the regulation of pain sensitization, inflammation and other physiological effects. By inhibiting this enzyme, the effects of pain and inflammation are no longer present.[52]

Fenbufen and S-(+)-ibuprofen were investigated to synthesise new salts, co-crystals and cyclodextrin inclusion complexes. Syntheses were carried out using liquid-assisted grinding (LAG), kneading and co-precipitation methods. Where new phases/inclusion complexes were identified they were characterised using PXRD, SCXRD, thermal analysis and spectroscopic techniques. The working

hypothesis was that new co-crystals, salts and inclusion complexes should enhance the properties of the API being investigated, in particular its aqueous solubility, and decrease side effects.

1.4.1. Fenbufen

Figure 1.13 shows the molecular structure of fenbufen. Table 1.3 lists its salient properties.

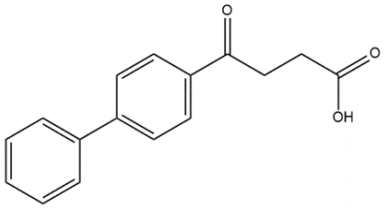

Figure 1.13: The molecular structure of fenbufen.

Table 1.3: Selected properties of fenbufen.

Molecular formula	**$C_{16}H_{14}O_3$**
Molar mass (g/mol)	254.28
Aqueous solubility (mg/mL)	0.0121
Melting point (°C)	182
pKa	4.22

Specific objectives:

Co-crystals and salts:

1) Synthesise salts of fenbufen using GRAS metal ions Na^+, K^+, Ca^{2+} and Mg^{2+}.
2) Perform computational co-crystal screening using the program Mercury[17] to generate a list of coformers that are most likely to form co-crystals with fenbufen.
3) Attempt co-crystal synthesis using LAG and co-precipitation experiments with MeCN, ethyl acetate and EtOH.
4) Characterise all new co-crystals and salts using PXRD, SCXRD, thermal and elemental analysis and spectroscopic techniques.
5) Perform solubility studies on all new co-crystals and salts.

Cyclodextrin inclusion complexes:

1) Attempt the inclusion of the neutral and ionised forms of fenbufen in both native and methylated CDs.
2) Characterise all new CD inclusion complexes using PXRD, SCXRD, thermal analysis and spectroscopic techniques.
3) Carry out aqueous solubility studies on the new inclusion complexes.
4) Perform phase solubility experiments of fenbufen using GCD, HPBCD, SBEBCD and RAMEB.

1.4.2. S-(+)-ibuprofen

Figure 1.14 shows the molecular structure of unionised S-(+)-ibuprofen. Table 1.4 shows several relevant properties of the API.

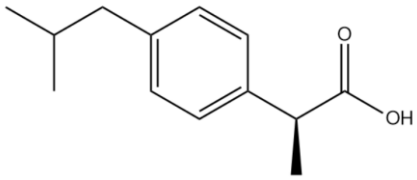

Figure 1.14: Molecular structure of S-(+)-ibuprofen.

Table 1.4: Properties of S-(+)-ibuprofen.

Molecular formula	**$C_{13}H_{18}O_2$**
Molar mass (g/mol)	206.28
Aqueous solubility (mg/mL) at 25°C	0.0684
Melting point (°C)	49-53
pKa	4.85

Specific objectives:

Co-crystal and salts:

1) Perform computational co-crystal screening using Mercury[17] to generate a list of coformers most likely to form co-crystals with S-(+)-ibuprofen.
2) Attempt co-crystal synthesis with GRAS coformers (including zwitterions) using LAG and co-precipitation experiments.

3) Characterise all new co-crystals/salts using PXRD, SCXRD, thermal analysis, elemental analysis and spectroscopic techniques.
4) Perform solubility studies of the new co-crystals/salts.

Cyclodextrin inclusion complexes:

1) Attempt the synthesis of a complex between the host dimethylated β-cyclodextrin (DMB) and S-(+)-ibuprofen.
2) Characterise the new inclusion complex using PXRD, SCXRD, thermal analysis and spectroscopic techniques.
3) Determine whether the inclusion of the API in DMB has a positive effect on the solubility of the API.

The chapter which follows provides details of all the experimental methods employed in these studies.

References

1. Surwase, S. A.; Boetker, J. P.; Saville, D.; Boyd, B. J.; Gordon, K. C.; Peltonen, L.; Strachan, C. J., Indomethacin: new polymorphs of an old drug. *Molecular Pharmaceutics* **2013,** *10* (12), 4472-4480.
2. Saokham, P.; Muankaew, C.; Jansook, P.; Loftsson, T., Solubility of cyclodextrins and drug/cyclodextrin complexes. *Molecules* **2018,** *23* (5), 1161.
3. Thakuria, R.; Sarma, B., Drug-drug and drug-nutraceutical cocrystal/salt as alternative medicine for combination therapy: a crystal engineering approach. *Crystals* **2018,** *8* (2), 101.
4. Datta, S.; Grant, D. J., Crystal structures of drugs: advances in determination, prediction and engineering. *Nature Reviews Drug Discovery* **2004,** *3* (1), 42-57.
5. Steed, J. W., The role of co-crystals in pharmaceutical design. *Trends in Pharmacological Sciences* **2013,** *34* (3), 185-193.
6. Yadav, A.; Shete, A.; Dabke, A.; Kulkarni, P.; Sakhare, S., Co-crystals: a novel approach to modify physicochemical properties of active pharmaceutical ingredients. *Indian Journal of Pharmaceutical Sciences* **2009,** *71* (4), 359.
7. Nangia, A.; Desiraju, G. R., Supramolecular synthons and pattern recognition. *Design of Organic Solids* **1998**, 57-95.
8. Biradha, K., Crystal engineering: from weak hydrogen bonds to co-ordination bonds. *CrystEngComm* **2003,** *5* (66), 374-384.
9. Ghosh, S.; Bag, P. P.; Reddy, C. M., Co-crystals of sulfamethazine with some carboxylic acids and amides: co-former assisted tautomerism in an active pharmaceutical ingredient and hydrogen bond competition study. *Crystal Growth & Design* **2011,** *11* (8), 3489-3503.
10. Kavanagh, O. N.; Croker, D. M.; Walker, G. M.; Zaworotko, M. J., Pharmaceutical cocrystals: from serendipity to design to application. *Drug Discovery Today* **2019,** *24* (3), 796-804.
11. Kumar, S.; Nanda, A., Pharmaceutical Cocrystals: An Overview. *Indian Journal of Pharmaceutical Sciences* **2017,** *79* (6).
12. Fleischman, S. G.; Kuduva, S. S.; McMahon, J. A.; Moulton, B.; Bailey Walsh, R. D.; Rodríguez-Hornedo, N.; Zaworotko, M. J., Crystal engineering of the composition of pharmaceutical phases: multiple-component crystalline solids involving carbamazepine. *Crystal Growth & Design* **2003,** *3* (6), 909-919.
13. Aakeröy, C. B.; Sinha, A. S., Co-crystals: Introduction and scope. In *Co-crystals: Preparation, Characterization and Applications*, The Royal Society of Chemistry: 2018; pp 1-32.
14. Burdock, G. A.; Carabin, I. G., Generally recognized as safe (GRAS): history and description. *Toxicology Letters* **2004,** *150* (1), 3-18.

15. Li, Z.; Matzger, A. J., Influence of coformer stoichiometric ratio on pharmaceutical cocrystal dissolution: three cocrystals of carbamazepine/4-aminobenzoic acid. *Molecular Pharmaceutics* **2016,** *13* (3), 990-995.
16. Sušanj, R.; Nemec, V.; Bedekovic, N.; Cincic, D., Halogen Bond Motifs in Cocrystals of N, N, O and N, O, O Acceptors Derived from Diketones and Containing a Morpholine or Piperazine Moiety. *Crystal Growth & Design* **2022,** *22* (9), 5135-5142.
17. Macrae, C. F.; Sovago, I.; Cottrell, S. J.; Galek, P. T.; McCabe, P.; Pidcock, E.; Platings, M.; Shields, G. P.; Stevens, J. S.; Towler, M., Mercury 4.0: From visualization to analysis, design and prediction. *Journal of Applied Crystallography* **2020,** *53* (1), 226-235.
18. Wicker, J. G.; Crowley, L. M.; Robshaw, O.; Little, E. J.; Stokes, S. P.; Cooper, R. I.; Lawrence, S. E., Will they co-crystallize? *CrystEngComm* **2017,** *19* (36), 5336-5340.
19. Almansa, C.; Frampton, C. S.; Vela, J. M.; Whitelock, S.; Plata-Salamán, C. R., Co-crystals as a new approach to multimodal analgesia and the treatment of pain. *Journal of Pain Research* **2019**, 2679-2689.
20. Wang, X.; Du, S.; Zhang, R.; Jia, X.; Yang, T.; Zhang, X., Drug-drug cocrystals: opportunities and challenges. *Asian Journal of Pharmaceutical Sciences* **2021,** *16* (3), 307-317.
21. Serajuddin, A. T., Salt formation to improve drug solubility. *Advanced Drug Delivery Reviews* **2007,** *59* (7), 603-616.
22. Kumar, L.; Amin, A.; Bansal, A., Salt selection in drug development. *Pharmaceutical Technology* **2008,** *32* (3).
23. Bharate, S. S., Modulation of biopharmaceutical properties of acidic drugs using cationic counterions: A critical analysis of FDA-approved pharmaceutical salts. *International Journal of Pharmaceutics* **2021,** *607*, 120993.
24. Bharate, S. S., Recent developments in pharmaceutical salts: FDA approvals from 2015 to 2019. *Drug Discovery Today* **2021,** *26* (2), 384-398.
25. Fini, A.; Fazio, G.; Gonzalez-Rodriguez, M.; Cavallari, C.; Passerini, N.; Rodriguez, L., Formation of ion-pairs in aqueous solutions of diclofenac salts. *International Journal of Pharmaceutics* **1999,** *187* (2), 163-173.
26. Surov, A. O.; Manin, A. N.; Voronin, A. P.; Drozd, K. V.; Simagina, A. A.; Churakov, A. V.; Perlovich, G. L., Pharmaceutical salts of ciprofloxacin with dicarboxylic acids. *European Journal of Pharmaceutical Sciences* **2015,** *77*, 112-121.
27. Bharate, S. S., Carboxylic acid counterions in FDA-approved pharmaceutical salts. *Pharmaceutical Research* **2021,** *38*, 1307-1326.

28. Elder, D. P.; Holm, R.; De Diego, H. L., Use of pharmaceutical salts and cocrystals to address the issue of poor solubility. *International Journal of Pharmaceutics* **2013,** *453* (1), 88-100.
29. Garbacz, G.; Kandzi, A.; Koziolek, M.; Mazgalski, J.; Weitschies, W., Release characteristics of quetiapine fumarate extended release tablets under biorelevant stress test conditions. *AAPS PharmSciTech* **2014,** *15*, 230-236.
30. Verdugo-Escamilla, C.; Alarcón-Payer, C.; Acebedo-Martínez, F. J.; Domínguez-Martín, A.; Choquesillo-Lazarte, D., New Metformin–Citric Acid Pharmaceutical Molecular Salt: Improving Metformin Physicochemical Properties. *Crystals* **2022,** *12* (12), 1748.
31. Poulson, B. G.; Alsulami, Q. A.; Sharfalddin, A.; El Agammy, E. F.; Mouffouk, F.; Emwas, A.-H.; Jaremko, L.; Jaremko, M., Cyclodextrins: Structural, chemical, and physical properties, and applications. *Polysaccharides* **2021,** *3* (1), 1-31.
32. Tiwari, G.; Tiwari, R.; Rai, A. K., Cyclodextrins in delivery systems: Applications. *Journal of Pharmacy and Bioallied Sciences* **2010,** *2* (2), 72.
33. Kim, D.-H.; Lee, S.-E.; Pyo, Y.-C.; Tran, P.; Park, J.-S., Solubility enhancement and application of cyclodextrins in local drug delivery. *Journal of Pharmaceutical Investigation* **2020,** *50*, 17-27.
34. Wüpper, S.; Lüersen, K.; Rimbach, G., Cyclodextrins, natural compounds, and plant bioactives—a nutritional perspective. *Biomolecules* **2021,** *11* (3), 401.
35. Szejtli, J., Cyclodextrins and molecular encapsulation. In *Encyclopedia of Nanoscience and Nanotechnology*, American Scientific Publishers Stevenson Ranch, CA, USA: 2004; Vol. 2, pp 283-304.
36. Zhang, X.; Wu, D.; Lai, J.; Lu, Y.; Yin, Z.; Wu, W., Piroxicam/2-hydroxypropyl-β-cyclodextrin inclusion complex prepared by a new fluid-bed coating technique. *Journal of Pharmaceutical Sciences* **2009,** *98* (2), 665-675.
37. Bibby, D. C.; Davies, N. M.; Tucker, I. G., Mechanisms by which cyclodextrins modify drug release from polymeric drug delivery systems. *International Journal of Pharmaceutics* **2000,** *197* (1-2), 1-11.
38. Puskás, I.; Varga, E.; Tuza, K.; Szemán, J.; Fenyvesi, É.; Sohajda, T.; Szente, L., Sulfobutylether-cyclodextrins: structure, degree of substitution and functional performance. *Nova Science Publishers Inc.: Hauppauge, NY, USA* **2015**.
39. Róka, E. Biocompatibility evaluation and synthesis of macrocyclic compounds. Université de Lyon; Debreceni egyetem (Debrecen, Hongrie), 2017.
40. Stella, V. J.; Rajewski, R. A., Sulfobutylether-β-cyclodextrin. *International Journal of Pharmaceutics* **2020,** *583*, 119396.

41. Loftsson, T.; Duchene, D., Cyclodextrins and their pharmaceutical applications. *International Journal of Pharmaceutics* **2007,** *329* (1-2), 1-11.
42. Shende, P. K.; Gaud, R.; Bakal, R.; Patil, D., Effect of inclusion complexation of meloxicam with β-cyclodextrin-and β-cyclodextrin-based nanosponges on solubility, in vitro release and stability studies. *Colloids and Surfaces B: Biointerfaces* **2015,** *136*, 105-110.
43. Paczkowska-Walendowska, M.; Rosiak, N.; Tykarska, E.; Michalska, K.; Płazińska, A.; Płaziński, W.; Szymanowska, D.; Cielecka-Piontek, J., Tedizolid-cyclodextrin system as delayed-release drug delivery with antibacterial activity. *International Journal of Molecular Sciences* **2020,** *22* (1), 115.
44. Fillet, M.; Hubert, P.; Crommen, J., Enantiomeric separations of drugs using mixtures of charged and neutral cyclodextrins. *Journal of Chromatography A* **2000,** *875* (1-2), 123-134.
45. Fillet, M.; Fradi, I.; Pedrini, M.; Chiap, P.; Ivanyi, R.; Crommen, J.; Servais, A.-C. In *Enantioseparation of nonsteroidal anti-inflammatory drugs using single-isomer amino cyclodextrin derivatives in nonaqueous capillary electrophoresis*, 20th International Symposium on Microscale Bioseparations, 2006.
46. Perera, S.; Na, Y. C.; Doundoulakis, T.; Ngo, V. J.; Feng, Q.; Breitbach, Z. S.; Lovely, C. J.; Armstrong, D. W., The enantiomeric separation of tetrahydrobenzimidazoles cyclodextrins-and cyclofructans. *Chirality* **2013,** *25* (2), 133-140.
47. Shieh, W. J.; Hedges, A., Properties and applications of cyclodextrins. *Journal of Macromolecular Science, Part A: Pure and Applied Chemistry* **1996,** *33* (5), 673-683.
48. Fang, G.; Yang, X.; Chen, S.; Wang, Q.; Zhang, A.; Tang, B., Cyclodextrin-based host–guest supramolecular hydrogels for local drug delivery. *Coordination Chemistry Reviews* **2022,** *454*, 214352.
49. Davis, A.; Robson, J., The dangers of NSAIDs: look both ways. *British Journal of General Practice* **2016**, *66*, 172-173.
50. Crofford, L. J., Use of NSAIDs in treating patients with arthritis. *Arthritis Research & Therapy* **2013,** *15*, 1-10.
51. Ghlichloo, I.; Gerriets, V., Nonsteroidal anti-inflammatory drugs (NSAIDs). **2019**.
52. Díaz-González, F.; Sánchez-Madrid, F., NSAIDs: learning new tricks from old drugs. *European Journal of Immunology* **2015,** *45* (3), 679-686.

Chapter 2: Experimental methods and materials

The author used a wide variety of coformers and cyclodextrins in the attempt to create new co-crystals, salts and cyclodextrin inclusion complexes with the non-steroidal anti-inflammatory drugs (NSAIDs) fenbufen (FEN) and S-(+)-ibuprofen (S-IBU).

2.1. Active pharmaceutical ingredients (APIs)

The APIs selected for the study, fenbufen (purity <=100%) and S-(+)-ibuprofen, (purity <=100%) were purchased from Sigma-Aldrich (Johannesburg, South Africa) and not purified further.

2.2. Coformers and cyclodextrins

All coformers (Table 2.1) were purchased from Sigma-Aldrich Chemie GmbH (Steinheim, Germany). The following cyclodextrins were purchased from CycloLab (Budapest, Hungary): α-cyclodextrin (ACD), β-cyclodextrin (BCD), γ-cyclodextrin (GCD), hydroxypropyl β-cyclodextrin (HPBCD), sulfobutyl ether β-cyclodextrin (SBEBCD) sodium salt, heptakis(2,6-di-*O*-methyl)-β-cyclodextrin (DMB), heptakis(2,3,6-tri-*O*-methyl)-β-cyclodextrin (TRIMEB), and randomly methylated β-cyclodextrin (RAMEB). All chemicals were used as received.

Table 2.1: Structures of all coformers used in attempts to form co-crystals or salts.

Coformer	Structure	Coformer	Structure
4-hydroxybenzoic acid	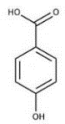	**L-malic acid**	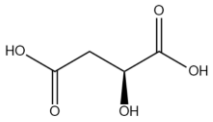
6-aminocaproic acid	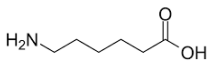	**Glycolamide**	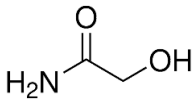
Adipic acid	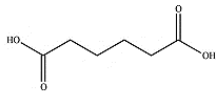	**Maleic acid**	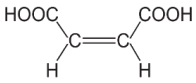
Benzamide	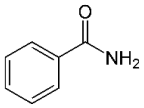	**Oxalic acid**	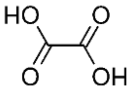
Citric acid	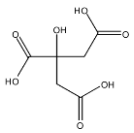	**Saccharin**	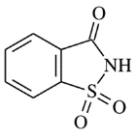
Fumaric acid	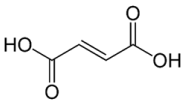	**Suberic acid**	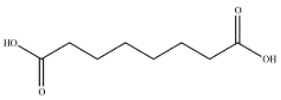
Ferulic acid	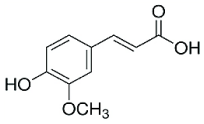	**Succinic acid**	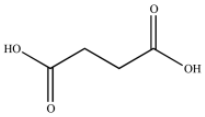
Hippuric acid	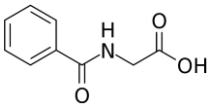	**Tranexamic acid**	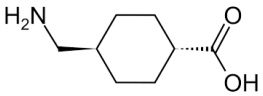
Isonicotinamide	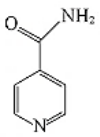	**Orotic acid**	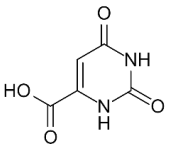
Pyrazinecarboxamide	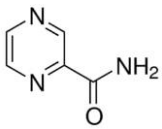	**Urea**	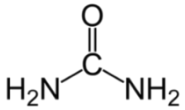
Ethylparaben	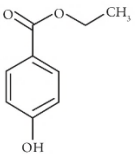	**Pimelic acid**	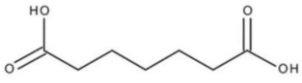

2.3. Co-crystal screening

2.3.1. Virtual screening

Before any attempt at preparing co-crystals, a screening for appropriate coformers was performed using the Molecular Complementarity Screening tool in the CSD Materials module of the program Mercury.[1] The structure of the selected API was uploaded and screened against a list of generally recognized as safe (GRAS) coformers. The list was returned with a 'pass' or 'fail' indicating whether or not a given coformer is most likely to form co-crystals with the API. This virtual screening process uses molecular descriptors to calculate the quantitative structure-activity relationship between the API and coformer. The possible supramolecular synthons between the molecules are also considered when predicting which combinations will result in a co-crystal. Based on the availability in our laboratory, the coformers returned as a 'pass' were tested first.

2.3.2. Liquid-assisted grinding (LAG)

The second screening process involved liquid-assisted grinding (LAG). An equimolar mixture of the API and the selected coformer was ground for a total of 20 minutes (unless stated otherwise) using a mortar and pestle. To effect possible co-crystal formation, the selected solvent for LAG was added to the mortar using increments of 20 μL at appropriate intervals. The powder sample was then analysed using PXRD to determine if a new phase was present.

2.3.3. Co-precipitation

The following procedures were performed in an attempt to produce single crystals for comprehensive structural analysis.

Slow evaporation: Equimolar quantities of the API and coformer were weighed accurately and dissolved separately in a common solvent via heating and stirring. The solution containing the coformer was then added to that of the API. The resulting solution was stirred for a minimum of 4 hours or overnight at approximately 10 °C below the boiling point of the solvent. The hot solution was filtered using a 0.45 μm nylon microfilter. The vial was then left on the benchtop and the solvent was allowed to evaporate slowly through holes pierced into the parafilm® used for sealing the vial.

Slow cooling: When slow evaporation did not produce single crystals large enough for X-ray data-collection, slow cooling was employed. The co-precipitation method was performed and thereafter the filtered, supersaturated solution was capped and sealed using parafilm®. A Dewar flask was filled

with water at the same temperature at which the solution had been stirred and the sealed vial was partially submerged in the water. Using cotton wool and aluminium foil, the flask was insulated to prevent rapid cooling of the water. After three days the insulation was removed, and the resulting crystals were examined.

2.4. Cyclodextrin inclusion complex synthesis

Before attempting the preparation of cyclodextrin (CD) inclusion complexes with the API, the water content of each selected CD was determined using thermal gravimetric analysis (TGA). This needs to be taken into account when calculating the mass of the hydrated CD that would provide the equivalent number of mmol of CD required for the reaction with the relevant number of mmol of the API needed in each experiment.

2.4.1. Kneading

Equimolar amounts of the CD and API were weighed and the mixture was kneaded for 20 minutes using a mortar and pestle. MilliQ® water was added to the powder using increments of 10 µL at suitable intervals to maintain a paste-like texture. The PXRD pattern of the powder product was then compared with reference patterns for isostructural families of CDs and their complexes,[2] in order to establish unequivocally whether complexation had occurred, and if so, the unit cell dimensions and the space group of the new complex could also be predicted. It is important that when recording the PXRD pattern the powder maintains that paste-like texture, because the presence of water molecules in the sample ensures that the CD complex crystals retain optimum crystallinity.

2.4.2. Co-precipitation

The following procedures were performed in an attempt to produce single crystals for comprehensive structural analysis of native and methylated CDs.

Native CD species: Equimolar amounts of CD and API were initially used in attempts to produce single crystals of CD complexes. The CD was dissolved in the minimum amount of MilliQ® water based on its aqueous solubility. While stirring the CD solution at 70 °C, the API was added in small successive increments. The resulting solution was then stirred for a minimum of 4 hours or overnight. If the API did not dissolve in the CD solution after one hour of stirring, temperature cycling was performed. This was achieved by successively increasing and decreasing the temperature between 30

and 80 °C. The solution was then filtered through a 0.45 μm nylon microfilter and allowed to evaporate slowly, until crystals appeared.

Methylated CDs: Methylated CDs and their inclusion complexes, unlike the native species, have negative solubility coefficients in water, readily dissolving in cold water and precipitating from their aqueous solutions at high temperatures.[3] The selected CD was dissolved in the minimum amount of cold water. While stirring at room temperature, small masses of the API were added piecemeal to the CD solution until these additions were complete. If the API did not dissolve after one hour of stirring, temperature cycling was performed using temperatures between 40 and 50 °C. After stirring for 4 - 6 hours, the cool solution was filtered using a 0.45 μm nylon microfilter, capped and placed in an oven set at 60 °C to effect complex crystallization.

2.5. Qualitative and quantitative analysis

2.5.1. Powder X-ray Diffraction (PXRD)

This was the first analytical step after the LAG and kneading experiments were carried out. All powder X-ray diffraction (PXRD) patterns were recorded with a Bruker D2 Phaser desktop powder diffractometer (Billerica, Massachusetts, USA) using a CuKα_1 radiation source (λ = 1.5406 Å) with X-ray generator settings at 30 kV and 10 mA. A small quantity of the powder product or the ground crystalline material was placed on the silicon zero-background sample holder. Each sample was scanned from 4.0 to 40.0° 2θ with a step size of 0.0164°. The PXRD trace of the product was compared with those of the starting materials to determine if a new phase was present. The disappearance of significant peaks found in the starting materials and the presence of new peaks confirm that a new phase was present. PXRD was also used when comparing the predicted pattern based on single-crystal X-ray diffraction (SCXRD) data and the experimental PXRD pattern, to determine whether the selected crystal was representative of the bulk material.

2.5.2. Variable-temperature powder X-ray diffraction (VT-PXRD)

Variable-temperature powder X-ray diffraction (VT-PXRD) was used to complement thermal analyses in situations where the latter methods indicated possible phase transitions and other thermal events. Upon controlled heating of a multi-component material, numerous events (e.g., desolvation, phase changes, recrystallizations, decomposition) might occur, and a series of VT-PXRD patterns recorded at judiciously selected sample temperatures based on HSM, DSC and TGA data could

therefore contribute to the correct assignment of such events. VT-PXRD patterns in the 2θ-range 4.0 – 40.0° and a step size of 0.0164° were recorded *in vacuo* on a Bruker D8 Advance powder diffractometer (Billerica, Massachusetts, U.S.A) with CuKα_1 radiation (λ = 1.5406 Å) and with generator settings 30 mA and 30 kV.

2.5.3. Single-crystal X-ray Diffraction (SCXRD) and crystal structure determination

Single-crystal X-ray diffraction (SCXRD) was used to solve the structures of good quality single crystals produced by co-precipitation. The crystals were removed from their mother liquor and surface solvent was rapidly absorbed on filter paper. To preserve the crystals as well as any solvent that might be included in their crystal structure, the selected specimens were immersed in Paratone® N oil (Exxon Chemical Co., TX, USA). The unit cell parameters were then determined on a Bruker D8 VENTURE SCXRD diffractometer (Madison, Wisconsin, U.S.A) and compared with those in the CSD to avoid possible duplication of previously published results. When a unique unit cell was found, full intensity data-collection was performed with the crystal cooled to 100(2) K (unless otherwise stated) using an Oxford Cryostream-800 (Oxford Cryosystems, U.K.) which supplied a constant stream of N_2 vapour.

Data integration and unit cell refinement were performed with SAINT-Plus.[4] The software program XPREP[5] identifies the systematic absences in the measured intensities to determine the space group. Thereafter, the crystal structure was solved by direct methods using SHELXS-2018.[6] SHELXL-2019[6] was subsequently used for refinement of the model by full-matrix least-squares techniques. Both SHELXL-2018 and SHELXL-2019 were operated using the interface X-SEED.[7] The program SADABS[8] was used for empirical absorption correction of reflection intensities by the multi-scan method.

Non-hydrogen atoms were assigned to appropriate positions based on the known chemistry of the moieties involved, taking into account also their peak heights in the E-map. Once the non-hydrogen atoms were assigned, they were refined initially isotropically and subsequently anisotropically. All hydrogen atoms were first located in difference Fourier syntheses and were then generally placed in idealised positions on their parent atoms using a riding model. They were assigned isotropic displacement parameters (U_{iso}) with values 1.2 and 1.5 times those of their parent atoms, depending on their type (e.g. phenyl, methyl). For functional groups such as -NH_2 that showed coplanarity of the C-NH_2 unit, the H atoms were added in idealised positions, but in the case of pyramidal geometries, the observed electron density peaks for the H atoms were assigned as such and allowed

to refine freely, or with N-H bond length restraints in the event that the freely refined N-H distances were unreasonable. Similarly, following location of H atoms of water molecules, the observed electron density peaks were assigned and the H atoms refined freely and usually with O-H bond length restraints. For hydroxyl groups, the 'rotating model' was generally employed to ensure that the H atom placed by this model coincided with that of the observed electron density peak of the H atom.

Unequivocal hydrogen atom location was of pivotal concern when attempting to distinguish co-crystals and salts. Binary co-crystals were identified by locating all H atoms and finding that both components retained their original structures as neutral molecules. However, in the case of salt formation, transfer of a proton from e.g. a carboxylic acid group of one component to an acceptor atom in the second component, was evident from its new location. Furthermore, such transfer results in the -COOH group of the first component becoming a carboxylate group ($-COO^-$), with the two C-O bonds of the delocalised system having equal lengths within experimental error, providing further confirmation of salt formation.

The structures of CD inclusion complexes were solved either by direct methods (with SHELXS or SHELXD).[6] In favourable cases, subsequent refinement revealed the guest molecule and water molecules. Modelling, including anisotropic treatment of the non-H atoms and H atom location, followed in the usual manner. Bond length restraints were applied when refinement led to abnormal distances. Molecules of the host, guest and water molecules in CD complexes are frequently disordered, necessitating multiple refinements to optimise the structural model. Once the crystal structure had been finalised the intramolecular and intermolecular parameters were determined using PLATON.[9]

2.5.4. Proton nuclear magnetic resonance (^{1}H NMR) spectroscopy

^{1}H NMR spectra were recorded on a Bruker Ultrashield 300 Plus spectrometer, unless stated otherwise. All spectra were analysed using the software MestReNova.[10] Analysis was carried out by dissolving 3 - 5 mg of the sample in DMSO-d_6 or D_2O. The stoichiometric ratios of the components in co-crystals, salts and inclusion complexes were determined based on the observed proton integration values. Protons that would not undergo any exchange with the deuterated solvents were chosen for the integrations.

2.5.5. Hot stage microscopy (HSM)

Hot stage microscopy (HSM) is used to view any physical changes that a material undergoes upon heating, such as dehydration, melting, decomposition, sublimation and any phase changes. Samples were heated over the range ~20 to 350 °C using a Linkam THM600 hot stage, whose temperature was varied using a TP92 controller unit. Unless stated otherwise, the behaviour of each sample was recorded using a heating rate of 10 K min^{-1}. Crystals and powdered samples under investigation were viewed through a Nikon SMZ-10 stereo-microscope and micrographs of significant thermal events were captured using a Sony Digital Hyper HAD video camera. The data were processed using Soft Imaging Program AnalySIS software.[11] A few single crystals or small amounts of powdered samples were placed in silicone oil on a glass slide.

2.5.6. Thermogravimetric analysis (TGA)

Thermogravimetric analysis (TGA) curves were recorded using a TA-Q500 instrument (New Castle, Delaware, U.S.A) and analysed using TA universal analysis 2000 software.[12] An accurately weighed sample with mass between 3 and 5 mg was placed in the crucible. All measurements were recorded using a 10 K.min^{-1} heating rate. TGA curves for co-crystals were recorded from 20 to 350 °C and CD complexes from 20 to 400 °C, unless otherwise stated. A constant stream of dry N_2 purge gas was supplied to the instrument at a flow rate of 60 ml.min^{-1}. The experiment was generally stopped after major sample decomposition had taken place. Thermal events such as desolvation and decomposition were identified based on the TGA curve. The measured mass loss percentage for desolvation enabled the amount of solvent in the crystal structure to be determined. Both the loss of a component from a multi-component system on heating and the extent of decomposition could likewise be determined from their accompanying mass loss percentages.

2.5.7. Differential scanning calorimetry (DSC)

Differential scanning calorimetry (DSC) indicates thermal events such as melting, crystallizations, glass transitions, phase transitions, and decomposition. The stability of a new product can therefore be compared with those of the starting materials. DSC was carried out using a TA Discovery DSC 25 instrument (New Castle, Delaware, U.S.A) and analysed using TRIOS software.[13] Onset and peak temperatures for observed exotherms and endotherms in the DSC curve were quantified using the processing software. The temperature range for DSC analysis of a given material was chosen based on the previously recorded TGA curve and HSM images. To prevent any damage to the instrument

the temperature could not be increased beyond the onset of sample decomposition. An accurately weighed sample in the range 1 - 2 mg was placed in an aluminium pan. Single crystal samples were removed of excess surface solvent and finely ground before analysis to ensure uniform particle size. All experiments were performed using a heating rate of 10 $K.min^{-1}$.

2.5.8. Fourier-transform infrared (FT-IR) spectroscopy

Fourier-transform infrared (FT-IR) spectroscopy identifies characteristic vibrational frequencies and the appearance or disappearance of spectral bands in the product compared to those of the starting materials, enabling the identification of new interactions such as hydrogen bonds and proton transfers. The spectra were recorded using a PerkinElmer Spectrum Two instrument (Waltham, MA, U.S.A) fitted with an attenuated total reflectance (ATR) attachment (Waltham, MA, USA). Before collecting spectra, the diamond was cleaned and the background radiation spectrum was recorded. A small amount of the sample was then placed on the diamond crystal and sealed with the ATR attachment to ensure tight contact. All measurements were recorded over the range 4000 - 400 cm^{-1} with a spectral resolution of 4 cm^{-1} and 32 accumulations.

2.5.9. Elemental analysis (EA)

Elemental analysis (EA) was used to determine the percentages of C, N and H in the samples, from which the stoichiometry of the co-crystals and salts could be ascertained. All analyses were performed on an Elementar Vario EL Cube Elemental Analyzer (Elementar Analysensysteme GmbH, Langenselbold, Germany). Before analysis the ground single crystals/powder product was dried to ensure that no solvent remained on the surface. Samples with masses in the range 4 - 12 mg were weighed accurately to 3 decimal places. To ensure that the results were trustworthy, a standard was run after each sample. If the elemental composition of each element was found to be within the acceptable range, the results were deemed reliable. In order for the results to be acceptable, the experimental % composition of each element should not exceed ± 0.4% of the calculated value.[14]

2.6. Solubility studies

Solubility studies are carried out to determine whether there is an increase or a decrease in the solubility of a new multi-component compound containing an API relative to that of the untreated API. For new materials that have potential medicinal application, such measurements in water or

simulated intestinal fluid are essential to have an indication as to how API bioavailability might be affected by oral administration of the new material. Various solubility studies were performed based on the nature of the sample. Before carrying out the experiment the purity of the sample was confirmed by PXRD or DSC.

2.6.1. Calibration curves

A standard solution of the API was prepared by dissolving an accurately weighed amount of the API in a known volume of EtOH (unless stated otherwise). The serial dilutions were prepared by diluting the EtOH standard solution with MilliQ® water to make 2% EtOH solutions of varying API concentrations. This was necessary due to the poor aqueous solubility of the APIs in question. A five- or ten-point calibration curve was constructed for HPLC or UV-Vis quantification respectively. Each standard solution was prepared using a 10 ml volumetric flask filled to the mark using MilliQ® water. Either an absorbance *vs* concentration, or area *vs* concentration curve was constructed from UV-Vis or HPLC measurements respectively (all of which will be described later in this chapter). The concentration of API in solution was determined using the equation of the linear graphs produced.

2.6.2. Gravimetric solubility studies

A gravimetric solubility study was performed when UV-Vis or HPLC could not be used for quantification of saturated solution concentrations. The material of interest (API or multi-component material containing the API) was added to an accurately measured volume of Fasted State Simulated Intestinal Fluid (FaSSIF) solution buffered at pH 2.0 or 6.5 in accurately weighed increments of approximately 0.10 mg each to achieve saturation. This biological medium mimics the conditions found in the fasted state, enabling a more realistic representation of the effects that a co-crystal or salt might have on the solubility of the API component than is possible using pure water as a dissolution medium. Before adding another increment, the solution was stirred for a sufficient length of time to ensure that all the material had dissolved. The incremental masses were added until it was evident that the sample no longer dissolved. The saturated solution was stirred at 250 rpm and 25 ± 1 °C and was closely monitored for 72 hours. The total amount of the sample added was then determined by calculating the average value of the penultimate and final cumulative masses. The final API concentration in the product was determined by calculating the API equivalent in the salt/co-crystals/CD complex. The solubility change was determined by comparing the solubility of the API equivalent in the product to that of the pure API (control).

A second method was employed in which an excess amount of the API/co-crystal was added to 4.0 ml of MilliQ® water. The saturated solution was then stirred at 250 rpm and 25 ± 1 °C for 72 h. A 1.0 ml aliquot was removed and filtered through a 0.45 µm nylon microfilter. The water was then allowed to evaporate and the sample left to dry in an oven set at 60 °C. The mass of the precipitate remaining was measured, and the solubility determined in units of mg/ml. The measurements were carried out in duplicate and the average value recorded.

2.6.3. Dynamic solubility studies

Dynamic solubility studies are carried out to record the change in the concentration of the API/co-crystal with respect to time. The dissolution profile indicates if the behaviour of the sample is in accord with the 'spring and parachute' model[15], shown in Figure 2.1. In this model there is a sharp increase in the concentration of the API (the 'spring'). Thereafter, there is a steady decrease (the 'parachute') in the concentration with time. The sharp increase occurs when the API, which is hydrophobic, becomes supersaturated in the solution as the water-soluble coformer is removed from the crystal. This is beneficial, allowing maximum absorption of the API *in vivo* if the high concentration is maintained for an adequate amount of time. This is the preferred dissolution profile in comparison to that of the API in its crystalline form, which shows poor solubility. If only a spring (sharp increase followed by a drop in the solubility) is observed, the metastable species is transient and will not allow for sufficient time to absorb the API. The addition of substances (in this case the coformer) that slow down nucleation of the final product will render the dissolution profile that of the 'spring and parachute' model. This *in vitro* study allows us to determine the way in which the cocrystal/salt might behave *in vivo.*

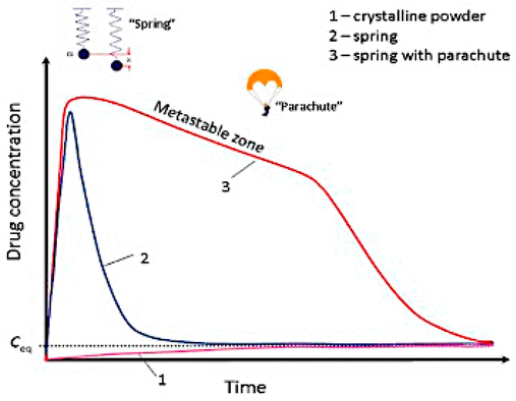

Figure 2.1: Dissolution profile of 1) stable crystalline form of the API, 2) Spring – rapid metastable form of the API present, and 3) Spring and parachute concept – a long lasting metastable form of the API.[15]

The dynamic solubility studies were carried out in 20 ml of the FaSSIF solution in a HCl (pH 2.0) or phosphate (pH 6.5) buffer. The API or co-crystal/salt (using the API equivalent) was sieved to ensure that the particle size was in the range 50 - 150 µm. The sieved material was then added to the FaSSIF solution at the selected pH. The solution was stirred at 250 rpm and 37 ± 2 °C, for the duration of the experiment. Aliquots of 0.7 ml were removed at times 1, 5, 10, 15, 30 min, and 1, 1.5, 2, 3, 4, and 6 h after the addition of the material. The aliquots were filtered through a 0.45 µm nylon microfilter and diluted using EtOH or water to concentrations within the detection limits of the UV-Vis/HPLC instrument used. It is important that the material should be soluble in the solvent used for dilution to ensure that it does not precipitate from solution.

2.6.4. Phase solubility studies

Phase solubility studies were performed to investigate how an increasing CD concentration in water as a medium affects the solubility of the API. From these experiments phase-solubility profiles were produced that provide information on the stoichiometries and stability constants of the inclusion complexes investigated. The greater the stability constant the greater the affinity of the API for the CD. The intrinsic solubility of the drug (S_0) and the slope of the graph are used to calculate a) the stability constant ($K_{1:1}$) and b) the complexation efficiency (CE),[16] as defined in the equations below:

a) $$K_{1:1} = \frac{\text{Slope}}{S_0(1-\text{Slope})}$$

b) $$\text{CE} = K_{1:1} \cdot S_0 = \frac{\text{Slope}}{(1 - \text{Slope})}$$

The phase-solubility profiles are categorised into types A and B as shown in Figure 2.2. The A-type profiles display a positive increase in the API concentration with increasing [CD] and are subdivided into types A_L, A_P and A_N. A_L represents the linear behaviour. A_P and A_N show positive and negative deviations from the linear graph with increasing CD concentrations respectively. B-type profiles on the other hand are observed when the complex is insoluble in the media after a certain concentration is attained. These are categorised into types B_S and B_I which occur when the complex is slightly soluble and insoluble respectively.[17]

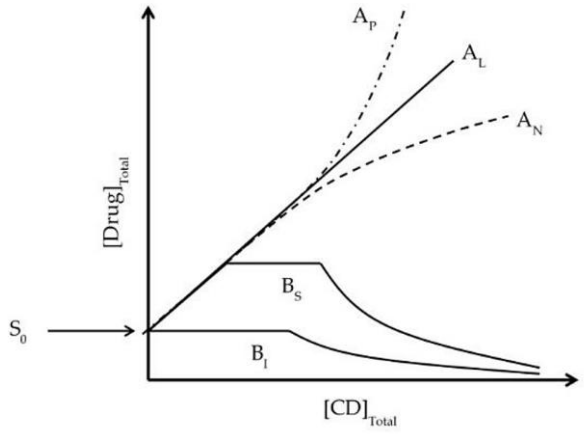

Figure 2.2: Representative phase-solubility profiles of types A and B.[17]

A 20 mM standard solution of the selected CD was prepared using MilliQ® water and stirred for 72 hours at room temperature. Serial dilutions of the CD solution were made ranging from 10 to 100% and diluted to 5 ml using MilliQ® water. Excess API was added to each CD solution and the contents of the vials were left to stir at 250 rpm for 72 hours at 25 ± 1 °C. The solutions were then filtered through a 0.45 μm nylon microfilter and thereafter the concentration of the API was determined using UV-Vis spectroscopy.

2.6.5. Equilibrium solubility studies

Equilibrium solubility studies were carried out by adding an excess quantity of the salt/CD complex to 1.0 ml of MilliQ® water. The mixture was stirred for 72 hours at 25 ± 1 °C and then filtered using a 0.45 μm nylon microfilter and the concentration of API was quantified using HPLC. When necessary, the solution was diluted using water in order for the API concentration to be within the detection limits of the HPLC.

2.7. Quantitative analysis of solubility studies

2.7.1. UV-Vis spectroscopy

The UV-Vis absorbance was measured on a UV Cary 60 spectrophotometer. First, the solutions for API assay were filtered through a 0.45 µm syringe filter, as any precipitation will influence the absorbance. The λ_{max} of the compound of interest was determined by recording the absorbance from 200 - 800 nm. In the case of co-crystals, it is important that there should be no overlap in the absorbance of the API and the coformer. All measurements were recorded at the selected λ_{max} value using the simple scan method. By means of the calibration curve (method described in section 2.6.1. Calibration curve), the concentration of API in solution was determined.

2.7.2. High-performance liquid chromatography (HPLC)

When UV-Vis spectroscopy showed overlap in the absorbance profiles of the API and coformer, High-performance liquid chromatography (HPLC) was instead used to determine the API concentration. All measurements were recorded on an Agilent 1220 Infinity LC system and the data analysed using Agilent ChemStation.[18] The HPLC equipment contains a UV-Vis variable wavelength detector that measures the absorbance at a specified wavelength. All analyses were performed using an autosampler and passed through the temperature-controlled oven. Quantification and separation were achieved using an Agilent Poroshell 120 EC - C18 (4.6 mm × 50 mm) column with a particle size of 2.7 µm. The mode was set to gradient elution. MeOH was used as the mobile phase along with phosphate buffer (pH 7.5, 50 mM). The specific method was modified based on the retention times and the nature of the sample. All samples were diluted with MilliQ® water or EtOH, to be within the detection limits of the HPLC instrument.

References

1. Macrae, C. F.; Sovago, I.; Cottrell, S. J.; Galek, P. T.; McCabe, P.; Pidcock, E.; Platings, M.; Shields, G. P.; Stevens, J. S.; Towler, M., Mercury 4.0: From visualization to analysis, design and prediction. *Journal of Applied Crystallography* **2020,** *53* (1), 226-235.
2. Caira, M. R., On the isostructurality of cyclodextrin inclusion complexes and its practical utility. *Revue Roumaine de Chimie* **2001,** *46* (4), 371-386.
3. Cho, E. C.; Lim, H. J., Monitoring Processes for the Heat-Induced Crystallization of Heptakis (2, 6-di-O-methyl)-β-cyclodextrin in Water. *Crystal Growth & Design* **2011,** *11* (10), 4296-4299.
4. Bruker AXS Inc., Program SAINT, Version 7.60a, Bruker AXS Inc., Madison, WI, USA, **2006**.
5. XPREP *Data Preparation and Reciprocal Space Exploration*, 2008/2; Bruker Analytical X-Ray Systems: **2008**.
6. Sheldrick, G. M., A short history of SHELX. *Acta Crystallographica Section A: Foundations of Crystallography* **2008,** *64* (1), 112-122.
7. Barbour, L. J., X-Seed—A software tool for supramolecular crystallography. Elsevier: **2001**.
8. Sheldrick, G., SADABS, version 2.05; University of Göttingen: Göttingen, Germany.
9. Spek, A. L., Structure validation in chemical crystallography. *Acta Crystallographica Section D: Biological Crystallography* **2009,** *65* (2), 148-155.
10. *MestReNova*, Version: 6.0.2-5475; Chemistry Software Solutions: Spain, **2023**.
11. *Soft Imaging System GmbH*, Version 3.1 for Windows; Digital Solutions for Imaging and Microscopy.
12. Universal Analysis 2000 (TA Instruments-Waters LLC), Version 4.5A for Windows 2000/XP/Vista (Copyright, 1998 – 2007).
13. TA Instruments-Waters LLC. 159 Lukens Drive, New Castle, DE19720 2020.
14. Kuveke, R. E.; Barwise, L.; van Ingen, Y.; Vashisth, K.; Roberts, N.; Chitnis, S. S.; Dutton, J. L.; Martin, C. D.; Melen, R. L., An international study evaluating elemental analysis. *ACS Central Science* **2022** *8* (7), 855-863.
15. Karimi-Jafari, M.; Padrela, L.; Walker, G. M.; Croker, D. M., Creating cocrystals: A review of pharmaceutical cocrystal preparation routes and applications. *Crystal Growth & Design* **2018,** *18* (10), 6370-6387.
16. Loftsson, T.; Hreinsdóttir, D.; Masson, M., Evaluation of cyclodextrin solubilization of drugs. *International Journal of Pharmaceutics* **2005,** *302* (1-2), 18-28.
17. Saokham, P.; Muankaew, C.; Jansook, P.; Loftsson, T., Solubility of cyclodextrins and drug/cyclodextrin complexes. *Molecules* **2018,** *23* (5), 1161.

18. *OpenLab CDS ChemStation Edition for LC & LC/MS Systems*, Version A.01.05; Agilent Technologies: Santa Clara, CA, USA, **2013**.

Chapter 3: Synthesis of fenbufen metal salts

3.1. Literature review

Elements such as lithium, vanadium, manganese, iron, copper and rubidium are just a few that are used in the pharmaceutical industry.[1] Lithium is widely used to treat psychiatric disorders while manganese and rubidium are used in MRI contrast agents for the diagnosis of tumours and heart disease respectively. Group I metals are also used to a large extent, namely Na^+ and K^+ due to their non-toxic nature. As discussed in Chapter 1, pharmaceutical salts have a wide range of benefits such as increased solubility and stability. Fenbufen (FEN), having an acidic group (Figure 3.1), requires a basic environment to be deprotonated.

Due to the deficiency of co-crystal formation and cyclodextrin complexation with the API fenbufen noted in Chapters 4 and 5 of this dissertation, an attempt was made to synthesise a series of fenbufen metal salts. Many advantages of ionised drugs have been reported, such as an increased stability, solubility and dissolution rate, as has been discussed in Chapter 1 (1.3.3. Salts, pg. 5).

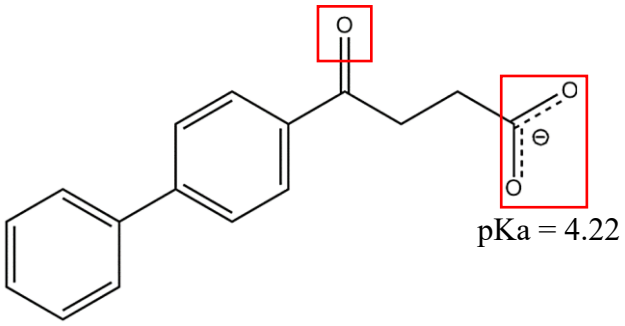

Figure 3.1: The anionic structure $(fenbufen)^-$ with possible hydrogen bonding sites (red).

Attempts to ionise fenbufen and form salts with sodium, potassium, magnesium and calcium salts were carried out. Group 1 metals, sodium and potassium, were the only ones which led to successful syntheses. The isolated salts were subsequently reacted with the cyclodextrins ACD, BCD, GCD and DMB with the intention of forming complexes. The results of those experiments appear in the next chapter of this dissertation.

3.2. Fenbufen sodium salt – Fen^-Na^+

The sodium salt was synthesised using equimolar amounts of FEN and NaOH (1M) dissolved in 1.0 ml of water. The base was added dropwise to the FEN solution while stirring at 70 ± 5 °C. As the base was being added, the solution became clear, indicating that FEN was being ionised. The solution was left to stir at 250 rpm for 4 h and thereafter the hot solution was filtered through a 0.45 μm nylon microfilter. Once the solution had cooled, the product precipitated. The crystals that formed were thin, needle-shaped specimens with poor X-ray diffraction. The rate of cooling was therefore reduced by using the slow cooling method described in Chapter 2 (2.3.3. Co-precipitation, pg. 22). The filtered solution was capped, sealed and placed inside a Dewar flask filled with water at 70 °C. The vial was removed after 3 days and thereafter placed in the refrigerator to further retard crystallisation. After 7 days, single crystals suitable for X-ray data-collection were harvested.

3.2.1. Proton nuclear magnetic resonance (^{1}H NMR) spectroscopy.

Table 3.1 lists the chemical shifts of the signals in the ^{1}H NMR spectra of FEN and Fen^-Na^+ recorded in DMSO-d_6. The signals were assigned using the numbering scheme shown in Figure 3.2. The proton of the -COOH group of FEN, resonating at 12.17 ppm, is not present in the Fen^-Na^+ spectrum. This confirms that the product is deprotonated. There is an upfield shift in the signals produced by the methylene groups in FEN. The spectrum can be found in the Appendix (Section 1.1, pg. 2).

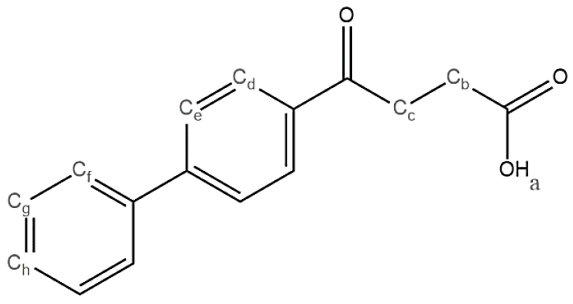

Figure 3.2: Numbering scheme of FEN for the assignment of protons.

Table 3.1: The chemical shifts of diagnostic peaks in the ^{1}H NMR spectra of FEN and $Fen^{-}Na^{+}$.

Assignment	FEN δ (ppm)	$Fen^{-}Na^{+}$ δ (ppm)
COOH (a)	12.17	-
CH aromatic (f)	8.09 - 8.06	8.05 - 8.03
CH aromatic (d, e)	7.86 - 7.75	7.82 - 7.73
CH aromatic (g, h)	7.55 - 7.42	7.53 - 7.40
CH_2 (b)	3.32 - 3.28	3.15 - 3.10
CH_2 (c)	2.64 - 2.59	2.28 - 2.23

3.2.2. Thermal analysis

3.2.2.1. Hot stage microscopy (HSM)

Figure 3.3 shows the HSM images of $Fen^{-}Na^{+}$ recorded from 26 to 236 °C. The crystals, which are clear plates at room temperature, were dried to remove surface water and thereafter placed in silicone oil. The crystals begin changing from clear to brown at 45 °C. As the temperature increases, the browning continues and there is a phase change of a solid to liquid from 65 °C which continues until 87.7 °C. At this point bubbling begins and the crystal has now liquefied. The bubbling represents the dehydration of the crystal structure.

At 104.1 °C the liquid begins solidifying, indicating another phase change taking place. At 116.8 °C the phase change is complete, with the product being a white solid. This form was then stable with increasing temperatures and did not undergo any changes. However, decomposition, indicated by the browning of the sample, began at 224.7 °C and was completed by 232.4 °C.

Figure 3.3: The HSM images of $Fen^{-}Na^{+}$ salt crystals from 26 to 236 °C, heated at 5 °C/min.

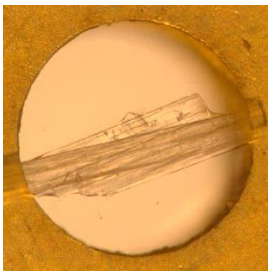

26.4 °C: $Fen^{-}Na^{+}$ salt at room temperature.

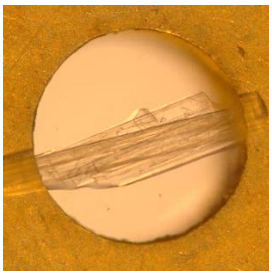

45.0 °C: First sign of browning.

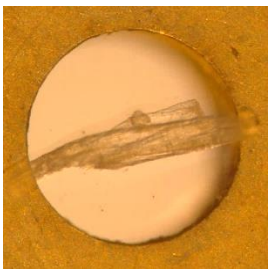

65.0 °C: Phase change from solid to liquid begins.

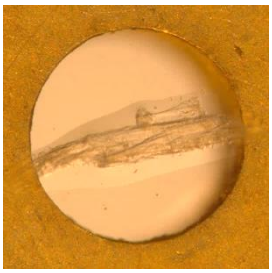

77.7 °C: Continued melting.

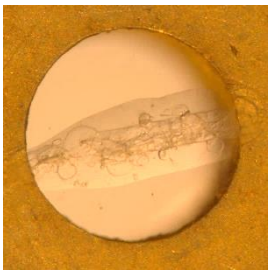

87.7 °C: The crystal has now liquefied, and bubbles appear.

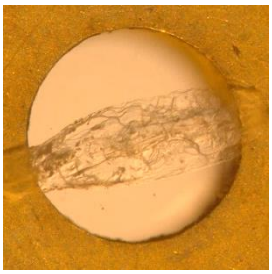

104.1 °C: Phase change begins as the liquid solidifies.

116.8 °C: Phase change to fibre-like crystals.

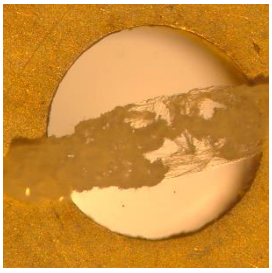

140.6 °C: Phase change is complete.

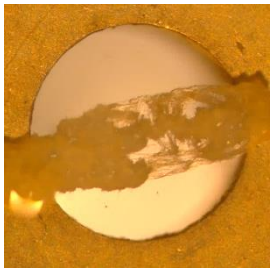

224.7°C: The start of the second decomposition step.

232.4 °C: Complete decomposition reached.

3.2.2.2. Thermal gravimetric analysis (TGA) and differential scanning calorimetry (DSC)

The TGA (n = 2) and DSC curves of $Fen^{-}Na^{+}$ are shown in Figure 3.4. The TGA curve, recorded from 20 to 350 °C, shows four thermal events. The first and second mass losses with a combined mass loss of 23.6 ± 0.3 % and an onset temperature of 20.6 °C, is the dehydration. The total mass loss is equivalent to 4.7 ± 0.1 water molecules for each $(FEN)^{-}$ ion. The third step involves a 1.29 ± 0.8 % loss with onset temperature 222.6 °C. The final decomposition step has an onset temperature of 287 °C.

The DSC curve, recorded from 20 to 300 °C, coincides with the mass losses seen in the curve produced by TGA, with three thermal events taking place. The first endothermic peak at 55.2 °C and

the broad endotherm from 61 to 89 °C correspond with the phase change as well as the bubbling that is observed in the HSM. Based on the curve and the HSM images the salt melts at 55.2 °C. The small endotherm at 142.9 °C coincides with the second mass loss seen in the TGA curve. The HSM images show that at this temperature a phase change has taken place. The sharp endothermic peak present at 231.7 °C has a temperature range 215.1 – 233.0 °C, corresponding to the third mass loss seen in the TGA. The HSM images show that decomposition begins within this range at 224.7 °C. The inconsistency in these onset temperatures may be due to the difference in the instrumental conditions, or due to the possibility that minor colour changes were not clear at lower temperatures. As the temperature increases to 300 °C the DSC curve shows that decomposition is taking place. The melting point of the salt is significantly lower than that of FEN, therefore indicating that the sodium salt has the lower thermal stability.

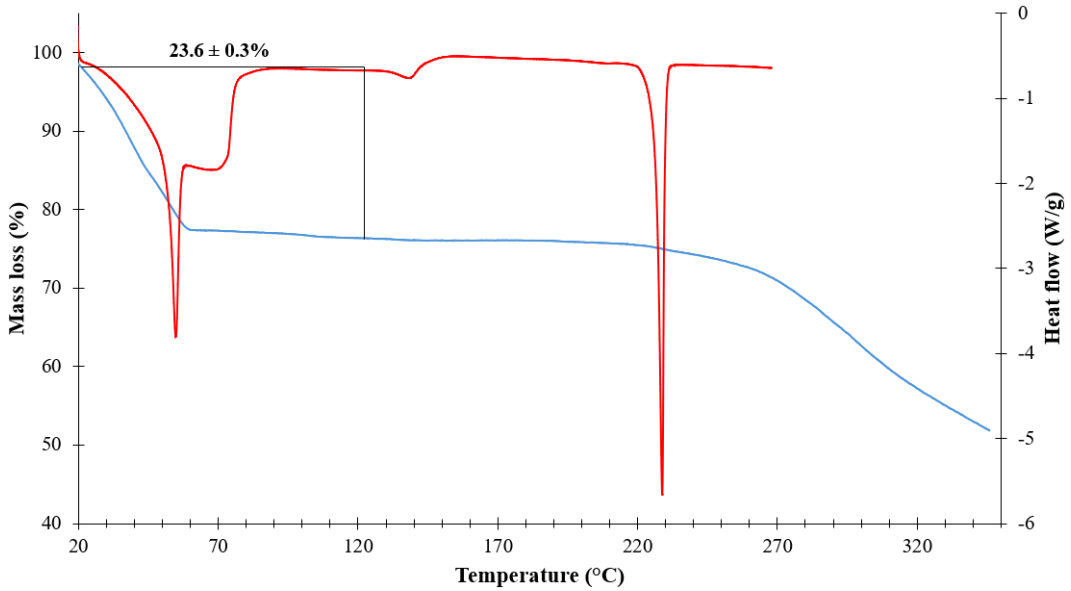

Figure 3.4: The TGA (blue) and DSC (red) curves for the salt $Fen^{-}Na^{+}$.

3.2.3. Crystal structure analysis

Data-collection and space group determination

The full data-collection for the determination of the $Fen^{-}Na^{+}$ crystal structure was performed with the crystal cooled to 100(2) K by the Oxford nitrogen cryostream system. It was determined that the Laue symmetry was $\bar{1}$, which indicated that the crystal belongs to the triclinic system. Using XPREP,[2] the space group was confirmed to be $P\ \bar{1}$, based on the value of $|E^2 - 1| = 1.016$.

Structure solution and refinement

The structure was solved by direct methods using SHELXS-2018 and refined with SHELXL-2019.[3] All non-hydrogen atoms were assigned to appropriate electron density peaks and were then refined isotropically, and subsequently anisotropically, before adding hydrogen atoms. The hydrogen atoms were added to the phenyl rings, methylene and methyl carbon atoms using the riding model. It was confirmed that during salt formation FEN had been deprotonated by observing that the C-O bond lengths were equal within experimental error, the C-O distance range for the four crystallographically independent anions being 1.244(4) -1.277(4) Å. The electron density peaks indicated the presence of water molecules, both in isolated sites, as well as bonded to sodium ions. The resulting moieties in the latter case were repeated di-μ-aqua-bis[triaquasodium(I)] units with $(FEN)^{-}$ ions (Figure 3.5) that crystallize in an infinite polymeric chain. Hydrogen atoms of water molecules were located unequivocally in difference Fourier maps and added to the oxygen atoms, with restrained O-H lengths of 0.84 Å. Table 3.2 shows the final crystal data and least-squares refinement details for the hydrated salt $Fen^{-}Na^{+}$.

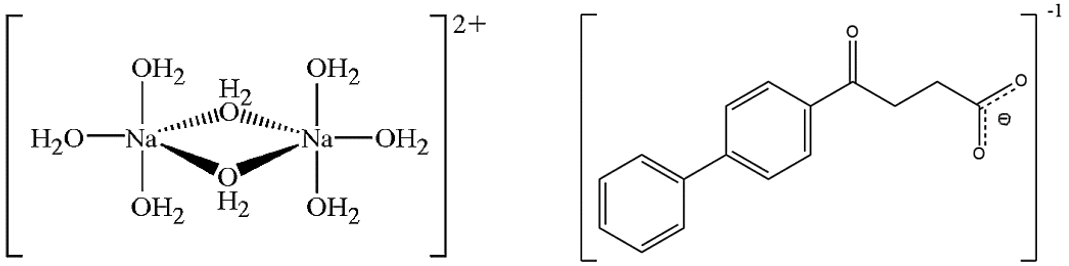

Figure 3.5: A di-μ-aqua-bis[triaquasodium(I)] unit (left) and the $(FEN)^{-}$ ion (right) occurring in the crystal structure of $Fen^{-}Na^{+}$.

Table 3.2: The final crystal data and refinement details for the $Fen^{-}Na^{+}$ crystal structure.

Chemical formula	$4(C_{16}H_{13}O_3)^{-}\,2(H_{16}Na_2O_8)^{2+}\cdot 4H_2O$
Formula weight (g.mol^{-1})	1465.35
Temperature (K)	100(2)
Wavelength (Å)	0.71073
Crystal system	Triclinic
Space group	$P\ \bar{1}$
a (Å)	5.8753(5)
b (Å)	15.1221(14)
c (Å)	39.637(4)
α (°)	82.250(3)
β (°)	89.940(3)
γ (°)	87.926(3)
V (Å^3)	3487.1(6)
Z	2
Calculated density (g.cm^{-3})	1.396
μ (Mo Kα) (mm^{-1})	0.132
F(000)	1552
Crystal size (mm^3)	0.020 × 0.140 × 0.260
θ-range scanned (°)	$4.40 < 2\theta < 51.23$
Index ranges ±h, ±k, ±l	h:-7, 7; k:-18, 18; l:-48, 48
No. reflections (total)	91089
No. unique reflections	13185
No. of parameters	1021
Goodness-of-fit, S	1.173
Final R indices R1, wR2, [I>2σ(I)]	0.0839, 0.1319
R indices, all data (R1, wR2)	0.1044, 0.1662
Largest diff. peak and hole (e Å^{-3})	0.29, -0.34

Molecular structure

Figure 3.6 shows the labelling scheme for the $Fen^{-}Na^{+}$ crystal structure. The ASU consists of four distinct $(FEN)^{-}$ ions with two distinct di-μ-aqua-bis[triaquasodium(I)] cations. The Na-O(water) bond lengths in the sodium complex range between 2.340(3) and 2.467(3) Å. Four free (i.e. unbound to Na^{+} ions) water molecules are also present in the ASU, which gives a total of 5 water molecules per $(FEN)^{-}$ ion. This is near to the value determined by TGA which resulted in 4.7 ± 0.1 water molecules. The discrepancy may be due to the loss of water from the onset of heating noted in TGA analysis.

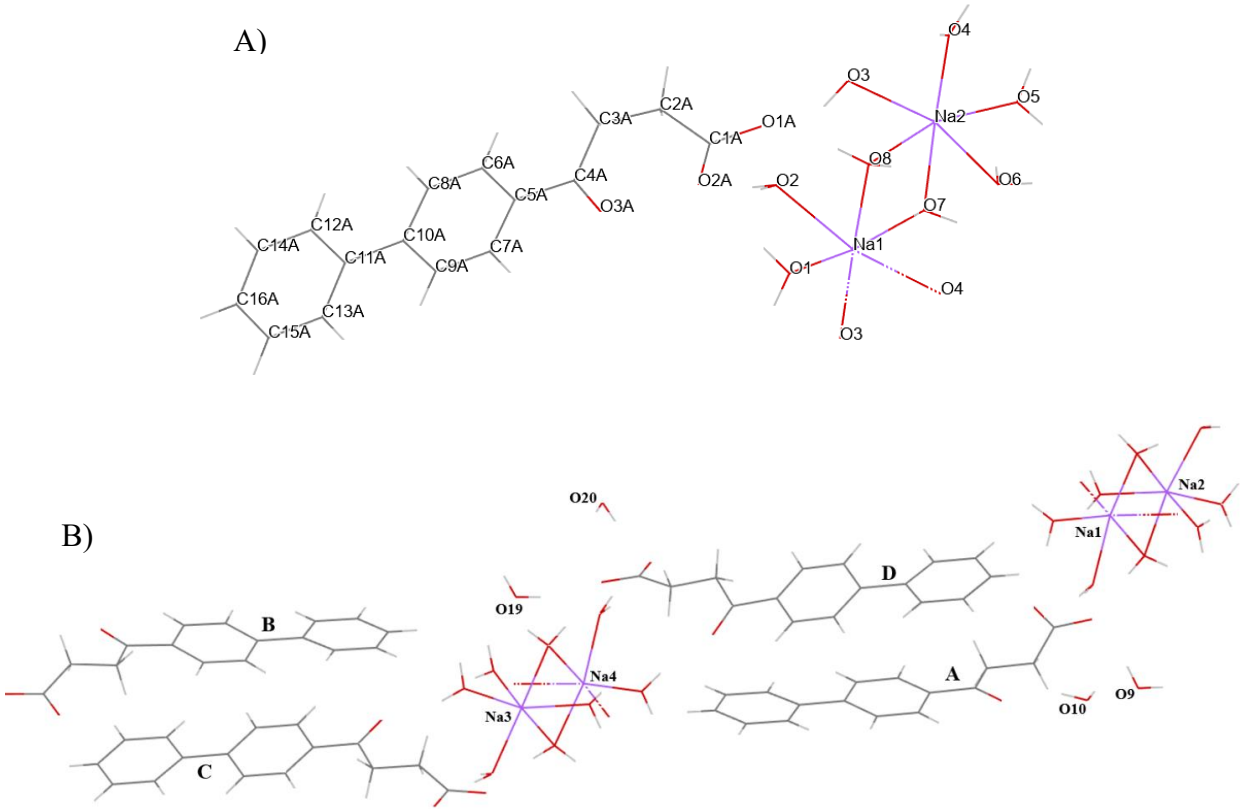

Figure 3.6: Labelling scheme of A) $(FEN)^{-}$ ion and di-μ-aqua-bis[triaquasodium(I)] cation and B) the ASU of the $Fen^{-}Na^{+}$ crystal structure.

Hydrogen bonding

Figure 3.7 shows the hydrogen bonding found in the ASU and in the packing arrangement of the $Fen^{-}Na^{+}$ crystal structure. There is a complex network of hydrogen bonds in the structure due to the presence of the sodium water complex. The latter creates a hydrogen bonding motif between $(FEN)^{-}$ and the water molecules. The packing arrangement shows alternating rows of $(FEN)^{-}$ and sodium

water complexes. Each free (i.e. unbound to Na^+) water molecule participates in hydrogen bonding with other water molecules as well as the carbonyl oxygen atoms in $(FEN)^-$.

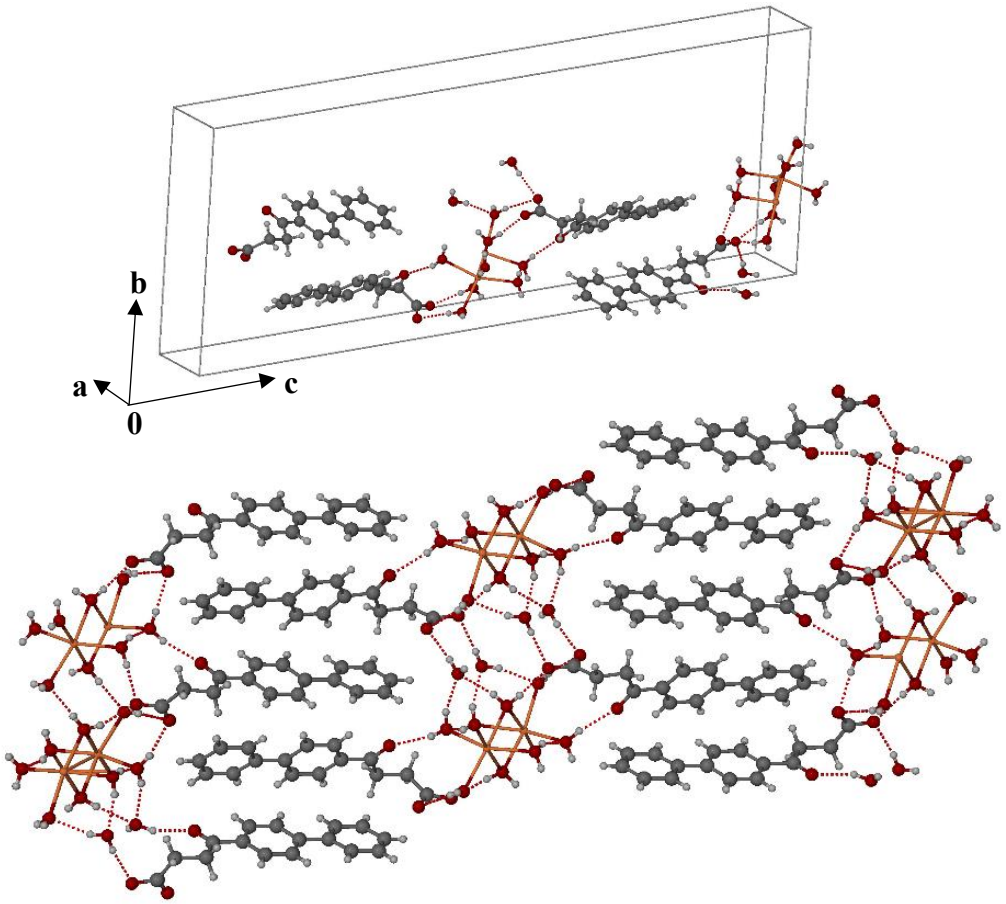

Figure 3.7: Hydrogen bonding occurring in the ASU (top) and in a more extended packing arrangement of Fen^-Na^+(bottom).

Table 3.3 lists the hydrogen bonds in the crystal structure. All O···H bond lengths range between 1.91(3) and 2.16(4) Å. The strengths of these hydrogen bonds are also confirmed, with the O-H···O angles all within a reasonable range of 154(4) - 175(3)° and O···O distances between 2.743(4) and 2.971(4) Å. It is expected that these hydrogen bonds would be particularly strong in the case of the charge-assisted variety occurring between the sodium-bound water molecules and the carboxylate oxygen atoms of $(FEN)^-$, evident in Figure 3.7.

Table 3.3: Hydrogen bonding present in the hydrated $Fen^{-}Na^{+}$salt.

Hydrogen bond interaction	D-H (Å)	H···A (Å)	D···A (Å)	D-H···A (°)	Symmetry code
O3-H5···O2*	0.83(4)	2.11(4)	2.898(4)	158(4)	
O4-H8···O6*	0.83(3)	2.00(3)	2.808(4)	166(4)	1+x,y,z
O8-H15···O1A	0.83(4)	1.94(4)	2.761(4)	170(4)	x,y,z
O2-H3···O2A	0.85(3)	1.98(3)	2.830(4)	175(3)	x,y,z
O1-H2···O2A	0.85(4)	2.09(4)	2.903(4)	162(4)	x,y,z
O10-H20···O3A	0.86(3)	1.99(2)	2.805(4)	160(4)	x,y,z
O9-H17···O1A	0.85(3)	1.94(3)	2.768(4)	165(4)	x,y,z
O12-H24···O14*	0.84(4)	2.16(4)	2.936(4)	155(3)	-1+x,y,z
O13-H25···O15*	0.83(4)	2.13(3)	2.896(4)	154(4)	
O20-H40···O2D	0.84(3)	1.91(3)	2.743(4)	172(3)	x,y,z
O16-H32···O2D	0.83(4)	2.15(4)	2.971(4)	168(4)	x,y,z
O19-H38···O16	0.83(2)	2.00(3)	2.808(4)	164(4)	x,y,z
O18-H35···O1D	0.84(4)	1.93(4)	2.766(4)	175(3)	x,y,z
O15-H29···O3D	0.83(3)	2.07(3)	2.893(4)	170(4)	x,y,z
O17-H34···O1B	0.83(3)	2.00(3)	2.829(4)	173(4)	x,y,z
O11-H21···O2B	0.83(3)	2.00(3)	2.823(4)	175(5)	x,y,z
O14-H28···O3B	0.83(3)	2.03(3)	2.834(4)	164(4)	x,y,z

*Intramolecular interaction

C-H···π interactions

Given the significant number of crystallographically unique phenyl rings in the ASU, namely eight, it was expected that C-H···π interactions might be prominent in the crystal structure. This was duly confirmed. Table 3.4 provides a list of the ring-centroid labels (Cgn) and the carbon atom names in each of the unique phenyl rings.

Table 3.4: The centroid labels and the names of the carbon atoms comprising each ring.

Label	Atoms
Cg1	C5A → C6A → C8A → C10A → C9A → C7A →
Cg2	C11A → C12A → C14A → C16A → C15A → C13A →
Cg3	C5C → C6C → C8C → C10C → C9C → C7C →
Cg4	C11C → C12C → C14C → C16C → C15C → C13C →
Cg5	C5B → C6B → C8B → C10B → C9B → C7B →
Cg6	C11B → C12B → C14B → C16B → C15B → C13B →
Cg7	C5D → C6D → C8D → C10D → C9D → C7D →
Cg8	C11D → C12D → C14D → C16D → C15D → C13D →

Table 3.5 lists the most significant C-H···π interactions in the crystal structure with their geometrical parameters. The C···Cg distances all range within 3.401(5) and 3.728(5) Å, the sum of the van der Waals radii of two carbon atoms being 3.40 Å. However, the C-H···Cg angles lack linearity, lying in the range 124 – 142°.

Table 3.5: C-H···π interactions in the crystal structure of $Fen^{-}Na^{+}$.

Interaction	H···Cg (Å)	C···Cg (Å)	C-H···Cg (°)	Symmetry code
C3A-H3A1···Cg8	2.82	3.637(5)	140	x,y,z
C6B-H6B···Cg8	2.81	3.606(4)	142	2-x,1-y, 1-z
C6D-H6D···Cg2	2.63	3.413(4)	139	1+x,y,z
C7A-H7A···Cg4	2.90	3.640(5)	136	-x,-y,1-z
C7C-H7C···Cg6	2.84	3.614(5)	142	-x,-y,1-z
C3B-H3B2···Cg4	2.77	3.579(5)	139	x,y,z
C8A-H8A···Cg7	2.94	3.688(5)	136	x,y,z
C8C-H8C···Cg1	2.79	3.525(5)	135	1-x,-y, 1-z
C9B-H9B···Cg3	2.83	3.551(5)	133	x,y,z
C9D-H9D···Cg5	2.68	3.476(5)	141	1-x,1-y, 1-z
C3C-H3C2···Cg2	2.57	3.401(5)	141	1-x,-y,1-z
C12D-H12D···Cg1	2.99	3.614(5)	124	1+x,y,z
C13A-H13A···Cg3	2.96	3.653(5)	131	-x,-y,1-z
C13C-H13C···Cg5	2.99	3.728(5)	136	-1+x,y,z
C3D-H3D1···Cg6	2.80	3.555(5)	134	1-x,1-y,1-z

Figure 3.8 shows the C-H···π interactions involving the $(FEN)^-$ rings. The top image shows H···Cg distances to Cg7 and Cg8. C-H···π interactions occur between the H atoms of the neighbouring phenyl ring and the methylene group. The short distances of 2.82 and 2.94 Å indicate that these are significant interactions which repeat throughout the crystal structure holding the neighbouring $(FEN)^-$ ions together (Figure 3.8, bottom image).

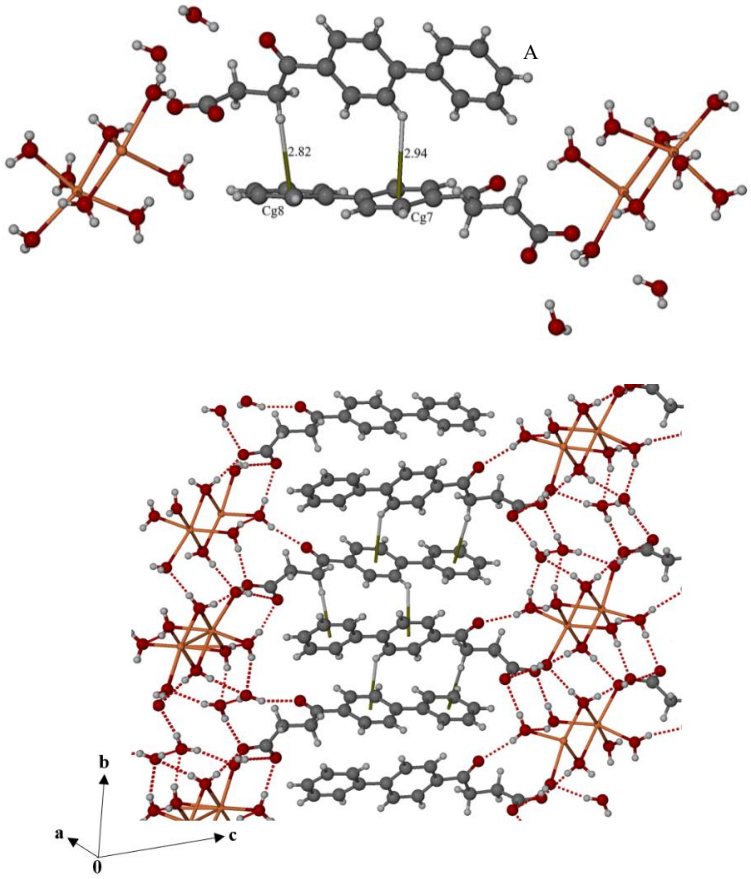

Figure 3.8: C-H···π interactions in the crystal structure of Fen^-Na^+. The two representative H···Cg distances illustrated above are in Å.

Packing

Figure 3.9 shows the [100] projection of the unit cell and the packing arrangement of Fen^-Na^+. The alternating rows of $(FEN)^-$ anions and di-μ-aqua-bis[triaquasodium(I)] units are evident. Hydrogen bonding involving the free water molecules, as well as those bound to the sodium ions, contribute to the cohesion of the packing arrangement. The rows of $(FEN)^-$ moieties are stabilised by C-H···π interactions.

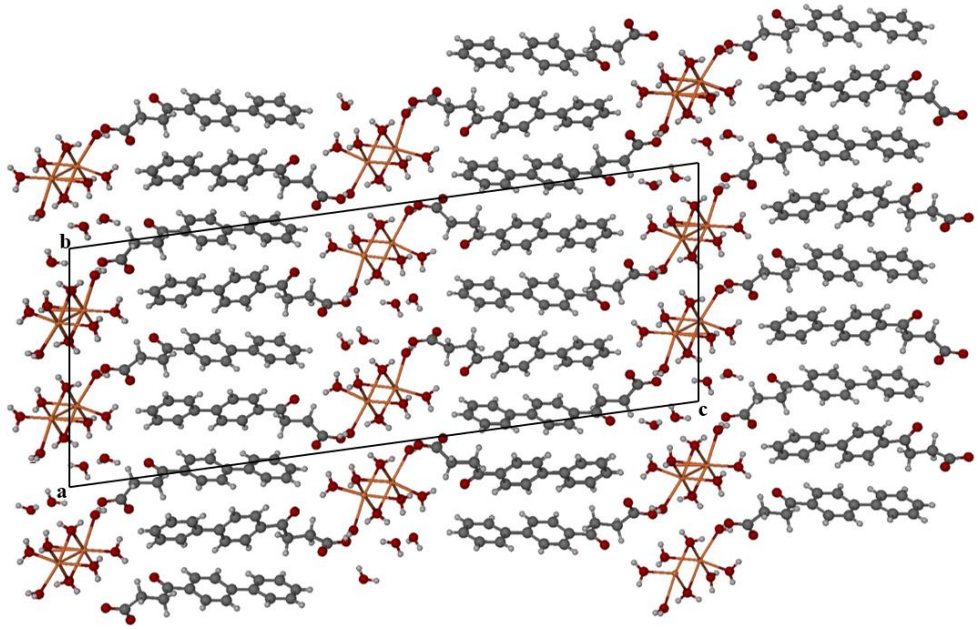

Figure 3.9: The [100] projection of the packing arrangement of the Fen^{-}Na^{+} crystal structure.

3.2.4. Fourier-transform infrared (FT-IR) spectroscopy

The stacked spectra of FEN and Fen^{-}Na^{+} can be seen in Figure 3.10. FEN shows a strong absorbance band at 1401 cm^{-1}, representing the in-plane O-H bending vibration of the -COOH functional group. In contrast, the two intense absorption peaks at 1403 and 1591 cm^{-1} in the spectrum of Fen^{-}Na^{+} are the symmetric and antisymmetric stretching vibrations respectively of the carboxylate group, hence indicating that the product is a salt.

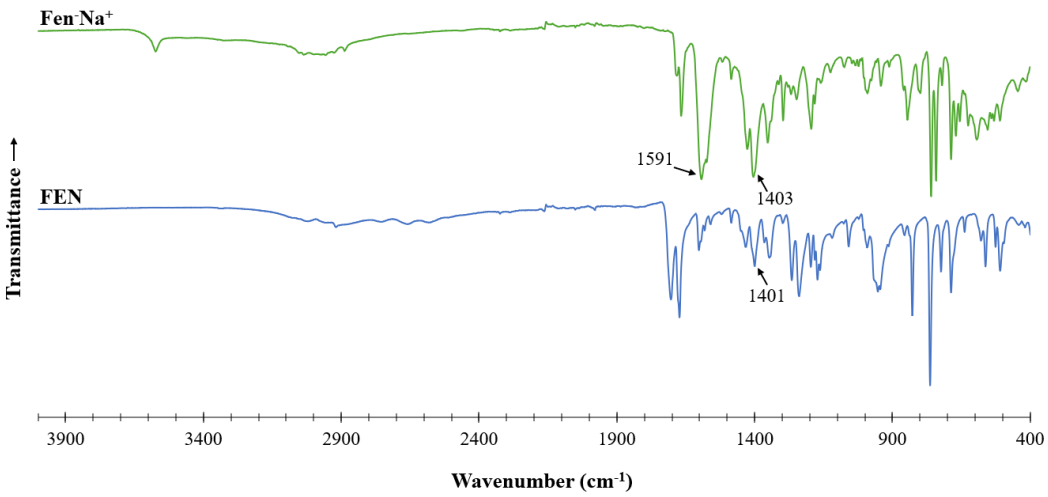

Figure 3.10: Stacked FT-IR spectra of FEN and Fen^{-}Na^{+}.

3.2.5. Calculated powder X-ray diffraction (PXRD) pattern

A definitive experimental PXRD pattern of the single crystals could not be obtained. When grinding the crystals of Fen^-Na^+ for PXRD analysis, there was a significant loss in the crystallinity which resulted in one broad peak in the PXRD pattern, indicating an amorphous powder. If the crystals were not ground, it was evident that there was severe preferred orientation present due to large particles with irregular sizes and hence this resulted in a pattern that was not representative of the salt. The purity of the sample was therefore confirmed based on a reliable FT-IR spectrum as well as DSC and ^1H NMR data. The calculated PXRD pattern of Fen^-Na^+ produced using Mercury[4] is found in the Appendix (Section 1.5.1., pg. 9).

3.2.6. Solubility study

The standard curve and all HPLC measurements (recorded in duplicate), can be found in the Appendix (Section 1.3.1., pg. 5). The solubility of the salt was determined in both an aqueous solution and in FaSSIF (Fasted State Simulated Intestinal Fluid) solution, the latter buffered at pH 6.5. The procedures, described in Chapter 2 (2.6.2. Gravimetric solubility studies, pg. 29 and 2.6.5. Equilibrium solubility studies, pg. 32) were used for FaSSIF and aqueous solubility determination respectively.

The measurements in Table 3.6 show that there is a significant ~480-fold increase in the solubility of FEN in the form of the Fen^-Na^+ salt compared to that of FEN. It should be noted that while synthesising and characterising Fen^-Na^+ it was clear that the solubility was much greater at higher temperatures. At ~60 °C the Fen^-Na^+ solution was clear and as soon as the solution was filtered and cooled the product would immediately crash out of solution. In a FaSSIF solution there is, however, a solubility decrease. The reason for this may be due to the lowered pH of 6.5 used in the study. As a weak acid, $(FEN)^-$ ions are more soluble in basic medium.[5] The decreased concentration in an acidic environment was clear when the metal salts could not be quantified using Microwave Plasma Atomic Emission Spectrometry (MP-AES). All metal complexes precipitated out when the solution was acidified with 1% HNO_3. The metal concentrations could therefore not be determined. Another reason for the solubility decrease may be that the concentration of FaSSIF used may not have been enough to accurately solubilise the salt.

Table 3.6: Aqueous and FaSSIF solubility values of FEN and Fen$^-$Na$^+$ at 25 ± 1 °C.

	Aqueous (mM)	FaSSIF, pH 6.5 (mg/ml)*
FEN	0.002	6.92 ± 0.8
Fen$^-$Na$^+$	7.7	3.82 ± 0.2

***** The mass fraction of FEN in the product Fen$^-$Na$^+$ is 0.72 which has been taken into account in the final concentration stated above.

3.3. Fenbufen potassium salt – Fen$^-$K$^+$

The potassium salt was synthesised using equimolar amounts of FEN and KOH (2M) dissolved in 0.8 ml MilliQ® water. The base was added dropwise to the FEN solution while stirring at 70 ± 5 °C. The solution was left to stir at 250 rpm for 3 hours and thereafter the hot solution was filtered through a 0.45 µm nylon microfilter and left to evaporate slowly. This did not result in single crystals forming, but instead a precipitate resembling a powder formed. The rate of crystallization was slowed down using the methods described for the synthesis of Fen$^-$Na$^+$, but this approach was unsuccessful. Attempts to recrystallise the powder product from EtOH, MeOH, MeCN, 1,4-dioxane and ethyl acetate did not produce single crystals.

3.3.1. Powder X-ray diffraction (PXRD)

Figure 3.11 shows the PXRD pattern of FEN and that of the Fen$^-$K$^+$ powder product. These are quite distinct, as expected. It was therefore confirmed that the powder product was a new phase.

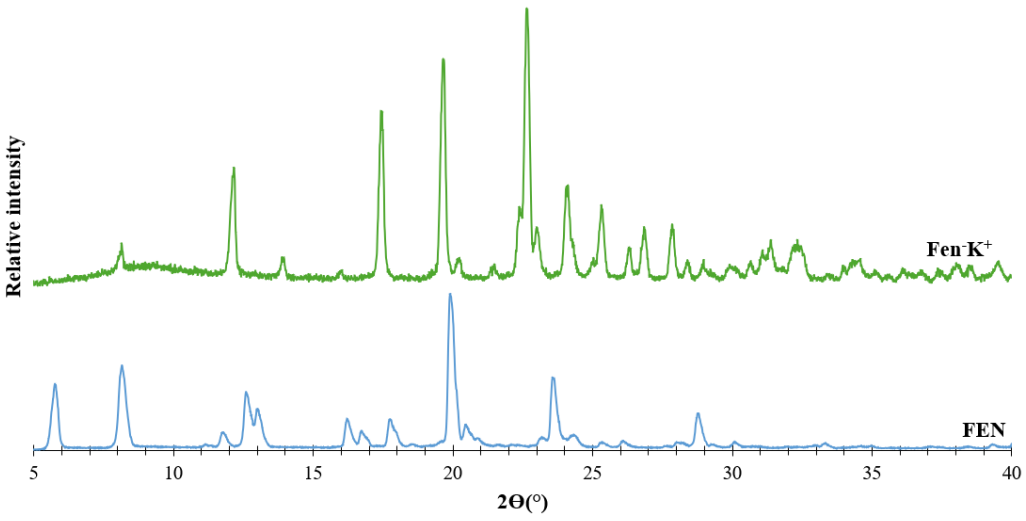

Figure 3.11: The PXRD patterns of FEN and the Fen$^-$K$^+$ co-precipitation product.

3.3.2. Proton nuclear magnetic resonance (^{1}H NMR) spectroscopy

Table 3.7 shows the chemical shifts of the diagnostic signals in the ^{1}H NMR spectra of FEN and the Fen^-K^+ product based on the labelling scheme in Figure 3.12. The -COOH proton of FEN produces a peak at 12.17 ppm. This peak is no longer present in the spectrum of the product indicating that FEN has been deprotonated. As observed for the Fen^-Na^+ salt, there is also a shift in the methylene proton peaks of the product compared with those of FEN. The stacked spectra can be found in the Appendix (Section 1.1.2, pg. 2).

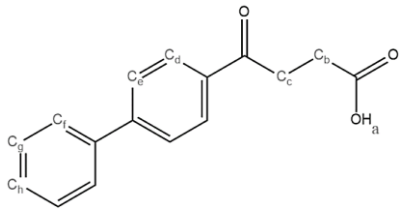

Figure 3.12: Proton labelling scheme of FEN.

Table 3.7: Comparison of the chemical shifts of the signals for FEN and Fen^-K^+.

Assignment	FEN δ (ppm)	Fen^-K^+ δ (ppm)
COOH (a)	12.17	-
CH aromatic (f)	8.09 - 8.06	8.05 - 8.02
CH aromatic (d, e)	7.86 - 7.75	7.82 - 7.74
CH aromatic (g, h)	7.55 - 7.42	7.54 - 7.40
CH_2 (b)	3.32 - 3.28	3.09 - 3.05
CH_2 (c)	2.64 - 2.59	2.20 - 2.15

3.3.3. Thermal analysis

3.3.3.1. Hot stage microscopy (HSM)

Figure 3.13 shows the HSM images of the Fen^-K^+ powder product recorded from 23.8 to 270 °C, at 10 °C/min. Since single crystals could not be obtained, the powdered product was used. The product is stable until 140 °C, and does not undergo any physical change upon heating. One would expect that water would be removed from the structure, but no bubbling is observed. There is a physical change in the product at 140 °C when the powdered product becomes glossier in appearance.

The next thermal event, that is evident by the cloudy appearance of the glass slide, begins at 180 °C. From this point the images could not be seen very clearly, but the first sign of decomposition appears to be at 246.8 °C. This continues until 270 °C when decomposition is complete.

Figure 3.13: The HSM images of $Fen^{-}K^{+}$ from 23 to 270 °C at a heating rate of 10 °C/min.

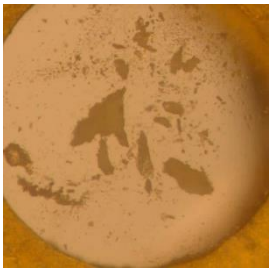

23.8 °C: Powder product at room temperature.

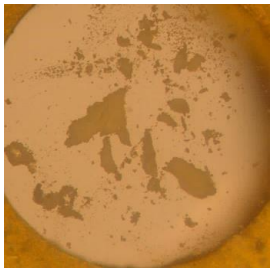

140 °C: The powder product has a cloudy appearance.

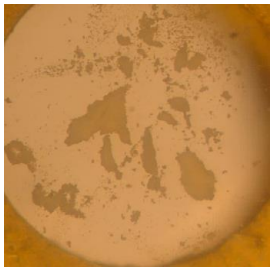

180 °C: The image becomes cloudy.

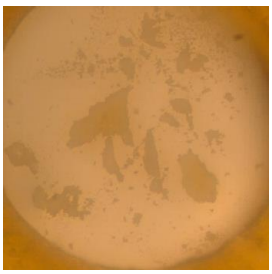

224.1 °C: The cloudiness becomes more prominent.

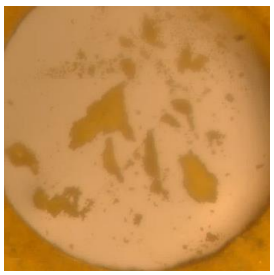

246.8 °C: The onset of decomposition.

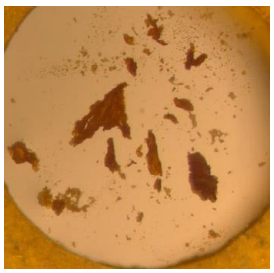

270 °C: Decomposition is complete.

3.3.3.2. Thermal gravimetric analysis (TGA) and differential scanning calorimetry (DSC)

Both the TGA (n = 2) and DSC curves are present in Figure 3.14. The TGA curve of $Fen^{-}K^{+}$, recorded from 20 to 350 °C, shows three mass losses. The first and second mass loss percentages are 14.4 ± 0.1 % and 5.3 ± 0.2 % with onset temperatures of 30.6 °C and 152 °C respectively. The first and second mass losses (total 19.7 ± 0.2%) are attributed to dehydration of the crystal and correspond to 3.98 ± 0.05 waters for each $(FEN)^{-}$ anion, assuming a 1:1 stoichiometry for FEN^{-} and K^{+}. This is consistent with the DSC curve which shows a broad endotherm present during the first mass loss. The second mass loss, with an onset temperature of 152 °C, corresponds to the onset of cloudiness seen in the HSM images. This is also consistent with the broad endotherm in the DSC curve which spans the temperature range 150 - 200 °C.

The third mass loss has an onset temperature of 269 °C. The HSM images show that decomposition begins at 246.8 °C, which precedes the event observed in the TGA. The third endotherm has a peak

at 278.8 °C, over a range of 256.3 – 286.9 °C. The broad shape of the endotherm as well as the HSM images indicate that decomposition is taking place.

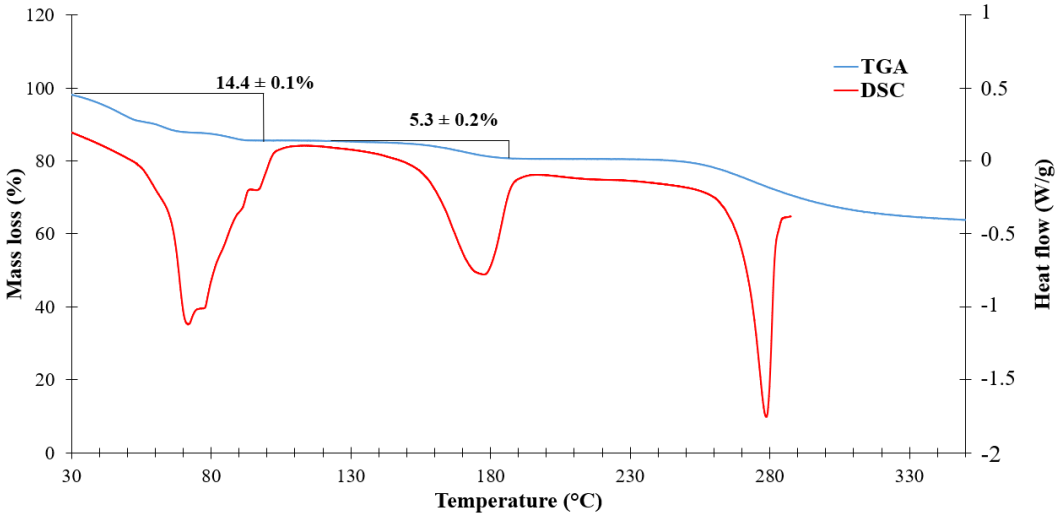

Figure 3.14: TGA (blue) and DSC (red) curves for the $Fen^{-}K^{+}$ co-precipitation powder product.

3.3.4. Fourier-transform infrared (FT-IR) spectroscopy

The stacked spectra of FEN and $Fen^{-}K^{+}$ can be seen in Figure 3.15. FEN shows a strong absorption band at 1401 cm^{-1}, representing the O-H bending vibration of the -COOH functional group. In contrast, the two intense absorption peaks at 1403 and 1599 cm^{-1} in the spectrum of $Fen^{-}K^{+}$ are the symmetric and antisymmetric stretching vibrations respectively of the carboxylate group, hence indicating that the product is a salt. The broad peak at ~3121 cm^{-1} represents the water in the crystal structure.

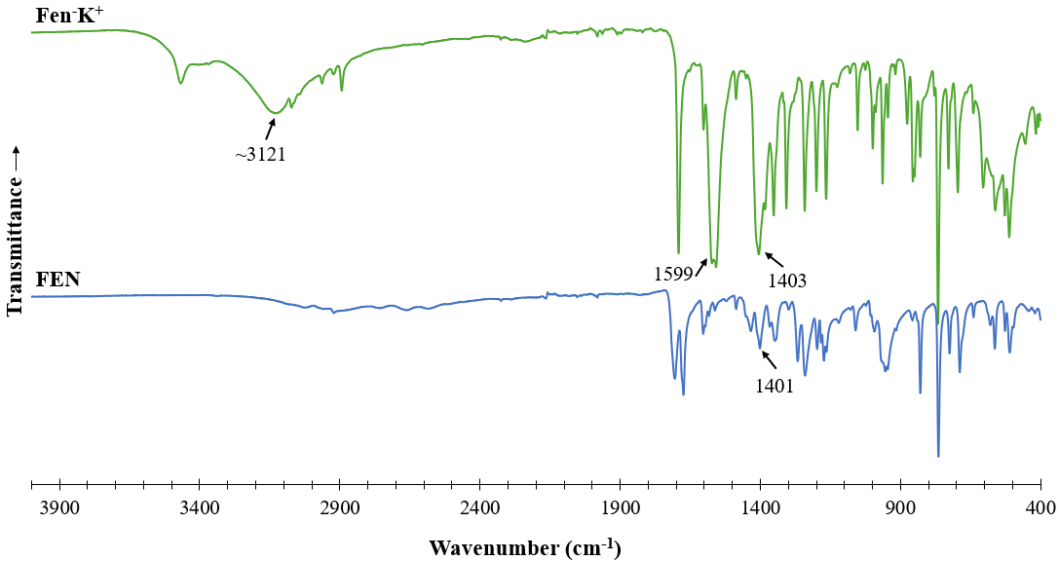

Figure 3.15: Stacked FT-IR spectra of FEN and $Fen^{-}K^{+}$.

3.3.5. Solubility

The solubility of the hydrated salt was determined using the procedure and standard curve that was used for the solubility determination of $Fen^{-}Na^{+}$. Table 3.8 shows the very significant difference in the solubility of the $Fen^{-}K^{+}$ salt compared to that of FEN. The solubility of the $Fen^{-}K^{+}$ salt in FaSSIF (buffered at pH 6.5), however, shows a 5.3-fold decrease relative to that of FEN. The same solubility decrease in the FaSSIF is seen in $Fen^{-}Na^{+}$ above. Once again this may be due to the acidic API being in a weakly acidic environment.

Table 3.8: Solubility data for FEN and hydrated $Fen^{-}K^{+}$ salt in both water and FaSSIF at 25 ± 1 °C.

	Aqueous (mM)	**FaSSIF, pH 6.5 (mg/ml)***
FEN	0.002	6.92 ± 0.8
$Fen^{-}K^{+}$	87.0	1.31 ± 0.1

* The mass fraction of $(FEN)^{-}$ in the product $Fen^{-}K^{+}$ is 0.69 which has been taken into account in the final concentration stated above.

3.4. Attempted synthesis of a calcium salt of fenbufen

The synthetic method described by Caira *et al.* was employed.[6] Two synthetic methods were used in the attempt to prepare a Ca^{2+} salt of FEN. One method involved dissolving $CaCl_2$ and Fen^-Na^+ (using a 6:1 molar ratio) separately in MilliQ® water. The $CaCl_2$ solution was then added to the Fen^-Na^+ solution. Upon addition, the expected precipitate did not form. The solution was then stirred at 70 ± 5 °C for 6 hours, filtered and left to evaporate slowly. The result was a mixture of the fibrous Fen^-Na^+ and large $CaCl_2$ crystals in the mother solution. Unit cell parameter measurements on individual specimens from the mixture of crystals confirmed the presence of Fen^-Na^+. The unit cell parameters of the larger crystals yielded a volume of 432 $Å^3$ which would not accommodate $(FEN)^-$. Instead, these parameters were determined to be due to $CaCl_2$. HSM and FT-IR spectra also confirmed that a salt of FEN had not formed. The second attempt involved dissolving FEN (5 mg) in 1 ml EtOH. Excess $CaCl_2$ was added to the FEN solution and the resulting suspension was stirred overnight at 50 ± 5 °C. The hot solution was filtered and left to evaporate slowly. The crystals formed were a mixture of FEN and $CaCl_2$; this was confirmed based on unit cell determinations, PXRD, FT-IR and HSM.

3.5. Attempted synthesis of a magnesium salt of fenbufen

Fen^-Na^+ and $MgSO_4$ (in a 1:6 molar ratio) were dissolved separately in 0.8 and 1.0 ml MilliQ® water respectively and stirred.[6] Once the $MgSO_4$ had completely dissolved, the solution was added to the Fen^-Na^+ solution. Upon addition of the $MgSO_4$ solution a white precipitate formed which was filtered using filter paper. The precipitate was washed and dried. In an attempt to isolate single crystals, the precipitate was recrystallised from MeOH. After 2 days, thin acicular crystals formed. These were unfortunately too small for single crystal X-ray analysis. The slow cooling method was then attempted to produce crystals of a suitable size and thereafter the vial was placed in the refrigerator at 4 °C. This unfortunately did not result in crystals suitable for full data-collection.

The PXRD patterns of the starting materials and the product are shown in Figure 3.16. Although a single crystal of the desired magnesium salt of FEN could not be obtained, comparing the PXRD pattern of the starting materials with that of the product showed a clear difference, which indicates a new phase. However, the FTIR spectrum, thermal and elemental analysis unfortunately did not confirm the new phase as being that of a magnesium salt. For this reason, a full description of the analyses undertaken is not recorded here and due to time constraints, no further attempt was made to isolate the desired phase.

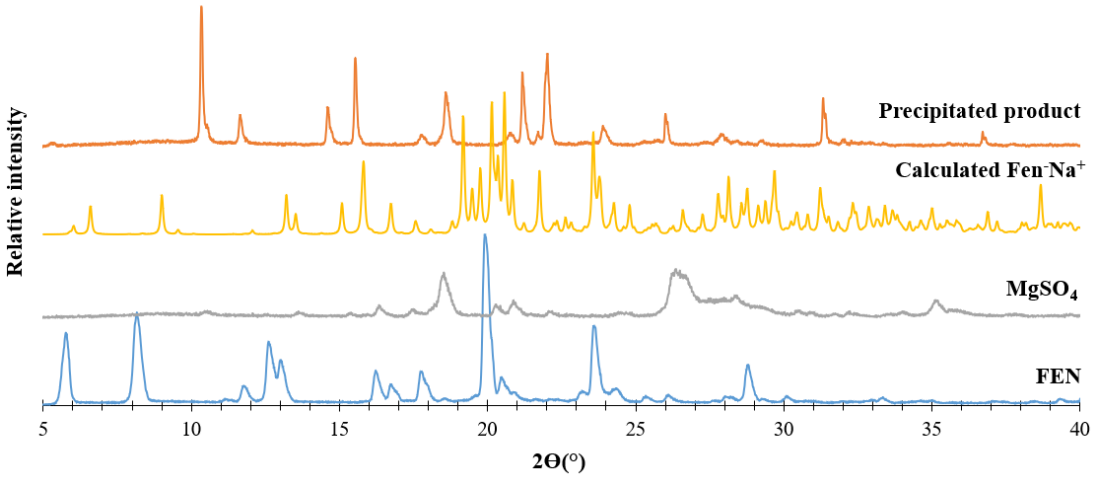

Figure 3.16: PXRD patterns of FEN, $Fen^{-}Na^{+}$, $MgSO_4$ and the precipitated product.

References

1. Blower, P. J., Inorganic pharmaceuticals. *Annual Reports Section" A"(Inorganic Chemistry)* **2001,** *97*, 587-603.
2. XPREP *Data Preparation and Reciprocal Space Exploration*, 2008/2; Bruker Analytical X-Ray Systems: **2008**.
3. Sheldrick, G. M., A short history of SHELX. *Acta Crystallographica Section A: Foundations of Crystallography* **2008,** *64* (1), 112-122.
4. Macrae, C. F.; Sovago, I.; Cottrell, S. J.; Galek, P. T.; McCabe, P.; Pidcock, E.; Platings, M.; Shields, G. P.; Stevens, J. S.; Towler, M., Mercury 4.0: From visualization to analysis, design and prediction. *Journal of Applied Crystallography* **2020,** *53* (1), 226-235.
5. Fritschka, E.; Sadowski, G., Rigorous modeling the pH-dependent solubility of weak acids, weak bases and their salts. *Fluid Phase Equilibria* **2024**, 114039.
6. Caira, M. R.; Miller, J. L.; Nassimbeni, L. R., β-Cyclodextrin inclusion complexes of Mg2+ and Ca2+ salts of meclofenamic acid: preparation and structural characterisation. *Supramolecular Chemistry* **2006,** *18* (7), 553-559.

Chapter 4: Cyclodextrin inclusion of uncharged and ionised fenbufen and phase solubility studies

4.1. Literature review

As mentioned in Chapter 1 (1.3.4. Cyclodextrin inclusion complexes, pg. 8) native cyclodextrins (CDs) differ by the number of glucose units in their structures, cavity sizes and solubilities. Fenbufen (FEN) is a small molecule API with a carboxylic acid functional group which, as previously mentioned, is known to cause gastric irritation and ulcers on API administration. CDs may reduce these negative side effects by encapsulating the carboxylic group and thus providing a drug delivery system.[1] It is therefore important to consider CDs when investigating ways to improve the physicochemical properties of FEN and develop appropriate delivery systems for this drug.

Using $Fen^{-}Na^{+}$ (syntheses described in Chapter 3) and neutral FEN, the synthesis of cyclodextrin inclusion complexes was attempted with native and methylated CDs. Phase solubility experiments were also performed using γ-CD (GCD) and the well-known derivatives of β-CD, shown in Figure 4.1.

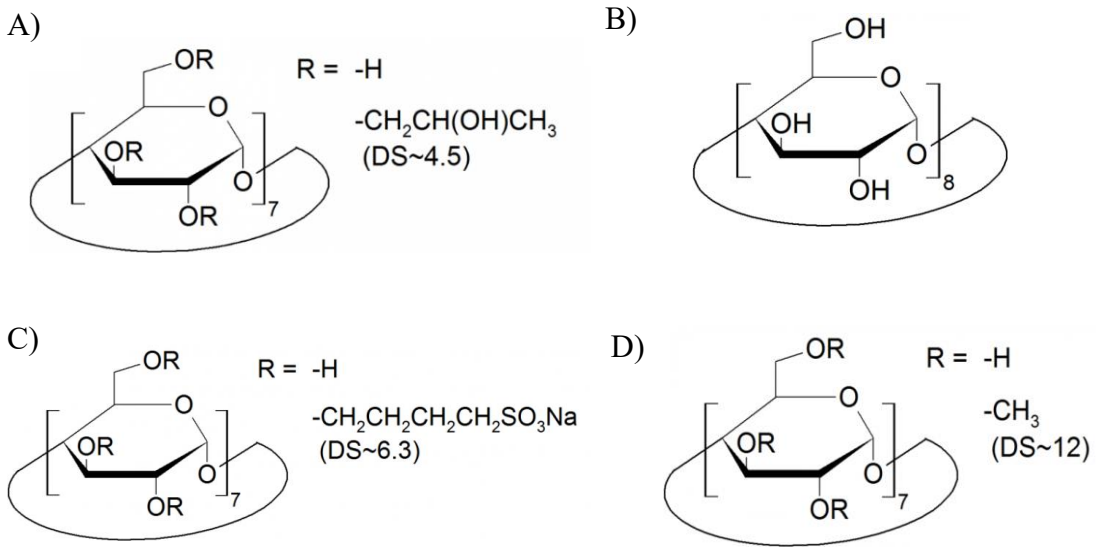

Figure 4.1: CD structures used in phase solubility studies. A) HPBCD, B) GCD, C) SBEBCD and D) RAMEB. (DS refers to the degree of substitution of the substituents in question).

4.2. Cyclodextrin inclusion with fenbufen salt Fen^-Na^+ as a potential guest

Table 4.1 shows the outcomes of the co-precipitation experiments using the salt Fen^-Na^+ with the selected CDs. All synthetic procedures followed the steps described in Chapter 2 (2.4.2. Co-precipitation, pg. 23), using equimolar amounts of Fen^-Na^+ and the selected CD dissolved in 0.8 ml and 0.6 ml MilliQ® water respectively. The CD solutions were stirred at 70 ± 5 °C and once dissolved, the hot salt solution was added to each CD solution. Each resulting solution was stirred for a total of 6 hours at 70 ± 5 °C, filtered into a clean vial through a 0.45 μm nylon microfilter and left to evaporate slowly. The inclusion experiment with DMB was performed by dissolving the salt and DMB separately in 0.8 ml water at room temperature and once fully dissolved the salt solution was added to the DMB solution. The resulting cool solution was stirred for a total of 6 hours and filtered into a clean vial. The capped vial was then placed in an oven set at 60 °C. Complexes of BCD and GCD, namely BCD·Fen^-Na^+ and GCD·Fen^-Na^+, were successfully synthesised, the former complex being characterised using SCXRD.

Table 4.1: Cyclodextrin inclusion experiments with FEN salts and CDs.

Cyclodextrin	Fen^-Na^+
α-cyclodextrin (ACD)	No complex
β-cyclodextrin (BCD)	Complex
γ-cyclodextrin (GCD)	Complex
Heptakis(2,6-di-*O*-methyl)-β-cyclodextrin (DMB)	No complex

4.3. The inclusion complex BCD·Fen^-Na^+ formed by reaction of β-CD with the fenbufen sodium salt

An inclusion complex consisting of Fen^-Na^+ and BCD was synthesised using the method described above. The crystals displayed poor crystallinity and was not suitable for intensity data-collection. To improve the quality of the crystals, the rate of crystallisation was reduced using the slow cooling method described in Chapter 2 (2.3.3. Co-precipitation, pg. 22) and thereafter the vial was placed in the refrigerator at 4 °C. After 2 weeks single crystals were harvested.

4.3.1. ^{1}H NMR spectroscopy

Table 4.2 shows the chemical shifts of the signals in the ^{1}H NMR spectrum of BCD and Fen^{-}Na^{+} recorded in DMSO-d_6. Figure 4.2 shows the labelling scheme of (FEN)$^{-}$ and BCD used in the assignment of peaks. The integration values confirm that BCD·Fen^{-}Na^{+} has 1:1 stoichiometry. The full spectrum can be found in the Appendix (Section 1.2.1, pg. 3).

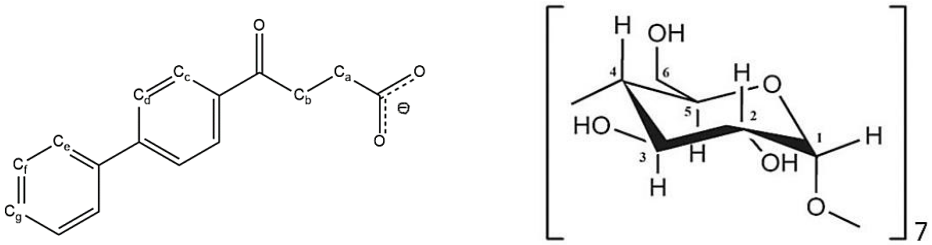

Figure 4.2: Labelling scheme of (FEN)$^{-}$ (left) and BCD (right) used in the assignment of ^{1}H NMR peaks.

Table 4.2: The chemical shifts of diagnostic peaks in the ^{1}H NMR spectrum of BCD·Fen^{-}Na^{+}.

Assignment	δ (ppm)	Integration	Multiplicity	Proton	Stoichiometric ratio	Integer
(FEN)$^{-}$						
CH aromatic (e)	8.07 - 8.04	2.20	Doublet	2H	1.10	1
CH aromatic (d,c)	7.83 - 7.75	4.47	Doublet of doublets	4H	1.12	1
CH aromatic (f,g)	7.54 - 7.43	3.46	Doublet of triplets	3H	1.15	1
BCD						
OH-6	6.02	14*	Singlet	14H	1	1
CH-1	4.83	7.47	Singlet	7H	1.07	1
OH-3 and OH-2	4.51	6.94	Singlet	7H	0.99	1

*Reference integral

4.3.2. Thermal analysis

4.3.2.1. Thermal gravimetric analysis (TGA) and differential scanning calorimetry (DSC)

Figure 4.3 shows the TGA (n = 2) and DSC curves of BCD·Fen^{-}Na^{+}. The TGA curve was recorded from 20 to 400 °C at 10 °C/min. The TGA curve shows that two mass losses take place, the first being

8.2 ± 0.6% with an onset temperature of 24.5 °C. This occurs as an overlapping two-step process due to the dehydration of the crystal structure and is equivalent to 7.0 ± 0.56 water molecules per BCD molecule. The second mass loss is 57.8 ± 0.3% with an onset temperature of 238.2 °C. This is attributed to the decomposition of the anhydrous complex upon heating.

The DSC curve, recorded from 20 to 260 °C, shows a broad endotherm that represents the dehydration of the complex over the range 20 – 140 °C. This is consistent with the range in which the first mass loss is observed. Due to the tendency for CD complexes to foam on heating to high temperature and possibly contaminate the DSC cell, the scan was terminated at 260 °C.

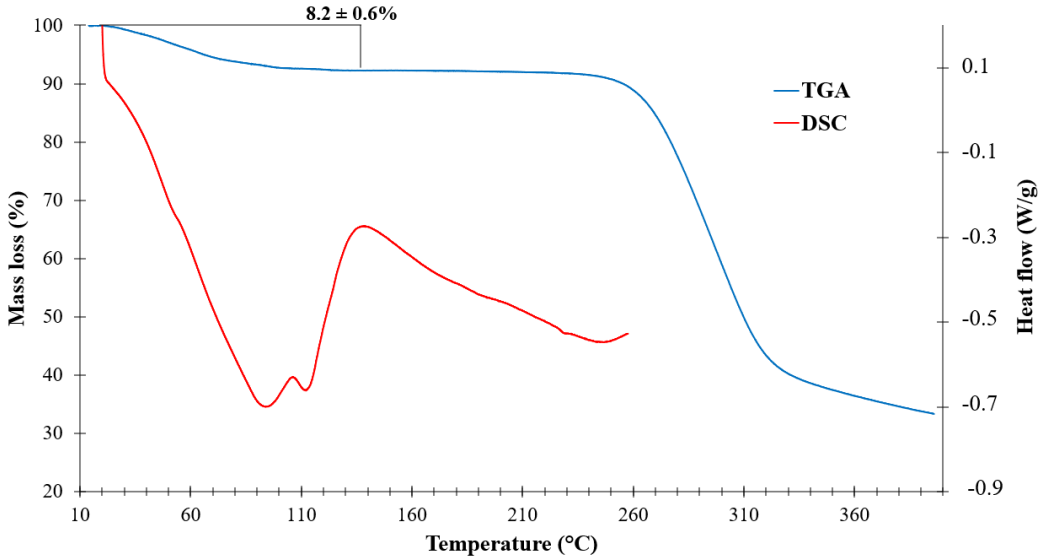

Figure 4.3: TGA and DSC curves of BCD·Fen^{-}Na^{+}.

4.3.3. Crystal structure analysis

Data-collection and space group determination

The intensity data-collection was performed at 100(2) K. The reflection intensities displayed *mmm* Laue symmetry, indicating the orthorhombic system. Using the program XPREP[2], the space group was determined as $C222_1$ from the reflection conditions hkl: $h + k = 2n$, and $00l$: $l = 2n$. The presence of the chiral host β-cyclodextrin in the complex is consistent with this chiral space group. Figure 4.4 shows the numbering scheme used in the description of the crystal structure.

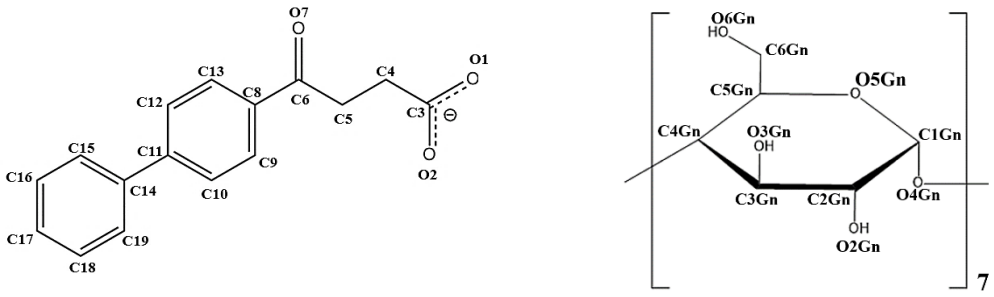

Figure 4.4: Numbering scheme of $(FEN)^-$ (left) and BCD glucose unit (right).

Structure solution and refinement

The crystal data and refinement parameters for the BCD·Fen^-Na^+ structure can be found in Table 4.3. Unfortunately, the intensity data were not of the highest quality due to less than optimum crystal diffraction quality and some disorder in the host and water molecules. The structure was solved by the dual-space small-molecule structure solution program SHELXD-97[3], the resulting E-map revealing all components of the ASU, namely those of the BCD molecule, the included $(FEN)^-$ anion, the sodium ion and oxygen atoms of water molecules. All atoms were refined isotropically and thereafter anisotropically. This refinement treatment was satisfactory for the majority of the non-H atoms in the ASU, but for three atoms in the BCD molecule (including disorder components of oxygen atoms bonded to C6G2 and C6C3), it was necessary to revert to refinement with isotropic thermal parameters. Most of the water oxygen atoms were disordered and isotropic refinement was also retained for these atoms. Using the riding model, all H atoms were placed at appropriate positions on the $(FEN)^-$ ion. Hydrogen atoms of hydroxyl groups on the BCD molecule were included using the rotating model, ensuring that their final positions would maximise intramolecular and intermolecular hydrogen bonding. The final refinement revealed six oxygen atoms or their disorder components with refined U_{iso} values exceeding 0.15 $Å^2$. It was also evident that with the available intensity data, refinement of the final model showed some instability, despite the 28 DFIX restraints which had been applied to maintain reasonable molecular geometries. Nevertheless, the salient structural features of the new inclusion complex were clearly evident and unequivocal.

Table 4.3: Crystal data and refinement details for the BCD·Fen^{-}Na^{+} structure.

Chemical formula	**$C_{42}H_{70}O_{35}\cdot(C_{16}H_{13}O_{30})^{-}Na^{+}\cdot 9.4H_2O$**
Formula weight (g.mol^{-1})	1580.60
Temperature (K)	100(2)
Wavelength (Å)	0.71073
Crystal system	Orthorhombic
Space group	$C222_1$
a (Å)	18.935(4)
b (Å)	24.391(5)
c (Å)	30.878(6)
α (°)	90
β (°)	90
γ (°)	90
V (Å^3)	14261(5)
Z	8
Calculated density (g.cm^{-3})	1.472
μ (Mo Kα) (mm^{-1})	0.132
F(000)	6591
Crystal size (mm^3)	0.040 × 0.140 × 0.320
Range scanned θ (°)	3.79° < 2θ < 50.28°
Index ranges ±h, ±k, ±l	h:-22, 22; k:-29, 29; l:-36, 36
No. reflections (total)	188823
No. unique reflections	12704
No. of parameters	984
Goodness-of-fit, S	1.05
Final indices R1, wR2, [I>2σ(I)]	0.1403, 0.3455
R indices, all data (R1, wR2)	0.1723, 0.3747
Largest diff. peak and hole (e Å^{-3})	1.12, -0.68

There were fourteen Δρ peaks present with low electron densities that were identified as oxygen atoms of water molecules with s.o.f.s less than or equal to one. Disorder of O71W, O7W and O11W, O13W were evident from their O···O distances of 1.163 and 1.685 Å respectively. The U_{iso} values of the former two disorder components were constrained to be equal with an EADP command, the final value being 0.066 Å^2. The latter disorder components were treated by assigning common U_{iso} values to the partial water oxygen atoms and then refining their s.o.f. values. The results of the U_{iso} and s.o.f.s

are listed in Table 4.4. Based on these values the total water content is therefore approximately 9.4 H_2O molecules per CD molecule.

Table 4.4: The s.o.f.s and U_{iso} values of the water oxygen sites identified from difference Fourier maps.

Atom	s.o.f.	U_{iso} (Å^2)	Atom	s.o.f.	U_{iso} (Å^2)
O2W	1	0.190(12)	**O8W**	0.383	0.031(5)
O3W	1.24(7)*	0.158(11)	**O9W**	0.5	0.024(3)
O4W	1	0.067(9)	**O10W**	0.289	0.041(8)
O5W	1	0.080(12)	**O11W**	0.73(3)	0.061(12)
O6W	1	0.12(2)	**O12W**	1	0.42(4)
O71W	0.70(2)	0.066(4)	**O13W**	0.27(3)	0.025(10)
O7W	0.30(2)	0.066(4)			

*The refined s.o.f. of O3W is clearly incorrect, exceeding 1.0 as a result of erroneous refinement with both U_{iso} and s.o.f. being refined simultaneously.

Molecular structure

Figure 4.5 shows the asymmetric unit of BCD·Fen$^-$Na$^+$ which consists of a BCD molecule, a (FEN)$^-$ ion and a sodium ion in a 1:1:1 stoichiometric ratio, and several water oxygen atoms. The figure shows a view from the primary (narrow) side of the CD, a side view and also the (FEN)$^-$ ion in isolation. The latter shows the geometry of (FEN)$^-$, including the significant dihedral angle of 35.5(8)° between the two phenyl rings.

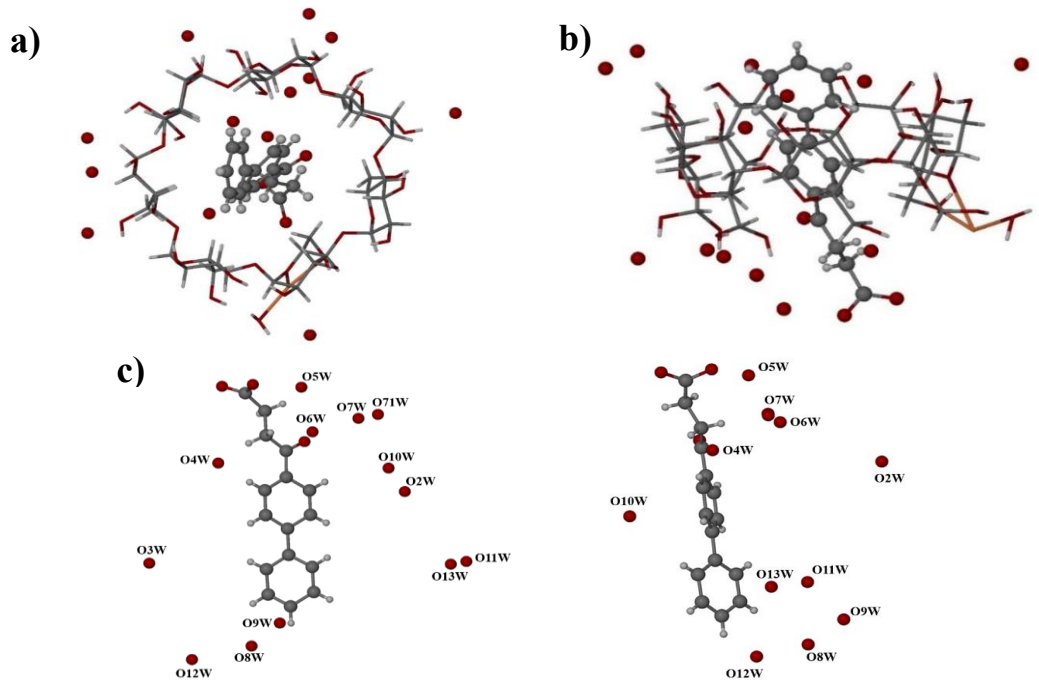

Figure 4.5: The ASU of BCD·Fen^{-}Na^{+} viewed from the a) primary (narrow) side, b) the side and c) (FEN)$^{-}$ on its own, viewed from two directions.

The stereoscopic images in Figure 4.6 highlight the salient representative structural motif in the crystal of the salt, namely two symmetry-related dimers of BCD (each containing two (FEN)$^{-}$ ions), connected by a six-coordinated sodium ion bound to oxygen atoms. The extended motif is a polymeric chain propagating along the directions +z and -z. In Figure 4.6(a) hydrogen atoms are omitted to clarify the details of sodium ion co-ordination. The view direction is nearly parallel to the *x*-axis, the sodium ion being located on the twofold rotation axis at 0.47048, ½, ½. Figure 4.6(b) includes the hydrogen atoms.

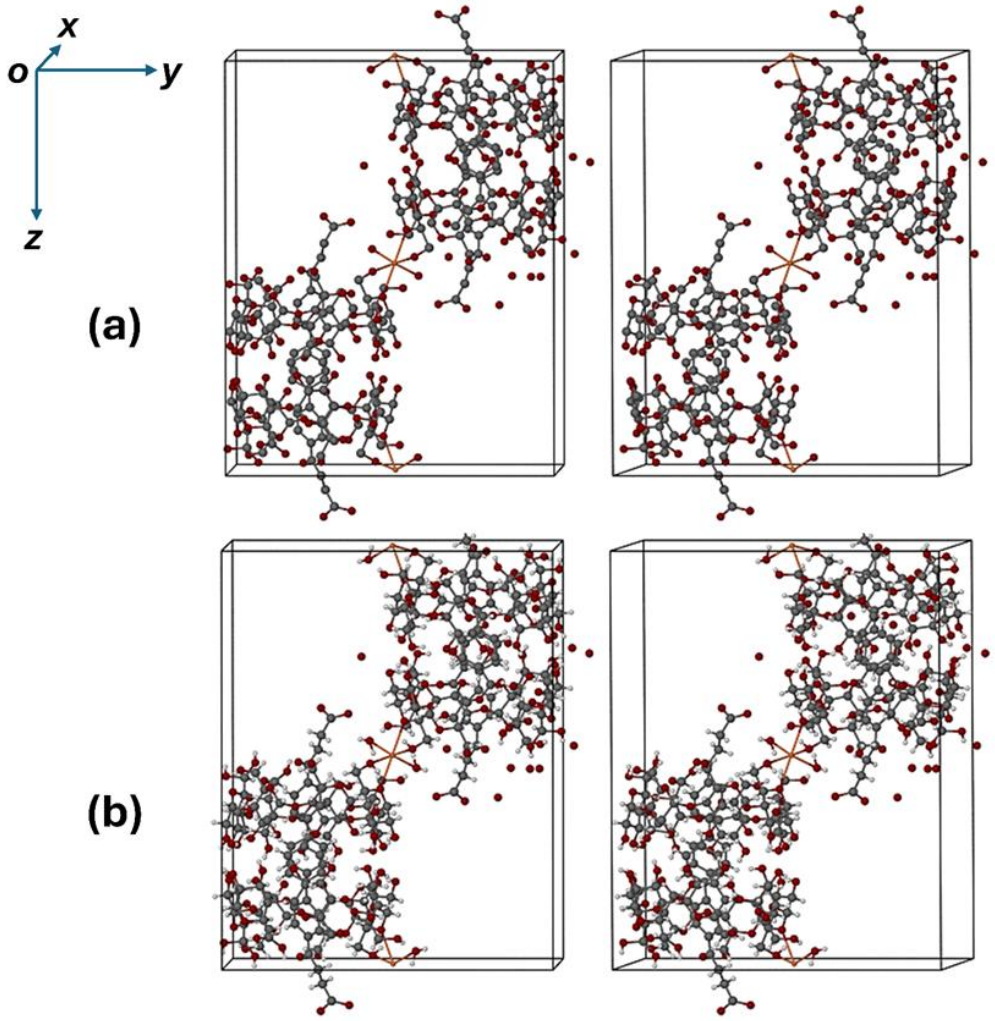

Figure 4.6: Stereoscopic views of the repeating motif drawn with (a) no H atoms included, (b) H atoms included.

Careful inspection shows that the Na^+ ion is bonded to (a) the oxygen atoms of two water molecules, and (b) to both the heteroatom O5 in a glucose ring and the hydroxyl oxygen atom O6 of the same glucose molecule, the two bonds being repeated for the glucose ring of the neighbouring BCD molecule via two-fold rotation. The three unique Na^+- O bond lengths are in the range 2.39(2) – 2.66(2) Å, reflecting the resulting, highly distorted pseudo-octahedral co-ordination environment of the sodium ion, with extreme values of the fifteen O - Na^+- O bond angles being 66.0(6)° and 175.9(7)°. A very significant feature of each BCD dimer and its included guest ions is that the two diads parallel to the crystal *b*-axis (at ½, y, ¼ and ½, y, ¾) pass through the interface of the dimer. It is then evident in both Figures 4.6 above and Figure 4.7 below that the terminal phenyl ring of an included $(FEN)^-$ ion engages in a π-π interaction with its twofold-related counterpart in the other

included $(FEN)^-$ ion. The ring centroid···centroid distance is 3.864(9) Å, with a slippage of only 0.781 Å, indicating a strong stabilising interaction.

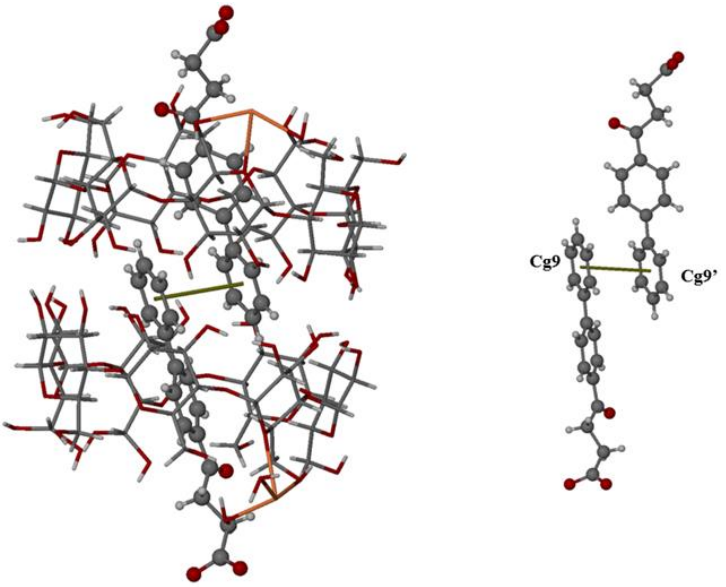

Figure 4.7: The π-π interaction between the terminal phenyl ring of $(FEN)^-$ (C14→C19) and its counterpart related by a two-fold rotation axis (respective equivalent positions x, y, z; 1-x, y, 1/2-z).

As shown above, the $(FEN)^-$ ion adopts an extended conformation, with the carboxylate group protruding from the primary side of the BCD molecule, being accommodated in the void formed at the junction of three neighbouring complex units. Both carboxylate oxygen atoms (O2 and O3) engage in multiple hydrogen bonds primarily with water molecules, the relevant O···O distances being in the range 2.49(3) – 3.14(4) Å.

Hydrogen bonding

Hydrogen bonds play a prominent role in the cohesion of the BCD·Fen^-Na^+ crystal. Figure 4.8 is a stereoscopic diagram highlighting all H-bonds within the BCD dimer and emanating from it. The figure shows several intramolecular O-H···O bonds forming a belt within each of the BCD molecules comprising the dimer, as well as intermolecular O-H···O bonds that link the secondary sides of the two BCD molecules, stabilising the dimeric structure. These are common features of BCD complexes. H-bonds that emanate from the dimer indicate links to oxygen atoms of water molecules and oxygen atoms of neighbouring CD molecules. In Table 4.5, only the intramolecular O-H···O bonds are listed.

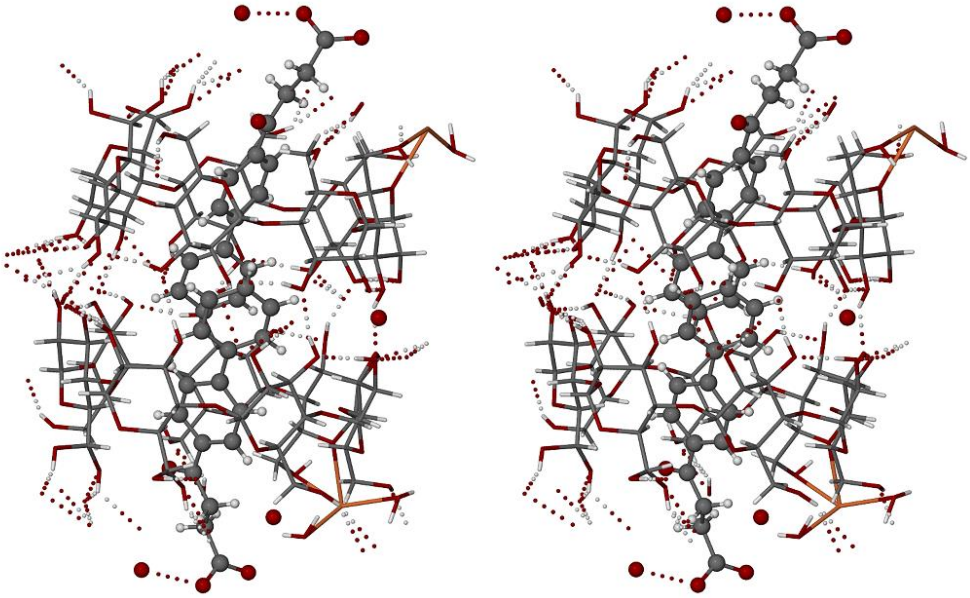

Figure 4.8: Perspective stereo-diagram showing H bonds in BCD·Fen^{-}Na^{+}.

Table 4.5: Intramolecular hydrogen bonding in BCD·Fen^{-}Na^{+}.

Hydrogen bond interaction	D-H (Å)	H···A (Å)	D···A (Å)	D-H···A (°)
O3G1-H3G1···O2G2	0.82	1.98	2.790(14)	168
O3G2-H3G2···O2G3	0.82	1.99	2.759(15)	156
O2G5-H2G5···O3G4	0.82	2.02	2.818(12)	163
O3G5-H3G5···O2G6	0.82	1.96	2.765(16)	165
O2G6-H2G6···O3G5	0.82	1.99	2.765(16)	159
O2G7-H2G7···O3G6	0.82	2.11	2.874(16)	156
O3G7-H3G7···O2G1	0.82	2.08	2.870(17)	163

Parameters for the intermolecular hydrogen bonds involving (FEN)$^{-}$, BCD and water molecules in BCD·Fen^{-}Na^{+} are listed in Table 4.6.

Table 4.6: Intermolecular hydrogen bonding involving $(FEN)^-$, BCD and water molecules in BCD·Fen^-Na^+.

Hydrogen bond interaction	D-H (Å)	H···A (Å)	D···A (Å)	D-H···A (°)	Symmetry code
O2G1-H2G1···O10W	0.82	1.85	2.64(4)	162	x,y,z
O2G2-H2G2···O11W	0.82	2.19	2.88(3)	141	x,y,z
O2G2-H2G2···O13W	0.82	1.74	2.34(3)	129	x,y,z
O2G2-H2G2···O3G2	0.82	2.40	3.035(13)	135	1-x,y,1/2-z
O2G3-H2G3···O13W	0.82	1.69	2.03(3)	103	1-x,y,1/2-z
O2G3-H2G3···O2G5	0.82	2.07	2.879(14)	171	3/2-x,1/2+y,1/2-z
O3G3-H3G3···O3G1	0.82	1.97	2.780(14)	171	1-x,y,1/2-z
O2G4-H2G4···O8W	0.82	2.09	2.87(2)	160	x,y,z
O2G4-H2G4···O3G7	0.82	2.59	3.074(14)	119	1-x,y,1/2-z
O3G4-H3G4···O3G7	0.82	1.95	2.751(14)	166’	1-x,y,1/2-z
O6G1-H24···O6G5	0.85(8)	1.99(9)	2.797(19)	159(12)	-1/2+x,1/2+y,z
O6G4-H6G5···O71W	0.82	2.08	2.85(2)	158	½+x,3/2-y,1-z
O6G4-H6G5···O7W	0.82	2.06	2.63(4)	125’	½+x,3/2-y,1-z
O3G6-H3G6···O3G5	0.82	2.05	2.81(2)	154	1-x,y,1/2-z
C4-H4A···O5G4	0.97	2.51	3.09(2)	118	-1/2+x,3/2-y,1-z
C2G3-H5···O3G6	0.98	2.41	3.328(16)	156	½+x,1/2+y,z
C6G1-H6G2···O71W	0.97	2.36	2.80(3)	106	x,y,z
C9-H9···O4W	0.93	2.54	3.41(3)	155	x,y,z
C2G5-H11···O3G1	0.98	2.39	3.352(16)	166	1/2+x,-1/2+y,z
C6G7-H27···O6B	0.97	2.25	2.78(6)	114	-1/2+x,3/2-y,1-z
C1G5-H1G5···O2G2	0.98	2.56	3.312(17)	133	1/2+x,-1/2+y,z

Crystal packing

Figure 4.8 above illustrated the repeating motif as viewed along the crystal *a*-axis. The other projections are shown in Figure 4.9. Water oxygen atoms have been omitted for clarity. The twofold rotational symmetry of the BCD complex dimers around the *b*-axis in the [001] projection is evident, as are the effects of the twofold screw axes parallel to the *c*-axis. In the [010] projection, twofold rotation axes parallel to the *a*-axis at z = 0 and ½ are evident.

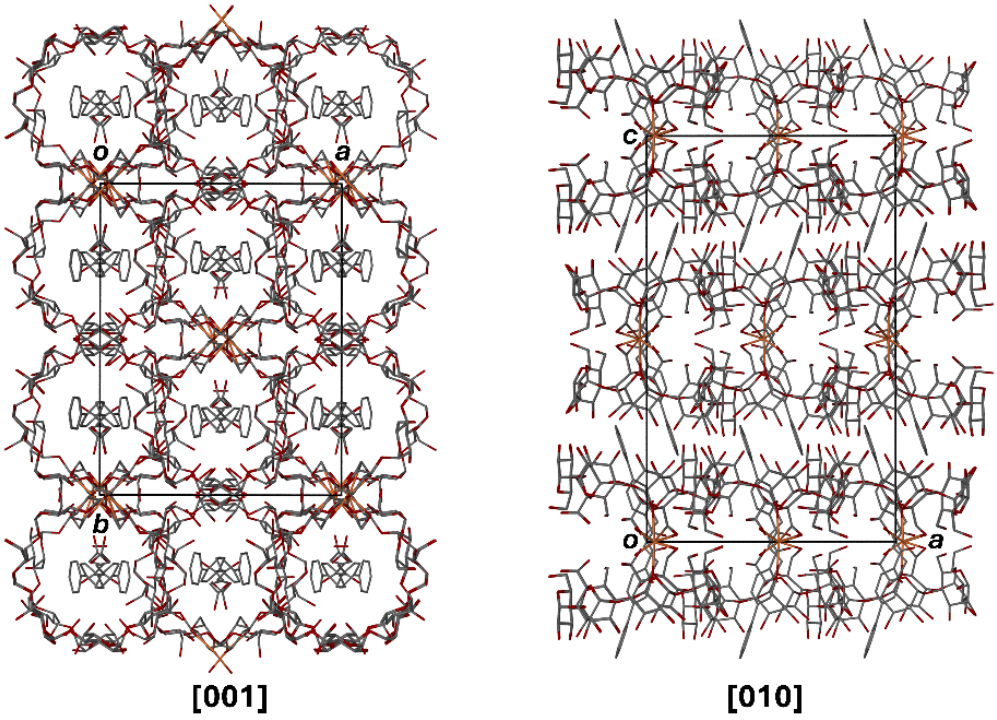

Figure 4.9: Packing diagrams for BCD·Fen^{-}Na^{+} viewed down the *c*-axis (left) and the *b*-axis (right).

4.3.4. Fourier-transform infrared (FT-IR) spectroscopy

Figure 4.10 shows the stacked FT-IR spectra of Fen^{-}Na^{+}, BCD and BCD·Fen^{-}Na^{+}, the latter lacking the characteristic Fen^{-}Na^{+} absorption peaks.[4] This is the first indication that there is an inclusion complex present. The broad band at ~3300 cm^{-1} is representative of the hydroxyl groups in pure BCD and is somewhat narrowed and sharper in the product. This further indicates that an inclusion complex has formed and represents the water that is present the complex. In the spectrum of Fen^{-}Na^{+}, the bands at 1591 and 1403 cm^{-1} represent the respective asymmetric and symmetric stretching vibrations of the carboxylate group. These shift to 1558 and 1392 cm^{-1} respectively in the product.

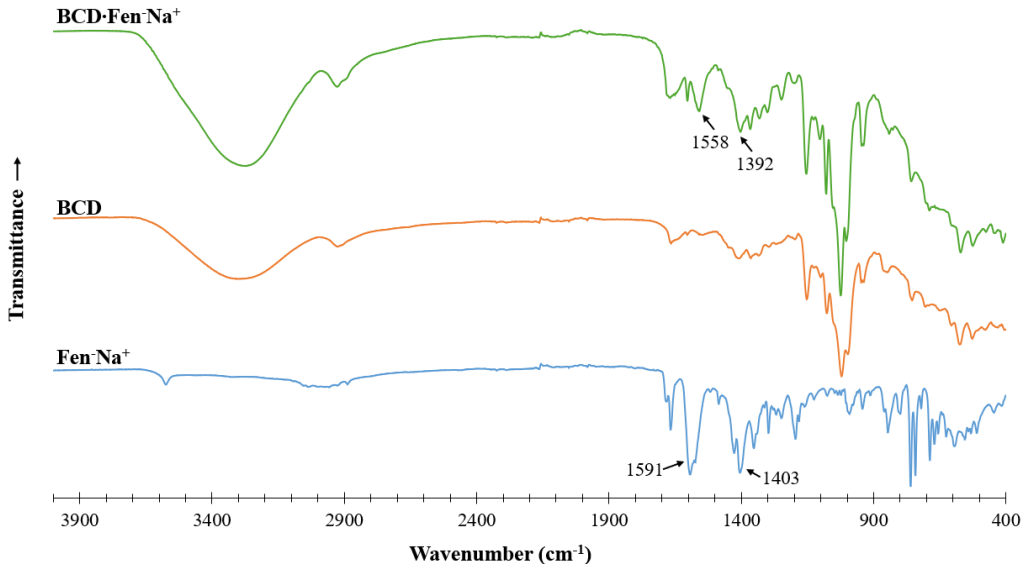

Figure 4.10: Stacked FT-IR spectra of Fen$^-$Na$^+$, BCD and the BCD·Fen$^-$Na$^+$ inclusion complex.

4.3.5. Comparative powder X-ray diffraction (PXRD) patterns

Figure 4.11 shows the calculated and experimental PXRD patterns of BCD·Fen$^-$Na$^+$. Although the calculated pattern shows some degree of similarity with that of the experimental pattern, there are a few discrepancies. While the general profiles are similar, it is noted that some peaks in the calculated pattern have shifted to lower angles, and others to higher angles, relative to their corresponding peaks in the experimental pattern. These effects are likely due to the differences in the temperatures at which the patterns were recorded (21 °C for the experimental pattern, -173 °C for the calculated pattern) and the consequent anisotropic shrinkage of the crystal on cooling.

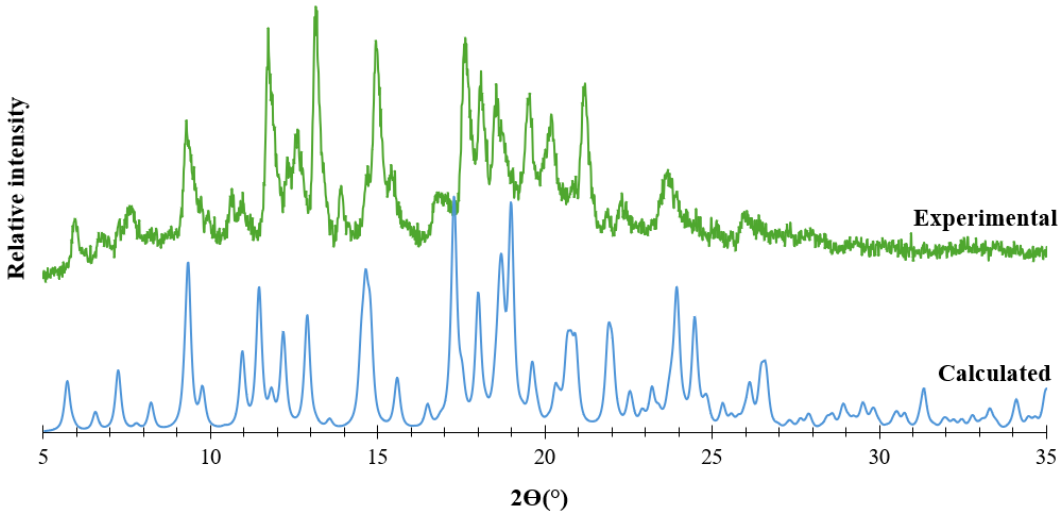

Figure 4.11: Calculated and experimental PXRD patterns of BCD·Fen$^-$Na$^+$.

4.3.6. Solubility study

The solubility of BCD·Fen$^-$Na$^+$ was determined in both aqueous and FaSSIF (Fasted State Simulated Intestinal Fluid) media, the latter buffered at pH 6.5. The procedures, described in Chapter 2 (2.6.2. Gravimetric solubility studies, pg. 29 and 2.6.5. Equilibrium solubility studies, pg. 32) were used for determination of the solubilities in FaSSIF and in water respectively. The standard curve used and all HPLC measurements can be found in the Appendix (Section 1.3.1., pg. 5). Table 4.7 shows the equivalent (FEN)$^-$ concentration of Fen$^-$Na$^+$ (control) and BCD·Fen$^-$Na$^+$ in both media, all solubility determinations having been performed in duplicate.

The aqueous solubility of (FEN)$^-$ when the salt is incorporated in the BCD complex, increases 11.5-fold compared to the solubility of Fen$^-$Na$^+$, but a decrease was recorded for dissolution in FaSSIF. As observed for the salts Fen$^-$Na$^+$ and Fen$^-$K$^+$, the decrease is most likely due to the lowered pH of 6.5, which is not favourable for a weakly acidic API. Another reason for this could be the effect that varying pH has on the solubility of CDs and the stability constant (K_c) for complex formation by reaction of the API and CD.[5] This could mean that the capacity of the buffer was not enough to maintain a stable pH value. This, along with the fact that the mass fraction of (FEN)$^-$ is much lower when it is incorporated in the CD complex, may also contribute to the decreased solubility.

Table 4.7: Total (FEN)$^-$ concentration (mg/ml) in aqueous and FaSSIF (pH 6.5) media, derived from solubility measurements of Fen$^-$Na$^+$ and BCD·Fen$^-$Na$^+$.

	Aqueous (mg/ml)	**FaSSIF, pH 6.5 (mg/ml)***
Fen$^-$Na$^+$	**7.7**	**3.8 ± 0.6**
BCD·Fen$^-$Na$^+$	**88.8**	**2.7 ± 0.4**
Solubility enhancement factor	**11.5**	**0.71 ± 0.01**

***** The mass fractions of (FEN)$^-$ in Fen$^-$Na$^+$ and BCD·Fen$^-$Na$^+$ are 0.72 and 0.18 respectively. This has been taken into account in the solubility calculations.

4.4 The inclusion complex GCD·Fen$^-$Na$^+$ formed by reaction of γ-CD with the fenbufen sodium salt

The inclusion complex of Fen$^-$Na$^+$ and GCD was synthesised using the method described at the beginning of this chapter. After 7 days, clear fibrous crystals not suitable for single crystal X-ray analysis were present. To improve the quality of the crystals the rate of crystallisation was slowed down. After a month of slow evaporation the resulting crystals were still not suitable for full intensity data-collection. Figure 4.12 shows the PXRD pattern of the co-precipitated product and that of a known representative GCD inclusion complex. Their general profiles match sufficiently well to conclude that the green trace represents a GCD inclusion complex that is isostructural with the authentic representative GCD complex.

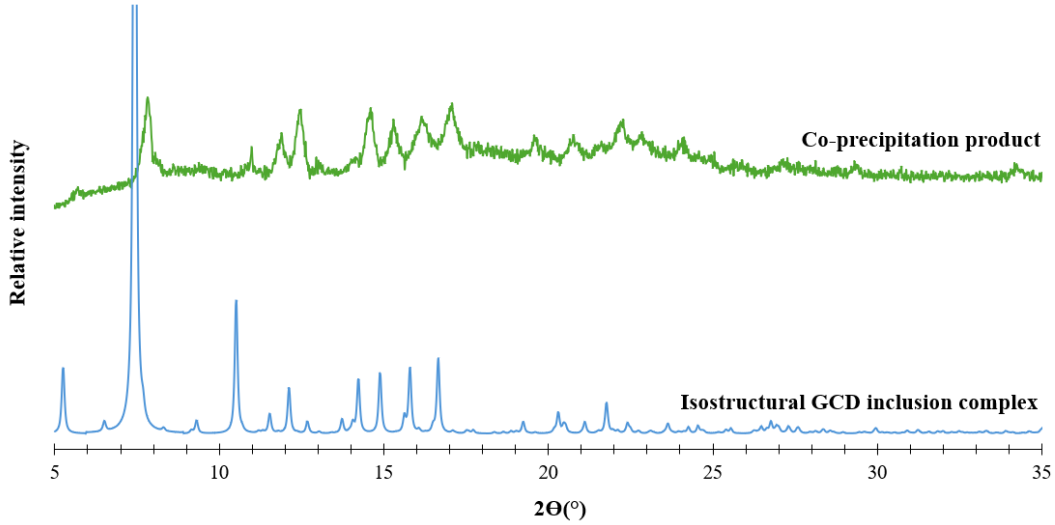

Figure 4.12: The experimental PXRD pattern of the putative complex GCD·Fen$^-$Na$^+$ (green trace) and the calculated PXRD pattern of a GCD complex (refcode: KECWOI) crystallizing in the space group $P42_12$ (blue trace).

4.4.1. ^{1}H NMR spectroscopy

Table 4.8 shows the chemical shifts of the signals belonging to GCD and Fen$^-$Na$^+$. The proton assignment is based on the labelling scheme in Figure 4.13. The integration values confirm that (FEN)$^-$ and GCD are present in the product in a 1:1 stoichiometric ratio. The full spectrum can be seen in the Appendix (Section 1.2.2., pg. 4).

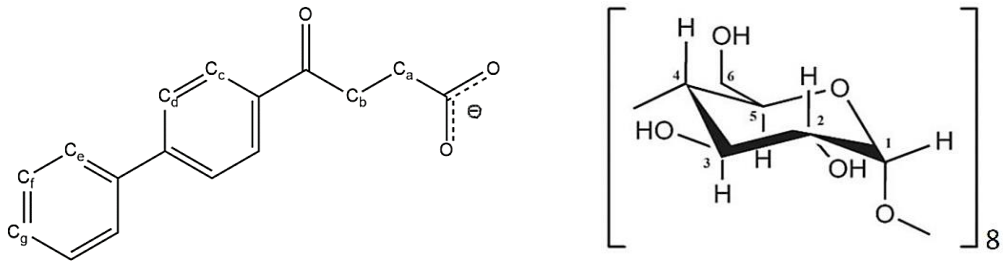

Figure 4.13: Labelling scheme of $(FEN)^-$ (left) and GCD (right) used for the assignment of peaks in the ^1H NMR spectrum.

Table 4.8: The chemical shifts of diagnostic peaks in the ^1H NMR spectrum of GCD·Fen^-Na^+.

Assignment	δ (ppm)	Integration	Multiplicity	Proton	Stoichiometric ratio	Integer
$(FEN)^-$						
CH aromatic (e)	8.07 - 8.05	2.25	Doublet	2H	1.13	1
CH aromatic (c,d)	7.83 - 7.75	4.58	Doublet of doublets	4H	1.15	1
CH aromatic (f,g)	7.53 - 7.40	3.47	Doublet of triplets	3H	1.16	1
GCD						
OH-3 and OH-2	6.01	16*	Singlet	16H	1	1
OH-6	4.88	7.72	Singlet	8H	0.97	1
CH-1	4.57	7.85	Singlet	8H	0.98	1

*Reference integral

4.4.2. Thermal analysis

4.4.2.1. Hot stage microscopy (HSM)

The HSM images (Figure 4.14) were recorded from 20 to 260 °C at a heating rate of 10 °C/min. The crystals which start as clear, fine fibres undergo a phase change from a solid to liquid that begins at 60.8 °C. This continues until the phase change is completed at 98.7 °C. Shortly after this, beginning at 102.2 °C, a second phase change occurs in which small regular crystals begin forming in the centre of the liquid. At 121.8 °C the phase change is complete, after which bubbling, and decomposition of the new phase begin at 126.3 °C. Decomposition continues with increasing temperature until it is complete at 260.0 °C.

Figure 4.14: HSM images of the GCD·Fen$^-$Na$^+$ co-precipitation product recorded in the range 50 – 260 °C.

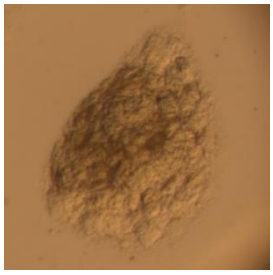

50.0 °C: Fibrous crystals at low temperature.

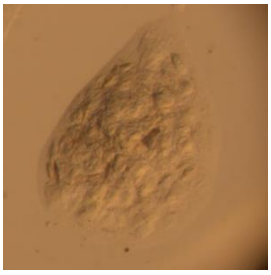

60.8 °C: Phase change from solid to liquid begins.

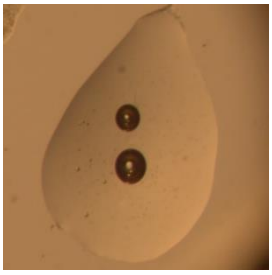

98.7 °C: Phase change complete.

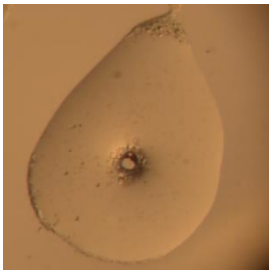

102.2 °C: Second phase change begins taking place.

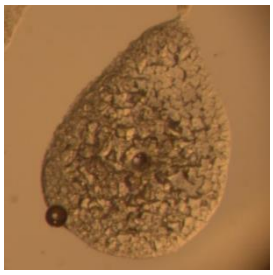

121.8 °C: Bubbles begin forming and first sign of decomposition.

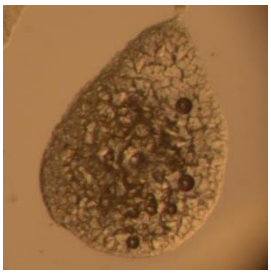

126.3 °C: Bubbles continue forming and browning continues.

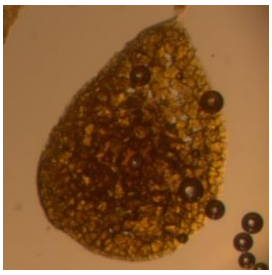

247.3 °C: Decomposition continues.

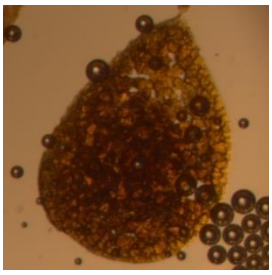

260.0 °C: Decomposition is complete.

4.4.2.2. Thermal gravimetric analysis (TGA) and differential scanning calorimetry (DSC)

Figure 4.15 shows the TGA (n = 2) and DSC curves of the GCD·Fen$^-$Na$^+$ co-precipitation product. The TGA curve shows two mass losses that take place over the range 20 – 400 °C. The first mass loss of 11.1 ± 0.1% with an onset temperature of 31.2 °C, is attributed to the dehydration of the complex and is equivalent to 10.9 ± 0.1 water molecules per GCD molecule. The DSC curve, which was recorded from 20 to 290 °C, shows a broad endotherm that occurs in the range 80 – 115 °C. This endotherm is within the temperature range in which the phase change from a liquid to a solid occurs, as observed in the HSM images. However, the overlapping dehydration process presumably also contributes to the size of this endotherm.

The second mass loss of 52.5 ± 0.5% with an onset temperature of 242.1 °C reflects the decomposition. The HSM images show that decomposition is complete at 260 °C; this is not consistent with the TGA curve. This is probably due to the different instruments used and the inability to distinguish the onset of the colour change in the HSM images. The DSC curve shows that there are thermal events taking place from 200 °C, with an exotherm present at 243 °C which is most likely the decomposition. Due to the sensitivity of the DSC instrument the temperature could not be taken

past the point of decomposition. Based on the ^{1}H NMR spectroscopic data and the TGA mass loss results, the final chemical formula of the inclusion complex can be designated as $C_{48}H_{80}O_{40}\cdot[C_{16}H_{13}O_3]^-Na^+\cdot 10.9\ H_2O$.

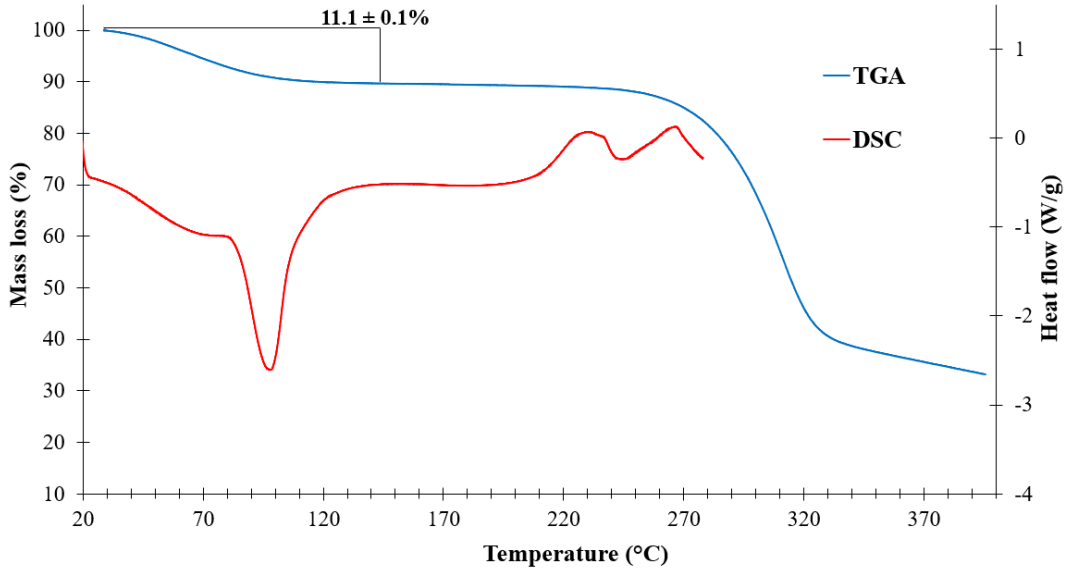

Figure 4.15: TGA and DSC curves for the GCD·Fen$^-$Na$^+$ co-precipitation product.

4.4.3. Fourier-transform infrared (FT-IR) spectroscopy

Figure 4.16 shows the stacked spectra of Fen$^-$Na$^+$, GCD and the GCD·Fen$^-$Na$^+$ co-precipitation product. The broad band at ~3350 cm^{-1} is representative of the hydroxyl groups in pure GCD and water in the complex. In the spectrum of Fen$^-$Na$^+$, the bands at 1591 and 1403 cm^{-1} correspond to the asymmetric and symmetric stretching vibrations of the carboxylate group. The former shifts to 1559 cm^{-1} in the product, indicating a change in the interactions of the carboxylate group of (FEN)$^-$ on complexation with GCD.

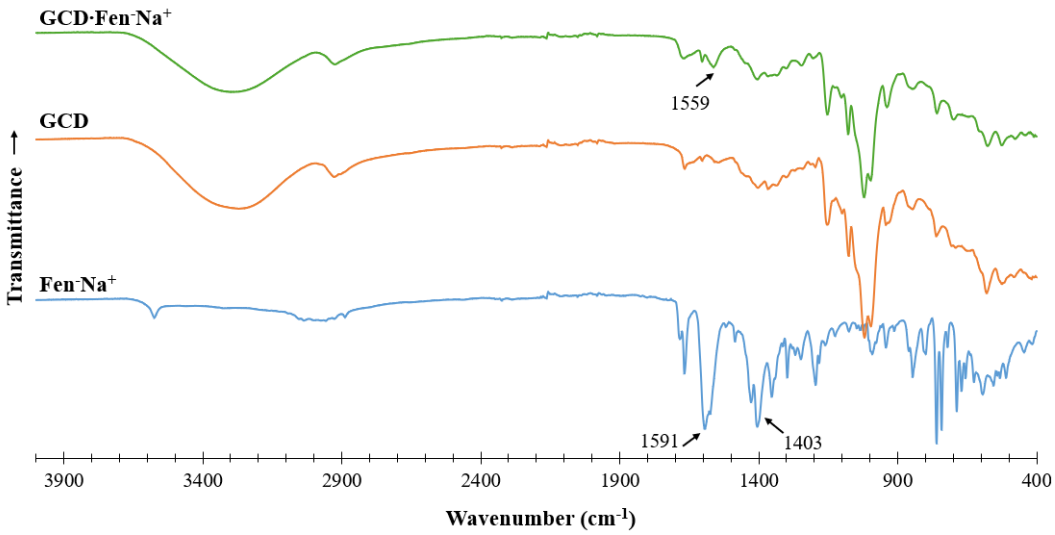

Figure 4.16: Stacked FT-IR spectra of Fen^-Na^+, GCD and the GCD·Fen^-Na^+ inclusion complex.

4.4.4. Solubility study

The solubility of GCD·Fen^-Na^+ was determined in both aqueous and FaSSIF (buffered at pH 6.5) media (Table 4.9) using the methods described for BCD·Fen^-Na^+. When $(FEN)^-$ is incorporated in the crystal of the inclusion complex, there is a 11.3-fold increase in its aqueous solubility. There is, however, a 0.48-fold solubility decrease in FaSSIF when compared to that of Fen^-Na^+. This could once again be explained using the argument mentioned in the analogous section above dealing with BCD·Fen^-Na^+.

Table 4.9: Total $(FEN)^-$ concentration (mg/ml) in aqueous and FaSSIF (pH 6.5) media, derived from solubility measurements of Fen^-Na^+ and GCD·Fen^-Na^+.

	Aqueous (mg/ml)	**FaSSIF, pH 6 (mg/ml)***
Fen^-Na^+	**7.7**	**3.8 ± 0.6**
GCD·Fen^-Na^+	**87.0**	**1.8 ± 0.2**
Solubility enhancement factor	**11.3**	**0.48 ± 0.02**

* The mass fractions of $(FEN)^-$ in Fen^-Na^+ and GCD·Fen^-Na^+ are 0.72 and 0.14 respectively. These have been taken into account in the solubility calculations.

4.5. Kneading and co-precipitation experiments with a series of cyclodextrins and guest compound fenbufen

Initially, kneading and co-precipitation experiments, as described in Chapter 2 (2.4. Cyclodextrin inclusion complex synthesis, pg. 23) were performed using equimolar amounts of FEN and the native CDs (Table 4.10). In all attempts, the recurring issue was the poor solubility of FEN in water. Because FEN is soluble in organic solvents, water:EtOH solvent mixtures with ratios varying from 10 – 80% EtOH were tested. FEN was dissolved in the appropriate quantity of EtOH that would give the desired solvent ratio and added dropwise to the aqueous CD solution. In each case, when the FEN solution was added to the CD it immediately crashed out of solution. When it was evident that a 1:1 ratio was not successful, increasing molar ratios of the CD to that of FEN were tested. In many cases, two cyclodextrin molecules could in principle encapsulate the API, especially when the guest is large. All these attempts unfortunately did not result in the formation of inclusion complexes. The table below lists the various preparative conditions employed and the results.

Table 4.10: Outcomes of attempted inclusion of FEN in various CDs via kneading and co-precipitation.

Cyclodextrin	Stoichiometric ratio	Solvent	Result
α-cyclodextrin (ACD)	1:1	H_2O, H_2O:EtOH, EtOH	No complex
β-cyclodextrin (BCD)	1:1, 2:1, 3:1	H_2O, H_2O:EtOH, EtOH	No complex
γ-cyclodextrin (GCD)	1:1, 3:1, 5:1	H_2O, H_2O:EtOH	Complex (kneading)
Heptakis(2,6-di-*O*-methyl)-β-cyclodextrin (DMB)	1:1, 2:1	H_2O, H_2O:EtOH	No complex, amorphous
Heptakis-(2,3,6-tri-*O*-methyl)-β-cyclodextrin (TRIMEB)	1:1, 2:1	H_2O	No complex, amorphous

With ACD as host, the PXRD patterns (Figure 4.17) of the products obtained after kneading and co-precipitation experiments indicate that they are physical mixtures of FEN and uncomplexed ACD (refcode: BANXUJ).

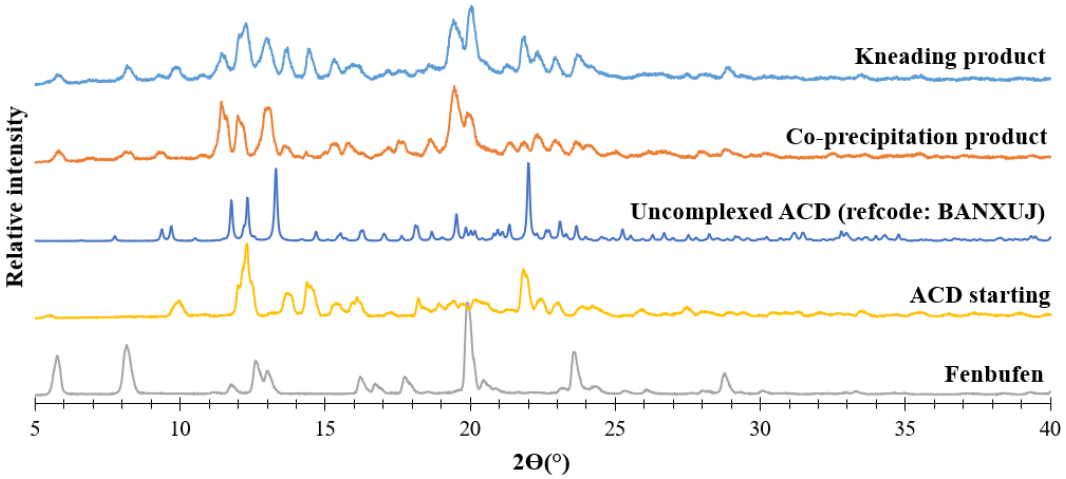

Figure 4.17: PXRD patterns of the products obtained by kneading and co-precipitation of ACD and FEN.

Results for the product obtained by kneading FEN and BCD are shown in Figure 4.18. Based on the known PXRD patterns of isostructural complex families, the co-precipitation product has a pattern which matches that of pure BCD. This is characteristic of small guest molecules which are fully encapsulated within the BCD cavity and would not be possible for a molecule as large as FEN. A visual observation of the crystalline product also showed a mixture of the acicular crystals of FEN and the uncomplexed BCD. All PXRD results can be found in the Appendix (Section 1.5.2., pg. 9).

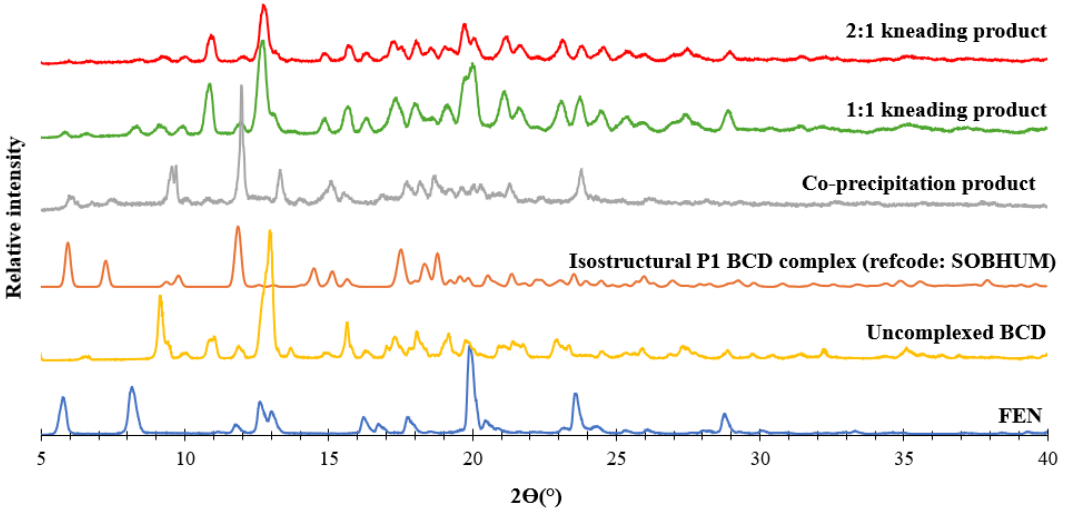

Figure 4.18: PXRD patterns of the products obtained by kneading and co-precipitation of BCD and FEN.

4.6. Inclusion complex of γ-cyclodextrin and fenbufen (GCD·FEN)

The GCD·FEN complex was synthesised by kneading, using equimolar amounts of FEN and GCD. The mixture was kneaded for 20 minutes using a total of 80 µL MilliQ® water. The PXRD pattern of the product (Figure 4.19) confirmed the formation of an inclusion complex; this was evident from the matching PXRD pattern of a known representative GCD inclusion complex crystallizing in the tetragonal space group $P42_12$.[6]

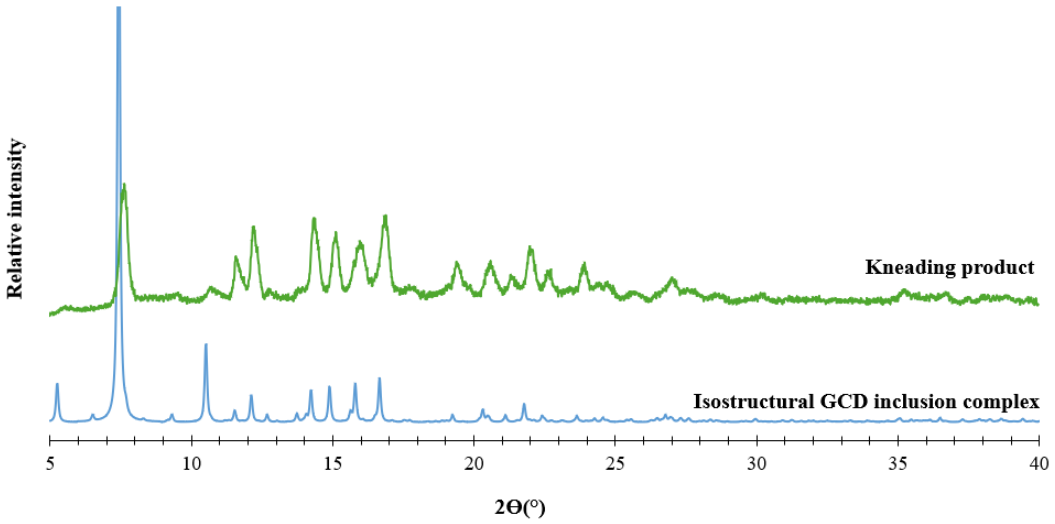

Figure 4.19: The PXRD pattern of the product obtained by kneading GCD and FEN, and that of a known representative GCD complex (refcode: KECWOI).

Co-precipitation experiments with various water:EtOH solvent ratios and increased stirring duration, along with temperature cycling, were performed. However, all attempts to obtain a single crystal of the GCD complex were unsuccessful. Figure 4.20 shows the PXRD pattern obtained by the co-precipitation of FEN and GCD when using a 50% EtOH solution. It contains peaks belonging to both pure FEN and those of a known GCD inclusion complex. This suggests that FEN is being displaced by EtOH, the latter forming a complex with GCD. When all co-precipitation reactions failed, the product obtained by kneading was recrystallised from water. This showed that the product was not as soluble in water as one would expect from a GCD complex. As a final attempt, co-precipitation was performed using a 5:1 GCD:FEN molar ratio. Since the complex has poor solubility, it was assumed that it might crystallise while the GCD would remain in solution as it is highly soluble. This was also unsuccessful, and the FEN did not completely dissolve in the GCD solution.

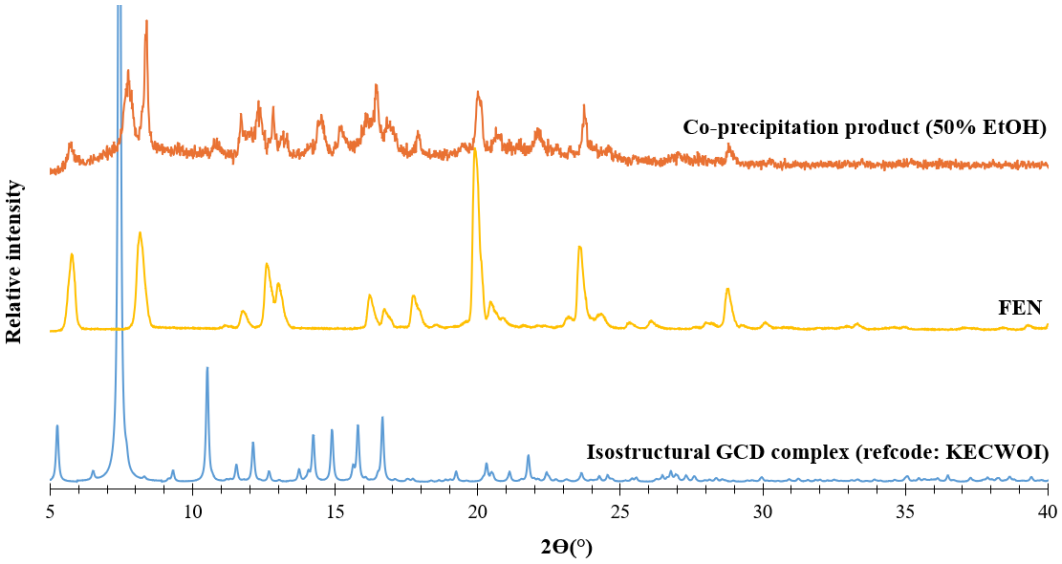

Figure 4.20: PXRD patterns of a representative GCD complex, pure FEN and the co-precipitation product of FEN and GCD from a water/ethanol solution (1:1 v/v).

4.6.1. Fourier-transform infrared (FT-IR) spectroscopy

The FT-IR spectrum (Figure 4.21) of the 1:1 GCD·FEN product obtained by kneading, shows the disappearance of many characteristic bands belonging to FEN. The disappearance and shifting of bands are expected upon complex formation.[4] There is a shift in the peak at 1401 cm^{-1} in the spectrum of FEN (representing the -OH bending frequency), to 1410 cm^{-1}, thus confirming a change in the interaction of FEN, and GCD·FEN complex formation. The broad peaks centred around ~3300 cm^{-1} in the spectra of both GCD and GCD·FEN correspond to the presence of water.

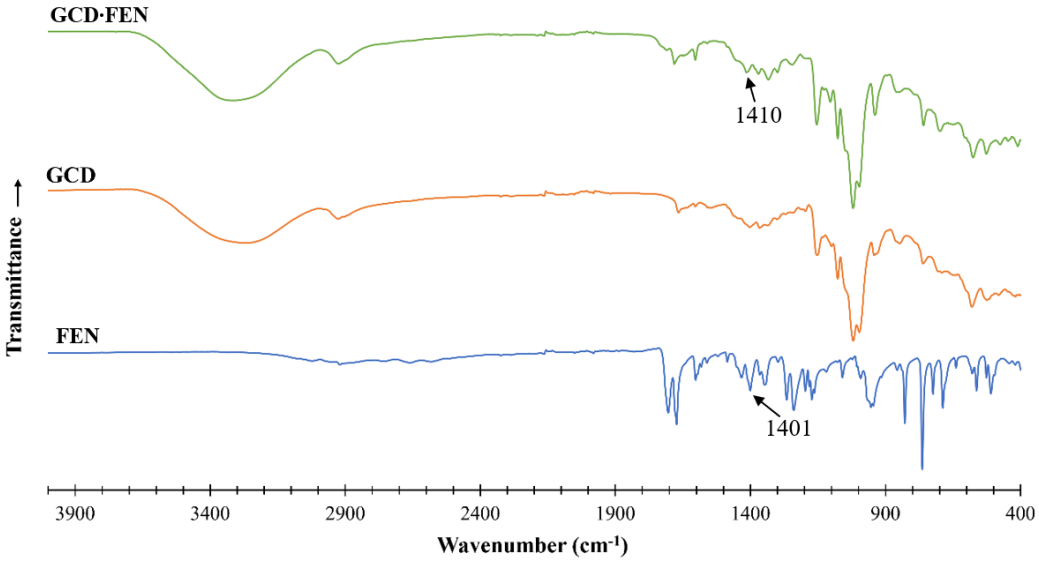

Figure 4.21: FT-IR spectra of FEN, GCD and GCD·FEN.

4.6.2. Thermal analysis

4.6.2.1. Thermal gravimetric analysis (TGA) and differential scanning calorimetry (DSC)

Because a single crystal of GCD·FEN could not be produced, DSC was used to confirm the stoichiometric ratio of FEN and GCD in the product (Figure 4.22). Any trace amounts of FEN present in the product obtained by the kneading method should result in an endotherm at 186.7 °C (melting point of FEN). To confirm the stoichiometry, mixtures of GCD and FEN with 1:2, 1:1and 2:1 molar ratios were kneaded and analysed using DSC. The DSC curve belonging to the 1:2 product shows a small endotherm present at 186.5 °C. The curves for the 1:1 and 2:1 samples show no FEN fusion endotherm. These results are consistent with a 1:1 stoichiometry for the complex.

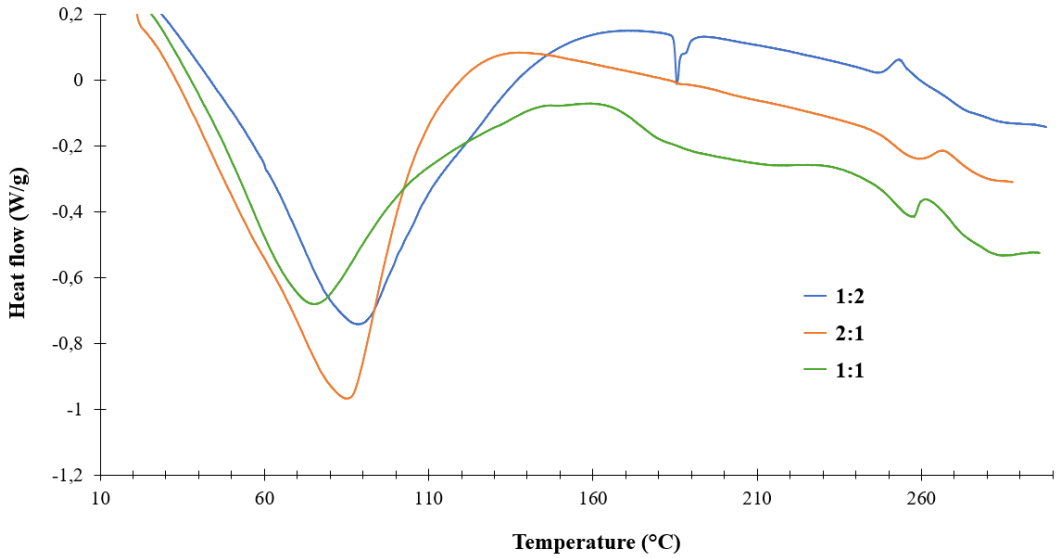

Figure 4.22: DSC curves recorded for samples obtained by kneading GCD and FEN mixtures with different molar ratios.

Figure 4.23 shows the TGA (n = 2) and DSC curves of the 1:1 complex. The TGA curve shows a 14.2 ± 0.5% and a 59.0 ± 0.3% mass loss with onset temperatures of 20.8 °C and 260.1 °C respectively. The first mass loss is due to the dehydration of the complex and is equivalent to 14.3 ± 0.6 water molecules per GCD molecule. The second mass loss is due to the decomposition of the complex.

The very broad endotherm in the DSC curve peaks at 75.3 °C and it reflects the heat absorbed during the dehydration of the crystal. The temperature range over which this occurs is well aligned with that for the TGA mass loss. There is a small endotherm at 257 °C which may represent a solid-solid transition. Based on the above results, the formula assigned to the complex is $C_{48}H_{80}O_{40}{\cdot}C_{16}H_{14}O_3{\cdot}14.3\ H_2O$.

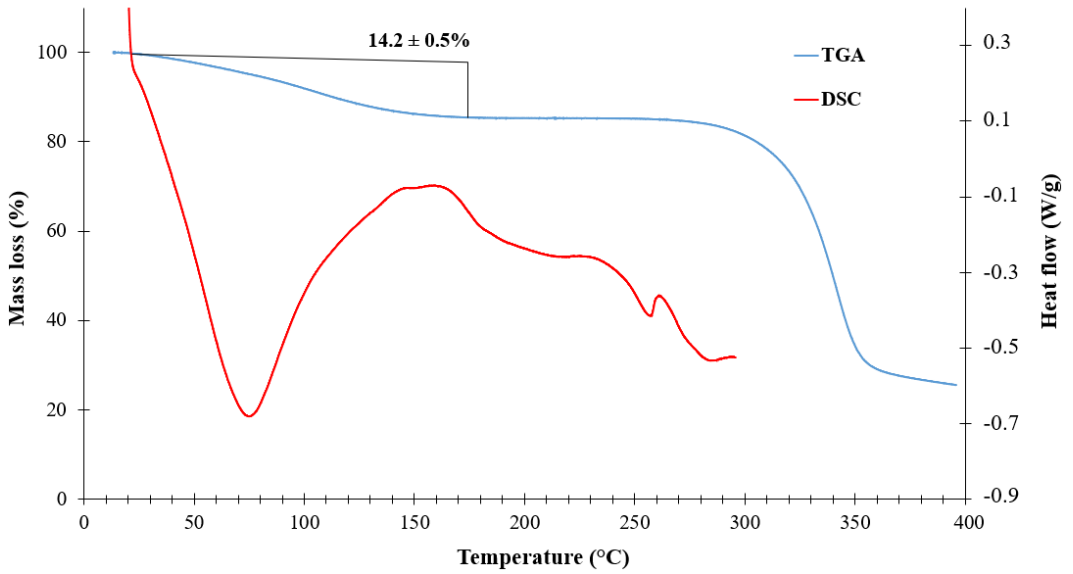

Figure 4.23: TGA and DSC curves for the GCD·FEN complex.

4.7. Phase solubility study

Phase solubility studies were performed using the technique developed by Higuchi and Connors.[7] The cyclodextrins used were HPBCD, GCD, SBEBCD and RAMEB. The standard solution preparation and the standard curve can be found in the Appendix (Section 1.3.2. pg. 6). All phase solubility experiments were performed using the procedure described in Chapter 2 (2.6.4. Phase solubility studies, pg. 31).

All of the experimental plots produced A_L-type phase-solubility curves (Figure 4.24). These show a positive increase in the concentration of FEN with an increase in the CD concentration. The complex formation constant (K_c) values were calculated using the Higuchi-Connors equation, with S_o = 0.028 mM for the aqueous solubility of FEN. The S_o value was determined by dissolving an excess amount of FEN in 5.0 ml water. Aliquots of 1 ml were filtered and the FEN concentration determined by UV-Vis spectroscopy using the standard curve.

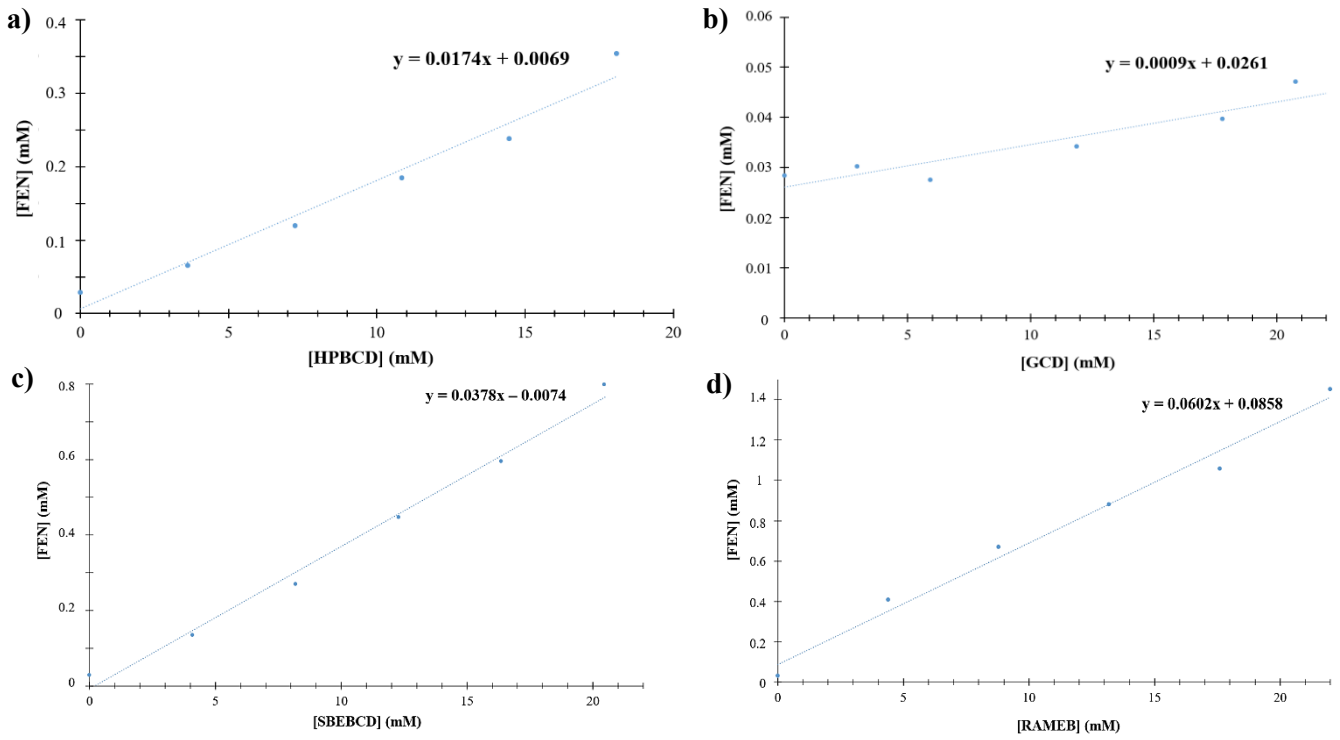

Figure 4.24: Phase solubility plots for FEN with the respective cyclodextrins a) HPBCD, b) GCD, c) SBEBCD and d) RAMEB.

Table 4.11 shows the solubility enhancement of FEN at 25 ± 1 °C and at a CD concentration close to the chosen maximum experimental value, as well as the stability constants for the complexation of FEN with each CD. The reported increases do create the possibility of using cyclodextrins to facilitate the delivery of FEN into the bloodstream. RAMEB resulted in the largest solubility increase for FEN of 206-fold, and GCD the lowest with a 1.5-fold increase. RAMEB has a high aqueous solubility which makes this a predicted result.[8] RAMEB also resulted in the largest K_c value of 2259.4 M^{-1}, indicating strong binding between the FEN molecule and this CD. Instead, with GCD, K_c has a low value of 31.8 M^{-1}, which may explain why it was challenging to isolate a single crystal of the complex.

Table 4.11: The solubility enhancement factors at 25 ± 1 °C and at CD concentration 18 mM, and K_c values using selected cyclodextrins.

Cyclodextrin	Slope	Solubility enhancement factor at 18 mM	K_c (M^{-1})
HPBCD	0.0174	11.3	624.6
RAMEB	0.0602	206.2	2259.4
GCD	0.0009	1.5	31.8
SBEBCD	0.0378	23.7	1385.7

References

1. Shende, P. K.; Gaud, R.; Bakal, R.; Patil, D., Effect of inclusion complexation of meloxicam with β-cyclodextrin-and β-cyclodextrin-based nanosponges on solubility, in vitro release and stability studies. *Colloids and Surfaces B: Biointerfaces* **2015,** *136*, 105-110.
2. XPREP *Data Preparation and Reciprocal Space Exploration*, 2008/2; Bruker Analytical X-Ray Systems: **2008**.
3. Sheldrick, G. M., A short history of SHELX. *Acta Crystallographica Section A: Foundations of Crystallography* **2008,** *64* (1), 112-122.
4. Mura, P., Analytical techniques for characterization of cyclodextrin complexes in the solid state: A review. *Journal of Pharmaceutical and Biomedical Analysis* **2015,** *113*, 226-238.
5. Sætern, A. M.; Nguyen, N. B.; Bauer-Brandl, A.; Brandl, M., Effect of hydroxypropyl-β-cyclodextrin-complexation and pH on solubility of camptothecin. *International Journal of Pharmaceutics* **2004,** *284* (1-2), 61-68.
6. Azzali, A.; d'Agostino, S.; Grepioni, F., Tuning the Solubility of the Herbicide Bentazon: from Salt to Neutral and to Inclusion Complexes. *ACS Sustainable Chemistry & Engineering* **2021,** *9* (37), 12530-12539.
7. Higuchi, T.; Connors, K.A., Phase Solubility Techniques. *Advanced Analytical Chemistry of Instrumentation*, **1965**, *4*, 117-212.
8. Nicolescu, C.; Aramă, C.; Nedelcu, A.; Monciu, C.-M., Phase solubility studies of the inclusion complexes of repaglinide with β-cyclodextrin and β-cyclodextrin derivatives. *Farmacia* **2010,** *58* (5), 620-628.

Chapter 5: Co-crystal screening with the non-steroidal anti-inflammatory drug fenbufen

5.1. Literature review

Fenbufen (FEN) is a non-steroidal anti-inflammatory drug (NSAID) in the aroylpropanoic acid class. It was synthesised in the 1980s to decrease inflammation caused by tendinitis, osteoarthritis or ankylosing spondylitis and may also be used to treat pain caused by fractures or sprains.[1, 2] In addition to its anti-inflammatory properties, FEN inhibits human dihydrofolate reductase. This enzyme is used in the regulation of folate which is essential for the reproduction of the malaria parasite. By inhibiting this enzyme it may be beneficial as an anti-malarial drug.[3] A metabolite of FEN, 4-biphenylacetic acid, is responsible for the anti-inflammatory properties of FEN. Thus, FEN is an example of a pro-drug, which means that it does not enter the body in its active form, but instead undergoes changes after ingestion[4], as depicted in Figure 5.1.[5] FEN enters the body and is then converted to gamma-hydroxy(1,1-biphenyl)-4-butanoic acid and thereafter 4-biphenylacetic acid.

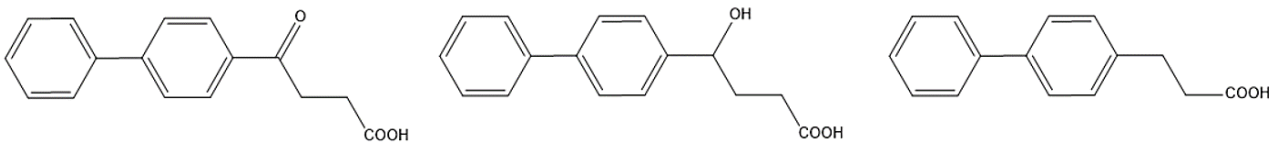

Figure 5.1: Molecular structures of fenbufen (left), gamma-hydroxy(1,1-biphenyl)-4-butanoic acid (centre) and 4-biphenylacetic acid (right).[5]

Pro-drugs offer advantages through increased solubility, selective targeting to the required tissue, decreasing toxicity and the rapid metabolism of the drug.[6] It may also decrease the gastrointestinal injury, which is a well-known side effect of NSAIDs. The mechanism of action of FEN, as with most NSAIDs, is the inhibition of cyclooxygenase (COX) isoforms COX-1 and COX-2.[7] The cyclooxygenase enzymes are inhibited to prevent the production of prostaglandins and thereby decrease inflammation.[8] Since the synthesis of FEN, it has been removed from the market in many countries. This is due to the hepatotoxicity and the drug induced liver injury.[9] Although it has been partially banned, it is still used in some countries. Investigating ways to modify this drug through crystal engineering may be an efficient way to improve its properties and decrease unwanted side effects. The possibility of producing co-crystals, salts and cyclodextrin inclusion complexes of FEN

was investigated to encapsulate or mask the effect of the -COOH functional group, which might increase the bioavailability of FEN and decrease its gastrointestinal effects respectively.

The -COOH group present in the FEN molecule allows the possible formation, via co-crystallization with appropriate coformers, of acid or amide homodimers as well as acid-amine or acid-pyridine heterosynthons[10] as described in Chapter 1 (1.3.2. Co-crystals, pg. 4). The aromatic rings allow the possibility of van der Waal forces as well as π-π stacking interactions in the putative co-crystals, these interactions being divided into four different types: eclipsed, displaced, T-shaped and C-H···π stacked (Figure 5.2), the latter being the weakest of the four. All the potential bonds and interactions would increase the chances of co-crystal synthesis. However, FEN has very poor aqueous solubility as well as wettability, rendering this API in particular, challenging to work with.[11]

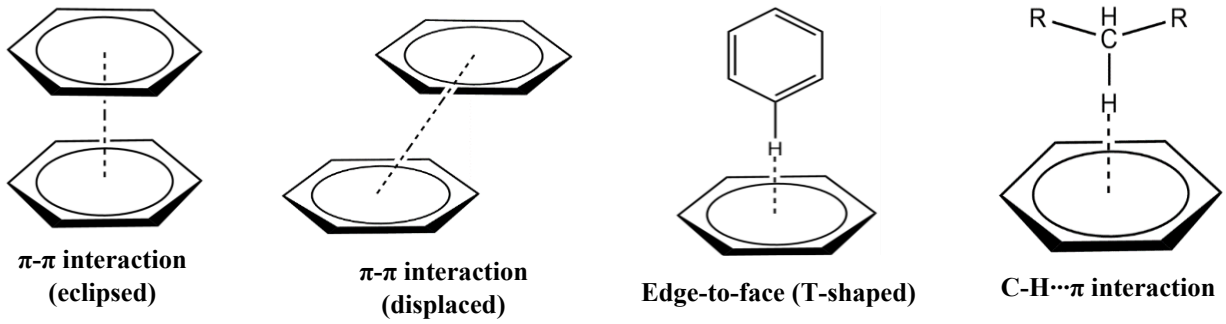

Figure 5.2: Possible π-π interactions (eclipsed or displaced), edge-to-face and C-H···π interactions that may be present in FEN co-crystals.

There are a few reported co-crystals of FEN, but these are not pharmaceutically relevant. Ge *et al.* reported co-crystals with 2-aminopyrazine, 4,4′-bipyridine, trans-1,2-bis(4-pyridyl)ethene and 4-(4-biphenylyl)-4-oxobutyric acid.[12] Due to the lack of reported co-crystals of FEN, it was decided that a fairly large number of coformers, as well as cyclodextrins, should be selected for possible co-crystallization with the drug.

The author of this dissertation was informed by her supervisor that a previous study in our laboratory had led to the isolation of a 1:1 co-crystal between FEN and isonicotinamide, whose essential structural features are described later. However, due to this incomplete study and its corresponding unfinished research report by the student involved,[13] it was decided that in the course of the present study, an attempt to reproduce this 1:1 co-crystal phase for full physicochemical characterization was also desirable.

5.2. Co-crystal screening

5.2.1. Virtual co-crystal screening

Computational co-crystal screening with FEN as the API was performed using the Molecular Complementarity Screening tool module in Mercury.[14] Table 5.1 shows the list of predicted coformer hits.

Table 5.1: List of coformer hits generated with FEN.

2-Amino-5-methylbenzoic acid	Ethylparaben	Apigenin
4-Acetamidobenzoic acid	Glutaric acid	Azelaic acid
4-Aminobenzoic acid	Hippuric acid	Benzoic acid
4-Hydroxybenzoic acid	Methylparaben	Biotin
L-Phenylalanine	Monobutyrin	Suberic acid
N-Ethylacetamide	Nicotinamide	Capsaicin
Acetophenone oxime	Pimelic acid	Sorbic acid
Adipic acid	Propylparaben	

The literature search for multi-component systems containing FEN, as well as a search of the CSD, showed that there are very few co-crystals/salts of FEN that have been reported to date. As previously stated, those that have been synthesised previously have no significant pharmaceutical relevance. This therefore allowed all coformers in our laboratory to be tested.

5.2.2. LAG and co-precipitation experiments

All coformers listed in Table 5.2 were used in both the LAG and co-precipitation experiments. These were chosen based on the functional groups present in their molecular structures. With one exception, all outcomes of the co-precipitation experiments resulted in single crystals of FEN only.

Table 5.2: Outcomes of equimolar FEN + coformer LAG experiments with solvents EtOH, ethyl acetate and MeCN, based on PXRD records.

Coformer	Product
Adipic acid	Physical mixture
Benzamide	Physical mixture
Citric acid	Physical mixture
Ferulic acid	Physical mixture
Fumaric acid	Physical mixture
Glycolamide	Physical mixture
Hippuric acid	Physical mixture
4-hydroxybenzoic acid	Physical mixture
Isonicotinamide	New phase
Lactamide	Physical mixture
L-Malic acid	Physical mixture
Maleic acid	Physical mixture
Orotic acid	Physical mixture
Oxalic acid	Physical mixture
Pimelic acid	Physical mixture
Pyrazinecarboxamide	Physical mixture
Saccharin	Physical mixture
Suberic acid	Physical mixture
Succinic acid	Physical mixture

LAG was performed using the method described in Chapter 2 (2.3.2. Liquid-assisted grinding (LAG), pg. 22). Equimolar amounts of FEN and coformer were ground for 20 minutes using 15 µL increments of the selected solvent at ±3 increments per minute. The powder product was then analysed using PXRD to determine if a new crystalline phase was present. Unfortunately, the PXRD patterns showed that no new products had formed, except in the case of the FEN-ISN combination. Representative examples of the PXRD patterns can be seen below. From Figure 5.3, the product is clearly a physical mixture of FEN and lactamide.

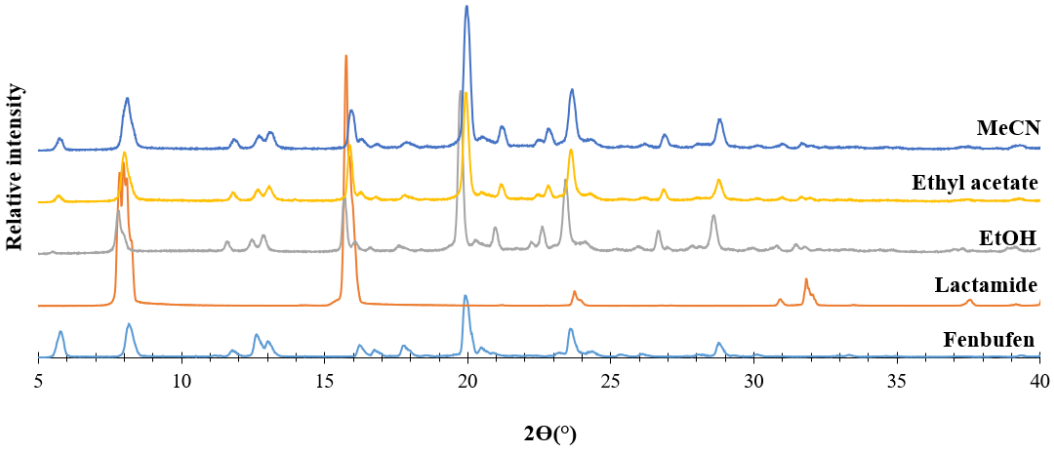

Figure 5.3: PXRD patterns of the starting materials FEN and lactamide and those of the products following LAG experiments using the solvents indicated.

The analogous conclusion, i.e., that the product is a physical mixture, can be drawn for the product of LAG with the coformer hippuric acid (Figure 5.4). PXRD patterns for the experiments with other coformers can all be found in the Appendix (Section 2.1., pg. 10).

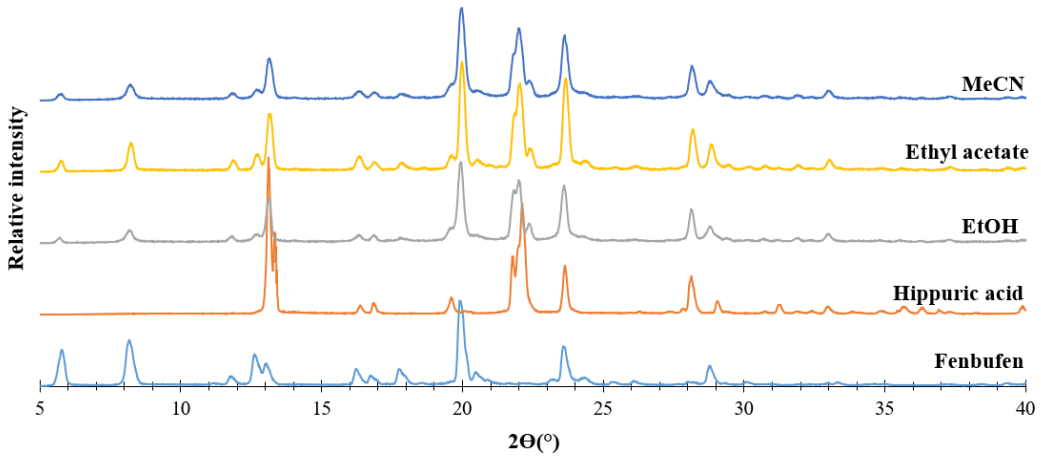

Figure 5.4: PXRD patterns of the starting materials FEN and hippuric acid and those of the products following LAG experiments using the solvents indicated.

The co-precipitation procedure for possible isolation of single crystals of products was followed, as described in Chapter 2 (2.3.3. Co-precipitation, pg. 22), using EtOH, ethyl acetate and MeCN. Each solution was stirred for a minimum of 6 hours. In each attempt clear thin acicular crystals appeared.

Using either PXRD, HSM or unit cell parameters measured by SCXRD, it was confirmed that these crystals were those of FEN, and no new co-crystals had formed.

5.3. Synthesis and characterization of a salt of fenbufen obtained by its reaction with isonicotinamide

As indicated at the end of section 5.1, a 1:1 co-crystal containing FEN and the coformer isonicotinamide (ISN) had been synthesised previously.[13] Crystallographic data for this phase are as follows: $(C_{16}H_{14}O_3)\cdot(C_6H_6N_2O)$, space group $P\ \bar{1}$, a = 5.9181(10), b = 10.8813(17), c = 29.701(5) Å, α = 83.638(4), β = 86.223(4), γ = 80.617(4)°, V = 1873.2(5) Å^3, Z = 4, T = 173(2) K, 48576 reflections (8611 unique), 507 parameters, R_1 [$I > 2\sigma(I)$] = 0.0459, wR_2 = 0.0519, S = 1.029.

The ASU of this co-crystal is shown in Figure 5.5. It consists of two independent, pseudo-centrosymmetrically related, 1:1 FEN-ISN co-crystal units (A and B), in each of which the carboxyl group of FEN is hydrogen bonded to the heterocyclic nitrogen atom of the coformer. Units A and B are linked by the amide-amide synthon occurring between the two coformer molecules.

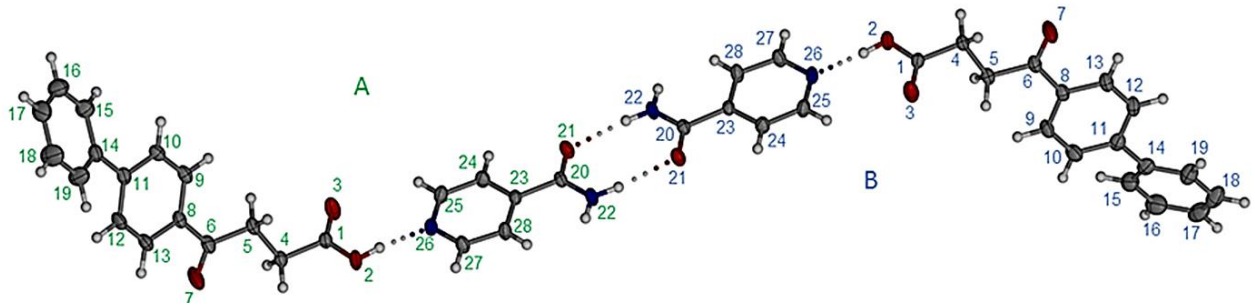

Figure 5.5: The ASU in the 1:1 co-crystal formed between FEN and ISN.[13]

The only additional data which had been recorded for this phase were its melting point (DSC onset 128.5 °C, peaking at 143.3 °C) and TGA analysis, which had indicated that the product was unsolvated.

One of the main goals of the present study was to reproduce this co-crystal phase and carry out its comprehensive characterization. Thus, the author of the present dissertation performed an extensive series of LAG and co-precipitation experiments in an attempt to recover it; however, this phase could not be reproduced. Additional experiments, with numerous solvents and different reaction conditions also failed to reproduce the co-crystal. Instead, only one product could be isolated and its PXRD

pattern showed that it represented a new crystalline phase. Figure 5.6 shows (a) the PXRD patterns of the starting materials, FEN and ISN, (b) those of the products from 1:1 FEN-ISN LAG experiments (solvents MeCN, EtOH), (c) that of the product from a 2:3 FEN-ISN LAG experiment, and (d) the PXRD pattern of the previously reported 1:1 FEN-ISN. Analysis of these patterns indicated that the products from the 1:1 LAG experiments produced a new phase containing, however, an excess of pure FEN. Subsequently, using a single crystal isolated from a co-precipitation experiment with MeCN (1:1 molar ratio), structural solution via SCXRD revealed that the product was a salt with an ASU in which the FEN:ISN molar ratio was, in fact, 2:3. A very small quantity of water was also evident in this crystal. (The solution and refinement of the crystal structure of the new phase, as well as its supramolecular structural features, are discussed in detail in the sections that follow). From Figure 5.6, it is also evident that this new phase did not correspond with that of the previously reported co-crystal product.

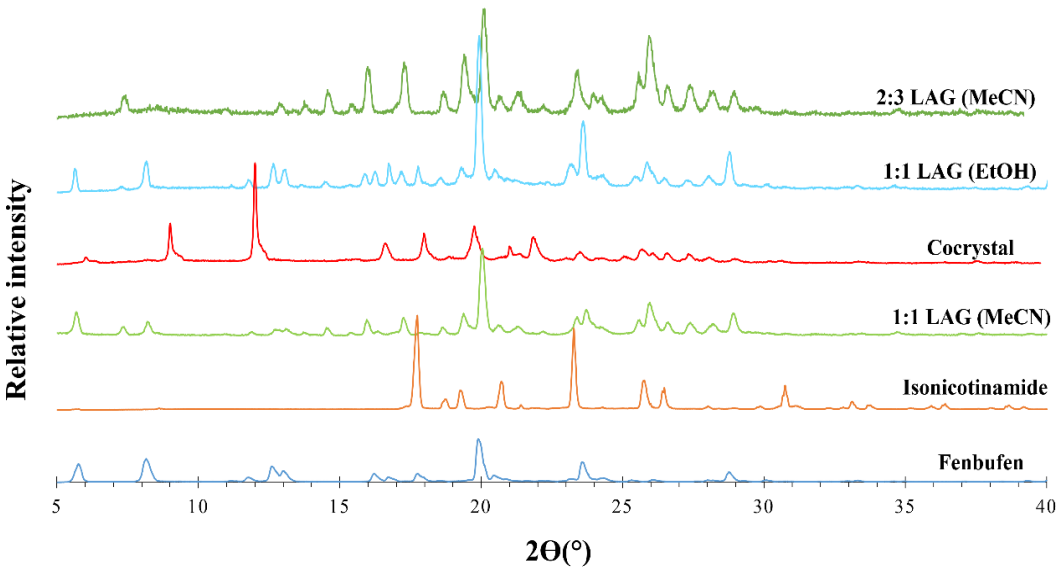

Figure 5.6: Experimental PXRD patterns used to glean information concerning the new FEN-ISN phase.

Having thus established the correct (2:3) FEN:ISN molar ratio for the new product, all further syntheses of this new phase (via either LAG or co-precipitation) were performed using these molar proportions. A description of the final preparative method for isolating the new phase follows.

Single crystals were synthesised using FEN (5.0 mg, 0.012 mmol) and ISN (3.6 mg, 0.018 mmol) each dissolved in 0.6 ml MeCN. The FEN solution was added to that of ISN, stirred at 55 ± 5 °C for

6 hours and filtered thereafter. For product crystallization, the slow cooling method described in Chapter 2 (2.3.3. Co-precipitation pg. 22) was followed: the filtered solution was sealed and placed in a Dewar flask containing water at 55 °C. After 3 days, the insulation was removed, and single crystals were isolated for X-ray data-collection.

5.3.1. Thermal analysis

5.3.1.1. Hot stage microscopy (HSM)

The HSM images of crystals of the new phase were recorded at 2 °C/min to ensure that all potential phase transitions could be clearly observed. The crystal, with rhombohedral habit, undergoes several physical changes, as shown in Figure 5.7.

The first observation was made at 89.5 °C, with the appearance of a large bubble (red circle). This is consistent with the indication from SCXRD that the very small amount of water present in the crystal structure is being released. At 133.9 °C, fine hair-like structures begin forming on the surface of the crystal. This is the first phase change that is observed upon heating. These fine structures continue to grow and become more prominent with increasing temperature. The crystal, which was brown, began melting at 146.2 °C and only liquid remained at 148.2 °C.

The second phase transition was observed from 150.5 °C. Close examination of the clear liquid product showed that it started solidifying. The emerging crystals continued growing until the liquid was no longer present. The second decomposition began at 157.9 °C and was completed by 188.9 °C.

Figure 5.7: HSM images of the new phase from 27.6 to 200 °C (heating rate 2 °C/min) immersed in silicone oil.

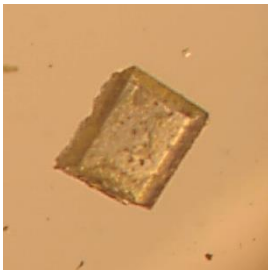

27.6 °C: Rhombohedrally shaped crystal at room temperature.

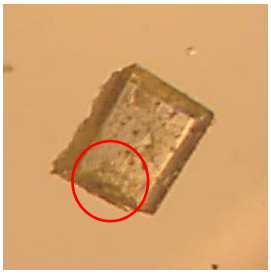

89.5 °C: Development of a bubble (red circle).

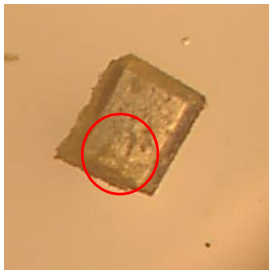

100.6 °C: Large water bubble at the centre of the crystal.

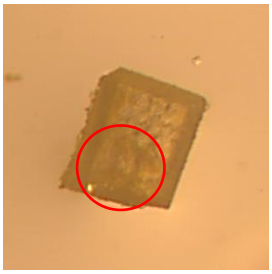

128.4 °C: Crystal begins turning from clear to brown.

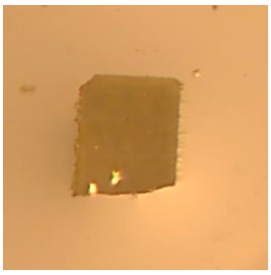

133.9 °C: Appearance of fine hair-like structures.

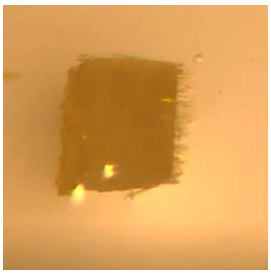

134.7 °C: Fine needles emanating from the crystal. The crystal also turns brown.

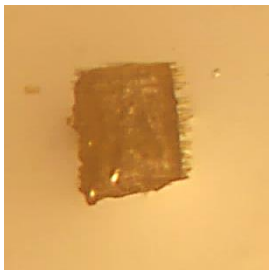

145.0 °C: Continuation of the fine crystal growth from the surface.

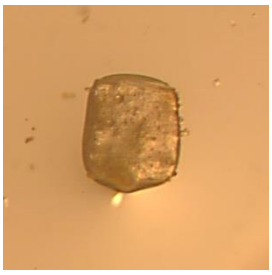

146.2 °C: Onset of melting.

148.2 °C: The melting process is complete.

150.5 °C: A crystalline solid begins forming at the centre of the liquid.

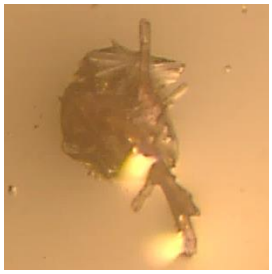

155.7 °C: Crystals continue to grow larger.

188.9 °C: Phase change from solid to brown liquid is complete.

5.3.1.2. Thermal gravimetric analysis (TGA)

Figure 5.8 shows the TGA curve (n = 3) which indicates that three thermal events take place in the temperature range 10 - 350 °C. The first step, which is attributed to dehydration, shows a mass loss of 1.72 ± 0.02%. The water content found within the crystal structure was therefore calculated as 0.85 ± 0.01 water molecules in the ASU. The onset temperature of the water loss occurred at 58 °C, which is lower than the temperature observed in the HSM images for the same process.

The second thermal event has an onset temperature of 152 °C and a mass loss of 52.5 ± 0.5%. The HSM show that at 152 °C the phase changes have taken place and the product is a liquid. Based on the results of the VT-PXRD that will be discussed below, the first mass loss would therefore account for 4.76 ISN molecules. There may therefore be an overlap of the loss of ISN and FEN upon heating. The final decomposition step has an onset temperature of 383.3 °C with a 19.7 ± 0.3% mass loss.

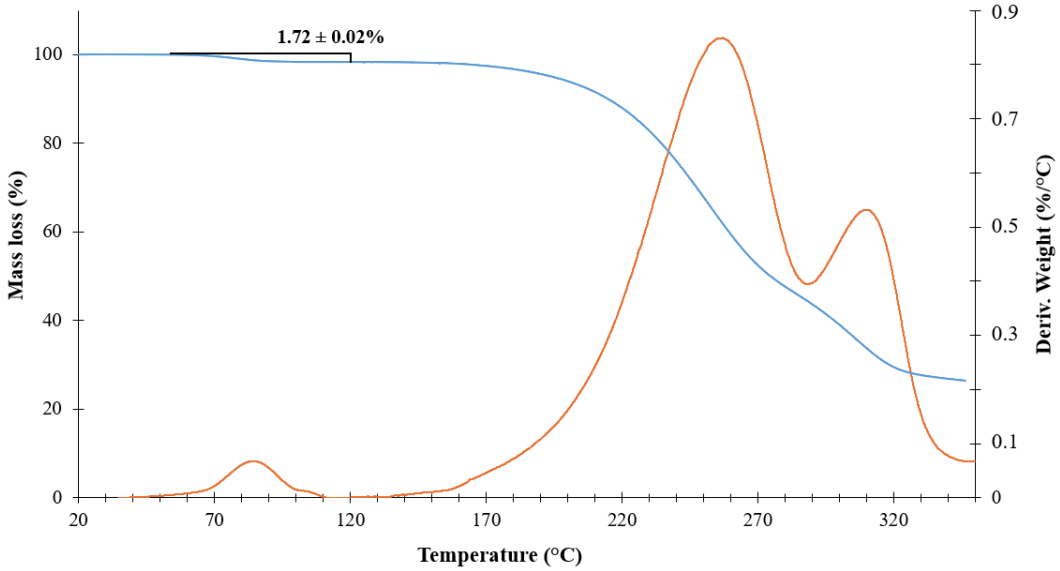

Figure 5.8: TGA curve of FEN-ISN (co-precipitation product) recorded from 10 to 350 °C.

5.3.1.3. Differential scanning calorimetry (DSC)

For the new phase, multiple endothermic peaks are observed in Figure 5.9 (green curve). The first endotherm appears at ~92 °C, which agrees with what is evident in both the HSM images and TGA. This is the dehydration process that occurs as water molecules are removed from the crystal structure.

Two peaks are then seen at 136.2 °C and 142.6 °C. These peaks indicate that upon heating there is a phase change that takes place. The DSC curve does not return to the baseline, and a second peak develops, representing the fusion of the crystal and simultaneous appearance of a new crystalline phase. The DSC curve of the co-crystal (previously reported, orange curve)[13] shows a melt at 142.7 °C, which overlaps the fusion endotherm of the new phase. [This is probably coincidental, since the new phase at this temperature should still retain its 2:3 FEN:ISN composition (see Figure 5.8), rather than the 1:1 composition of the co-crystal]. No further thermal events are evident after 150 °C, until the decomposition of the new phase which begins at 240 °C.

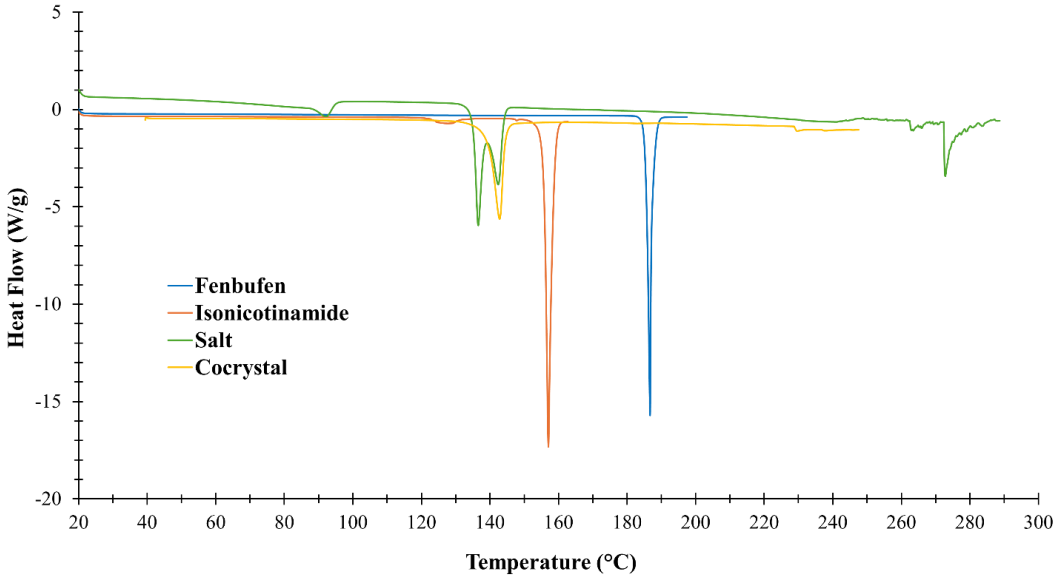

Figure 5.9: DSC curves of FEN (blue), ISN (orange), co-crystal (yellow)[13] and the salt (green).

5.3.1.4. Variable temperature powder X-ray diffraction (VT-PXRD)

The HSM images and DSC curve for the new FEN-ISN phase clearly show more than one phase transition taking place upon heating. To capture these phase transitions, variable temperature PXRD was carried out over the range 25–160 °C. Given the somewhat speculative interpretations above, the VT-PXRD technique turned out to be useful in clarifying the behaviour on heating the salt at increasing temperatures. The selected temperatures at which the PXRD patterns were recorded were based on the peaks observed in the DSC record. Figure 5.10 appears to show one major phase transition instead of the two distinct transitions observed in the HSM images and DSC; this is attributed to the occurrence of the two transitions in rapid succession and hence the difficulty of resolving them by VT-PXRD. The dehydration of the structure shows one minor change in the peaks located at 19.4 and 20.0 °2θ. The first peak becomes sharper and more well-defined from 75 °C to 95 °C. The second peak develops a shoulder on its left side which becomes larger with an increase in temperature.

As the temperature reaches 125 °C the three peaks at ~14, ~16 and ~17 °2θ begin decreasing in intensity and are no longer present at 140 °C. At this point it is clear that there is no trace of the salt remaining. The peak at 19.4° also begins to decrease in intensity and it is no longer present at 145 °C. The shoulder on the peak at ~20° increases in size until finally the peak becomes sharper and increases in intensity from 130 °C. At 135 °C new peaks begin forming, all of which correspond to FEN. This temperature corresponds to the second phase transition observed in the DSC and HSM.

Since the final recorded PXRD pattern at 160 °C shows the presence of only pure FEN (m.p. 186-187 °C), it can be concluded that upon heating the sample from ~140 °C, the ISN gradually becomes amorphous while the crystallization of FEN progresses, the coformer being gradually removed from the sample (consistent with the TGA curve showing major mass loss from around this temperature). These results thus confirm that the major decomposition step observed in the TGA is the loss of ISN. This is an unexpected result and indicates that the second phase transition is the loss of ISN, leaving FEN as the final product.

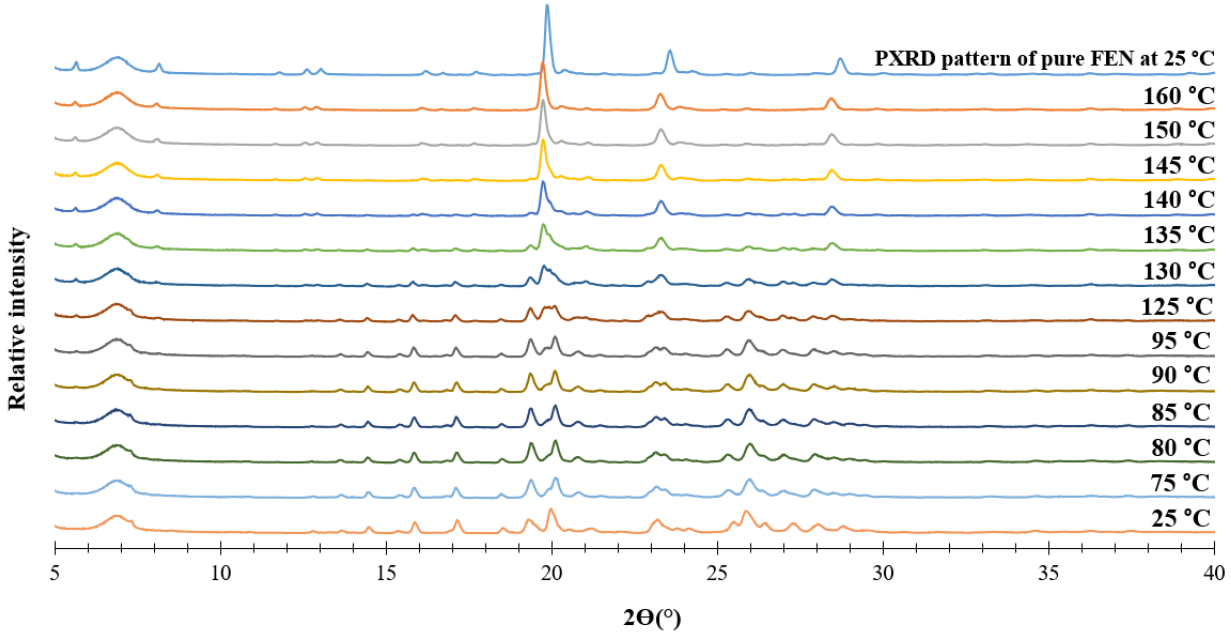

Figure 5.10: PXRD patterns of the FEN-ISN hydrate recorded at selected temperatures from 25 to 160 °C. The peak observed between 6 and 7.5 °2θ is an artifact due to the Mylar® material that covers the sample.

5.3.2. Elemental analysis (EA)

The stoichiometric formula of the new phase was determined using elemental analysis (EA). Based on the findings of the TGA and structural information from SCXRD, the chemical formula assigned to the new phase is $(C_{16}H_{14}O_3)(C_{16}H_{13}O_3)^- 2(C_6H_6N_2O)(C_6H_7N_2O)^+ \cdot H_2O$. Table 5.3 shows that the experimental EA values agree with the calculated values, as they are all within an acceptable 0.4% margin of error, confirming that the phase has a 2:3:~1 molar ratio of FEN, ISN and water.

Table 5.3: Mass percentage (%) values of the experimental* and calculated values of C, H and N for FEN-ISN.

	Experimental	Calculated
C	66.9	67.25
H	5.52	5.42
N	9.35	9.41

*single determination only

5.3.3. Crystal structure analysis

Data-collection and space group determination

The crystal intensity data were collected at 100(2) K. The Laue symmetry of the reciprocal lattice (2/m) indicated that the crystal belongs to the monoclinic system. The space group was determined as $P2_1/c$, based on the systematic absences *h0l*: $l = 2n+1$; *0k0:* $k = 2n+1$ and confirmed using the program XPREP.[15]

Structure solution and refinement

Table 5.4 shows the crystal data and refinement details for the FEN-ISN salt whose structure was solved by direct methods using SHELXS-97.[16] The asymmetric unit (Figure 5.11) was found to consist of one neutral molecule of FEN, one deprotonated molecule of FEN, two neutral molecules of ISN, one protonated molecule of ISN, and one molecule of water. The latter assignment is in agreement with the thermal analysis which revealed ~0.85 water molecules present.

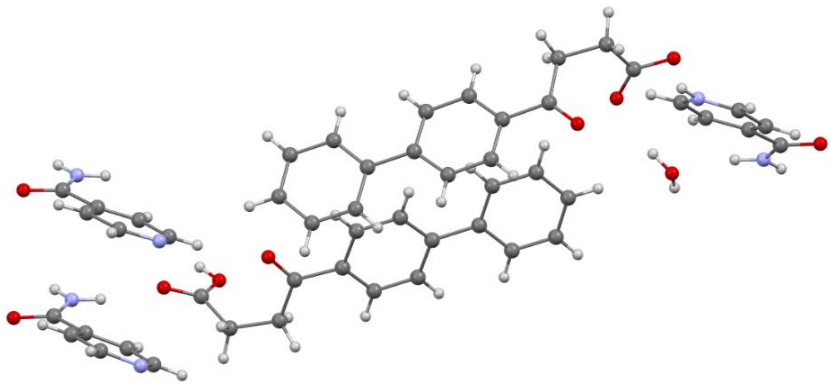

Figure 5.11: The asymmetric unit of FEN-ISN.

All non-hydrogen atoms were assigned based on the electron density peaks identified in the E-map produced by SHELXS-97. These were easily assigned as there was no disorder present in the structure. For structure refinement, SHELXL-97 was employed.[16] The non-hydrogen atoms were first refined isotropically and thereafter anisotropically before assigning hydrogen atoms. All hydrogen atoms were subsequently located in successive difference Fourier maps. Hydrogen atoms were added to the phenyl rings, methylene and methyl groups using the riding model. It was noted that a hydrogen atom had been transferred from the -COOH group of one of the two FEN molecules to the heterocyclic nitrogen atom of one molecule of ISN. This was confirmed by noting the C-O bond lengths of the ionised FEN which were 1.243(3) and 1.266(3) Å. Instead, the lengths of the carbon-oxygen bonds in the unionised FEN molecule were 1.215(2) and 1.321(2) Å respectively, indicating an intact carboxyl group. The H atom of the carboxyl group was located and added using the AFIX 147 instruction in SHELXL. A significant Δρ peak was assigned as the oxygen atom of a water molecule, given its favourable distances for intermolecular hydrogen bonding to neighbouring O and N atoms. The hydrogen atoms belonging to the water O atom were also located in the Δρ map and they were included in the model with O-H bonds restrained to 0.84 Å. As noted above, the experimental TGA mass loss for water (1.72 ± 0.02 %) corresponded to ~0.85 molecules. However, following refinement of the oxygen atom of the water molecule with s.o.f. fixed at 0.82, it was evident that alternative refinement with the s.o.f. set at 1.0 yielded very satisfactory U_{ij} thermal displacement parameters, in keeping with those of its H-bonded neighbours. With this assignment, the new phase was designated as a monohydrate of a complex salt, specifically (FEN) (FEN^-) 2(ISN) (ISN^+) H_2O.

Table 5.4: Crystal data and refinement details for FEN-ISN.

Chemical formula	$(C_{16}H_{14}O_3)(C_{16}H_{13}O_3)^- 2(C_6H_6N_2O)(C_6H_7N_2O)^+ \cdot H_2O$
Formula weight (g.mol^{-1})	892.94
Temperature (K)	100(2)
Wavelength (Å)	0.71073
Crystal system	Monoclinic
Space group	$P2_1/c$
a (Å)	11.4620 (17)
b (Å)	7.5967 (12)
c (Å)	48.860 (7)
α (°)	90.00
β (°)	90.096 (4)
γ (°)	90.00
V (Å^3)	4254.4 (11)
Z	4
Calculated density (g.cm^{-3})	1.3941(4)
μ (MoKα) (mm^{-1})	0.098
F(000)	1880
Crystal size (mm^3)	0.080 × 0.130 × 0.160
Range scanned θ (°)	1.96 - 28.35
Index ranges ±h, ±k, ±l	h:-14, 15; k:-10, 10; l:-65, 60
No. reflections (total)	68268
No. unique reflections	10232
No. of parameters	602
Goodness-of-fit, S	1.063
Final R indices R1, wR2, [I>2σ(I)]	0.0626, 0.1352
R indices, all data (R1, wR2)	0.0678, 0.1381
Largest diff. peak and hole (e Å^{-3})	0.77, -1.03

Molecular structure

Figure 5.12 shows the numbering scheme of the ASU. As previously stated, the proton transfer from one molecule of FEN to one molecule of ISN results in each of these moieties being in its ionised form. The ISN moieties have been labelled as A, B and C according to the FEN molecule to which each is hydrogen bonded.

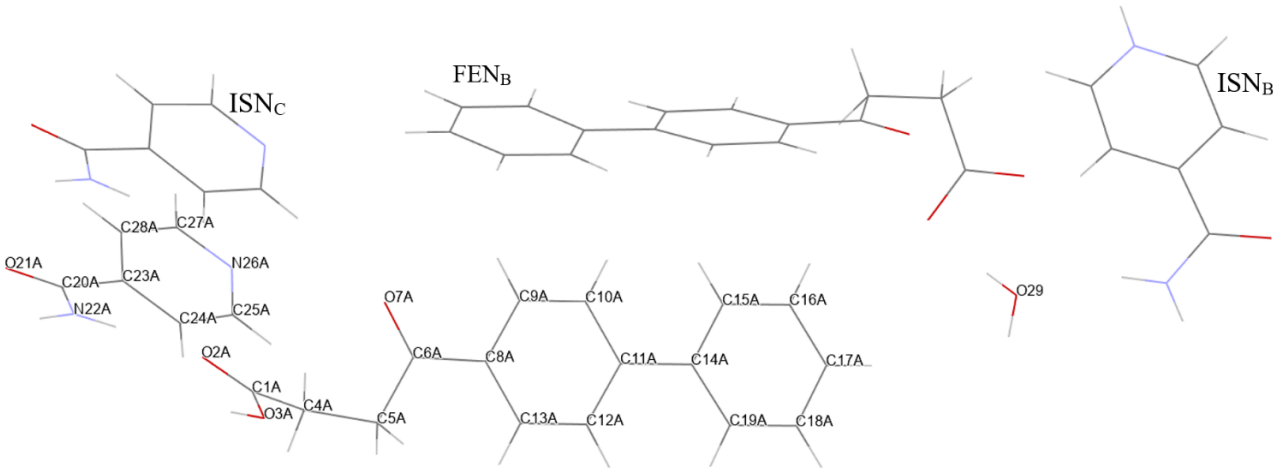

Figure 5.12: ASU numbering scheme of the salt FEN-ISN.

Hydrogen bonding

Both ISN molecules (A, C) and the ISN cation (B) engage in the formation of amide-amide homosynthons[17] with graph set descriptor $R_2^2(8)$. Figure 5.13 shows a representative example involving one neutral and one protonated ISN molecule. ISN molecule A, however, forms the same type of synthon with its inversion-related counterpart.

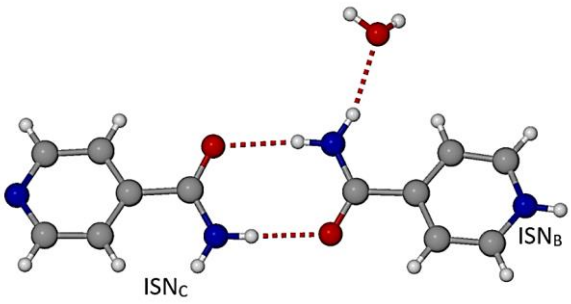

Figure 5.13: Amide-amide homosynthon formed between ISN molecule C and cation B.

The molecule FEN_A and the anion FEN_B engage in different hydrogen bonding roles. Figure 5.14 shows a centrosymmetric motif that illustrates the role of the -COOH group of molecule FEN_A, namely acting as both a donor and acceptor in H-bonds with different ISN molecules in the motif.

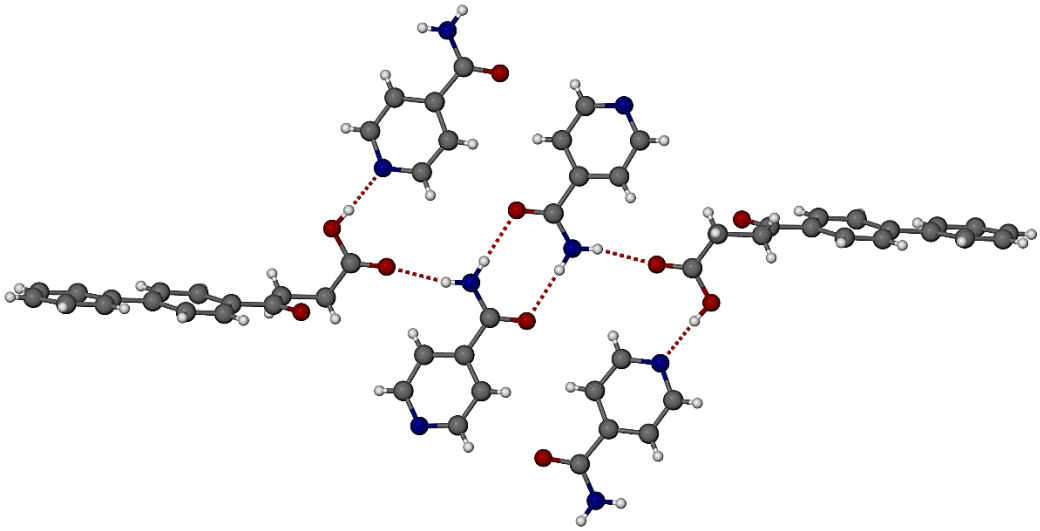

Figure 5.14: Hydrogen bonding involving the FEN_A molecule.

Instead, as shown in Figure 5.15, the carboxylate group of the anionic moiety FEN_B engages in charge-assisted H-bonding, as acceptor from both the protonated ISN moiety and the water molecule. Only the moiety labelled FEN_B is in the ASU, all other molecules or ions being generated by various symmetry operators.

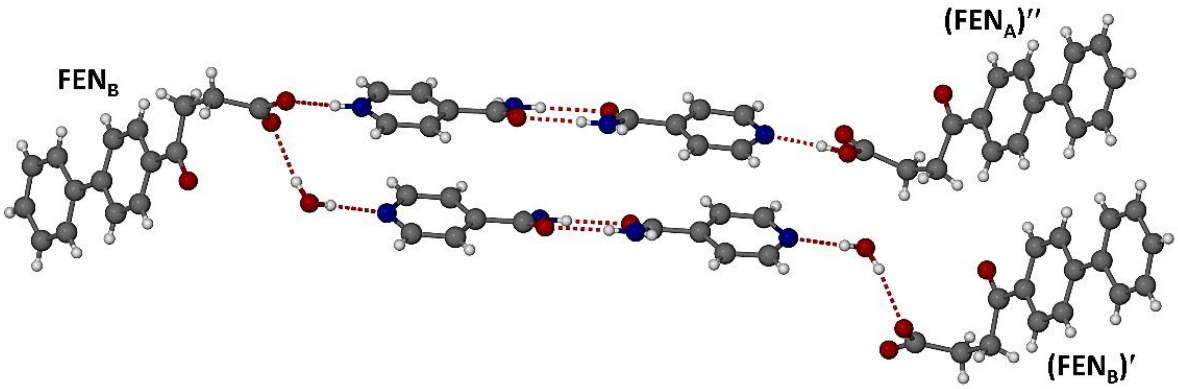

Figure 5.15: Hydrogen bonding involving the FEN_B anion. For clarity, the locations of $(FEN_A)''$ and $(FEN_B)'$ are x, -y + 7/2, ½ +z and 1-x, 3-y, 1-z respectively.

Table 5.5 shows the full listing of the hydrogen bonding interactions involving FEN, ISN and water. It includes the bond distances and angles, all of which were considered to confirm that each bond specified plays a role in the cohesion and packing of the crystal structure.

Table 5.5: Intermolecular H-bonding involving FEN, ISN and water in the FEN-ISN salt.

Hydrogen bond interaction	D-H (Å)	H···A (Å)	D···A (Å)	D-H···A (°)	Symmetry code (acceptor atom)
O29-H29A···O2B	0.846(19)	2.092(19)	2.926(2)	168.5(18)	x,y,z
O29-H29B···N26A	0.846(19)	2.092(19)	2.926(2)	168.5(18)	1-x,1/2+y,1/2-z
N22B-H22D···O29	0.88	2.08	2.937(2)	163	x,y,z
N22B-H22C···O2C	0.88	2.12	2.991(2)	173	x,3/2-y,-1/2+z
N22A-H22A···O21A	0.88	1.98	2.855(2)	178	1-x,2-y,-z
N22A-H22B···O2A	0.88	2.03	2.895(2)	166	x,y,z
N26B-H26B···O2B	0.88	2.23	2.972(4)	141	x,-1+y,z
N26B-H26B···O3B	0.88	1.86	2.677(3)	153	x,-1+y,z
N3C-H3C1···O21B	0.88	1.97	2.854(2)	177	x,3/2-y,-1/2+z
N3C-H3C2···O3B	0.88	2.19	2.983(3)	149	-x,1/2+y,1/2-z
O3A-H3A···N7C	0.84	1.82	2.656(2)	175	x,1+y,z

π-π and C-H···π interactions

The crystal structure is stabilised by C-H···π and π-π interactions, whose geometrical parameters are listed in Tables 5.6 and 5.7 respectively. There are interactions between several C-H groups of FEN and the phenyl rings of neighbouring FEN moieties. Table 5.6 shows the interaction distances between the phenyl rings of FEN moieties in the crystal structure. The table shows that all the X···Cg (Å) distances are within the range 3.512(2) - 3.711(2) Å and are therefore all considered strong interactions.

Table 5.6: List of C-H···Cg interactions found within the FEN-ISN structure.

Interaction	H···Cg (Å)	X···Cg (Å)	C-H···Cg (°)	Symmetry operations
C5A-H5A2···Cg2	2.81	3.604(2)	137	1-x,1/2+y,1/2-z
C5B-H5B2···Cg4	2.78	3.711(2)	158	-x,1/2+y,1/2-z
C9A-H9A···Cg4	2.71	3.512(2)	142	x,y,z
C9B-H9B···Cg2	2.90	3.639(2)	135	x,-1+y,z
C12A-H12A···Cg1	2.80	3.578(2)	140	1-x,1/2+y,1/2-z
C12B-H12B···Cg3	2.91	3.690(2)	141	-x,1/2+y,1/2-z
C15A-H15A···Cg3	2.96	3.689(2)	134	x,y,z

*Cg1 – C8A, C9A, C10A, C11A, C12A, C13A

*Cg2 – C14A, C15A, C16A, C17A, C18A, C19A

*Cg3 – C8B, C9B, C10B, C11B, C12B, C13B

*Cg4 – C14B, C15B, C16B, C17B, C18B, C19B

The C5A-H5A2···Cg2 and C9A-H9A···Cg4 interactions occur between the C-H group found in the side chain of FEN and the phenyl rings respectively. All other interactions are formed since the FEN rings arrange themselves in such a way that the aromatic C-H group is within bonding distance of the alternative Cg of FEN. Figure 5.16 shows the C-H···π interactions between H15A and H9A with Cg3 and Cg4 respectively as well as C5A-H5A2···Cg2.

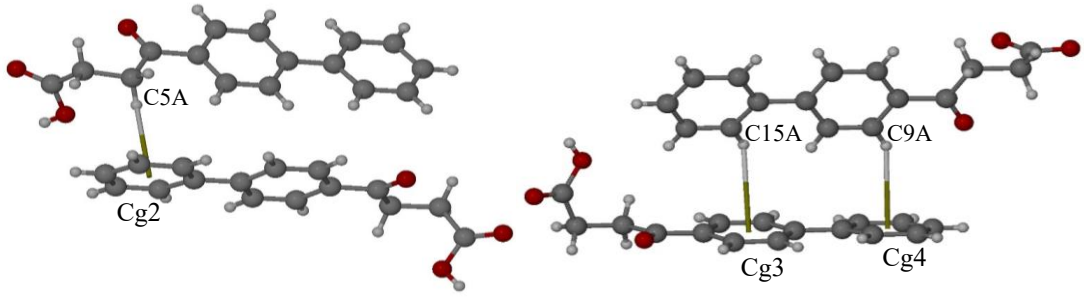

Figure 5.16: The C-H···π interactions C5A-H5A2···Cg2 (left) and T-shaped stacking of H15A and H9A with Cg3 and Cg4 respectively (right) occurring between FEN moieties.

The π-π stacking occurs between the ISN moieties. All π-π stacking interactions are relatively strong with Cg···Cg interaction distances in the range 3.677(1) - 4.039(1) Å. The slippages between the rings in question range between 1.146 and 1.911 Å, which also renders these interactions significant. All interaction distances and slippage values are shown in Table 5.7.

Table 5.7: π-π interactions between ISN rings (Å).

π-π interaction	$C_g \cdots C_g$ (Å)	Slippage (Å)	Symmetry code
Cg5···Cg6	3.808(1)	1.146	x,y,z
Cg5···Cg7	4.039(1)	1.911	-x,1/2+y,1/2-z
Cg6···Cg5	3.808(1)	1.182	x,y,z
Cg6···Cg7	3.677(1)	1.391	1-x,1/2+y,1/2-z
Cg7···Cg5	4.039(1)	1.825	-x, -1/2+y,1/2-z
Cg7···Cg6	3.677(1)	1.224	1-x,-1/2+y,1/2-z

*Cg5 – N7C, C6C, C5C, C4C, C9C, C8C

*Cg6 – N26A, C25A, C24A, C23A, C28A, C27A

*Cg7 – N26B, C25B, C24B, C23B, C28B, C27B

Figure 5.17 shows the stacking of the ISN moieties. The alternating rows of ionised and unionised FEN and ISN moieties are evident. These π-π stacking interactions are considered to be relatively strong based on the observed range of ring centroid···centroid (Cg···Cg) distances and they hold the ISN moieties/ions in place.

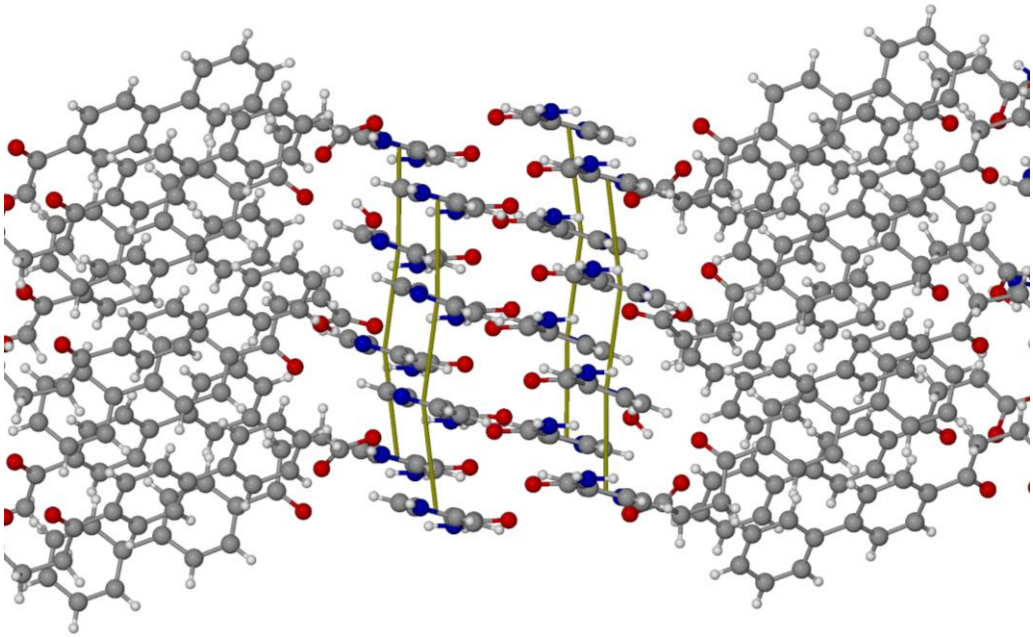

Figure 5.17: π-π stacking of ISN moieties in the crystal structure.

Packing

Figure 5.18 is the [010] projection of the crystal structure showing alternating zones of FEN moieties and ISN moieties. As previously stated, the ISN molecules and the ISN cation are held together by amide-amide homosynthons stacked on top of each other. The network of hydrogen bonding involving FEN, ISO and H_2O all contribute to the alternating packing arrangement.

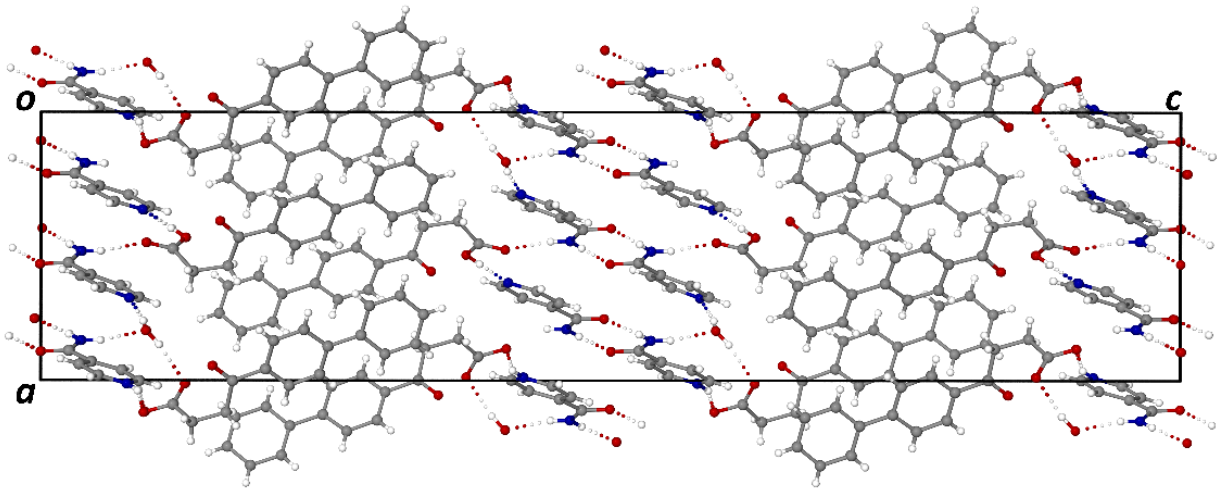

Figure 5.18: Packing arrangement of the FEN-ISN crystal structure viewed along the b-axis.

5.3.4. Fourier-transform infrared (FT-IR) spectroscopy

Figure 5.19 shows the FT-IR spectra of FEN, ISN and FEN-ISN. There is a band at 1701 cm^{-1} in the spectrum of pure FEN that shifts to 1718 cm^{-1} when incorporated in the salt product. The latter indicates the presence of a carboxyl carbonyl group whose bonding interactions change when it is a component of the salt. There is also a band present at 1391 cm^{-1} that shifts to 1394 cm^{-1} in the product. Although the shift is nearly negligible, these bands represent O-H bending, as one would expect in the product. Finally, the weak band at 1296 cm^{-1} in the salt product is within the range of C-O stretching vibrational frequencies that would be observed. The X-ray structure revealed a proton transfer from the -COOH group of one FEN molecule to one of the three ISN moieties.

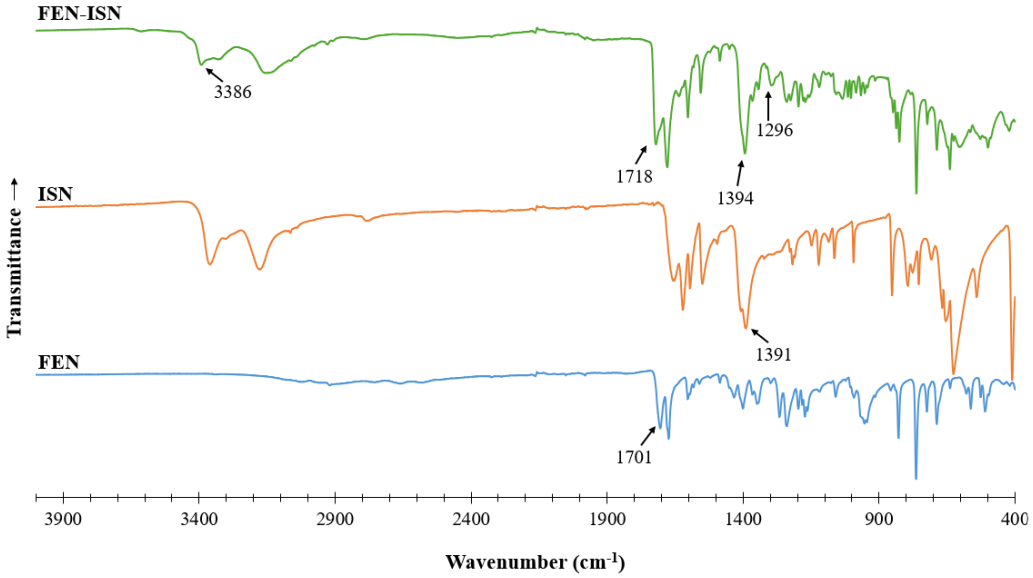

Figure 5.19: Stacked FT-IR spectra of FEN, ISN and FEN-ISN.

5.3.5. Comparative PXRD

The calculated PXRD pattern was generated using the program Mercury.[14] Figure 5.20 shows a very good correlation between the calculated pattern based on the X-ray structure and the experimental pattern. There are small shifts in the position of the peaks in the experimental pattern relative to the calculated pattern. These shifts are due to the significant difference between the temperature at which the reflection intensities for the SCXRD data were collected (100 K) and that at which the experimental pattern was recorded (294 K).

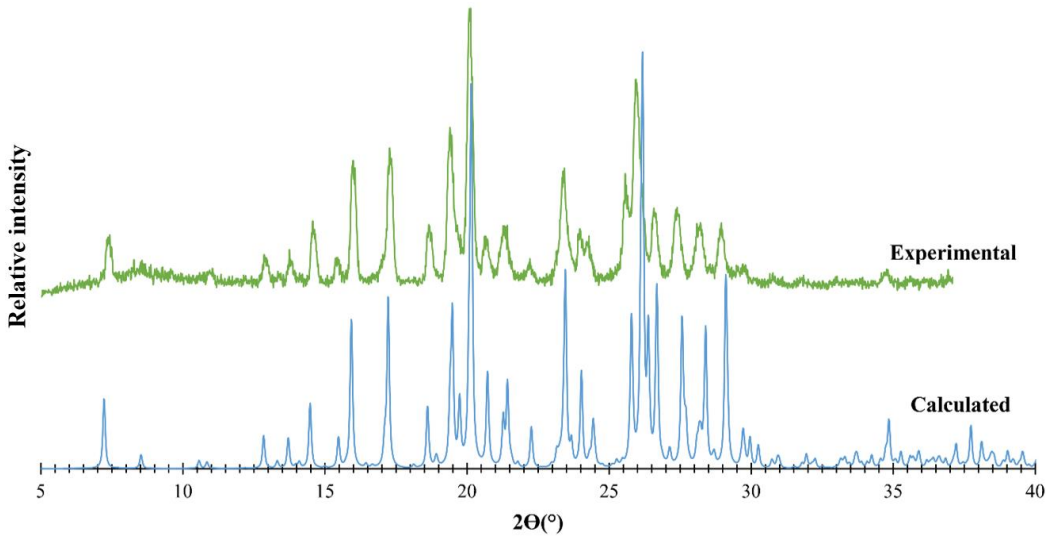

Figure 5.20: The experimental and calculated PXRD patterns of FEN-ISN.

5.3.6. Solubility studies

Initially the solubility study in FaSSIF (pH 2.0 and pH 6.5) was performed using the method described in Chapter 2 (2.6.5. Equilibrium solubility studies, pg. 32) with an excess amount of FEN and FEN-ISN dissolved in 1.0 ml FaSSIF. It was found that the concentration could not be quantified using UV-Vis spectroscopy. HPLC was then tested and although a peak of FEN did appear, an appropriate calibration curve could not be constructed. A standard solution of FEN was prepared using EtOH, but this did not have the same retention time of FEN when incorporated in the FEN-ISN salt. Another standard curve was constructed for concentration data at pH 6.5, but this was not reliable due to the poor solubility of FEN at that pH. Although the experiment was unsuccessful, it was clear that there was no peak present for FEN-ISN at pH 2.0, meaning that it was not soluble in an acidic environment.

Solubility studies in aqueous and FaSSIF (buffered at pH 6.5) media were therefore carried out using the gravimetric analysis method described in Chapter 2 (2.6.2. Gravimetric solubility studies, pg. 29). Table 5.8 shows the change in the solubility of FEN-ISN compared to that of FEN (control). In water and FaSSIF a 24.9 and a 1.26 increase in the respective solubilities were recorded.

Table 5.8: Total solubility (mg/ml) of FEN and FEN-ISN* in an aqueous medium and in FaSSIF (pH 6.5).

	Aqueous (mg/ml)	**FaSSIF, pH 6.5 (mg/ml)**
FEN	0.028	6.92 ± 0.8
FEN-ISN	0.68	8.65 ± 0.4
Solubility enhancement factor	24.29	1.26 ± 0.1

***** The mass fraction of FEN in the product FEN-ISN is 0.58, which has been taken into account in the final solubility calculations.

In summary, in the quest for repreparing a previously reported co-crystal formed between FEN and isonicotinamide, a new salt formed by reaction of these starting components was discovered and fully characterised, thus contributing to expanding the solid-state landscape of the API.

References

1. Fenbufen. https://go.drugbank.com/drugs/DB08981 (accessed 23 August 2023).
2. Fukte, S. R.; Wagh, M. P.; Rawat, S., Coformer selection: An important tool in cocrystal formation. *International Journal of Applied Pharmaceutics* **2014,** *6* (7), 9-14.
3. Moskovic, D. J.; Fogelman, D. R., Acute neurotoxicity induced by common chemotherapies. In *Supportive Oncology*, Elsevier Inc.: 2011; pp 56-66.
4. Dhaneshwar, S.; Kusurkar, M.; Bodhankar, S.; Bihani, G., Carrier-linked mutual prodrugs of biphenylacetic acid as a promising alternative to bioprecursor fenbufen: design, kinetics, and pharmacological studies. *Inflammopharmacology* **2014,** *22*, 235-250.
5. Kerwar, S., Pharmacologic properties of fenbufen. *The American Journal of Medicine* **1983,** *75* (4), 62-69.
6. Phelps, K. The Emergence Of Prodrugs: A Proficient Pathway To New Drug Development Through The 505(b)(2) Pathway 2014. https://www.outsourcedpharma.com/doc/the-emergence-of-prodrugs-a-proficient-pathway-to-new-drug-development-through-the-b-pathway-0001#:~:text=Prodrugs%20can%20improve%20how%20an,enzymatic%20cleavage%20or%20chemical%20reaction (accessed 23 August 2023).
7. Nørregaard, R.; Kwon, T.-H.; Frøkiær, J., Physiology and pathophysiology of cyclooxygenase-2 and prostaglandin E2 in the kidney. *Kidney Research and Clinical Practice* **2015,** *34* (4), 194-200.
8. Díaz-González, F.; Sánchez-Madrid, F., NSAIDs: learning new tricks from old drugs. *European Journal of Immunology* **2015,** *45* (3), 679-686.
9. Syed, M.; Skonberg, C.; Hansen, S. H., Inhibition of ATP synthesis by fenbufen and its conjugated metabolites in rat liver mitochondria. *Toxicology in Vitro* **2016,** *31*, 23-29.
10. Bolla, G.; Sarma, B.; Nangia, A. K., Crystal engineering of pharmaceutical cocrystals in the discovery and development of improved drugs. *Chemical Reviews* **2022,** *122* (13), 11514-11603.
11. Martino, P. D.; Barthelemy, C.; Piva, F.; Joiris, E.; Palmieri, G.; Martelli, S., Improved dissolution behavior of fenbufen by spherical crystallization. *Drug Development and Industrial Pharmacy* **1999,** *25* (10), 1073-1081.
12. Ge, F.-Y.; Huo, L.-H.; Zhao, S.-N.; Deng, Z.-P.; Zhang, Z.-Y.; Gao, S., Effect of Co-Crystal Formers on the Supramolecular Patterns and Luminescence Properties of Co-Crystals Comprising Fenbufen and Diverse N-Heterocycles. *Australian Journal of Chemistry* **2016,** *69* (8), 836-845.
13. Mancapa, R., Honours Research Project (unsubmitted and unpublished), University of Cape Town: Cape Town (Supervisor M.R. Caira), **2018**.

14. Macrae, C. F.; Sovago, I.; Cottrell, S. J.; Galek, P. T.; McCabe, P.; Pidcock, E.; Platings, M.; Shields, G. P.; Stevens, J. S.; Towler, M., Mercury 4.0: From visualization to analysis, design and prediction. *Journal of Applied Crystallography* **2020,** *53* (1), 226-235.
15. XPREP *Data Preparation and Reciprocal Space Exploration*, 2008/2; Bruker Analytical X-Ray Systems: **2008**.
16. Sheldrick, G. M., A short history of SHELX. *Acta Crystallographica Section A: Foundations of Crystallography* **2008,** *64* (1), 112-122.
17. Adalder, T. K.; Sankolli, R.; Dastidar, P., Homo-or heterosynthon? A crystallographic study on a series of new cocrystals derived from pyrazinecarboxamide and various carboxylic acids equipped with additional hydrogen bonding sites. *Crystal Growth & Design* **2012,** *12* (5), 2533-2542.

Chapter 6: New multi-component solids containing the non-steroidal anti-inflammatory drug S-(+)-ibuprofen

6.1. Literature review

S-(+)-ibuprofen (S-IBU), shown in Figure 6.1, is listed as a Class II non-steroidal anti-inflammatory drug (NSAID) in the Biopharmaceutical Classification System (BCS). It is used to treat cystic fibrosis, rheumatoid arthritis, inflammation and musculoskeletal conditions.[1, 2]

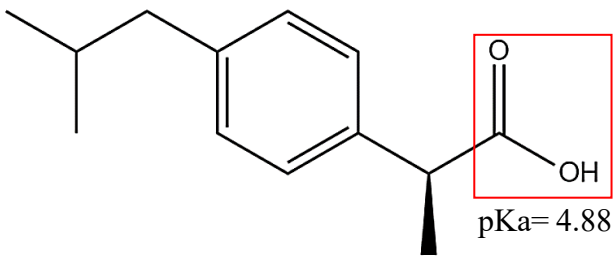

Figure 6.1: The molecular structure of S-(+)-ibuprofen.

Two enantiomeric forms, (R)- and (S)-ibuprofen exist, the latter being the eutomer i.e., the bioactive form of the drug.[3] Side effects of the drug include stomach ulceration, vomiting and nausea.[4] History has shown us that administering the correct enantiomeric form of a drug is essential in providing effective treatment as well as preventing the possibility of severe side effects. A notorious example of this is thalidomide, which in the 1950s, resulted in newborns having birth defects.[5] It was later discovered that the (R)-isomer is teratogenic and caused the defects in infants when pregnant women ingested it as a treatment for nausea.[6] In the case of racemic ibuprofen, the (S)- and (R)-ibuprofen enantiomers have different metabolic activities, inhibiting cyclooxygenase (COX) and the lipid metabolism pathway respectively.[7] It is therefore critically important to choose the correct enantiomer to treat a particular condition.

Salts of racemic ibuprofen (RS-IBU) have been synthesised using 2-amino-5-methylpyridine, 4-aminopyridine and 2,6-diaminopyridine as coformers.[2] With the successful synthesis of ionic co-crystals using amino acids as coformers, zwitterions that have similar chemical properties are therefore suitable coformers to attempt co-crystal synthesis with a drug such as S-IBU. Due to the negative side effects listed above, improving its pharmaceutical properties are the main motivation of

this study. New synthetic solid phases of S-IBU were considered to have potential for future improved formulations of the drug.

Prior to the study documented in this chapter, the author of this dissertation was informed by the supervisor that salts of S-IBU with the coformers 6-aminocaproic acid (ACA) and tranexamic acid (TXA), as well as an inclusion complex with the host compound heptakis(2,6-di-*O*-methyl)-β-cyclodextrin (DMB), had been previously synthesised and characterised.[8] However, for one of the salts ($S\text{-}IBU^{-}\cdot TXA^{+}$), the SCXRD data were unpublishable due to an abnormally high R_1 factor (0.14). Furthermore, given the short duration of the previous study (10-weeks) the intended detailed solubility studies of these salts, and that of the S-IBU complex with DMB, could not be performed. Thus, the author of the present dissertation was tasked by the supervisor with repeating all previous syntheses and analytical characterisations of these salts and extending them significantly in an effort to render the results publishable. It is important to note here that the contents of the previous report were withheld from the present author by the supervisor to avoid any bias. This plan of action proved to be vindicated, the outcomes being both the acquisition by the present author of publishable SCXRD data for the salt $(S\text{-}IBU)^{-}(TXA)^{+}$, as well as detailed solubility data for both salts. In addition, the author of this dissertation discovered a second crystal form of the S-IBU inclusion complex with DMB. Unless otherwise stated, all of the work presented in this chapter was performed by the author of this dissertation. Where necessary, for purposes of comparison, previously reported results[8] will be referred to in the discussion.

6.2. Co-crystal screening

6.2.1. Virtual screening

A computational co-crystal screening with S-IBU as the API was performed using the materials module in Mercury.[9] The results of the screening are listed in Table 6.1.

Table 6.1: List of coformer hits with S-IBU using the virtual screening process.

2-amino-5-methylbenzoic acid	Acetophenone oxime	Thymidine	Valerolactam
3-methylpyridine	Adipic acid	t-butylhydroxyanisole	N-ethylacetamide
4-acetamidobenzoic acid	Alitame	Suberic acid	Hippuric acid
D-pantothenol	Azelaic acid	Sorbic acid	Methylparaben
L-leucine	Biotin	Saccharin	L-tyrosine
L-mandelic acid	Capsaicin	Riboflavin	Hesperetin
L-methionine	Cholic acid	Propylparaben	Monobutyrin
L-phenylalanine	Ethylparaben	Pimelic acid	
L-tryptophan	Folic acid	Pamoic acid	

From the list above, coformers were selected based on their availability in our laboratory and with care to avoid using coformers which had been previously reported to form co-crystals with S-IBU.

6.2.2. Liquid-assisted grinding (LAG) and co-precipitation experiments

As described in Chapter 2 (2.3.2. Liquid-assisted grinding (LAG), pg. 22), LAG was performed using equimolar amounts of S-IBU and coformer with the solvents EtOH, MeOH and MeCN. Each solvent was added to the mixture in question using 20 μL increments at ±3 increments per minute. The mixture was ground for a total of 20 minutes using a mortar and pestle and thereafter analysed using PXRD. Co-precipitation (2.3.3. Co-precipitation**,** pg. 22) experiments were performed using the same solvents listed above. S-IBU and the chosen coformer were each dissolved in 0.5 ml of the selected solvent and stirred at ~10 °C below the boiling point of the solvent. Once completely dissolved, the solution of the coformer was added to that of S-IBU and the resulting solution was stirred at the same temperature for 4 – 6 hours. The hot solution was then filtered through a 0.45 μm nylon microfilter and left to evaporate slowly. The experiments resulted in either S-IBU or coformer precipitating out of the solution. This was confirmed by recording the PXRD pattern of the ground crystals, HSM images and by determining the unit cell parameters on the 4-circle diffractometer. The LAG and co-precipitation experiments were performed using the coformers listed in Table 6.2.

Table 6.2: Outcomes of the LAG experiments with equimolar S-IBU + coformer with solvents EtOH, MeOH and MeCN.

Coformer	Product
Adipic acid	Physical mixture
Ethylparaben	Physical mixture
Ferulic acid	Physical mixture
Fumaric acid	Physical mixture
Glutaric acid	Physical mixture
Hippuric acid	Physical mixture
Orotic acid	Physical mixture
Oxalic acid	Physical mixture
Pimelic acid	Physical mixture
Pyrazinecarboxamide	Physical mixture
Saccharin	Physical mixture
Suberic acid	Physical mixture
Urea	Physical mixture

The PXRD patterns of LAG products of S-IBU with adipic acid (Figure 6.2) and orotic acid (Figure 6.3) are shown below as representative examples. Based on these PXRD patterns the products are clearly physical mixtures of the respective starting materials. The PXRD patterns of the co-precipitation products indicated that they were either S-IBU or coformer alone. All PXRD patterns derived from the LAG experiments can be found in the Appendix (Section 3.1., pg. 18).

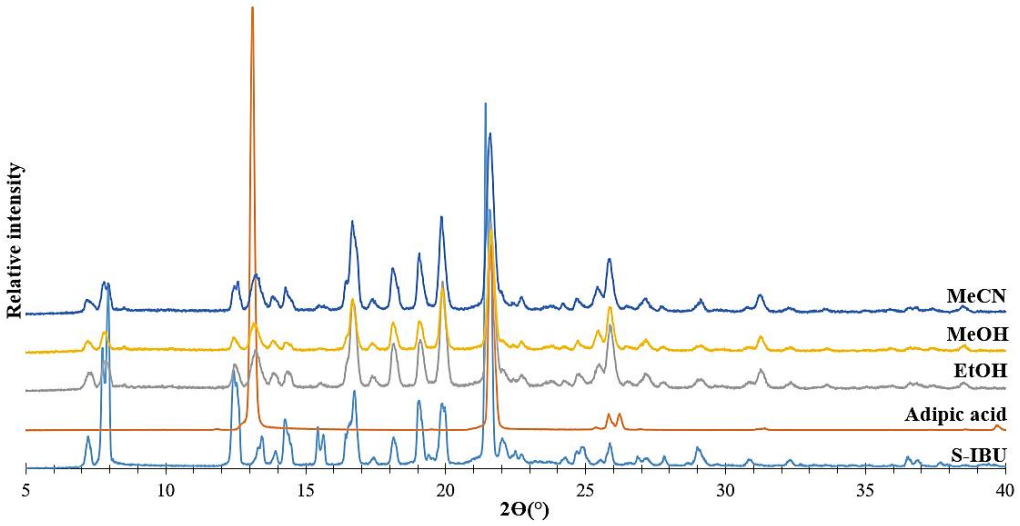

Figure 6.2: PXRD patterns of the starting materials S-IBU and adipic acid and those of the products following LAG experiments using the solvents indicated.

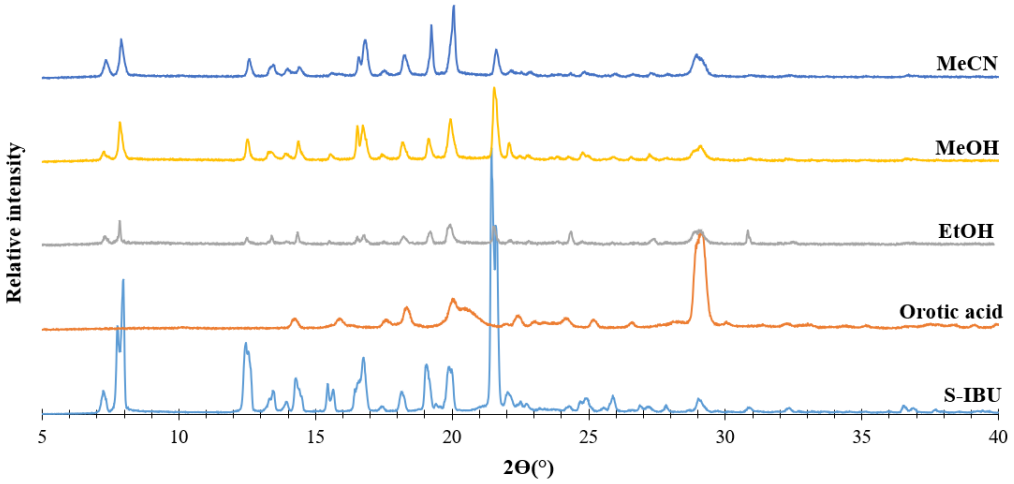

Figure 6.3: PXRD patterns of the starting materials S-IBU and orotic acid and those of the products following LAG experiments using the solvents indicated.

As mentioned in section 6.1 of this chapter, zwitterions are strong candidates for salt synthesis with S-IBU. The results of LAG and co-precipitation experiments using S-IBU and amino acids are listed in Table 6.3. The main challenge in this case was the difference in the solubility of S-IBU and those of the amino acids. S-IBU is insoluble in water and soluble in organic solvents; amino acids on the other hand, are only soluble in water with poor solubility in organic solvents. To facilitate the salt/co-crystal synthesis several organic solvent/water ratios were tested. In each attempt, either S-IBU or the amino acid immediately crashed out as the solution cooled. To overcome this issue the stirring times

were increased along with temperature cycling, which were all unfortunately unsuccessful. A different approach was taken in which the pH of the medium was altered using NaOH. This was done to facilitate the deprotonation of S-IBU through the synthesis of the sodium salt and simultaneous protonation of the amino group of the amino acid. This allowed both components to be completely dissolved in water. This resulted in the sodium salt ($S\text{-}IBU^{-}Na^{+}$) precipitating from solution.

Table 6.3: LAG and co-precipitation experiments using S-IBU and zwitterionic coformers.

Zwitterion	Product	Solvent used in co-precipitation
6-aminocaproic acid (ACA)	New phase	MeOH
Tranexamic acid (TXA)	New phase	MeOH
L-glutamine	Physical mixture	Various vol. ratios - MeOH:H_2O, EtOH:H_2O, MeCN:H_2O
L-threonine	Physical mixture	Various vol. ratios - MeOH:H_2O, EtOH:H_2O, MeCN:H_2O

It should be noted here that the significance of the coformers ACA and TXA in the context of S-IBU as an API is as follows. The original motivation was to attempt to mitigate a major adverse side effect of the NSAID S-IBU, namely gastrointestinal damage, by preferably coupling the drug with one or more bioactive compounds that arrest bleeding. The coformers ACA and TXA are, in fact, the most effective and widely used antifibrinolytic drugs, and they were thus specifically chosen with the aim of synthesising fixed-dose 'drug-drug' co-crystals or salts with S-IBU.

6.3 Synthesis and characterisation of the salt [$(S\text{-}IBU)^{-}(ACA)^{+}$] resulting from the reaction of S-IBU and 6-aminocaproic acid (ACA)

Using LAG, $(S\text{-}IBU)^{-}(ACA)^{+}$ was synthesised with S-IBU (5.00 mg, 0.0242 mmol) and ACA (3.17 mg, 0.0242 mmol) using three different solvents with a total volume (in µL) of EtOH (580), MeOH (620) and MeCN (680). The PXRD patterns of the products (Figure 6.4) indicate that all three LAG experiments resulted in a new common phase, although its nature (salt or co-crystal) was not yet established. Single crystals were synthesised by dissolving S-IBU (5.00 mg) and ACA (3.17 mg) separately in MeOH (0.80 mL). The solutions were stirred at 50 ± 5 °C until the components

completely dissolved. The S-IBU solution was then added to that of the coformer and stirred for 6 hours at 50 ± 5 °C. The hot solution was filtered through a 0.45 µm syringe filter and left to evaporate slowly for 2 days. The vial was then capped and placed in the refrigerator for ~3 weeks, after which suitable crystals for X-ray data-collection were harvested.

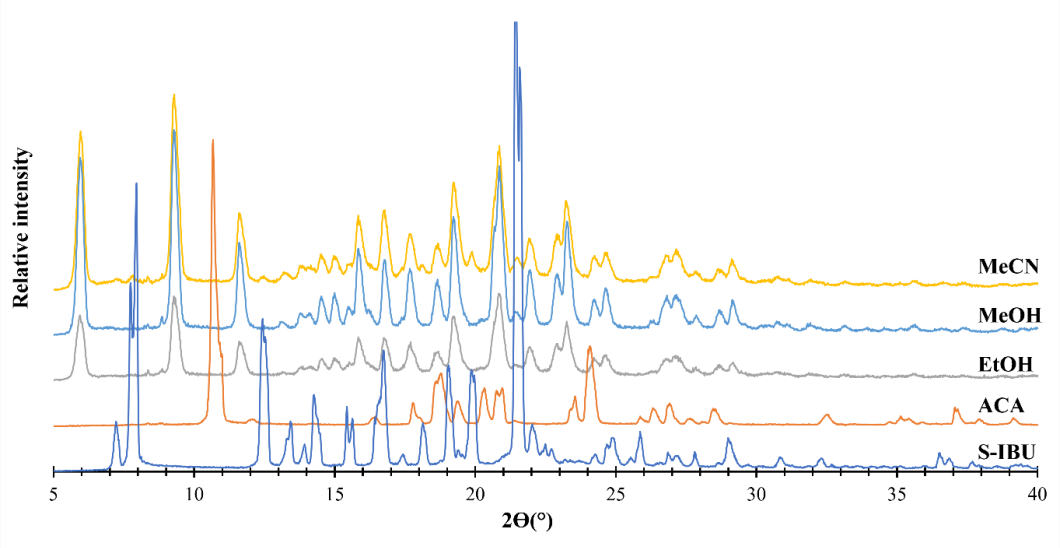

Figure 6.4: PXRD patterns of the starting materials S-IBU and ACA and those of the products following LAG experiments using the solvents indicated.

6.3.1. ^{1}H NMR spectroscopy and elemental analysis (EA)

Single crystals of the S-IBU and ACA co-precipitation product were analysed using ^{1}H NMR spectroscopy with DMSO-d_6 as solvent and at 298 K. The chemical shifts of the signals from $(S\text{-}IBU)^-$ and $(ACA)^+$ (proton labelling in Figure 6.5) are listed in Table 6.4. Although the individual stoichiometric ratio estimates span a wide range, the average value (0.91) indicates that the product probably has 1:1 stoichiometry. The solubility of the product was poor in DMSO-d_6 and insoluble in chloroform-d_6. The poor solubility may be the reason why the integration of both $(S\text{-}IBU)^-$ and $(ACA)^+$ protons are not accurate. The full spectrum can be found in the Appendix (Section 3.3.1., pg. 24).

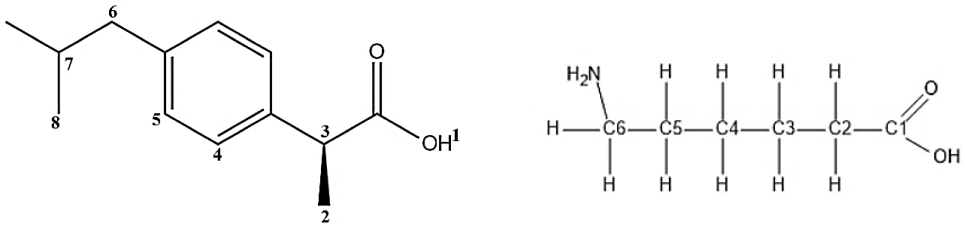

Figure 6.5: Labelling scheme of S-IBU (left) and ACA (right) used in assigning ^{1}H NMR peaks. It should be emphasised that ACA is a zwitterion in the solid state, the terminal groups being -NH_3^+ and -COO^-.

Table 6.4: ^{1}H NMR data used to determine the stoichiometry of the salt.

Assignment	δ (ppm)	Integration	Multiplicity	Proton	Stoichiometric ratio	Integer
S-IBU						
CH aromatic (4,5)	7.19-7.08	3.14	Doublets	4H	0.79	1
CH_2 (6)	2.42-2.40	1.57	Doublet	2H	0.79	1
CH (7)	1.87-1.74	1.00*	Multiplet	1H	1.0	1
2 x CH_3 (8)	0.86-0.84	4.56	Doublet	6H	0.76	1
ACA						
CH_2 (4)	1.34-1.31	2.45	Doublet	2H	1.23	1

Because of the solubility issues encountered with ^{1}H NMR spectroscopy, elemental analysis of the co-precipitation product was performed as an alternative analytical method. The experimental C, H and N percentages (Table 6.5) showed a deviation from the calculated values of 0.46, 0.30 and 0.58 % respectively. Although the latter deviation is high, this, along with the ^{1}H NMR results, confirms that the salt synthesised has a 1:1 S-IBU:ACA stoichiometry.

Table 6.5: Mass percentage (%) values of the experimental* and calculated values of C, H and N for $(S\text{-}IBU)^-(ACA)^+$.

Element	Theoretical	Experimental
C	67.63	67.17
H	9.26	9.56
N	4.15	3.57

*single determination only

6.3.2. Thermal analysis

6.3.2.1. Hot stage microscopy (HSM)

Figure 6.6 shows the HSM images of the single crystals from 19 to 253 °C. These crystals, which are initially clear plates, begin changing from clear to brown at 130.1 °C. As the temperature increases the brown colour becomes more prominent. A phase change from solid to liquid is then observed from 140.3 to 153.0 °C, indicating that the product is melting.

Figure 6.6: HSM images of $(S\text{-}IBU)^-(ACA)^+$ recorded between 19.3 and 153.0 °C, at 10 °C/min.

19.3 °C: Single crystals at room temperature.

130.1 °C: Crystals begin turning brown.

140.3 °C: A phase change takes place from solid to liquid.

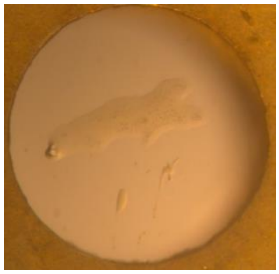

153 °C: Melting is complete.

6.3.2.2. Thermal gravimetric analysis (TGA) and differential scanning calorimetry (DSC)

Figure 6.7 shows both the TGA and DSC curves of $(S\text{-}IBU)^-(ACA)^+$. The TGA curve (n = 3) was recorded from 20 to 250 °C. There is no initial mass loss, indicating that there is no solvent present in the crystal structure. A single mass loss of 81.3 ± 0.1% is observed with an onset temperature of 141 °C. This indicates that there is no loss of either $(S\text{-}IBU)^-$ or $(ACA)^+$ upon heating and instead the new phase decomposes as a single unit.

The DSC curve, recorded from 20-150 °C, shows a single endothermic peak at 134 °C with a melting range of 128-138 °C. The HSM images show a change in the sample from solid to liquid between 140.3 and 153 °C. This temperature range does not agree with the melting observed in the DSC. This is attributed to the different instruments used. Since the melting point of $(S\text{-}IBU)^-(ACA)^+$ is 134 °C and that of S-IBU is 49-53 °C, the salt therefore has the higher thermal stability.

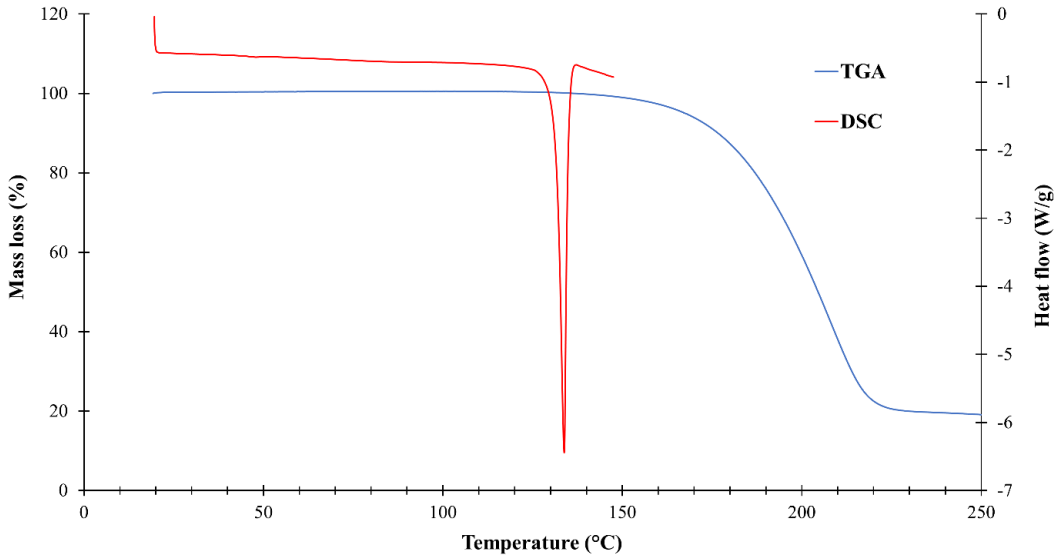

Figure 6.7: TGA and DSC curves of $(S\text{-}IBU)^{-}(ACA)^{+}$.

6.3.3. Crystal structure analysis

Data-collection and space group determination

Intensity data for the selected acicular crystal specimen were collected at 100(2) K. The observed 2/m Laue symmetry of the intensities indicated that the crystal belonged to the monoclinic system. Since S-IBU is a chiral molecule, the space group was expected to be chiral. Systematic absences *0k0*: $k = 2n+1$ confirmed this, indicating a two-fold screw-axis parallel to the crystal *b*-axis and hence the space group $P2_1$.

Structure solution and refinement

The crystal structure was solved using the direct methods program SHELXS-97.[10] Table 6.6 shows the refinement data for the crystal structure of $(S\text{-}IBU)^{-}(ACA)^{+}$. Based on the known structures of S-IBU and ACA, non-hydrogen atoms were assigned to appropriate electron density peaks. The ASU comprises two independent S-IBU moieties and two independent ACA moieties. The non-hydrogen atoms were refined isotropically and thereafter anisotropically before placing hydrogen atoms. The latter were located unequivocally in difference Fourier maps and were placed using the riding model, with U_{iso} values in the range 1.2 – 1.5 times those of their parent atoms. The C-O bond lengths in the two independent S-IBU moieties (A, B), namely C1A-O2A, C1A-O3A, C1B-O2B and C1B-O3B were measured and found to be 1.258(5), 1.260(5), 1.245(5) and 1.267(6) Å respectively. This

indicated that the carboxyl groups in the S-IBU moieties had been deprotonated, resulting in carboxylate ions, the two protons having been transferred to carboxylate oxygen atoms on the ACA moieties, converting them to -COOH groups. This provided the proof that the new crystal structure was therefore a salt, with formula $(S\text{-}IBU)^-(ACA)^+$.

Table 6.6: Crystal data and refinement details for $(S\text{-}IBU)^-(ACA)^+$.

Chemical formula	**$(C_{13}H_{17}O_2)^-(C_6H_{14}NO_2)^+$**
Formula weight (g.mol^{-1})	337.45
Temperature (K)	100(2)
Wavelength (Å)	0.71073
Crystal system	Monoclinic
Space group	$P2_1$
a (Å)	15.0085(17)
b (Å)	6.7385(8)
c (Å)	19.232(2)
α (°)	90
β (°)	97.005(4)
γ (°)	90
V (Å^3)	1930.5(4)
Z	4
Calculated density (g.cm^{-3})	1.161
μ (Mo Kα) (mm^{-1})	0.080
F(000)	736
Crystal size (mm^3)	0.020 × 0.040 × 0.420
Range scanned θ (°)	4.2° < 2θ < 54.6°
Index ranges ±h, ±k, ±l	h:-19, 19; k:-8, 8; l:-24, 24
No. reflections (total)	30623
No. unique reflections	8439
No. of parameters	443
Goodness-of-fit, S	1.08
Final indices R1, wR2, [I>2σ(I)]	0.0727, 0.1864
R indices, all data (R1, wR2)	0.1124, 0.2119
Largest diff. peak and hole (e Å^{-3})	0.56, -0.55

Molecular structure

Figure 6.8 shows the labelling scheme of the asymmetric unit of $(S\text{-}IBU)^-(ACA)^+$ which consists of two $(S\text{-}IBU)^-$ and two $(ACA)^+$ moieties. The atomic numbering scheme of $S\text{-}IBU_A$ and ACA_A is repeated in $S\text{-}IBU_B$ and ACA_B.

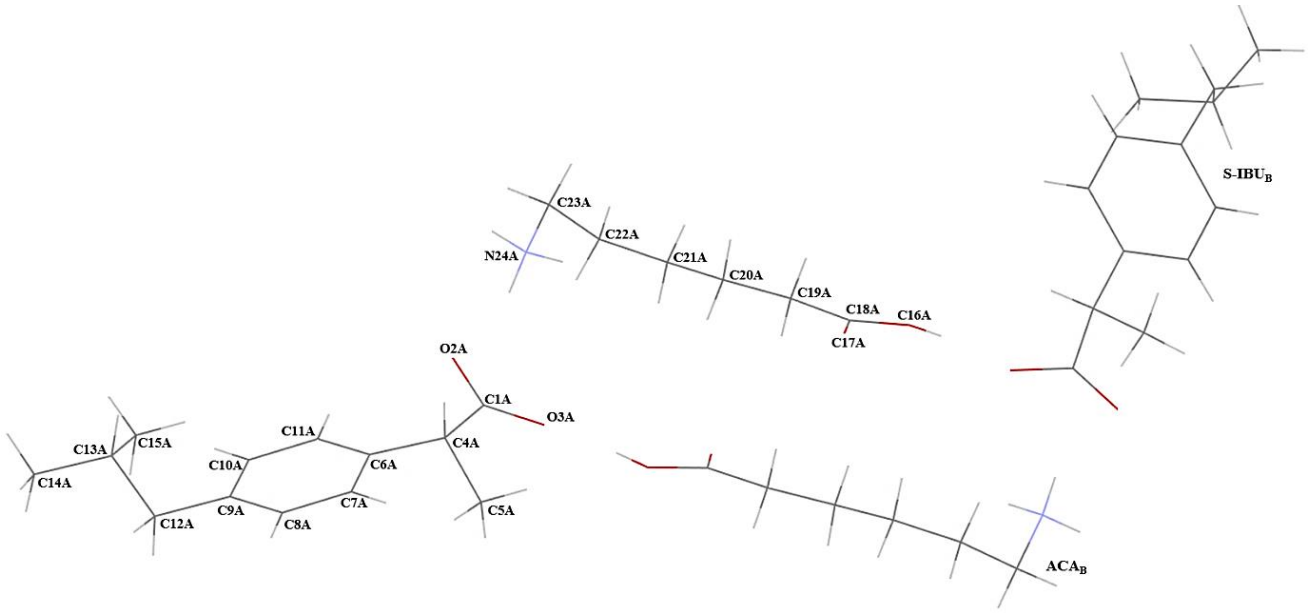

Figure 6.8: The labelling scheme of the ASU of the salt $(S\text{-}IBU)^-(ACA)^+$.

Hydrogen bonding

Figure 6.9 shows the hydrogen bonding in the ASU. The cyclic motif is formed via four charge-assisted hydrogen bonds ACA(COOH)···(carboxylate O)S-IBU, and $ACA(NH_3^+)$···(carboxylate O)S-IBU. Table 6.7 lists all the intermolecular hydrogen bonds involving the $(S\text{-}IBU)^-$ and $(ACA)^+$ ions in the crystal structure.

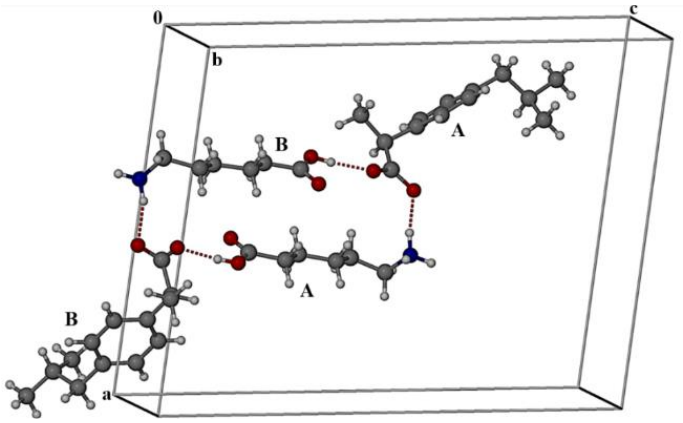

Figure 6.9: Hydrogen bonding in the ASU of $(S\text{-}IBU)^{-}(ACA)^{+}$. For clarity, only the H-bonds that link the four moieties of the ASU into a cyclic motif are shown.

Table 6.7: Intermolecular hydrogen bonds in $(S\text{-}IBU)^{-}(ACA)^{+}$.

Hydrogen bond interaction	D-H (Å)	H···A (Å)	D···A (Å)	D-H···A (°)	Symmetry operation
O18A-H18A···O3B	0.84	1.73	2.561(4)	170	x,y,z
O18B-H18B···O3A	0.84	1.77	2.607(4)	177	x,y,z
N24A-H24A···O2A	0.91	1.88	2.765(4)	163	x,y,z
N24A-H24B···O3A	0.91	2.06	2.879(5)	148	-1+x,1/2+y,1-z
N24A-H24B···O17B	0.91	2.55	3.136(4)	122	-1+x,1/2+y,1-z
N24A-H24C···O2A	0.91	1.95	2.843(5)	165	1-x,-1/2+y,1-z
N24B-H24D···O2B	0.91	1.91	2.803(5)	168	1-x,1/2+y,-z
N24B-H24E···O3B	0.91	1.97	2.812(5)	153	1-x,-1/2+y,-z
N24B-H24F···O2B	0.91	1.99	2.857(4)	158	x,y,z
N24B-H24F···O3B	0.91	2.40	3.167(4)	143	x,y,z
C5A-H5A2···O18B	0.98	2.48	3.304(6)	141	x,y,z
C4A-H4A···O17B	1.00	2.49	3.376(5)	147	x,1+y,z
C15A-H15A···O18A	0.98	2.53	3.422(7)	151	1-x,3/2+y,1-z
C19B-H19C···O17A	0.99	2.58	3.356(5)	135	x,y,z

Packing arrangement

Figure 6.10 shows the [010] projection of the packing arrangement of $(S\text{-}IBU)^-$ and $(ACA)^+$ counterions in the crystal structure. The packing consists of horizontal rows of repeating, concatenated cyclic motifs alternating with interleaving double-strand ribbons of $(S\text{-}IBU)^-$ ions.

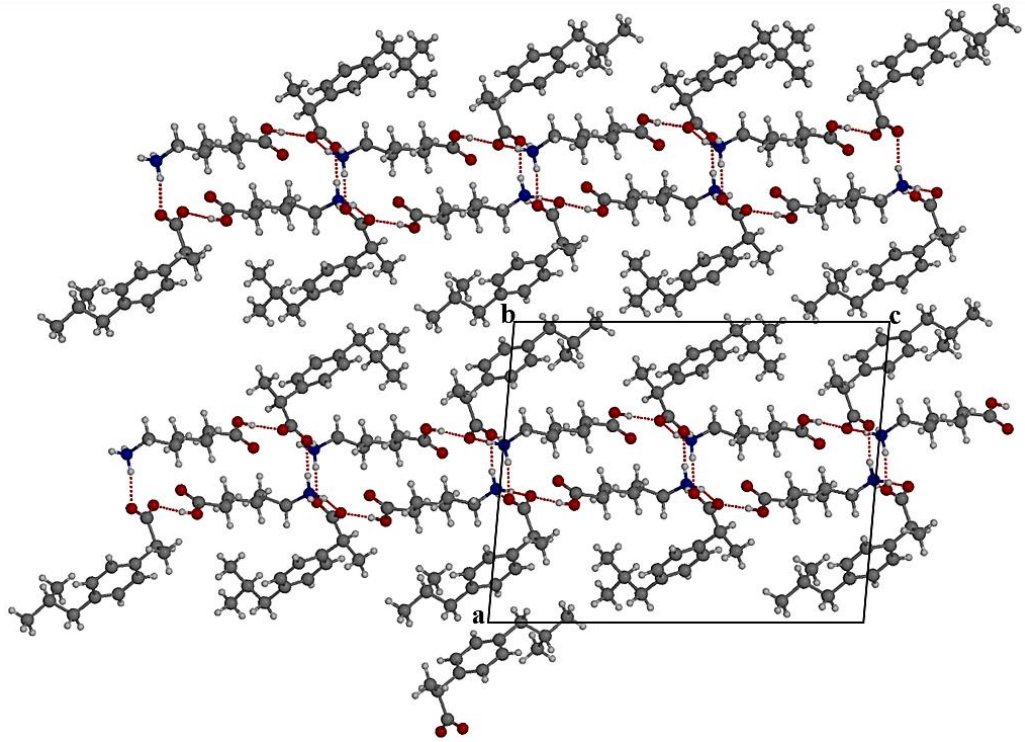

Figure 6.10: Packing arrangement of $(S\text{-}IBU)^-(ACA)^+$.

6.3.4. Fourier-transform infrared (FT-IR) spectroscopy

Figure 6.11 shows the stacked spectra of the starting materials and that of the $(S\text{-}IBU)^-(ACA)^+$ co-precipitation product. In the spectrum of S-IBU, the peak at 1699 cm^{-1} is due to the C=O group. The spectrum of ACA (which is zwitterionic in the solid state) displays two strong peaks at 1387 and 1535 cm^{-1}, indicative of a carboxylate group. These carboxylate bands are attributed to the C-O symmetric and asymmetric stretching vibrations respectively. The spectrum of the product also shows the presence of a carboxylate group, with however, the two characteristic strong peaks appearing at distinctly different frequencies (viz., 1391 and 1500 cm^{-1}) from those of ACA. These can be interpreted as being due to the presence of a $-COO^-$ group of S-IBU in the product phase, which resulted from the transfer of a proton to the carboxylate group of ACA, the latter displaying a carbonyl stretching band at 1716 cm^{-1}.

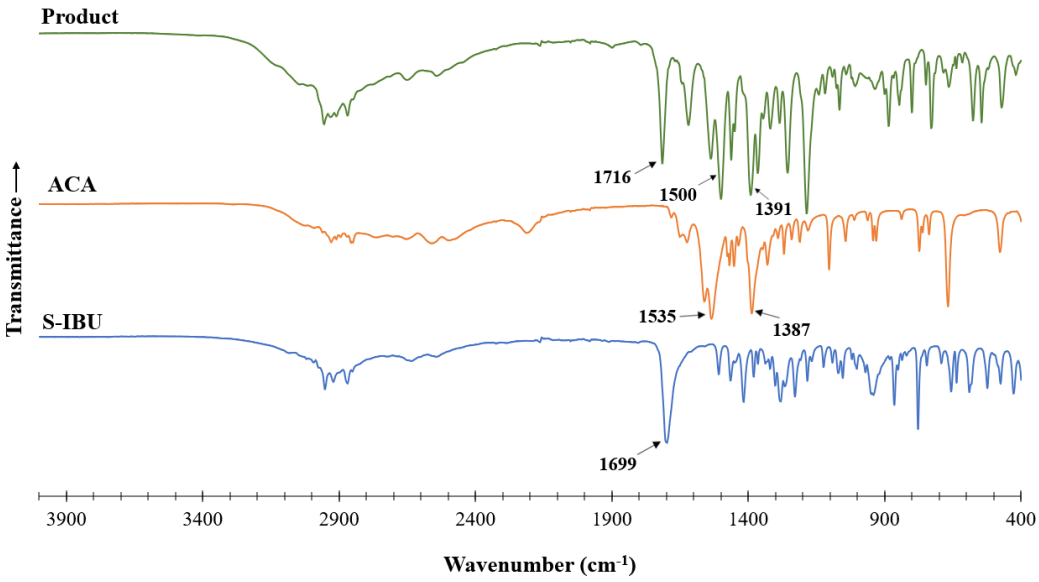

Figure 6.11: Stacked FT-IR spectra of S-IBU, ACA and $(S\text{-}IBU)^{-}(ACA)^{+}$.

6.3.5. Comparative powder X-ray diffraction (PXRD) patterns

Figure 6.12 shows a reasonable level of agreement between the experimental and calculated PXRD patterns of $(S\text{-}IBU)^{-}(ACA)^{+}$. There are a few discrepancies in both relative peak intensities as well as angular positions, which can be attributed to the difference in the temperatures at which the pattern of the sample was recorded and the SCXRD data were collected.

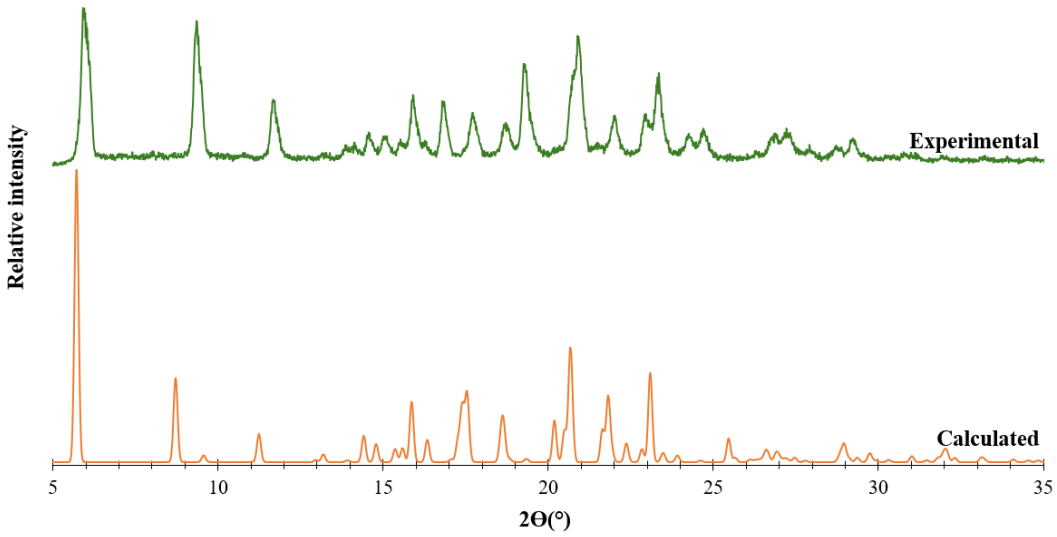

Figure 6.12: Calculated and experimental PXRD patterns of the $(S\text{-}IBU)^{-}(ACA)^{+}$ salt.

6.4 Synthesis and characterisation of the salt [(S-IBU)$^-$(TXA)$^+$] resulting from the reaction of S-IBU and tranexamic acid

Using LAG, (S-IBU)$^-$(TXA)$^+$ was synthesised with S-IBU (5.00 mg, 0.0242 mmol) and TXA (3.80 mg, 0.0242 mmol) with a total volume (in µL) of MeOH (680), EtOH (740) and MeCN (680) while grinding the powder mixture for a total of 20 minutes. The PXRD patterns (Figure 6.13) show that all solvents tested in the LAG experiments resulted in a common new phase. Single crystals were synthesised via co-precipitation, by dissolving equimolar amounts of S-IBU (5.00 mg) and TXA (3.80 mg) separately in MeOH (1.0 ml). The solutions were stirred at 50 ± 5 °C and once fully dissolved, the hot S-IBU solution was added to that of TXA. The resulting solution was then stirred for 6 hours at 50 ± 5 °C after which it was filtered through a 0.45 µm syringe filter and left to evaporate slowly. After 3 days crystals suitable for X-ray data-collection were harvested.

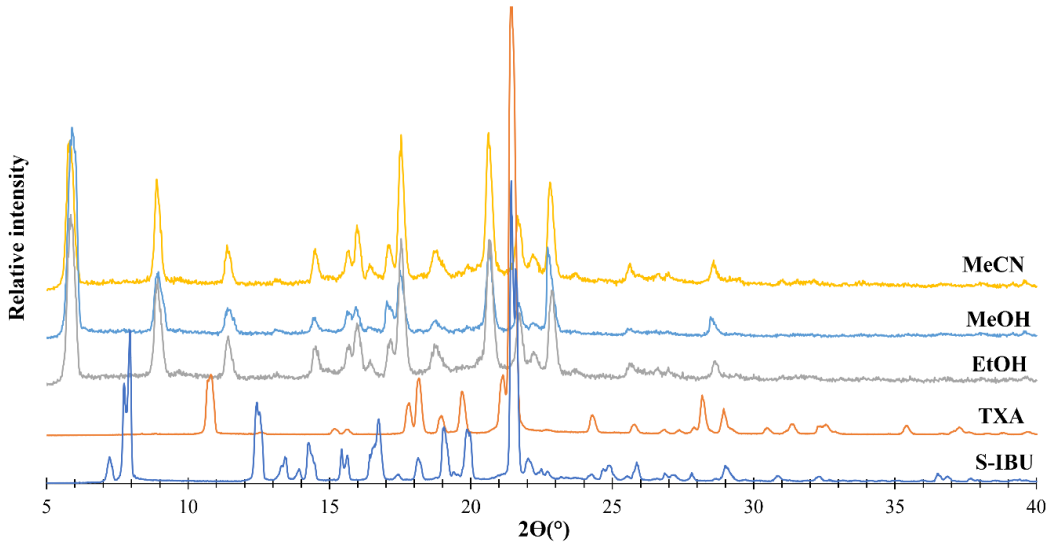

Figure 6.13: PXRD patterns of the starting materials S-IBU and TXA and those of the products following LAG experiments using the solvents indicated.

It was noted at this point that there is a remarkable resemblance between the PXRD pattern of the product in Figure 6.13 and that of the product in Figure 6.12, suggesting a significant level of isostructurality of the new phase with the (S-IBU)$^-$(ACA)$^+$ salt, a special feature that will be discussed later in this chapter.

6.4.1. ^{1}H NMR spectroscopy and elemental analysis (EA)

The stoichiometric ratio of $(S\text{-}IBU)^{-}(TXA)^{+}$ could not be determined using ^{1}H NMR spectroscopy. Both DMSO-d_6 and D_2O were used in attempts to record a reliable spectrum. TXA was not soluble in DMSO-d_6 and only partially soluble in D_2O at increased temperatures. Elemental analysis was therefore performed to determine the stoichiometric ratio of the product. Table 6.8 shows the experimental and calculated mass percentage (%) values of C, H and N in $(S\text{-}IBU)^{-}(TXA)^{+}$. The experimental C, H and N mass percentages differ from the calculated values by only 0.2, 0.01 and 0.5% respectively, all of which are reasonable, thus confirming the stoichiometric ratio of the salt as 1:1.

Table 6.8: Mass percentage values of the experimental* and calculated values of C, H and N for the salt $(S\text{-}IBU)^{-}(TXA)^{+}$.

Element	Theoretical	Experimental
C	69.39	69.19
H	9.15	9.16
N	3.85	3.35

*single determination only

6.4.2. Thermal analysis

6.4.2.1. Hot stage microscopy (HSM)

Figure 6.14 shows the HSM images recorded in the range 18 – 252 °C. The crystals which are clear thin needles at room temperature begin turning brown at 148 °C. This continues until the crystals begin decreasing in size from 155 °C. Thereafter the slide becomes clouded at 235.6 °C as melting with decomposition occurs.

Figure 6.14: HSM images of $(S\text{-}IBU)^{-}(TXA)^{+}$ crystals (heating range 8 - 235.6 °C, rate 10 °C/min).

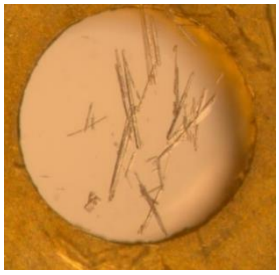

18.0 °C: Needle-shaped single crystals at room temperature.

148.1 °C: Crystals change from clear to brown.

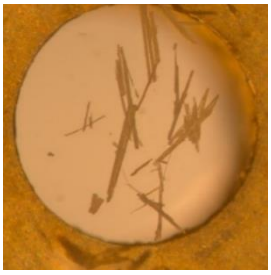

174.0 °C: No significant change is oberseved.

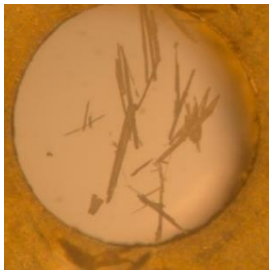

188.2 °C: Onset of melting with decomposition.

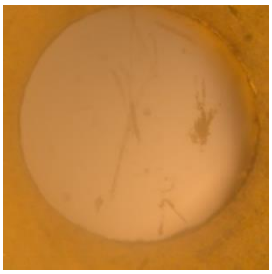

235.6 °C: Complete decomposition of the crystals.

6.4.2.2. Thermal gravimetric analysis (TGA) and differential scanning calorimetry (DSC)

Figure 6.15 shows the TGA and DSC curves of $(S\text{-}IBU)^{-}(TXA)^{+}$. The TGA curve (n = 3), recorded from 20 to 300 °C, shows two mass losses that take place over this temperature range. There is no initial mass loss at the lowest temperatures, indicating that there is no solvent present in the crystal. The first and second mass losses are 54.3 ± 0.2% and 24.2 ± 0.1% with onset temperatures of 137.8 °C and 221.8 °C respectively. The first mass loss is in reasonable agreement with the theoretical percentage of (S-IBU) (56%) for the 1:1 stoichiometry established by EA. The second mass loss, which corresponds to the temperature range of clouding and decomposition in the HSM images, is therefore due to the loss of TXA. This further confirms that the product has a stoichiometric ratio of 1:1.

The DSC trace shows a very small endotherm at ~46 °C, which may signal a minor phase change, but the major event is represented by the sharp endotherm with peak temperature 181 °C occurring over the range 174 – 183 °C. The HSM images indicate that this is the melting of the compound with decomposition. As observed for the salt $(S\text{-}IBU)^{-}(ACA)^{+}$, the significantly increased melting point of $(S\text{-}IBU)^{-}(TXA)^{+}$ compared with that of S-IBU shows that salt formation results in a product with increased thermal stability.

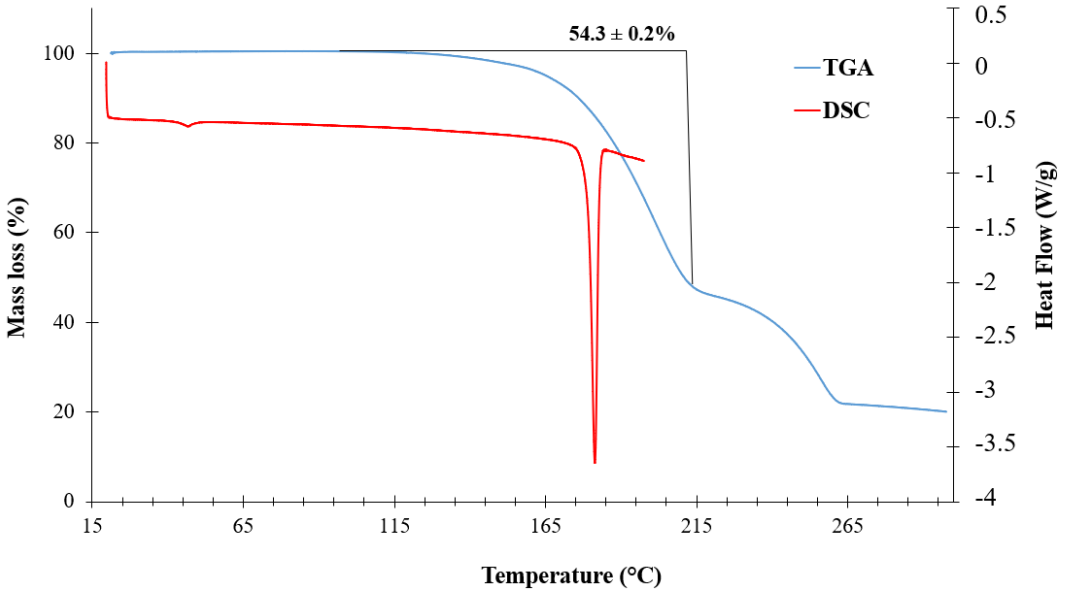

Figure 6.15: TGA and DSC curves of $(S\text{-}IBU)^{-}(TXA)^{+}$.

6.4.3. Crystal structure analysis

Data-collection and space group determination

The same temperature as that used for the intensity data-collection for $(S\text{-}IBU)^{-}(ACA)^{+}$, namely 100(2) K, was selected for data-collection of the new crystal phase. Inspection of the measured intensities indicated the Laue symmetry 2/m, indicating the monoclinic system, and from the observed reflection condition *0k0*: $k = 2n$ the space group $P2_1$ was duly assigned, given that the S-IBU molecule is chiral. It was noted at this point that the new phase crystallised in the same space group as that of the salt $(S\text{-}IBU)^{-}(ACA)^{+}$, and furthermore that their unit cell dimensions were very similar, confirming some degree of crystal isostructurality, first detected by PXRD.

Structure solution and refinement

The crystal structure was solved using the direct methods program SHELXS-97,[10] which revealed two S-IBU and two TXA moieties in the ASU. The refinement procedure was identical to that described earlier for $(S\text{-}IBU)^{-}(ACA)^{+}$, and is therefore not repeated here. For the four carbon-oxygen bonds in the two independent S-IBU moieties, the refined model yielded accurate lengths as follows: C1A-O2A 1.257(6) Å, C1A-O3A 1.244(7) Å, C1B-O2B 1.238(6) Å and C1B-O3B 1.250(7) Å. This confirmed the presence of two distinct carboxylate groups (as opposed to carboxyl groups) and that the independent S-IBU molecules had therefore both been deprotonated during the reaction with

TXA. In contrast, for the two independent TXA moieties, the C-O bond lengths were C16A-O17A 1.198(8) Å, C16A-O18A 1.309(9) Å (moiety A), and C16B-O17B 1.192(7) Å, C16B-O18B 1.310(9) Å (moiety B), clearly indicating that both of the original carboxylate groups of the zwitterionic coformer TXA had been converted to carboxyl groups, -COOH. Hence the new crystal phase was unequivocally designated as a salt. Table 6.9 lists the crystal and refinement parameters for $(S\text{-}IBU)^-(TXA)^+$.

Table 6.9: Crystal data and refinement details for $(S\text{-}IBU)^-(TXA)^+$.

Chemical formula	**$(C_{13}H_{17}O_2)^-(C_8H_{16}NO_2)^+$**
Formula weight (g.mol^{-1})	363.48
Temperature (K)	100(2)
Wavelength (Å)	0.71073
Crystal system	Monoclinic
Space group	$P2_1$
a (Å)	15.623(5)
b (Å)	6.687(2)
c (Å)	20.571(6)
α (°)	90
β (°)	99.867(12)
γ (°)	90
V (Å^3)	2117.3(11)
Z	4
Calculated density (g.cm^{-3})	1.140
μ (Mo Kα) (mm^{-1})	0.078
F(000)	792
Crystal size (mm^3)	0.02 × 0.09 × 0.42
Range scanned θ (°)	4.0° ≤ 2θ ≤ 51.8°
Index ranges ±h, ±k, ±l	h:-19, 19; k:-8, 8; l:-24, 25
No. reflections (total)	41905
No. unique reflections	8052
No. of parameters	501
Goodness-of-fit, S	1.14
Final indices R1, wR2, [I>2σ(I)]	0.0878, 0.2074
R indices, all data (R1, wR2)	0.1042, 0.2170
Largest diff. peak and hole (e Å^{-3})	-0.32, 0.69

Molecular structure

The ASU of the salt contains two $(S\text{-}IBU)^-$ and two $(TXA)^+$ moieties confirming that Z = 4. Figure 6.16 shows the labelling scheme of the $(S\text{-}IBU)^-$ and $(TXA)^+$ ions.

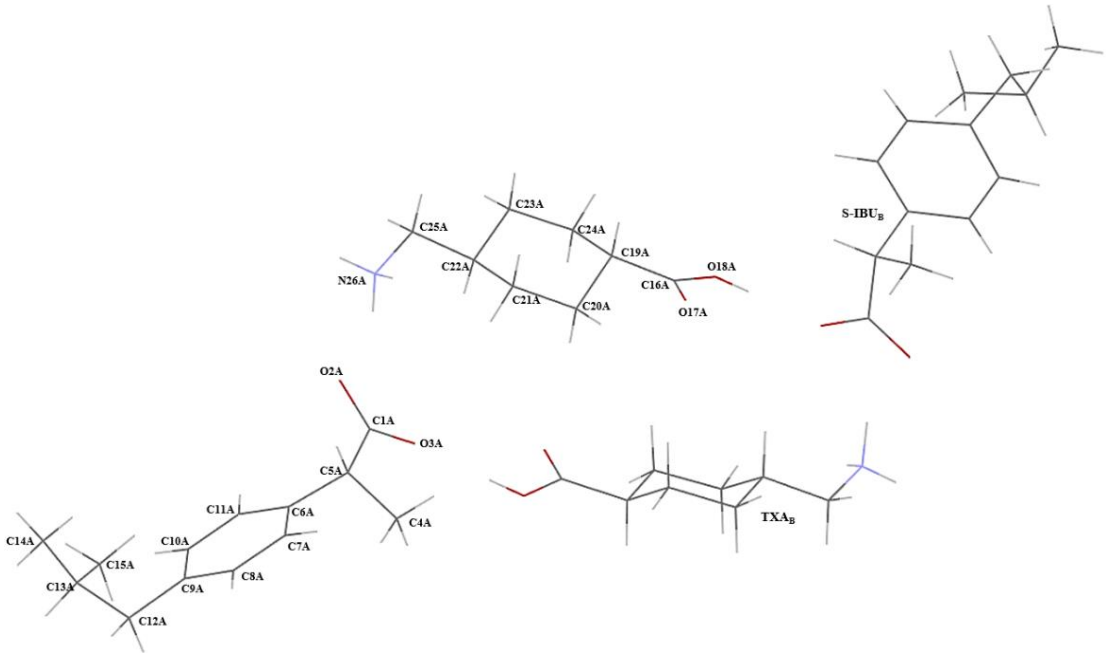

Figure 6.16: The labelling scheme of the ASU of $(S\text{-}IBU)^-(TXA)^+$.

Hydrogen bonding

Figure 6.17 shows the hydrogen bonding occurring in the ASU of $(S\text{-}IBU)^-(TXA)^+$. As observed in the crystal structure of $(S\text{-}IBU)^-(ACA)^+$, there is, in the new salt, an analogous cyclic motif consisting of two $(S\text{-}IBU)^-$ and two $(TXA)^+$ counterions in the ASU. These motifs repeat with alternating $(TXA)^+$ and $(S\text{-}IBU)^-$ ions. Table 6.10 lists the hydrogen bonding parameters in the crystal.

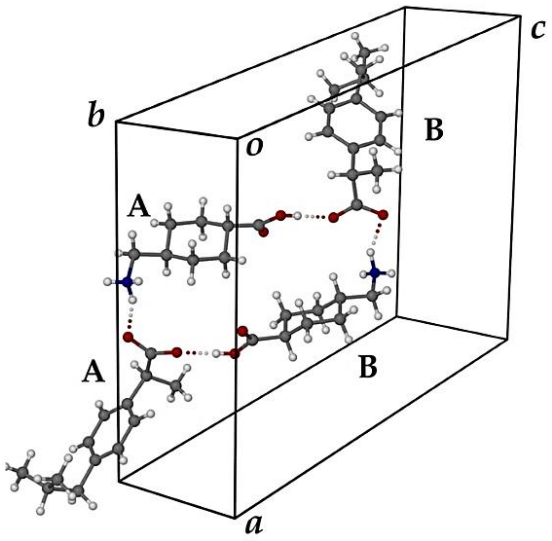

Figure 6.17: Hydrogen bonding in the ASU of $(S\text{-}IBU)^{-}(TXA)^{+}$.

Table 6.10: Intermolecular hydrogen bonds in $(S\text{-}IBU)^{-}(TXA)^{+}$.

Hydrogen bond interaction	D-H (Å)	H···A (Å)	D···A (Å)	D-H···A (°)	Symmetry operation
N26A-H1···O2A	0.83(7)	1.99(7)	2.818(7)	173(7)	1-x,-1/2+y,-z
O18A-H18A···O3B	0.84	1.74	2.576(6)	175	x,y,z
O18B-H18B···O3A	0.84	1.78	2.622(6)	178	x,y,z
N26A-H26B···O2A	0.94(8)	1.86(8)	2.756(6)	160(6)	x,y,z
N26A-H26C···O3A	0.84(7)	2.18(7)	2.928(7)	150(6)	1-x,1/2+y,-z
N26A-H26C···O17B	0.84(7)	2.47(6)	2.987(6)	121(6)	1-x,1/2+y,-z
N26B-H26D···O2B	1.00(6)	1.93(6)	2.847(7)	151(5)	x,y,z
N26B-H26D···O3B	1.00(6)	2.31(6)	3.190(7)	146(5)	x,y,z
N26B-H26E···O3B	0.81(6)	2.07(6)	2.824(7)	155(6)	1-x,-1/2+y,1-z
N26B-H26F···O2B	0.97(9)	1.88(9)	2.838(7)	169(7)	1-x,1/2+y,1-z
C21B-H21D···O2B	0.99	2.45	3.365(7)	153	1-x,1/2+y,1-z

Packing

Figure 6.18 shows the packing arrangement of the $(S\text{-}IBU)^{-}(TXA)^{+}$ crystal structure. As previously mentioned, there is a repeating cyclic motif found within the structure with alternating rows of $(S\text{-}IBU)^{-}$ and $(TXA)^{+}$ counterions. As observed in $(S\text{-}IBU)^{-}(ACA)^{+}$, there are repeating horizontal rows of concatenated cyclic motifs alternating with interleaving double-strand ribbons of $(S\text{-}IBU)^{-}$ ions.

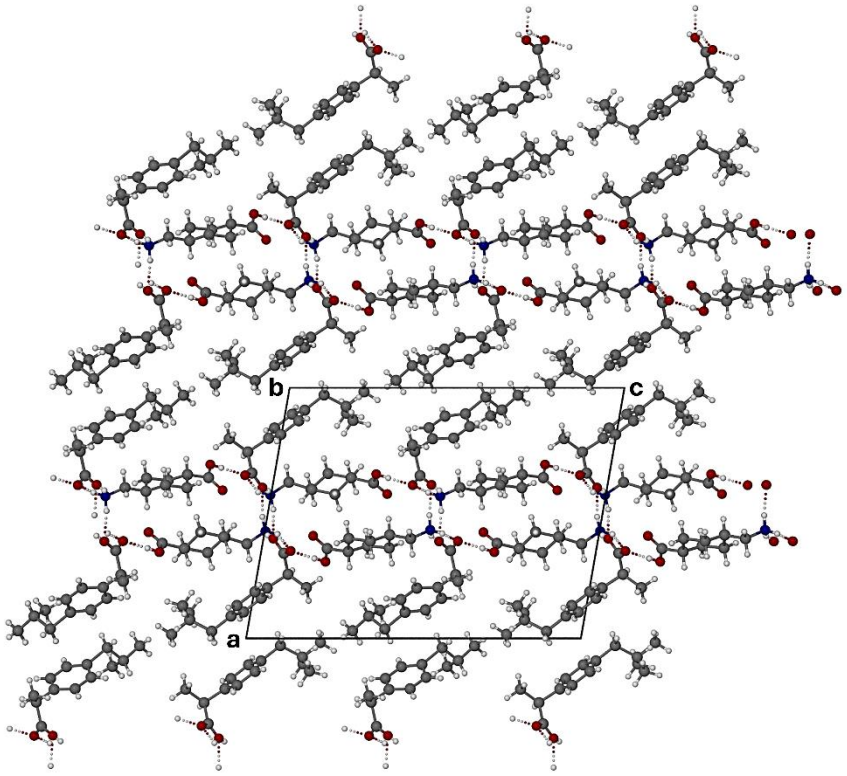

Figure 6.18: The packing arrangement in the crystal of $(S\text{-}IBU)^{-}(TXA)^{+}$.

6.4.4. Fourier-transform infrared (FT-IR) spectroscopy

Figure 6.19 shows the stacked spectra of the starting materials and that of the $(S\text{-}IBU)^{-}(TXA)^{+}$ co-precipitation product. The interpretation of the spectra is analogous to that presented in the discussion of Figure 6.11. In the spectrum of S-IBU, the peak at 1699 cm^{-1} is attributed to the carbonyl stretching mode. Two strong peaks at 1380 cm^{-1} (ν_{sym}) and 1532 ($\nu_{antisym}$) indicate the carboxylate group in the zwitterionic component TXA. A carboxylate group is also evident in the spectrum of the product, two characteristic strong peaks appearing at 1392 and 1503 cm^{-1}. These have different frequencies from the peaks identified in the spectrum of TXA, and can therefore be interpreted as indicating the presence of a $-COO^{-}$ group of S-IBU in the product phase. This resulted from the transfer of a proton to the carboxylate group of TXA, the latter now displaying a strong carbonyl stretching band at 1712 cm^{-1}.

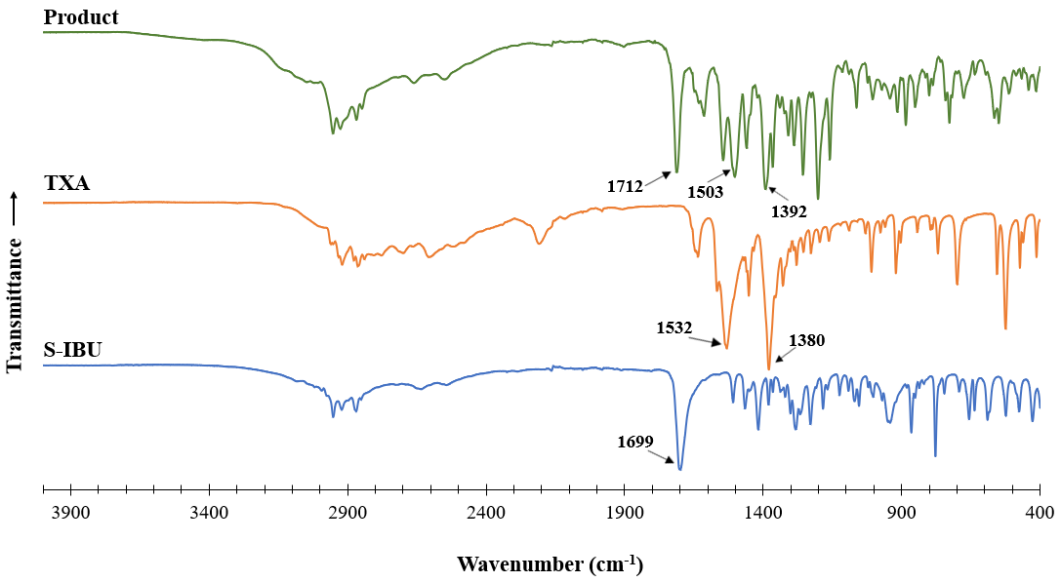

Figure 6.19: Stacked FT-IR spectra of S-IBU, TXA and $(S\text{-}IBU)^{-}(TXA)^{+}$.

6.4.5. Comparative powder X-ray diffraction (PXRD) patterns

Figure 6.20 shows the calculated and experimental PXRD patterns of $(S\text{-}IBU)^{-}(TXA)^{+}$, which display good correlation. Relative to the experimental pattern, there are small angular shifts of corresponding peaks, both to the left and to the right, in the calculated PXRD pattern. This indicates that on cooling the crystal specimen from 294 K to 100 K for SCXRD analysis, it undergoes anisotropic shrinkage.

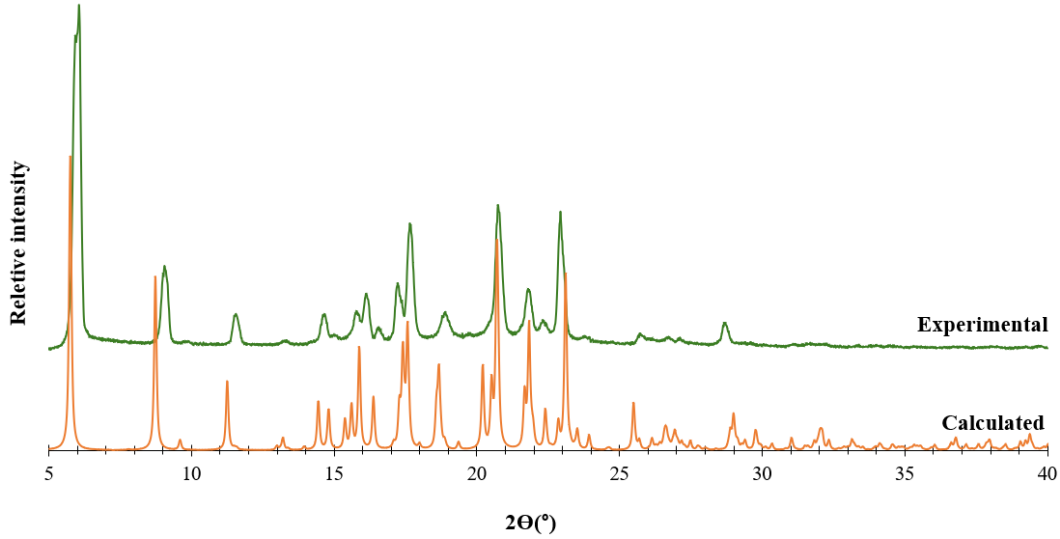

Figure 6.20: Experimental and calculated PXRD patterns of $(S\text{-}IBU)^{-}(TXA)^{+}$.

6.5. Isostructural nature of the $(S\text{-}IBU)^-(ACA)^+$ and $(S\text{-}IBU)^-(TXA)^+$ salts

When comparing the structural arrangements of the salts $(S\text{-}IBU)^-(ACA)^+$ and $(S\text{-}IBU)^-(TXA)^+$, it is evident that they display isostructural features. Both contain hydrogen-bonded cyclic motifs consisting of two S-IBU anions and two zwitterionic coformers. Figure 6.21 shows a spectroscopic overlay view of the ASUs of the ACA cations (red) and TXA cations (green) with their respective S-IBU anions. This figure reveals a fairly high degree of similarity between the ASUs of the salts.

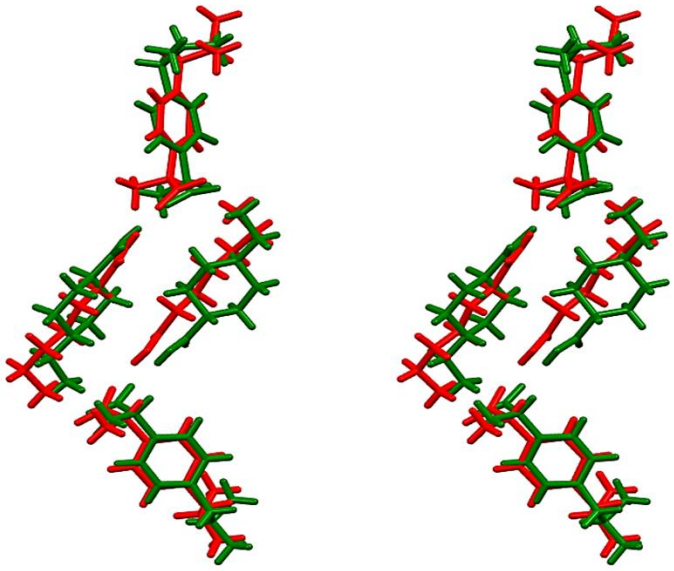

Figure 6.21: Spectroscopic view of the ASUs of the S-IBU salts with ACA (red) and TXA (green).[11]

The degree of isostructurality is also evident in the comparison of the PXRD patterns shown in Figure 6.22. At lower angles there is fairly close similarity between the patterns, with three distinct 'matching' peaks. The similarities are likewise evident from their unit cell parameters, the common crystal system (monoclinic) and their belonging to the same space group $P2_1$, as summarised in Table 6.11.

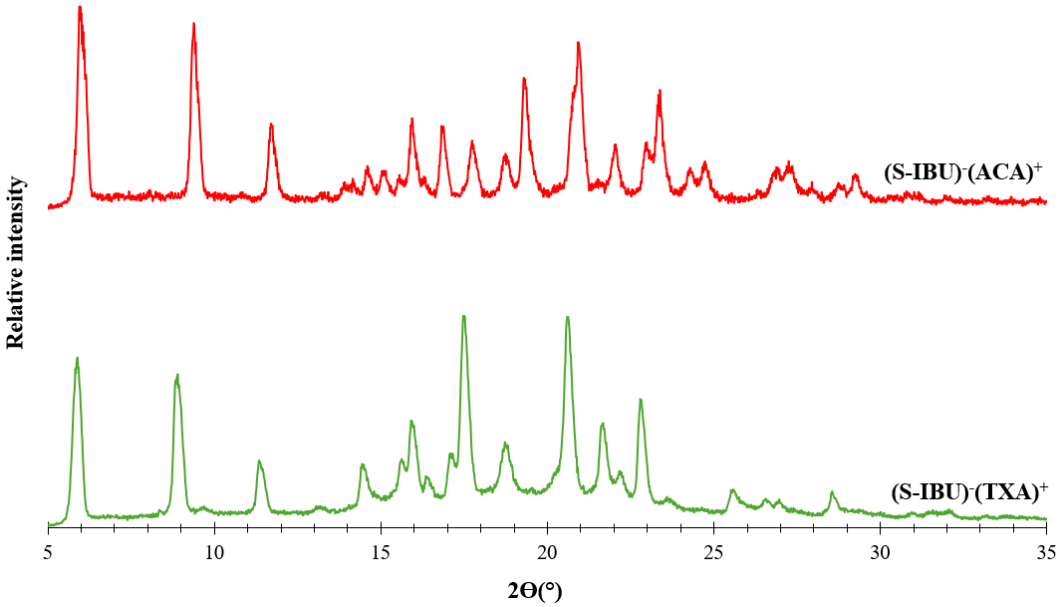

Figure 6.22: Stacked PXRD patterns of $(S\text{-}IBU)^-(ACA)^+$ and $(S\text{-}IBU)^-(TXA)^+$.

Table 6.11: Crystollographic data for the salts $(S\text{-}IBU)^-(ACA)^+$ and $(S\text{-}IBU)^-(TXA)^+$.

	$(S\text{-}IBU)^-(ACA)^+$	**$(S\text{-}IBU)^-(TXA)^+$**
Chemical formula	$(C_{13}H_{17}O_2)^-(C_6H_{14}NO_2)^+$	$(C_{13}H_{17}O_2)^-(C_8H_{16}NO_2)^+$
Crystal system	Monoclinic	Monoclinic
Space group	$P2_1$	$P2_1$
a (Å)	15.0085(17)	15.623(5)
b (Å)	6.7385(8)	6.687(2)
c (Å)	19.232(2)	20.571(6)
α (°)	90	90
β (°)	97.005(4)	99.867(12)
γ (°)	90	90
V (Å^3)	1930.5(4)	2117.3(11)
Z	4	4

The origin of the isostructural nature of the salts is evident when considering the similarities in the molecular structures of ACA and TXA, in particular the distances between their respective terminal units (viz. 7.75, 7.83 Å) for the intramolecular $N^+\cdots$(terminal)O lengths in the two ACA cations and (7.37, 7.38 Å) in the two TXA cations. These features are responsible for the analogous H-bonding interactions in which the two cations engage. Both being zwitterions, ACA and TXA have pKa values

of 10.8 and 10.2 respectively. Based on the "rule of three" pKa rule discussed in Chapter 1 (pg. 6) a ΔpKa [pKa(base) – pKa(acid)] greater than 3 is most likely to result in salt formation with the proton transfer from the acid (S-IBU in this case) to the base (ACA/TXA). As indicated at the beginning of this Chapter, S-IBU has a pKa of 4.88. The ΔpKa values of both products are therefore greater than 3 which also confirms that the products are salts. Because ACA and TXA have the same terminal functional groups and pKa values, the deprotonation of S-IBU and the protonation of ACA and TXA result in $-COO^-$, -COOH and $-NH_3^+$ functional groups in both salts, all contributing to the hydrogen bonding. The presence of these functional groups and the close similarity in the lengths of the intramolecular $N^+\cdots$(terminal)O lengths in the two cations mentioned above result in the same hydrogen bonded cyclic motifs occurring in both crystal structures.

6.6. Solubility studies of the 6-aminocaproic acid and tranexamic acid salts of S-(+)-ibuprofen

Dynamic solubility studies were performed with $(S\text{-IBU})^-(ACA)^+$ and $(S\text{-IBU})^-(TXA)^+$ at both pH 2.0 and pH 6.5 using the method described in Chapter 2 (2.6.3. Dynamic solubility studies, pg. 30). The standard curves, produced with UV-Vis spectroscopy and HPLC, and the preparation methods appear in the Appendix (Section 3.2., pg. 23).

Figure 6.23 shows the solubility profiles of $(S\text{-IBU})^+(ACA)^-$ and $(S\text{-IBU})^+(TXA)^-$ produced following the dynamic solubility study. The latter showed that $(S\text{-IBU})^-(ACA)^+$ had an overall higher solubility compared to $(S\text{-IBU})^-(TXA)^+$, but both showed a decrease in the solubility of S-IBU when it is incorporated in the salt forms. It was expected that the solubility of the API might increase and that the dissolution profile might show the 'spring and parachute' effect,[12] as described in Chapter 2 (pg. 30-31). However, this was not the case. It is well known that the solubilities of such salts may vary considerably with the pH of the medium. Thus, the solubilities in pH 2.0 were also tested. The UV-Vis absorption of S-IBU overlapped with both ACA and TXA at pH 2.0, which meant that HPLC had to be used to determine the concentration of S-IBU. Unfortunately, at pH 2.0 HPLC yielded erratic results and could not be relied upon for further investigation.

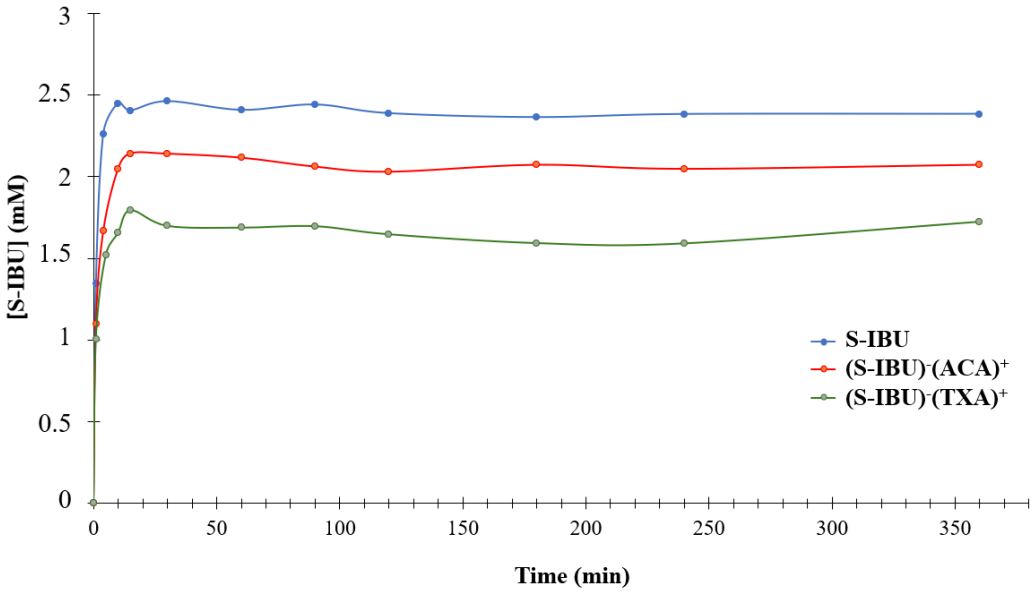

Figure 6.23: Dynamic solubility profiles of S-IBU, $(S\text{-}IBU)^{-}(ACA)^{+}$ and $(S\text{-}IBU)^{-}(TXA)^{+}$ at pH 6.5.

Due to the unreliable results obtained by HPLC, a kinetic solubility study was carried out in FaSSIF at pH 2.0 and 6.5. The method described in Chapter 2 (2.6.5. Equilibrium solubility studies, pg. 32) was used. The calibration curve produced by HPLC was used to quantify S-IBU in solution.

The intrinsic dissolution study in Table 6.12 shows the same result as observed in the dynamic dissolution study, namely the solubilities of S-IBU and both salts are lower at pH 2.0 compared to those at pH 6.5. This was expected as S-IBU has a pKa of 4.85.[2] It will therefore be protonated at pH 2.0, being less soluble than the salt form. The result shows a modest increase in the solubility of S-IBU when part of the salt.

Table 6.12: Relative solubilities of S-IBU, $(S\text{-}IBU)^{-}(ACA)^{+}$ and $(S\text{-}IBU)^{-}(TXA)^{+}$.

	Solubility (mg/mL)	**Solubility enhancement**
pH 2		
S-IBU	5.89×10^{-6}	1.00
$(S\text{-}IBU)^{-}(ACA)^{+}$	7.60×10^{-6}	1.29
$(S\text{-}IBU)^{-}(TXA)^{+}$	1.02×10^{-5}	1.73
pH 6.5		
S-IBU	3.33×10^{5}	1.00
$(S\text{-}IBU)^{-}(ACA)^{+}$	5.31×10^{-5}	1.59
$(S\text{-}IBU)^{-}(TXA)^{+}$	6.51×10^{-5}	1.95

6.7. Inclusion of S-(+)-ibuprofen in heptakis(2,6-di-*O*-methyl)-β-cyclodextrin

6.7.1. Motivation for the study

One of the aims of the present study was to recover a sample of the inclusion complex between the host DMB and S-IBU, previously reported by H. Ramulumo,[8] in 2019, in order to assess its synthetic reproducibility and carry out detailed solubility studies which were not performed earlier. A summary of the data for the inclusion complex reported by Ramulumo is as follows:

Crystal data for DMB·S-IBU (Form 1), $C_{56}H_{95}O_{35}\cdot C_{13}H_{18}O_2\cdot H_2O$, (M = 1550.44 g/mol): orthorhombic, space group $P2_12_12_1$ (no.19), a = 10.4845(2) Å, b = 14.9662(3) Å, c = 51.7354(11) Å, V = 8118.0(3) Å^3, Z = 4, T = 100(2) K, D_{calc} = 1.2686(1) g/cm^3, 34479 reflections measured ($4.8° \leq 2\theta \leq 54.2°$), R_{int} = 0.0430, observed reflections [$I > 2\sigma(I)$] 12270. 797 parameters, 14 restraints, final R1 = 0.1350 ($I > 2\sigma(I)$) and wR2 = 0.4035, goodness-of-fit = 1.729.

It will, however, become evident from what follows, that despite many attempts by the author of this dissertation to recover the crystalline phase referred to above (Form 1), it was never isolated and instead, a second crystalline form of a 1:1 DMB·S-IBU was discovered. Its synthesis and comprehensive characterisation are described below.

6.7.2. Complex preparation

Both kneading and co-precipitation experiments were carried out using equimolar amounts of S-IBU (5.0 mg, 0.0242 mmol) and DMB (32.27 mg, 0.0242 mmol). Kneading was performed for 20 minutes, while MilliQ® water was added to the mixture in increments of 10 µL at a rate of ±1 increment per minute to maintain a paste-like texture. Co-precipitation with 1:1 stoichiometric amounts of the reactants was performed by dissolving 32.27 mg of DMB in 1.5 ml MilliQ® water at room temperature; 5.00 mg of S-IBU was then added to the DMB solution in small increments. Initially S-IBU dissolved easily, but after approximately half of the S-IBU had been added, it no longer dissolved. To facilitate the dissolution of S-IBU, temperature cycling was performed over the temperature range 25 – 60 °C. Once the S-IBU had completely dissolved, the solution was left to stir at room temperature overnight before being filtered through a 0.45 µm syringe filter, capped and placed in a 60 °C oven. Crystals were isolated after 5 days. The PXRD pattern of the product obtained by kneading indicated that it was amorphous, while the co-precipitation experiments revealed that a new crystalline phase was present (Figure 6.24).

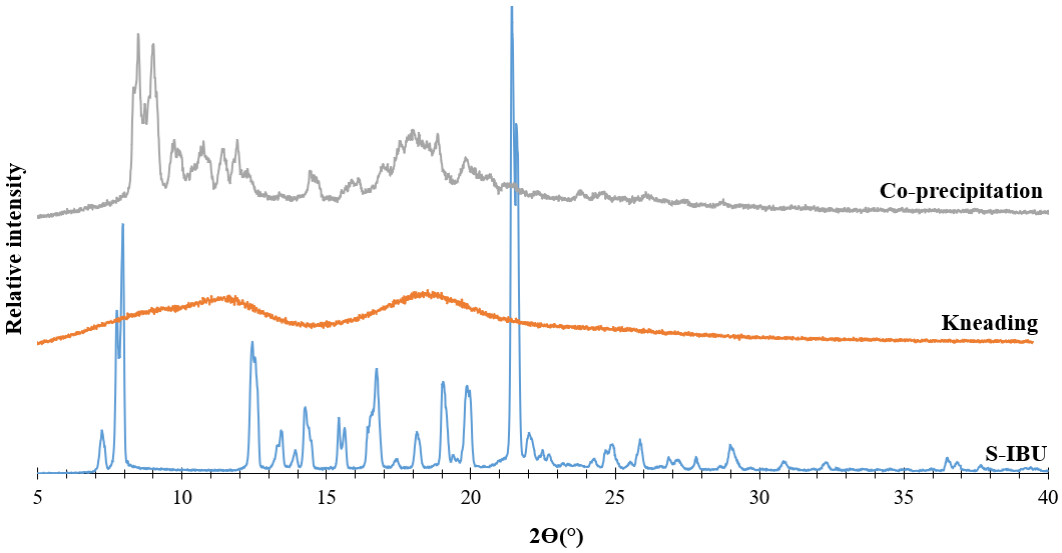

Figure 6.24: PXRD patterns of the products from kneading and co-precipitation of S-IBU and DMB.

6.7.3. ^{1}H NMR spectroscopy

The ^{1}H NMR spectrum of the solution formed by dissolving single crystals of the putative complex in DMSO-d_6 at 298 K was recorded. Table 6.13 shows the chemical shifts of the signals produced from S-IBU and DMB (Figure 6.25). The integration values confirm that the stoichiometric ratio of DMB and S-IBU in the product is 1:1, signifying the likelihood of this being an inclusion complex. The full spectrum can be seen in the Appendix (Section 3.3.2., pg. 25).

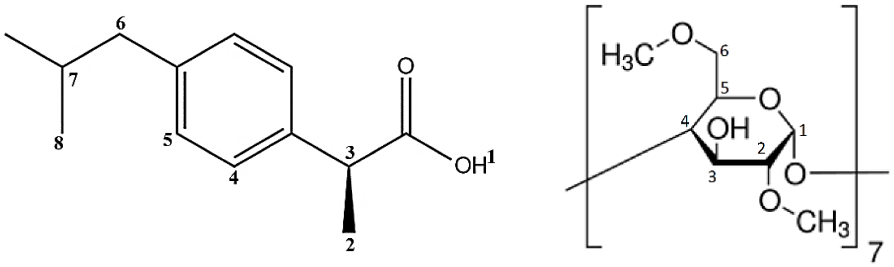

Figure 6.25: Labelling scheme of S-IBU (left) and DMB (right) used in the assignment of peaks in the ^{1}H NMR spectrum of the product.

Table 6.13: ^{1}H NMR integration table to determine the host-guest stoichiometry of DMB·S-IBU.

Assignment	δ (ppm)	Integration	Multiplicity	Proton	Stoichiometric ratio	Integer
S-IBU						
COOH (1)	12.25	1.10	Singlet	1H	1.10	1
CH aromatic (4,5)	7.21 - 7.10	4*	Doublet of doublets	4H	1	1
2 x CH_3 (8)	0.87 - 0.86	5.53	Doublet	6H	0.92	1
DMB						
CH and OH	4.99 - 4.97	13.30	Singlet	14H	0.95	1
OCH_3 methoxy	3.26	21.25	Singlet	21H	1.01	1

6.7.4. Thermal analysis

6.7.4.1. Hot stage microscopy (HSM)

Figure 6.26 shows the HSM images of the DMB·S-IBU recorded from 19.9 to 231.7 °C. The crystals, which are initially clear, display only decomposition upon heating. There is no bubbling, representing loss of water from the crystal. Thermal analysis as well as SCXRD showed that the water content in the crystal structure is very small, which is the likely reason that water loss is not observed in HSM. The only event observed was the decomposition that has an onset temperature of 154.5 °C.

Figure 6.26: HSM images of DMB·S-IBU crystals recorded from 19.9 to 231.7 °C, at 10 °C/min.

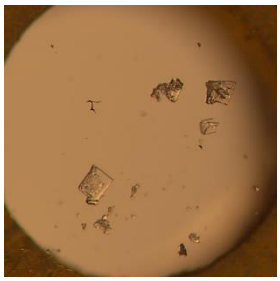

19.9 °C: Crystals at room temperature.

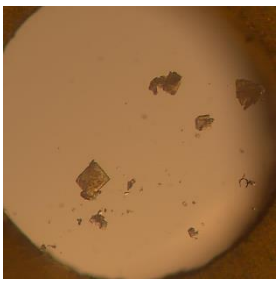

154.5 °C: The onset of decomposition.

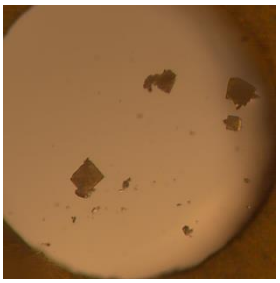

231.7 °C: Decomposition is complete.

6.7.4.2. Thermal gravimetric analysis (TGA) and differential scanning calorimetry (DSC)

Figure 6.27 shows the TGA (n = 2) and DSC curves of DMB·S-IBU crystals produced by co-precipitation. The TGA curve, recorded from 20 to 420 °C, indicates an average initial mass loss of 1.2 ± 0.1% which represents the dehydration of the crystal. This is equivalent to 1.03 ± 0.09 water molecules. The ^{1}H NMR findings and the TGA results together confirm that the inclusion complex possesses a 1:1:1 host:guest:water stoichiometric ratio. There is a second mass loss of 14.2 ± 0.2 % with an onset temperature of 177.1 °C. This is attributed to the loss of the S-IBU molecule upon heating (calculated mass loss 13.3%). There is a final mass loss with an onset temperature of 327.1 °C, which represents the decomposition of the host DMB.

The DSC curve, recorded from 20 to 350 °C, shows that there is a small endotherm present at 186 °C that coincides with the S-IBU mass loss. Multiple thermal events take place, two of which follow the second mass loss observed in the TGA. This complex series of endotherms would therefore represent the loss of S-IBU from DMB as well as possible phase changes that the crystal might have undergone following the loss of the guest. The run was terminated at 350 °C because of the risk of damaging the instrument by possible leakage of the hot material onto the DSC cell, a common problem with cyclodextrins and their inclusion complexes.

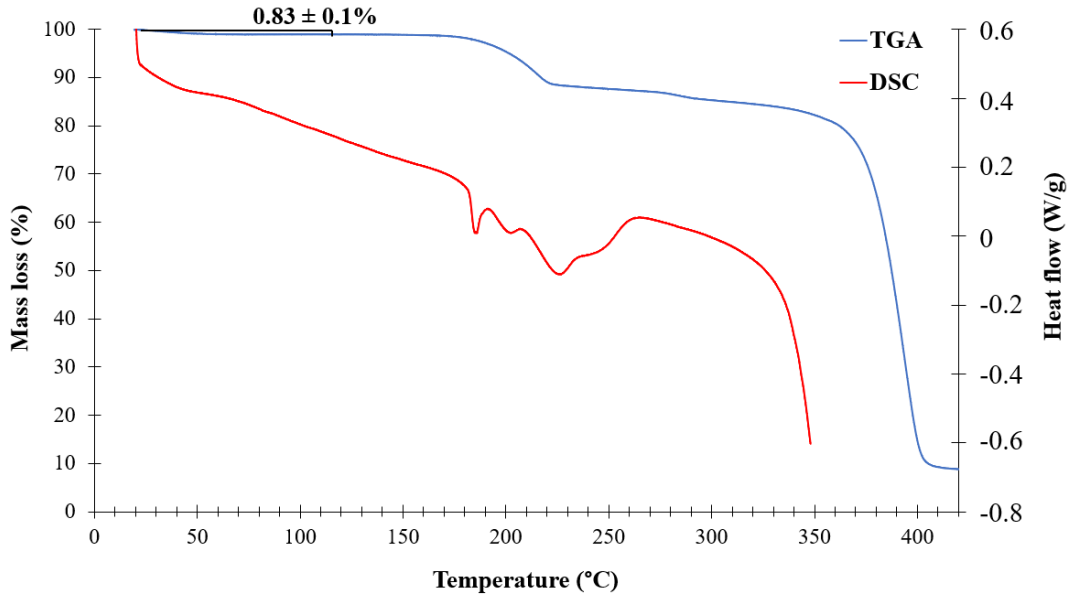

Figure 6.27: Representative TGA and DSC curves of DMB·S-IBU.

6.7.5. Crystal structure analysis

Data-collection and space group determination

The first intensity data were collected at 100(2) K. This revealed that the Laue symmetry of the intensity-weighted reciprocal lattice was 2/m and that the crystal system was monoclinic. Based on the systematic absences and the fact that the crystal contained chiral components, the space group was determined as *C*2, a result that was confirmed by the program XPREP.[13] (We note at this point that the crystal system and the unit cell parameters differ from those reported previously for a DMB·S-IBU complex.[8]). Because the first intensity dataset was less than satisfactory, multiple data-collections were recorded after the first with the aim of improving data quality. One full data-collection resulted in a unit cell with the dimensions a = 15.5939(8)Å, b = 21.3754(10)Å, c = 49.246(3)Å, $\alpha = 90°$, $\beta = 90°$, $\gamma = 90°$ and V = 16415(2) Å^3. However, the crystal structure could not be solved using these data. Data-collection was then repeated on a new crystal using CuKα_1 radiation, but the data capture was incomplete due to an insufficient nitrogen supply. Repeated attempts resulted in crystals displaying twinning, which could not be eliminated. Because all attempts to improve the data were unsuccessful, the first dataset collected was used and the results of the analysis are reported below. Figure 6.28 shows the numbering scheme used in the description of the crystal structure.

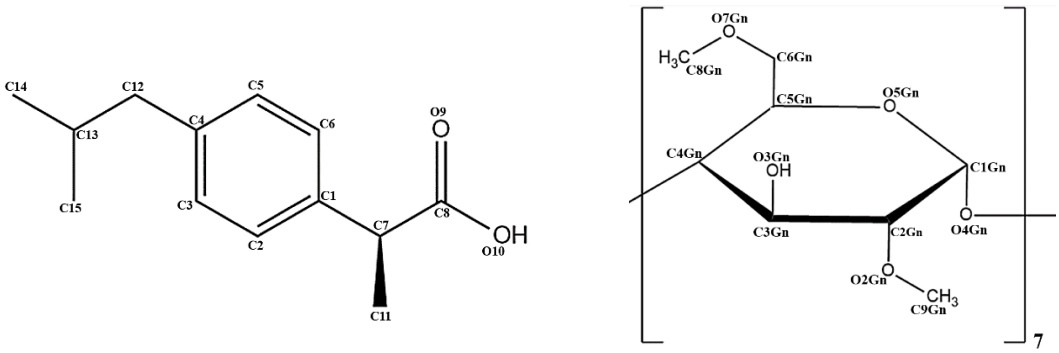

Figure 6.28: Numbering scheme of S-IBU (left) and DMB (right).

Structure solution and refinement

The crystal data and refinement parameters for the DMB·S-IBU structure are listed in Table 6.14. The new crystal form was designated as Form 2. Unfortunately, the intensity data were not of the highest quality, due to severe guest disorder. The structure was solved by direct methods using SHELXS-97,[10] the resulting E-map revealing peaks representing atoms of the host molecule relatively well.

These atoms were refined isotropically and thereafter anisotropically, except for atoms O7G1 and C8G1, which displayed excessive thermal motion and therefore isotropic refinement of these atoms was retained. Using the riding model, all H atoms were placed at appropriate positions that maximised intramolecular and intermolecular hydrogen bonding.

Table 6.14: Crystal data and refinement parameters for the DMB·S-IBU (Form 2) crystal structure.

Chemical formula	**$C_{56}H_{98}O_{35}\cdot C_{13}H_{18}O_2\cdot H_2O$**
Formula weight (g.mol^{-1})	1555.64
Temperature (K)	100(2)
Wavelength (Å)	0.71073
Crystal system	monoclinic
Space group	*C*2
a (Å)	56.6097(19)
b (Å)	15.2089(6)
c (Å)	9.8812(4)
α (°)	90
β (°)	90.061(1)
γ (°)	90
V (Å^3)	8423.4(6)
Z	4
Calculated density (g.cm^{-3})	1.225
μ (Mo Kα) (mm^{-1})	0.100
F(000)	3336
Crystal size (mm^3)	0.05 × 0.21 × 0.23
Range scanned θ (°)	$4.36 \leq 2\theta \leq 51.53$
Index ranges ±h, ±k, ±l	h:-68, 68; k:-18,18; l: -12,12
No. reflections (total)	68941
No. unique reflections	15947
No. of parameters	862
Goodness-of-fit, S	1.590
Final R indices R1, wR2, [I > 2σ(I)]	0.1332, 0.3596
R indices, all data (R1, wR2)	0.1466, 0.3730
Largest diff. peak and hole (e Å^{-3})	0.69, -1.07

Despite the fact that the intensity data had been collected at 100(2) K, modelling the S-IBU guest molecule was a significant challenge since the largest difference Fourier peaks within the DMB cavity had electron densities of only ~1 $eÅ^{-3}$, implying abnormally high thermal motion of the guest molecule as a whole, a not uncommon phenomenon in cyclodextrin complexes. In fact, the model of the guest was generally developed very gradually, atoms being added piecemeal with appropriate distance restraints to prevent their drifting to incorrect positions. Initially, six weak Δρ peaks that resembled a phenyl ring located near the centre of the DMB cavity were selected and modelled as a regular hexagon using the AFIX 66 command in SHELXL-97.[10] Thereafter, successive non-hydrogen atoms of the S-IBU molecule appeared and were assigned piecemeal to their respective Δρ peaks, until all were located in reasonable positions, effected by additional bond length restraints (final total 34). However, attempted individual isotropic or anisotropic refinement of the guest atoms was not feasible given the low electron densities of the guest atoms, and it was necessary to resort to a rather limited model involving refinement of these atoms with a common, constant isotropic thermal parameter (U_{iso} = 0.15 $Å^2$), effectively treating the whole guest molecule as a rigid body. Hydrogen atoms were placed using a riding model. Nonetheless, the mode of inclusion of the S-IBU molecule within the DMB was clearly evident and the extended packing arrangement could likewise be visualised.

There were three Δρ peaks present with low electron densities that were identified as oxygen atoms of partial water molecules with s.o.f.s less than one. Disorder of O1W and O3W was also evident from the O···O distance of only 2.04 Å. A common U_{iso} value was assigned to the three partial water oxygen atoms and this free variable refined to the somewhat unrealistic value of 0.35(3) $Å^2$ while their individual s.o.f.s. were allowed to refine freely to values < 1. The results are listed in Table 6.15. (It was clearly not possible to locate the hydrogen atoms on the partial water oxygen atoms and they were therefore omitted from the model). Based on the s.o.f. values below, the total water content is estimated as 1.71 H_2O molecules per complex unit. However, given the extremely low Δρ peak heights representing these partial water oxygen atoms, the reliability of this estimate is questionable. Instead, since the calculated value based on the more reliable TGA measurements yielded a total of 1.03 ± 0.09 water molecules per complex unit, the final stoichiometry of the DMB·S-IBU·water complex was designated as 1:1:1.

Table 6.15: The refined s.o.f.s and U_{iso} values of the water oxygen atoms based on their Δρ peaks.

Atom	s.o.f.	U_{iso} (Å^2)
O1W	0.740	0.35(3)
O2W	0.680	0.35(3)
O3W	0.290	0.35(3)

Molecular structure

Figure 6.29 is a stereoscopic view of the asymmetric unit of DMB·S-IBU, which consists of one molecule of each of the components DMB, S-IBU and water. Figure 6.29(a) shows the labelling scheme for the seven dimethylated glucose residues comprising the macrocyclic host and highlights the conformation adopted by the S-IBU molecule when it is encapsulated within the host cavity. From Figure 6.29(b) (a 'side-view') it is evident that the carboxylic acid group protrudes from the primary side of the DMB molecule. As detailed below, the -COOH group engages in hydrogen bonding with an oxygen atom of a neighbouring DMB molecule, this connection, together with a weaker (guest)C-H···O(guest carbonyl) interaction, resulting in an extended complex stacking motif.

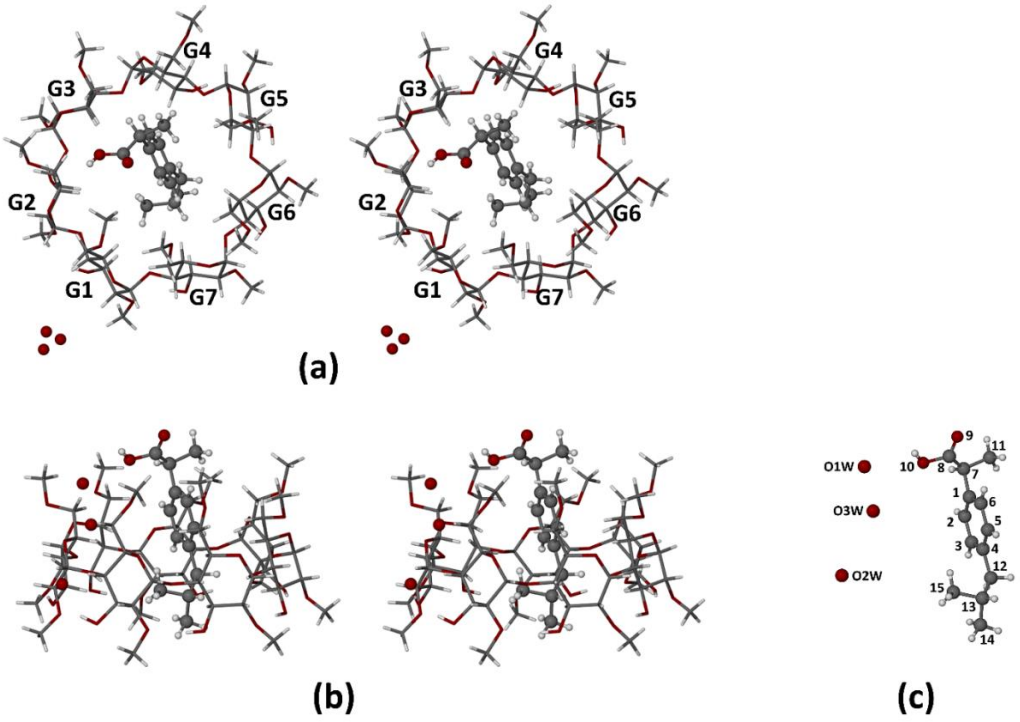

Figure 6.29: Stereoscopic diagrams of the ASU of DMB·S-IBU viewed (a) from the (narrow) primary side of the host molecule, (b) from the side; (c) is the numbering scheme for the S-IBU molecule and water oxygen atoms.

Hydrogen bonding

Both intra- and intermolecular hydrogen bonding occur in the crystal structure. Figure 6.30 shows a stereoview of a representative portion of the extended motif that results from the specific intermolecular H-bonding interactions referred to above, namely: (a) an intermolecular hydrogen bond O10-H10···O3G2[a] (a = x, y, 1 + z) that links the carboxyl group of S-IBU with atom O3G2 on the secondary rim of the DMB molecule located above it, and (b) an intermolecular C-H···O interaction, namely C15-H15C···O9[a] (a = x, y, 1 + z) that links the isopropyl group of the S-IBU molecule with the carbonyl group of a translated S-IBU molecule. The complex units are not aligned like 'coins in a roll'; instead, the stacking arrangement is such that there is a constant horizontal offset between successive units. Table 6.16 lists the intermolecular H-bonds between the DMB moieties, between DMB and S-IBU, and between symmetry-related S-IBU molecules.

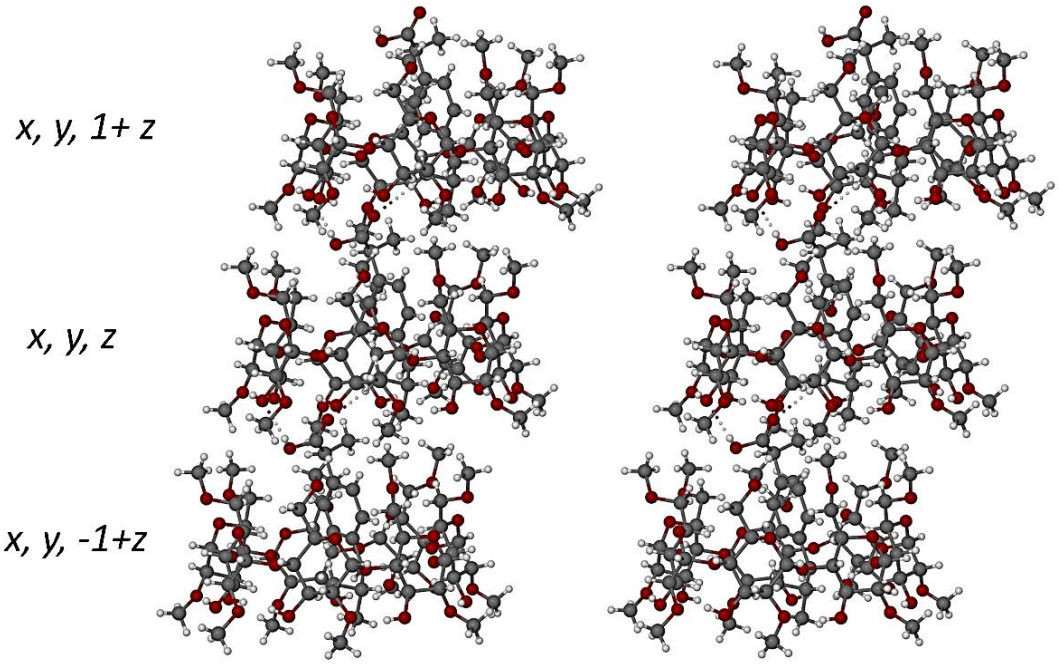

Figure 6.30: A stereoview highlighting the stacking of complex units in the crystal of DMB·S-IBU.

Table 6.16: Intermolecular hydrogen bonding in the crystal of DMB·S-IBU.

Hydrogen bond interaction	D-H (Å)	H···A (Å)	D···A (Å)	D-H···A (°)	Symmetry operation
O10-H10···O3G2	0.84	2.16	2.898(1)	146	x,y,1+z
C9G1-H9G2···O3G3	0.98	2.51	3.260(2)	133	x,-1+y,z
C2G2-H2G2···O5G2	1.00	2.54	3.404(1)	145	1-x,y,1-z
C8G4-H8G7···O5G7	0.98	2.58	3.121(1)	114	x,1+y,z
C2G5-H2G5···O7G6	1.00	2.56	3.474(1)	151	3/2-x,1/2+y,2-z
C2G6-H2G6···O5G5	1.00	2.56	3.548(1)	169	3/2-x,-1/2+y,2-z
C4G7-H4G7···O5G4	1.00	2.55	3.432(1)	148	x,-1+y,z

Figure 6.31 is a stereoscopic view of the DMB molecule from the (wider) secondary side, illustrating the well-known 'belt' consisting of seven intramolecular O-H···O hydrogen bonds that typically occur in this molecule. Each bond links a hydroxyl group O3Gn-H3Gn of one dimethylated glucose ring and the oxygen atom acceptor O2G(n+1) on the adjacent ring. This 'belt' is responsible for the 'round' shape of the macrocycle. All intramolecular bonds are listed in Table 6.17.

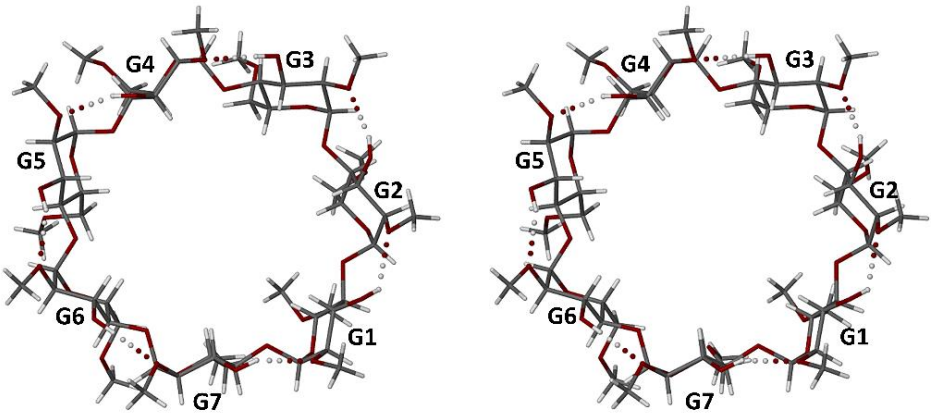

Figure 6.31: Stereoview of the intramolecular O-H···O hydrogen bonds which stabilise its 'round' shape.

Table 6.17: Intramolecular bonding occurring in the DMB molecule.

Hydrogen bond interaction	D-H (Å)	H···A (Å)	D···A (Å)	D-H···A (°)
O3G7-H3G7···O2G1	0.84	2.09	2.866(1)	153
O3G1-H3G1···O2G2	0.84	2.17	2.741(1)	125
O3G2-H3G2···O2G3	0.84	2.01	2.928(1)	156
O3G3-H3G3···O2G4	0.84	1.93	2.767(1)	174
O3G4-H3G4···O2G5	0.84	2.10	2.902(9)	160
O3G5-H3G5···O2G6	0.84	2.10	2.879(1)	155
O3G6-H3G6···O2G7	0.84	2.00	2.840(9)	173

Host molecular geometry

Despite the 'round' shape of the DMB molecule, maintained by the intramolecular O-H···O hydrogen bonds, the angles at which the seven glucose rings are tilted may vary over a considerable range. Generally, in an undistorted cyclodextrin molecule, all glucose rings will tend to tilt in such a way that their primary rims are inclined towards the seven-fold rotation axis of the molecule, while their secondary rims are inclined away from the axis, these features resulting in the 'truncated toroidal' shape of the molecule. However, on encapsulation of a guest molecule, the angles may adopt different values as the host and guest molecules simultaneously engage in an 'induced fit' inclusion mechanism. The various distortions of the host molecule that may occur upon guest inclusion can be quantified by calculating several well-established geometrical parameters,[14,15] which are defined as follows:

***l* (Å):** the distance of each glycosidic O4 atom from the centroid of the O4-heptagon;
D (Å): the glycosidic O4*n*···O4(*n*+1) distances;
Φ (°): the O4(*n*-1)···O4*n*···O4(*n*+1) angles;
d (°): the O4(*n*-1)···O4*n*···O4(*n*+1)···O4(*n*+2) torsion angles;
α (Å): the deviations of the glycosidic O4n atoms from their least-squares plane;
D_3 (Å): the inter-ring hydrogen bond O2(*n*)···O3(*n*-1) distances;
τ_2 (°): the tilt angle between the mean O(4) plane and the mean plane through the four pyranose ring atoms, namely O4, C4, C1 and O4′ of each glucose unit.

For convenience, the numbering of the atoms of a representative dimethylated glucose residue is shown in Figure 6.32, and the atom numbers highlighted in red refer to one of the planes involved in determining the tilt angle (τ_2) of the ring.

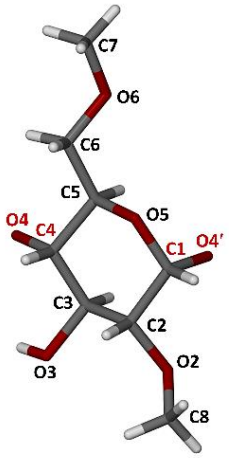

Figure 6.32: Atom numbering of the 2,6-dimethylated unit in DMB.

Table 6.18 lists the calculated geometrical parameters defining the conformation of the DMB molecule.

Table 6.18: Geometrical parameters of the DMB molecule in the complex DMB·S-IBU.

Residue	*l* (Å)	D (Å)	Φ (°)	d (°)	α (Å)	D_3 (Å)	τ_2 (°)
G1	5.043	4.469	129.4	-10.6	-0.079(5)	2.866(12)	12.5(3)
G2	5.022	4.254	127.3	6.2	-0.127(5)	2.741(12)	10.6(3)
G3	4.930	4.419	130.0	4.8	0.186(5)	2.799(11)	14.2(2)
G4	5.004	4.249	129.4	-8.2	0.007(5)	2.767(11)	-10.0(2)
G5	5.130	4.361	124.3	1.4	-0.169(4)	2.902(9)	16.4(4)
G6	4.848	4.467	133.8	3.1	0.081(5)	2.879(10)	15.8(4)
G7	5.112	4.260	124.7	3.2	0.100(5)	2.840(9)	9.0(3)

The values for the first three parameters in Table 6.18, namely *l*, D and Φ, span fairly narrow ranges, reflecting the relatively small distortions of the O4-heptagon and hence the 'roundness' of the DMB macrocycle. Some variation in the torsion angle parameter d indicates a slight pucker in the O4-heptagon, which is also reflected in the range of O4-atom deviations from their mean plane, the maximum being ~0.2 Å. Six of the seven tilt angles (τ_2) of the glucose rings span the fairly narrow

range 9.0(3) - 16.4(4)°, the seventh, that for G4, being negative, indicating that the secondary rim (rather than the primary rim) of this unit is inclined towards the centre of the cavity.

Crystal packing

Figure 6.33 shows the packing of the DMB·S-IBU complex units in the monoclinic crystal. The view direction is approximately perpendicular to the macrocyclic DMB rings and in projection there is considerable overlap of the DMB molecules, owing to their 'offset' stacking illustrated previously in the motif of Figure 6.30 above. Clearly evident is the twofold symmetry of the structure, the left half of the unit cell content being related to that on the right by the central vertical diad (not shown) parallel to the *b*-axis. An interesting feature is revealed in this projection, namely the presence on the diad of successive voids in which the disordered components of the water molecule are accommodated.

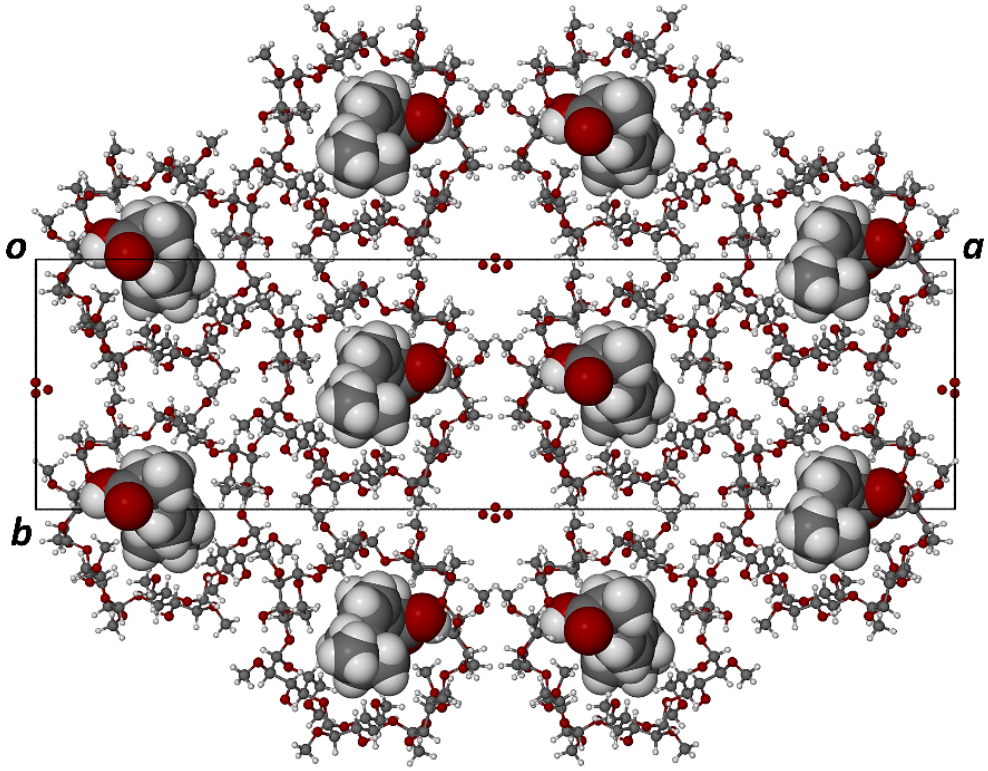

Figure 6.33: The [010] projection of the packing arrangement of the complex crystallizing in the monoclinic space group *C*2.

6.7.6. Fourier-transform infrared (FT-IR) spectroscopy

Figure 6.34 shows the FT-IR spectra of the starting materials DMB and S-IBU, as well as those of the products obtained by kneading and co-precipitation. The broad peak present at 3450 cm^{-1} represents the water present in DMB and in the products. There is a shift in the carbonyl stretching frequency from 1699 cm^{-1} in pure S-IBU to 1724 cm^{-1} when it is incorporated in the inclusion complex. This indicates that the extent of hydrogen bonding by the C=O group is reduced on inclusion of DMB relative to that in the uncomplexed acid. This is easily rationalised as it was indicated in Figure 6.30 that the C=O group in the complex is involved in only a relatively weak C-H···O=C interaction in the DMB·S-IBU complex, whereas in pure S-IBU (CSD refcode JEKNOC), carboxylic acid dimer formation results in very strong O-H···O hydrogen bonding, with O···O ~2.65 Å. Analogous results were recently reported for the inclusion of the antiepileptic drug valproic acid in its inclusion complex with DMB,[16] where ν(C=O) was found to shift from 1702 cm^{-1} in the pure acid to 1731 cm^{-1} in the complex.

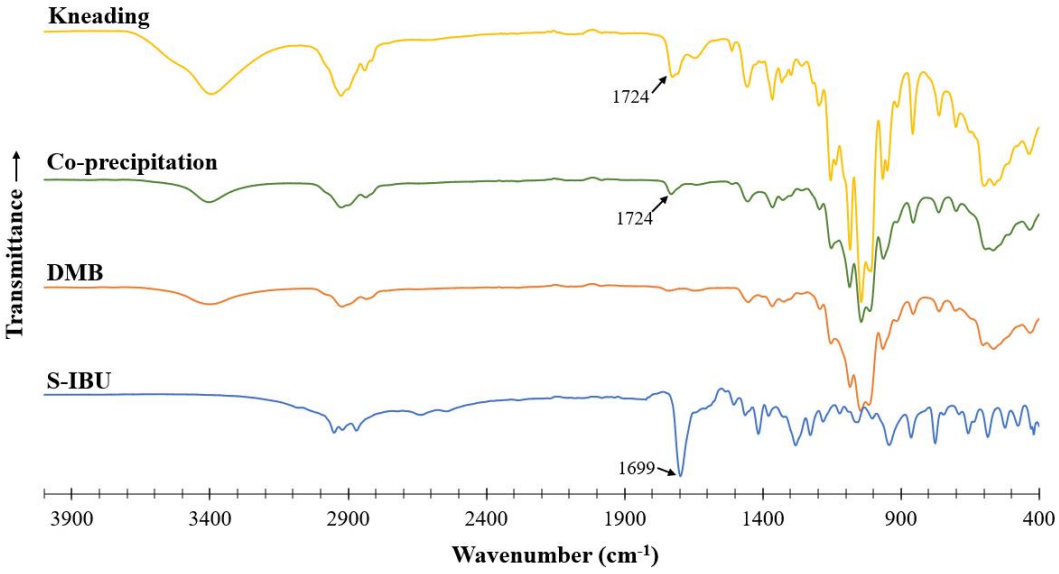

Figure 6.34: Stacked FT-IR spectra of S-IBU, DMB and the products obtained by kneading and co-precipitation.

6.7.7. Comparative powder X-ray diffraction (PXRD) pattern

The PXRD pattern of the co-precipitation product is seen in Figure 6.35. Because of the poor crystallinity of the recorded sample, the pattern was calculated using a peak width of '5' units, instead of the usual value of '2'. The resulting pattern has a slight correlation with the dry product, with a

discrepancy at low angles. When the inclusion complex is removed from the mother liquor the water that is part of the complex may leave the complex and cause changes in the experimental pattern. This is plausible as TGA analysis indicates that the onset of decomposition occurs at 30.4 °C. To combat this, the crystals were finely ground which resulted in a PXRD pattern which resembled that of an amorph. The ground product was then wetted with a small amount of water in an attempt to restore its crystallinity. However, due to the abnormally high solubility of the amorphous product, it readily dissolved. A large amount of product was therefore prepared and the PXRD pattern of the moistened product recorded. The PXRD pattern produced was slightly more crystalline than that of the dry sample, but it still did not match the calculated pattern.

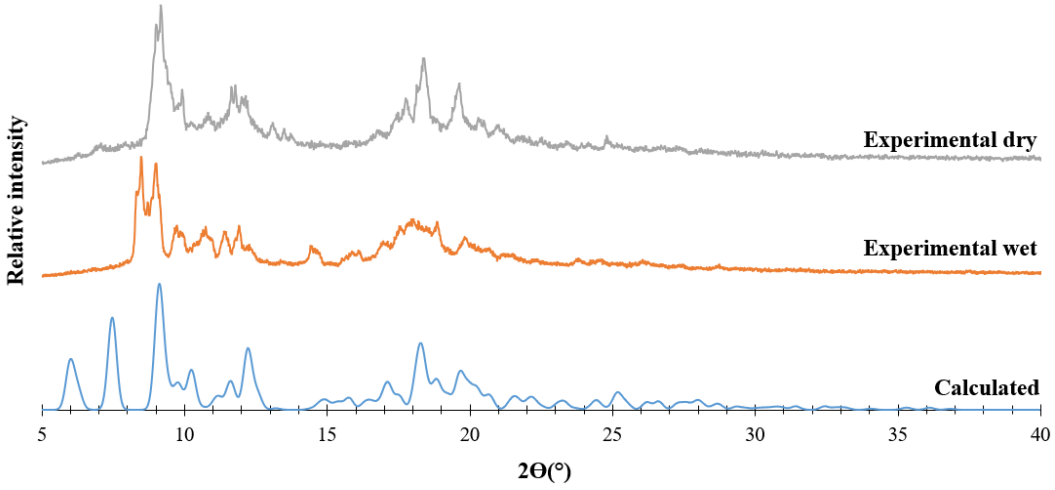

Figure 6.35: The experimental and calculated PXRD patterns of DMB·S-IBU.

6.7.8. Comparison of Forms 1 and 2 of the DMB·S-IBU·H_2O complex.

All of the above documented physicochemical characterization referred to the monoclinic form of the complex discovered by the present author of this work, this form being designated Form 2, to distinguish it from the orthorhombic modification, 'Form 1', reported previously.[8] It was stated above that in Form 2 there is a motif consisting of stacked complex units that are offset from one another (Figure 6.30) and that the crystal structure of Form 2 (space group *C*2) is based on the packing of these motifs in a specific manner (Figure 6.33). On inspection of the crystal structure of Form 1, it was found that the mode of inclusion of the S-IBU molecule is similar to that in Form 2, and furthermore, that an analogous complex stacking motif with regular offsets occurs. However, the Form 1 (space group $P2_12_12_1$) motif differs in detail and the result is that its overall crystal packing is different from that of Form 2. This is shown in Figure 6.36 below. Whereas the complex units in

the Form 1 structure are spatially related by three mutually perpendicular twofold screw-axes, the Form 2 assembly is based on twofold rotation axes only. Given that the complexes have essentially the same chemical composition, one could refer to them as 'polymorphs'.

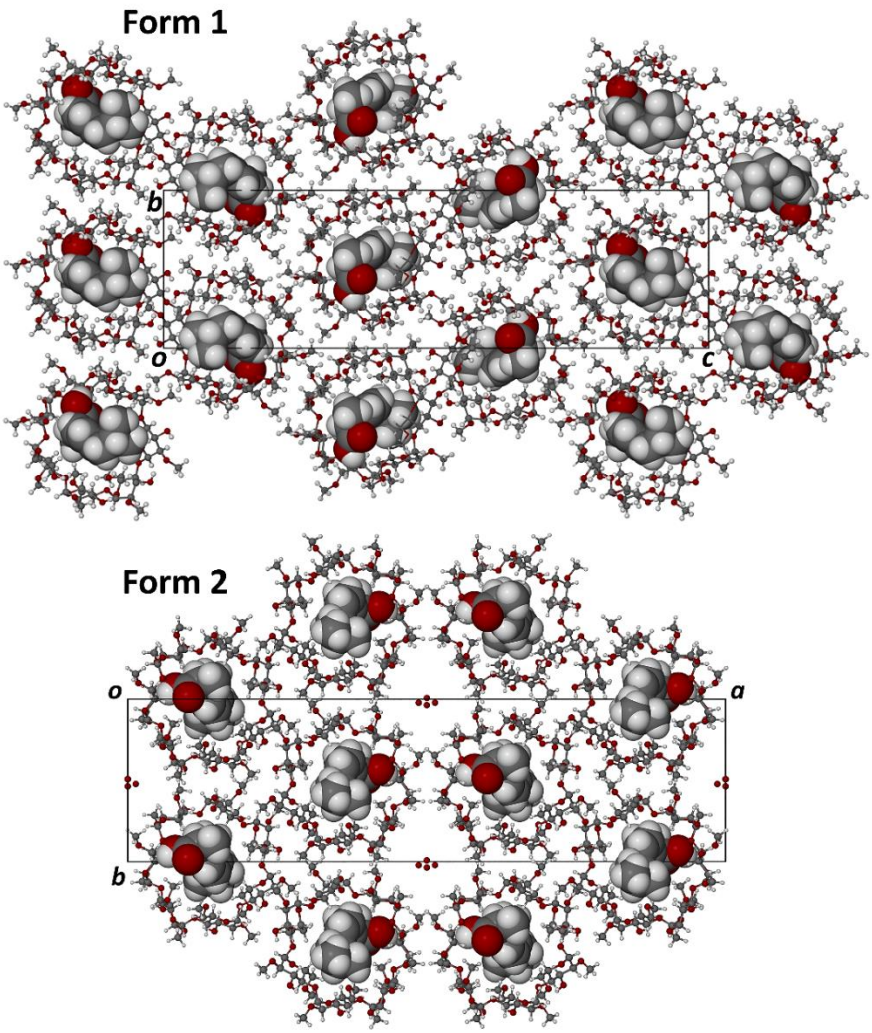

Figure 6.36: Scaled packing diagrams viewed approximately perpendicular to the planes of the respective DMB macrocycles: Form 1 ($P2_12_12_1$) viewed along the *a*-axis (~10.8 Å) and Form 2 ($C2$) viewed approximately along the *c*-axis (~9.9 Å).

6.7.9. Solubility study

The solubility was determined by gravimetric analysis in FaSSIF medium at pH 6.5 using the method described in Chapter 2 (2.6.2. Gravimetric solubility studies, pg. 29). When incorporated in the inclusion complex, there is a 1.28-fold increase in the S-IBU concentration in FaSSIF (Table 6.19).

Since the previously reported form of the complex (Form 1) could not be reproduced, its solubility remains unknown, but given some structural similarities with Form 2, its solubility is not expected to be radically different.

Table 6.19: Concentration of S-IBU on its own and when included in DMB·S-IBU in FaSSIF (pH 6.5)

Sample	Concentration (mg/ml)
S-IBU	1.21 ± 0.3
DMB·S-IBU	2.13 ± 0.3
Solubility enhancement factor	1.28 ± 0.3

* The mass fraction of S-IBU in the product DMB·S-IBU is 0.13 which was considered when calculating the final concentrations.

References

1. Rainsford, K., Ibuprofen: pharmacology, efficacy and safety. *Inflammopharmacology* **2009,** *17*, 275-342.
2. Ma, D.; Pei, T.; Bai, Y.; Zhou, L.; Bao, Y.; Yin, Q.; Xie, C., Salts formation between ibuprofen and pyridine derivatives: Effect of amino group on supramolecular packing and proton transfer. *Journal of Molecular Structure* **2019,** *1179*, 487-494.
3. Geisslinger, G.; Stock, K.-P.; Bach, G.; Loew, D.; Brune, K., Pharmacological differences between R (−)-and S (+)-ibuprofen. *Agents and Actions* **1989,** *27*, 455-457.
4. Bushra, R.; Aslam, N., An overview of clinical pharmacology of Ibuprofen. *Oman Medical Journal* **2010,** *25* (3), 155.
5. Kim, J. H.; Scialli, A. R., Thalidomide: the tragedy of birth defects and the effective treatment of disease. *Toxicological Sciences* **2011,** *122* (1), 1-6.
6. Ridings, J. E., The thalidomide disaster, lessons from the past. *Teratogenicity Testing: Methods and Protocols* **2013**, 575-586.
7. Evans, A. M., Comparative pharmacology of S (+)-ibuprofen and (RS)-ibuprofen. *Clinical Rheumatology* **2001,** *20*, 9-14.
8. Ramulumo, H.S., "Co-crystallization and Cyclodextrin Inclusion Complexation for Beneficiation of Medicinal Agents and Other Bioactive Compounds". Chemistry Honours Project, Department of Chemistry, University of Cape Town: Cape Town, **2019** (unpublished).
9. Macrae, C. F.; Sovago, I.; Cottrell, S. J.; Galek, P. T.; McCabe, P.; Pidcock, E.; Platings, M.; Shields, G. P.; Stevens, J. S.; Towler, M., Mercury 4.0: From visualization to analysis, design and prediction. *Journal of Applied Crystallography* **2020,** *53* (1), 226-235.
10. Sheldrick, G. M., A short history of SHELX. *Acta Crystallographica Section A: Foundations of Crystallography* **2008,** *64* (1), 112-122.
11. Frösler, H. M.; Ramulumo, H. S.; Edmonds-Smith, C.; Caira, M. R., Salts of S-(+)-Ibuprofen Formed via Its Reaction with the Antifibrinolytic Agents Aminocaproic Acid and Tranexamic Acid: Synthesis and Characterization. *Crystals* **2023,** *13* (8), 1222.
12. Bavishi, D. D.; Borkhataria, C. H., Spring and parachute: How cocrystals enhance solubility. *Progress in Crystal Growth and Characterization of Materials* **2016,** *62* (3), 1-8.
13. XPREP *Data Preparation and Reciprocal Space Exploration*, 2008/2; Bruker Analytical X-Ray Systems: **2008**.
14. Atwood, J.; Davies, J.; MacNicol, D., Academic Press: London, 1984; Vols. 1-3. Oxford University Press: Oxford, UK: 1991; pp 4-5.

15. Harata, K., Structural aspects of stereodifferentiation in the solid state. *Chemical Reviews* **1998,** *98* (5), 1803-1828.
16. Vicatos, A.I; Caira, M.R., Cyclodextrin complexes of the anticonvulsant agent valproic acid. *CrystEngComm* **2021,** *23* (37), 6582-6590.

Chapter 7: Conclusions and future work

The author successfully synthesised a new ionic co-crystal containing fenbufen and isonicotinamide (FEN-ISN), and the metal salts of fenbufen, $Fen^{-}Na^{+}$ and $Fen^{-}K^{+}$. Using the neutral and ionised forms of fenbufen, GCD·FEN, GCD·$Fen^{-}Na^{+}$, and BCD·$Fen^{-}Na^{+}$ were successfully synthesised, all with 1:1 stoichiometry, and characterised. New 'drug-drug' salts of S-(+)-ibuprofen, namely $(S\text{-}IBU)^{-}(ACA)^{+}$ and $(S\text{-}IBU)^{-}(TXA)^{+}$, as well as an inclusion complex DMB·S-IBU, were synthesised and comprehensively characterised.

Fenbufen

Co-crystal formation with fenbufen was attempted using 19 coformers, of which only one was successful. Co-precipitation experiments generally resulted in fenbufen crystallising out while the coformer remained in solution. This indicates that in the solvents selected as co-precipitation media, fenbufen had a lower solubility compared to that of the coformer. The only successful multicomponent compound isolated was FEN-ISN, a hydrated ionic co-crystal, which has a very unusual composition and interesting structural features. The inability to recover the previously synthesised 1:1 anhydrous co-crystal of FEN and ISN may have resulted from the presence of atmospherically-absorbed water in the recrystallization solvent. Water molecules increase the opportunities for strong intermolecular hydrogen bonding, thus increasing the stability of the hydrated 2:3 salt. The proton transfer leading to salt formation would also increase the possibility of charge-assisted hydrogen bond formation, thus rendering this structure more favourable than that of the co-crystal. The observed proton transfer from a FEN molecule to a coformer molecule is consistent with the ΔpKa [ΔpKa = pKa(base) - pKa(acid)] rule, since the calculated ΔpKa value exceeds 3 (ΔpKa = 13.39 - 4.22). The recorded 24-fold increase in the aqueous solubility of FEN as a result of FEN-ISN salt formation is significant, but in vivo testing would be required to determine whether this might translate into an increase in the bioavailability of the API.

The synthesis of cyclodextrin inclusion complexes of neutral fenbufen also proved to be challenging. The only complex that was successfully synthesised was GCD·FEN which, however, could not be isolated in the form of single crystals. Nevertheless, a definitive formula for the complex was established and since the low toxicity of GCD renders it favourable as a vehicle for drug delivery, in vivo study of the complex is warranted.

Phase solubility studies with FEN indicated that its solubility in solutions of selected CDs decreases in the CD order RAMEB > SBEBCD > HPBCD > GCD. The low value of the stability contant (K_s) obtained for the GCD complex may be the reason that obtaining a single crystal was challenging. The significant solubility increases for FEN observed with the host compounds RAMEB, SBEBCD and HPBCD indicate that alternative drug delivery systems using these CDs may be worth further investigation. These CDs may also mask the included FEN molecule effectively and thereby mitigate the gastrointestinal injury that this NSAID is known to cause.

The observed lack of affinity of FEN for cyclodextrins and GRAS coformers may be explained by its poor wettability and low aqueous solubility. This was evident while attempting various syntheses with this API. Due to these challenges, the ionised forms of FEN were explored, resulting in the successful syntheses of Fen^-Na^+ and Fen^-K^+. These new salts showed significant increases in their aqueous solubilities relative to that of FEN. Using Fen^-Na^+, further increases in aqueous solubility were effected when complexed with CDs to form BCD·Fen^-Na^+ and GCD·Fen^-Na^+, which also represent potential alternative drug delivery systems for FEN.

S-(+)-ibuprofen

Of the 13 coformers and 4 zwitterions tested for possible co-crystallization with S-IBU, only 6-aminocaproic acid and tranexamic acid formed new products, namely the salts $(S\text{-}IBU)^-(ACA)^+$ and $(S\text{-}IBU)^-(TXA)^+$. The coformers ACA and TXA are antifibrinolytic drugs which are beneficial for their clotting abilities and they therefore have potential to reduce the negative side effects of gastric ulceration caused by S-IBU. Dynamic solubility studies showed that dissolution of the salts did not behave according to the 'spring and parachute' mechanism. Although they appeared to produce a relatively poor increase in aqueous solubility, the new salts have increased thermal stability, as indicated by their melting points which are significantly higher than that of S-IBU.

Finally, extensive attempts to recover a previously reported cyclodextrin inclusion complex, DMB·S-IBU (Form 1, space group $P2_12_12_1$), were unsuccessful. Instead, a new polymorph of the inclusion complex, designated Form 2 (space group $C2$), was discovered. Its full structural characterization revealed that, while the guest inclusion mode was very similar to that in the Form 1 complex, the packing arrangements of the two complexes differed significantly. The new polymorph was found to enhance the solubility of S-IBU by a modest factor of 1.28.

In summary, the aims and objectives of this project were duly fulfilled with the successful isolation and physicochemical characterisation of numerous new solid phases of the two APIs, fenbufen and S-(+)-ibuprofen, several of which show enhanced pharmaceutically relevant properties and hence potential for further development as alternative candidates for the delivery of the APIs.

Future work

It would be appropriate to conduct dynamic solubility studies with FEN-ISN and S-IBU salts in an aqueous medium at different pH values to try to optimise the conditions for its dissolution.

To increase the potential for co-crystal formation between the APIs and GRAS coformers, an obvious strategy would be to increase the number of solvents for LAG and co-precipitation experiments. This strategy would also be suitable in future attempts to reproduce the previously reported 1:1 co-crystal of FEN and ISN, for which accurate solubility data are not available.

More attempts to isolate single crystals of $Fen^{-}K^{+}$, GCD·$Fen^{-}Na^{+}$, GCD·FEN for full structural characterization are desirable. Improvements in the crystal quality of BCD·$Fen^{-}Na^{+}$ and DMB·S-IBU are also desirable in order to obtain more accurate structural parameters for these compounds via SCXRD. Finally, an alternative analytical technique should be used to quantify the metal content in the sodium and potassium salts of fenbufen.

Appendix

Section 1: Chapters 3 and 4

1.1. NMR spectra of fenbufen salts

1.1.1. ^{1}H NMR stacked spectra of $Fen^{-}Na^{+}$ and fenbufen.

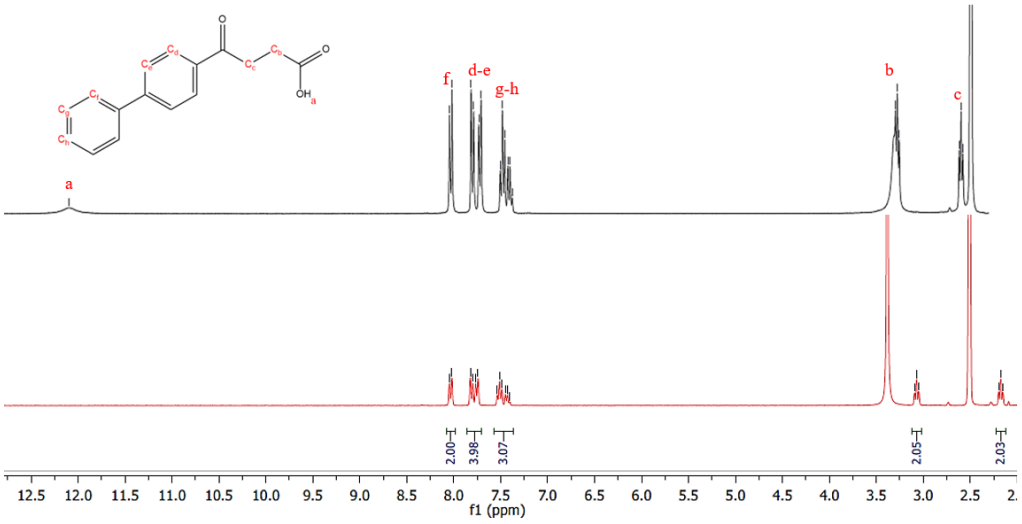

1.1.2. ^{1}H NMR stacked spectra of $Fen^{-}K^{+}$ and fenbufen.

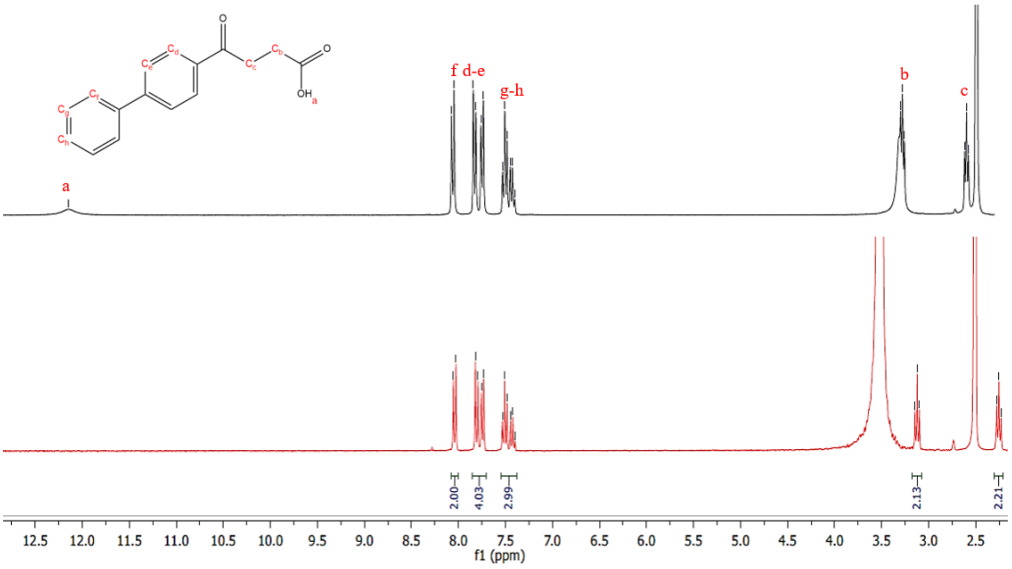

1.2. Stoichiometric determination of BCD·$Fen^{-}Na^{+}$ and GCD·$Fen^{-}Na^{+}$.

1.2.1. ^{1}H NMR spectrum of BCD·Fen^{-}Na^{+}.

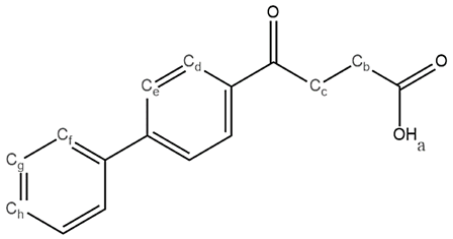

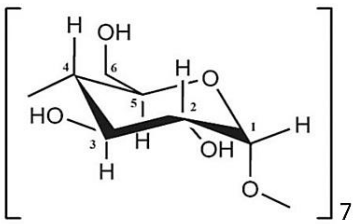

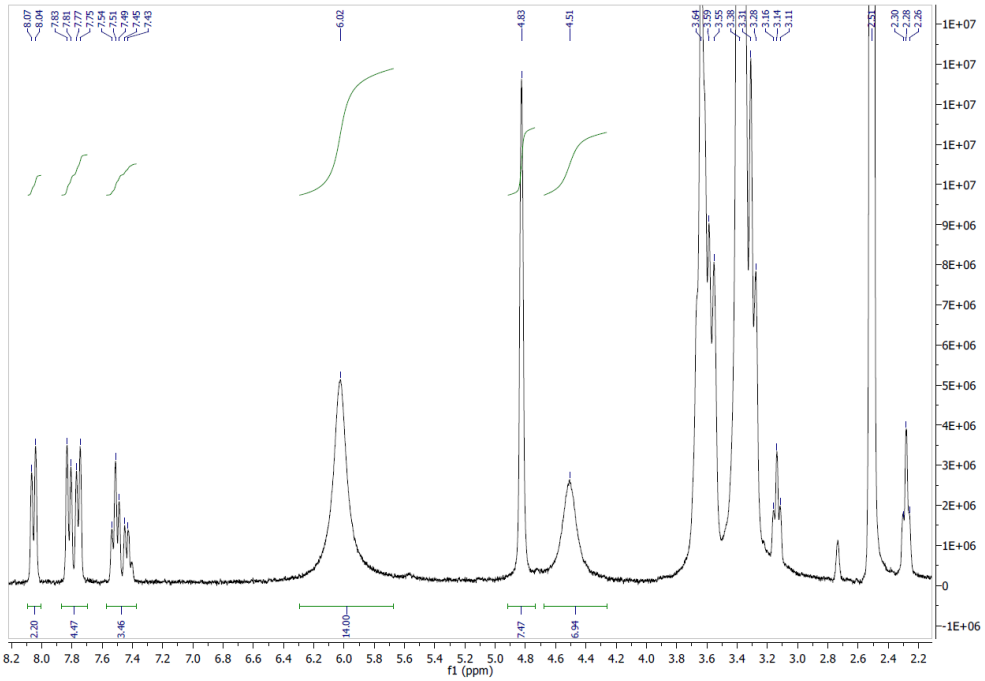

1.2.2. ^{1}H NMR spectrum of GCD·Fen$^{-}Na^{+}$.

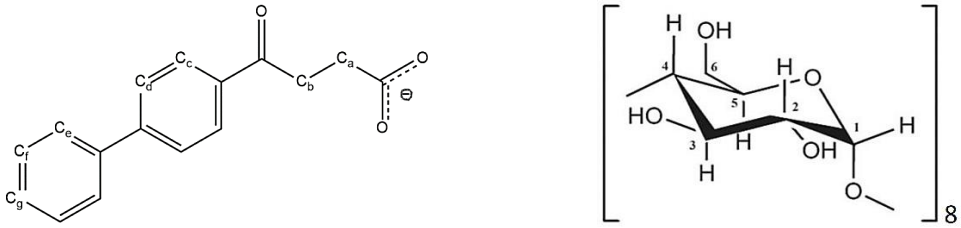

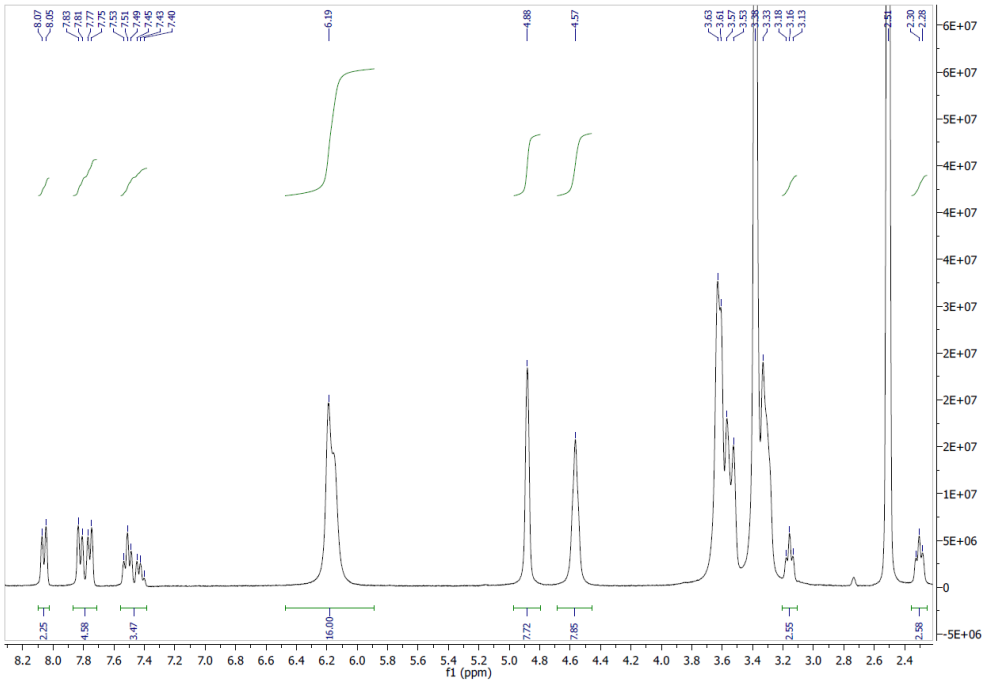

1.3. Standard curves and solution preparation methods

1.3.1. Solubility of Fenbufen salts

To determine the concentration of $(FEN)^-$ in the solubility study of Fen^-Na^+, a 4.102 mM standard solution of the salt was prepared in a pH 8.5 phosphate buffer. The solution was diluted using water accordingly and quantified using HPLC.

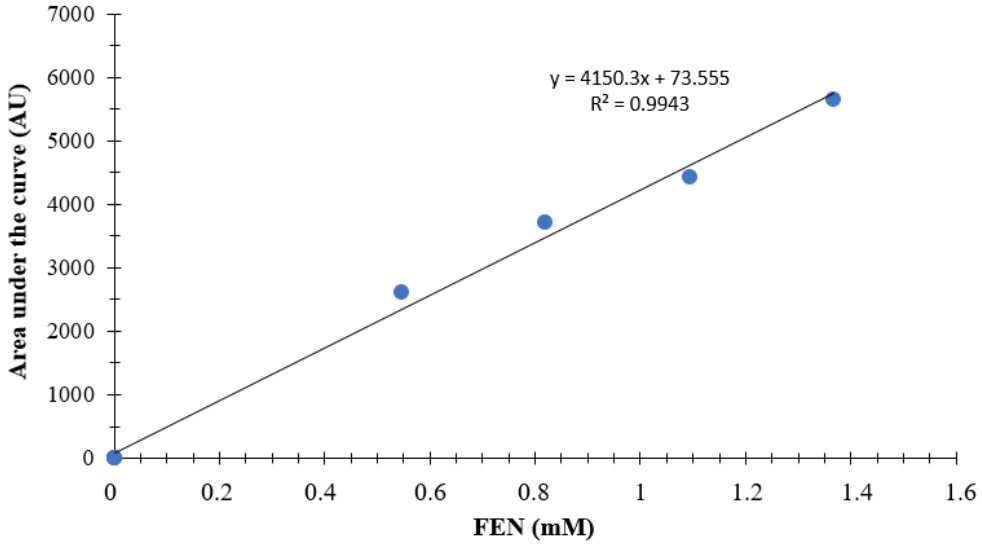

Figure 1.3.1: Standard curve produced by HPLC used for the quantification of FEN, Fen^-Na^+, Fen^-K^+, $BCD{\cdot}Fen^-Na^+$ and $GCD{\cdot}Fen^-Na^+$

Table 1.3.1: HPLC measurements of $(FEN)^-$ concentrations.

Compound	Area under the curve (AU) – 1	Area under the curve (AU) - 2	Average AU	Final $(FEN)^-$ concentration (mM)
Fen^-Na^+	8572.2	8572.78	8572.49	7.7
$BCD{\cdot}Fen^-Na^+$	10102.8	9692.39	9897.6	88.8
Fenbufen	76.6293	75.0056	75.8175	0.002
$GCD{\cdot}Fen^-Na^+$	1458.58	1473.28	1465.93	12.6
Fen^-K^+	9949.63	9449.16	9699.4	87.0

1.3.2. Phase solubility standard curve and solution preparation

Fenbufen standard curve, used for phase solubility study, produced by UV-Vis spectroscopy and measured at 283 nm. The standard solution was prepared by dissolving a known amount of FEN in 10.0 ml EtOH. The standard solution was serially diluted using the appropriate volume of water to ensure that the final solutions contained 2% EtOH. The FEN concentration in each solution was quantified using UV-Vis spectroscopy (measured at 283 nm).

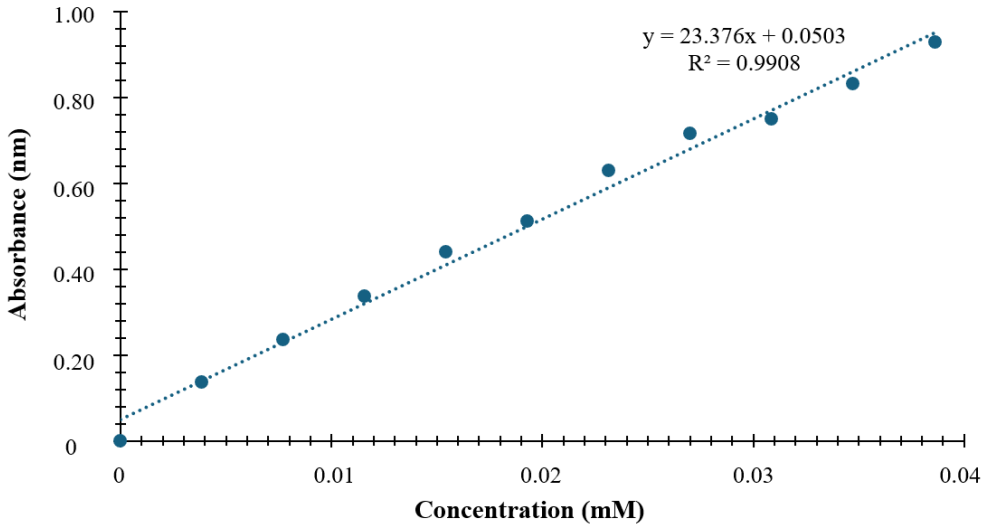

Figure 1.3.2. Standard curve produced with UV-Vis spectroscopy at 283 nm.

1.4. Calculation of the number of water molecules in fenbufen salts and cyclodextrin inclusion complexes:

Fen$^-$Na$^+$ - 23.6 ± 0.3% mass loss

$$0.233 = \frac{18.016n}{18.016n + 22.989 + 253.278}$$

4.198n + 5.356 + 59.014 = 18.016n

13.818n = 64.37

n = 4.658

$$0.239 = \frac{18.016n}{18.016n + 22.989 + 253.278}$$

4.306n + 5.494 + 60.533 = 18.016n

13.710n = 66.027

n = 4.816

4.7 ± 0.1 water molecules per fenbufen molecule.

Fen$^-$K$^+$ - 19.7 ± 0.2% mass loss

$$0.195 = \frac{18.016n}{18.016n + 39.098 + 253.278}$$

3.513n + 7.624 + 49.389 = 18.016n

14.503n = 57.013

n = 3.93

$$0.199 = \frac{18.016n}{18.016n + 39.098 + 253.278}$$

3.585n + 7.781 + 50.402 = 18.016n

14.431n = 58.183

n = 4.03

3.98 ± 0.05 water molecules per fenbufen molecule.

BCD·Fen$^-$Na$^+$ - 8.2 ± 0.6% mass loss

$$0.076 = \frac{18.016n}{18.016n + 22.989 + 1134.987 + \ 253.278}$$

1.369n + 1.747 + 86.259 + 19.249 = 18.016n

16.647n = 107.255

n = 6.44

$$0.088 = \frac{18.016n}{18.016n + 22.989 + 1134.987 + \ 253.278}$$

1.585n + 2.023 + 99.879 + 22.288 = 18.016n

16.431n = 124.19

n = 7.56

7 ± 0.56 water molecules per BCD molecule.

GCD·Fen$^-$Na$^+$ - 11.1 ± 0.1% mass loss

$$0.110 = \frac{18.016n}{18.016n + 22.989 + 1297.1 + \ 253.278}$$

1.982n + 2.529 + 142.681 + 27.861 = 18.016n

16.034n = 173.071

n = 10.79

$$0.112 = \frac{18.016n}{18.016n + 22.989 + 1297.1 + \ 253.278}$$

2.018n + 2.575 + 143.259 + 28.367 = 18.016n

15.998n = 174.201

n = 10.89

10.8 ± 0.1 water molecules per GCD molecule.

1.5. PXRD patterns

1.5.1. Calculated PXRD pattern of $Fen^{-}Na^{+}$

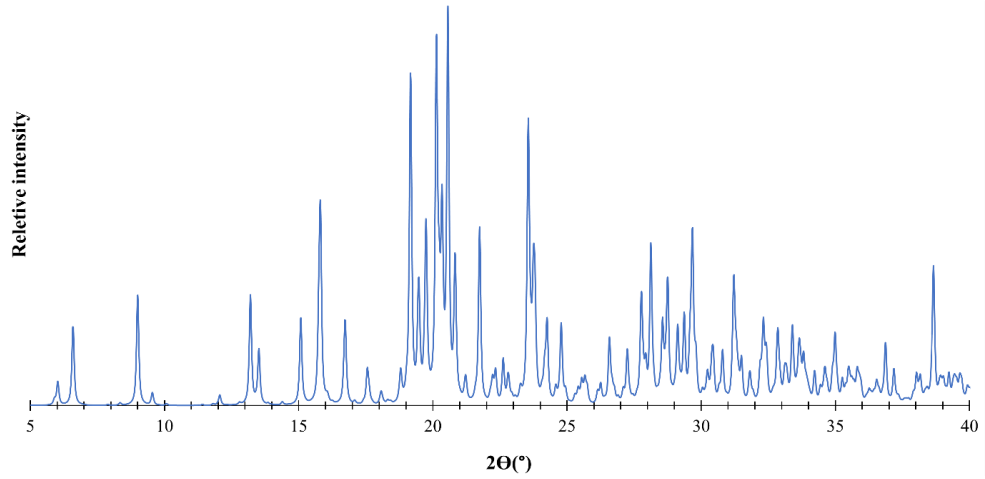

Figure 1.5.1: Calculated PXRD pattern of $Fen^{-}Na^{+}$.

1.5.2. PXRD patterns of co-precipitation products with fenbufen and cyclodextrins

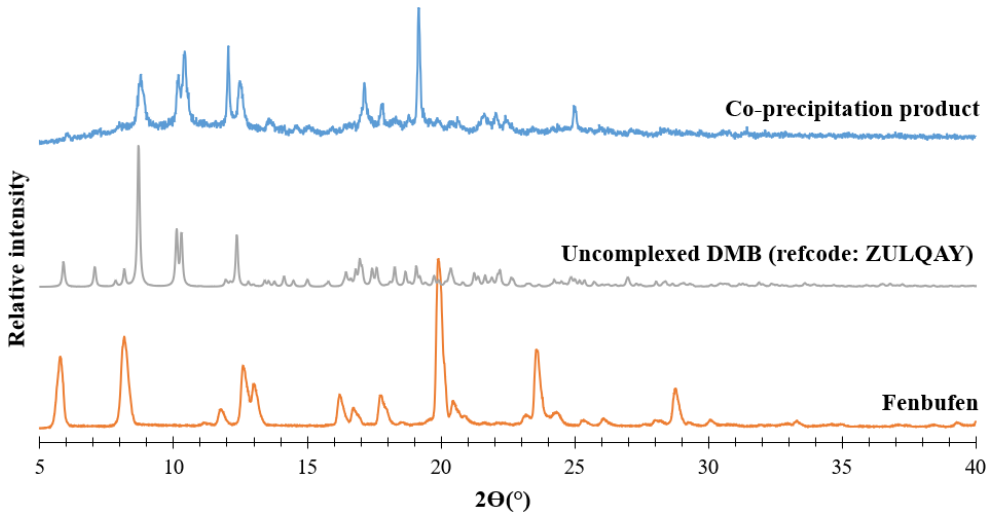

Figure 1.5.2.1: PXRD patterns of the starting materials FEN and uncomplexed DMB (refcode: ZULQAY) and their co-precipitation product.

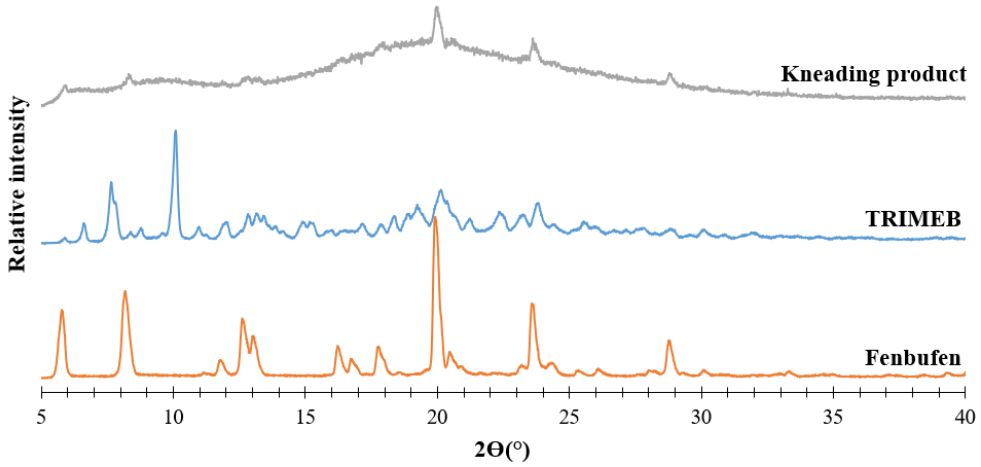

Figure 1.5.2.2.: PXRD patterns of the starting materials FEN and uncomplexed TRIMEB and the product obtained from kneading.

Section 2 - Chapter 5

2.1. PXRD patterns of LAG and co-precipitation experiments with fenbufen and coformers

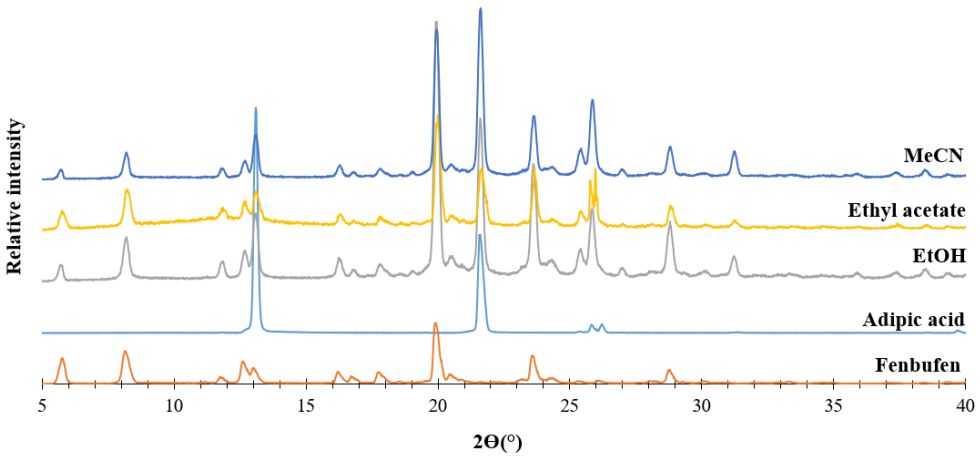

Figure 2.1.1: PXRD patterns of the starting materials FEN and adipic acid and those of the products following LAG experiments using the solvents indicated.

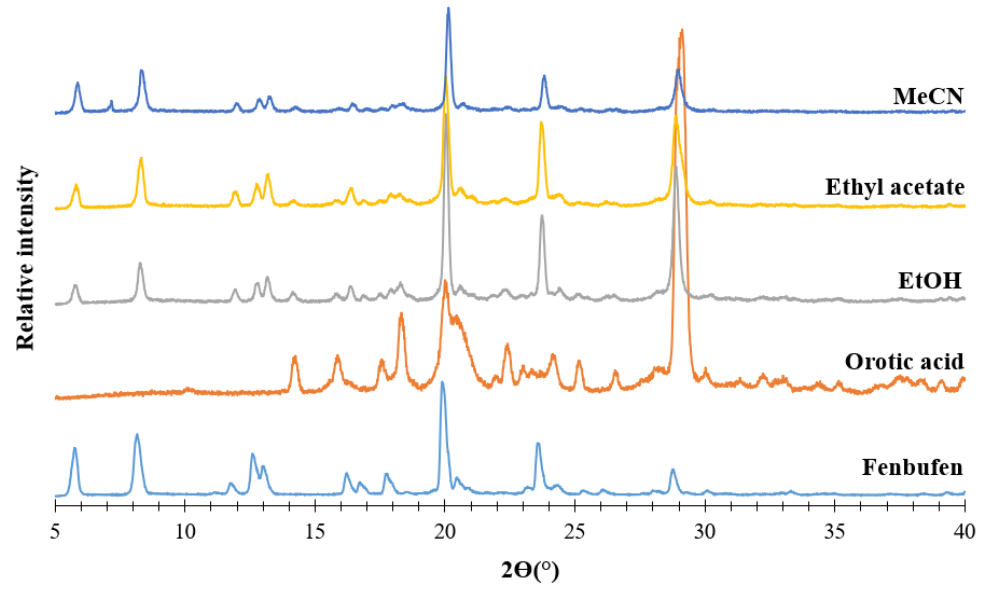

Figure 2.1.2: PXRD patterns of the starting materials FEN and orotic acid and those of the products following LAG experiments using the solvents indicated.

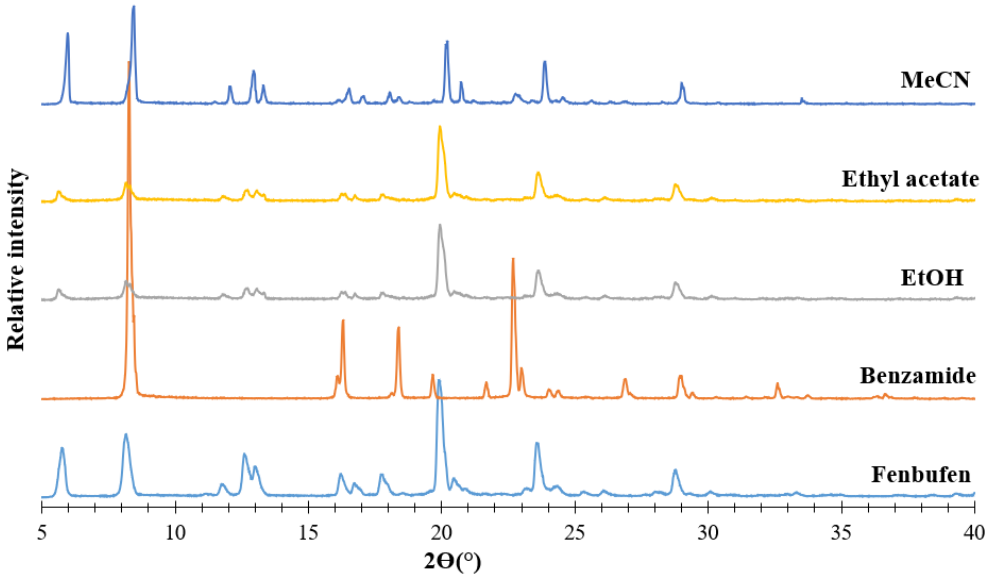

Figure 2.1.3: PXRD patterns of the starting materials FEN and benzamide and those of the products following co-precipitation experiments using the solvents indicated.

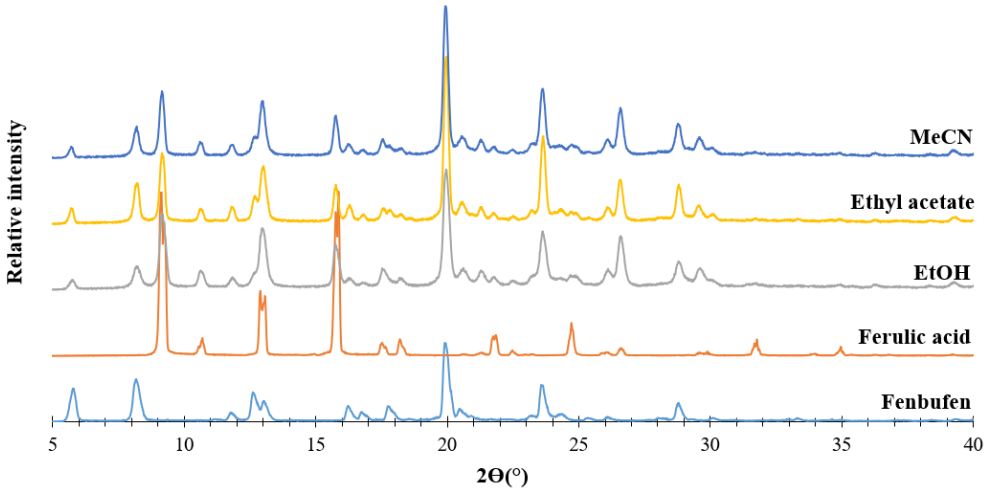

Figure 2.1.4: PXRD patterns of the starting materials FEN and ferulic acid and those of the products following LAG experiments using the solvents indicated.

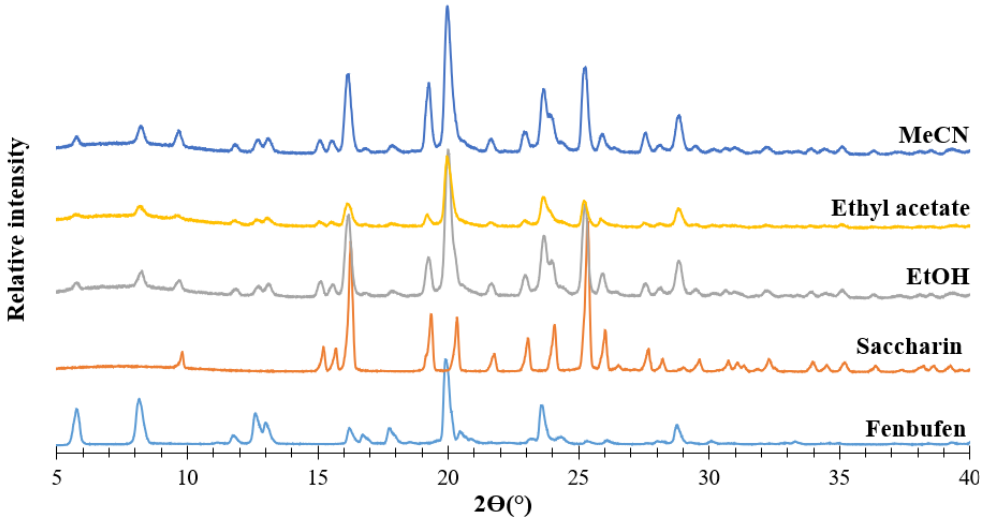

Figure 2.1.5: PXRD patterns of the starting materials FEN and saccharin and those of the products following LAG experiments using the solvents indicated.

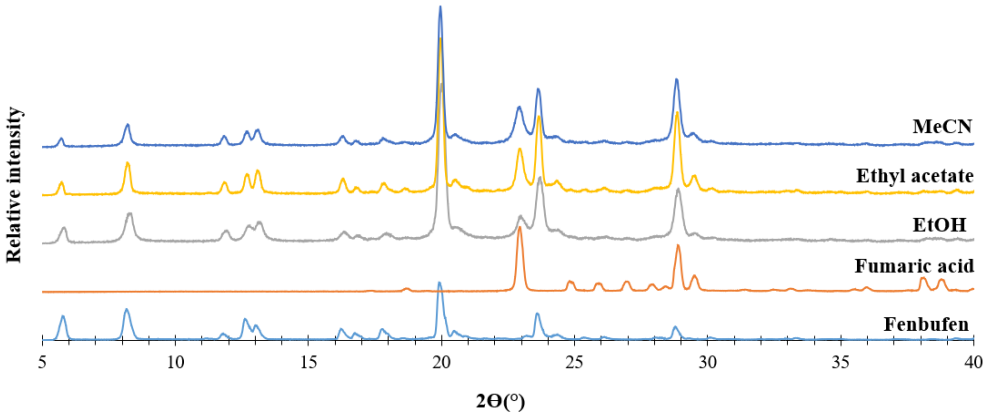

Figure 2.1.6: PXRD patterns of the starting materials FEN and fumaric acid and those of the products following LAG experiments using the solvents indicated.

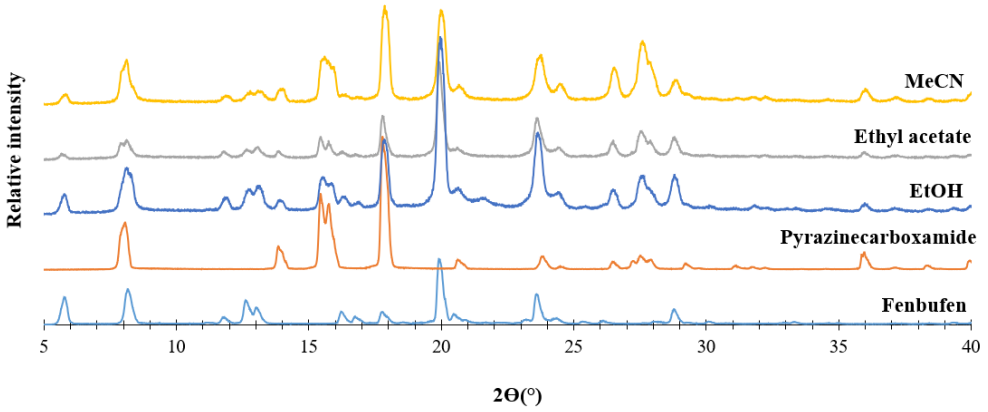

Figure 2.1.7: PXRD patterns of the starting materials FEN and pyrazinecarboxamide and those of the products following LAG experiments using the solvents indicated.

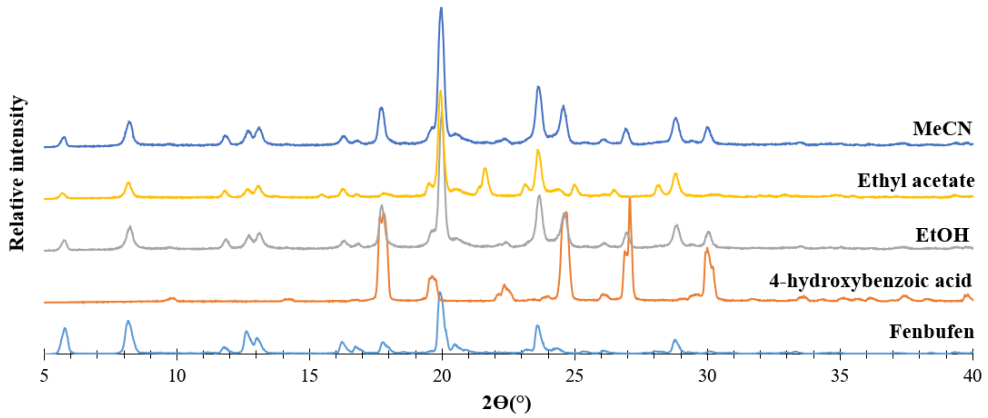

Figure 2.1.8: PXRD patterns of the starting materials FEN and 4-hydroxybenzoic acid and those of the products following LAG experiments using the solvents indicated.

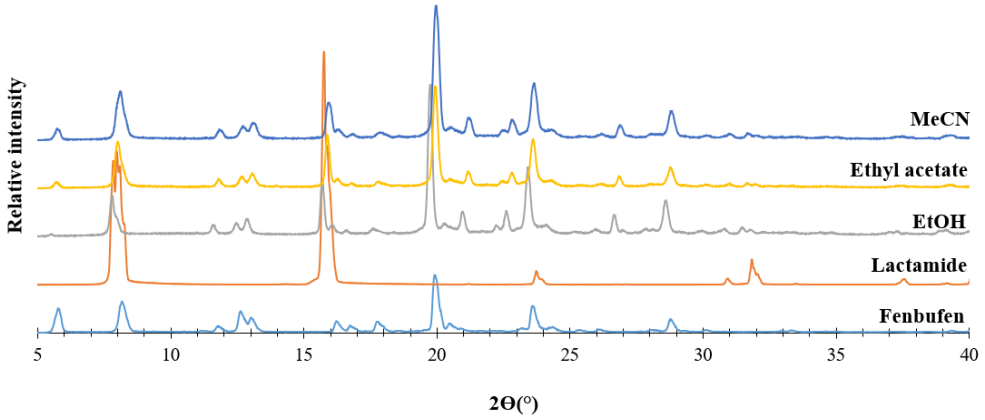

Figure 2.1.9: PXRD patterns of the starting materials FEN and lactamide and those of the products following LAG experiments using the solvents indicated.

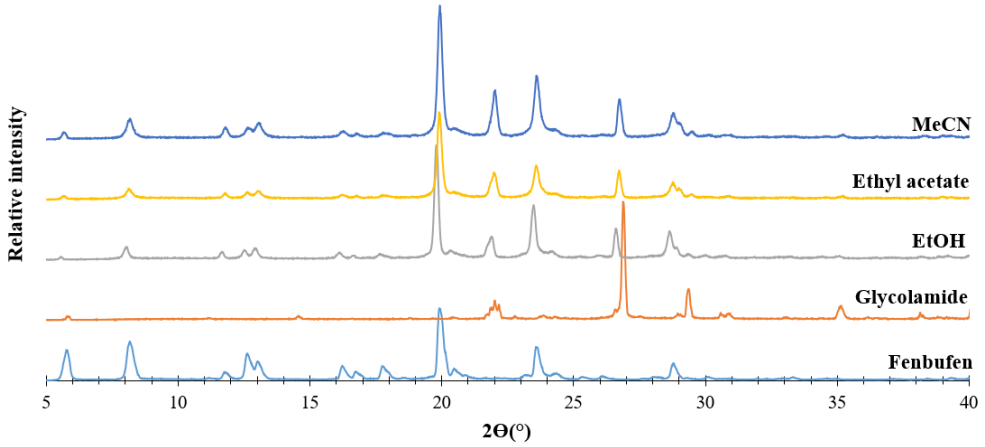

Figure 2.1.10: PXRD patterns of the starting materials FEN and glycolamide and those of the products following LAG experiments using the solvents indicated.

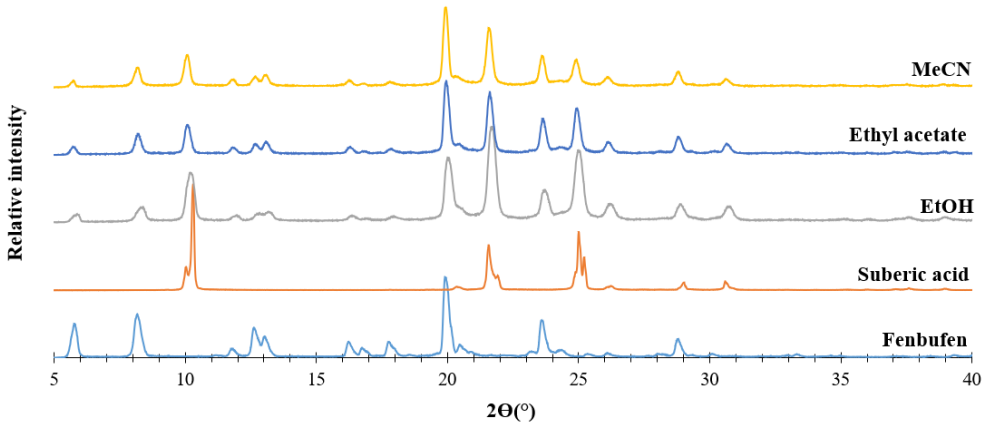

Figure 2.1.11: PXRD patterns of the starting materials FEN and suberic acid and those of the products following LAG experiments using the solvents indicated.

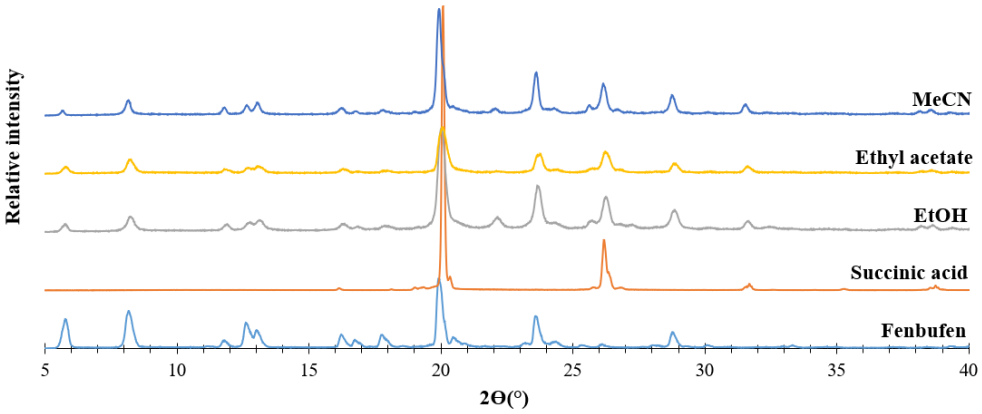

Figure 2.1.12: PXRD patterns of the starting materials FEN and succinic acid and those of the products following LAG experiments using the solvents indicated.

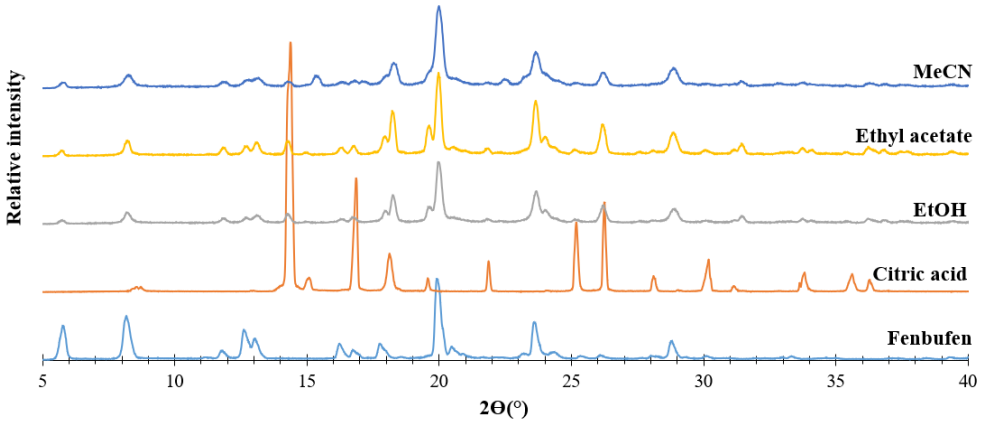

Figure 2.1.13: PXRD patterns of the starting materials FEN and citric acid and those of the products following LAG experiments using the solvents indicated.

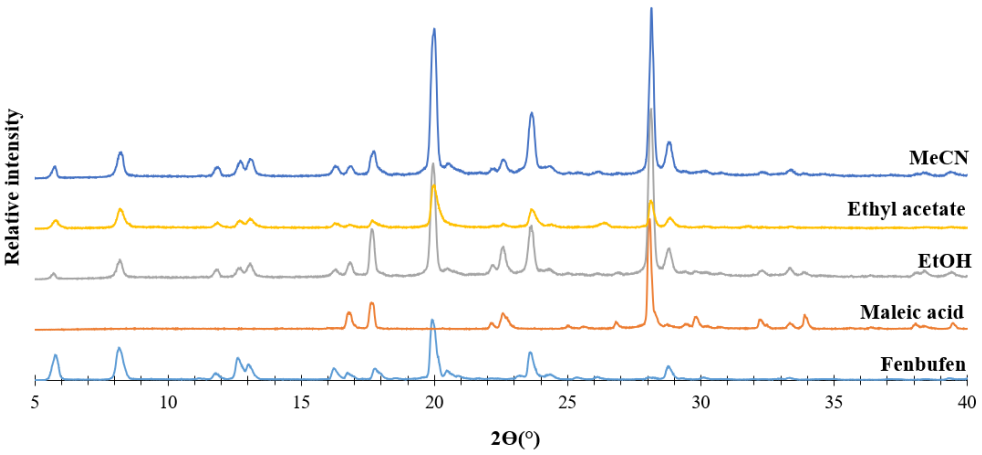

Figure 2.1.14: PXRD patterns of the starting materials FEN and maleic acid and those of the products following LAG experiments using the solvents indicated.

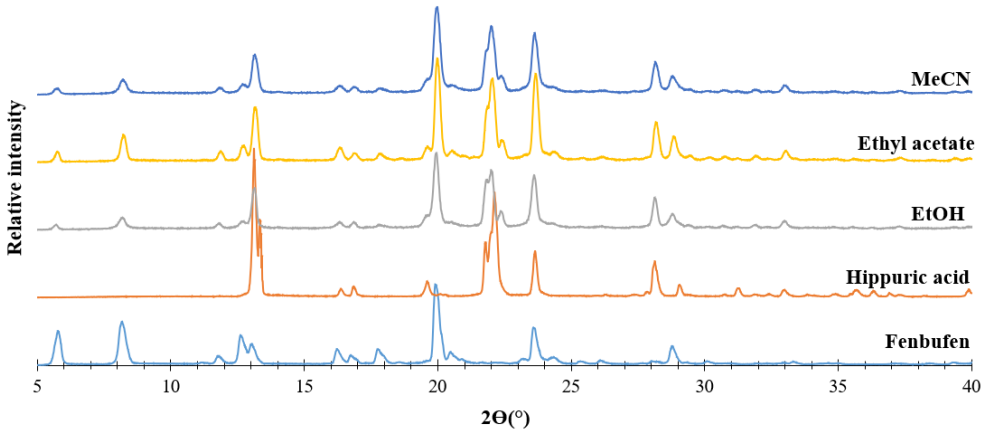

Figure 2.1.15: PXRD patterns of the starting materials FEN and hippuric acid and those of the products following LAG experiments using the solvents indicated.

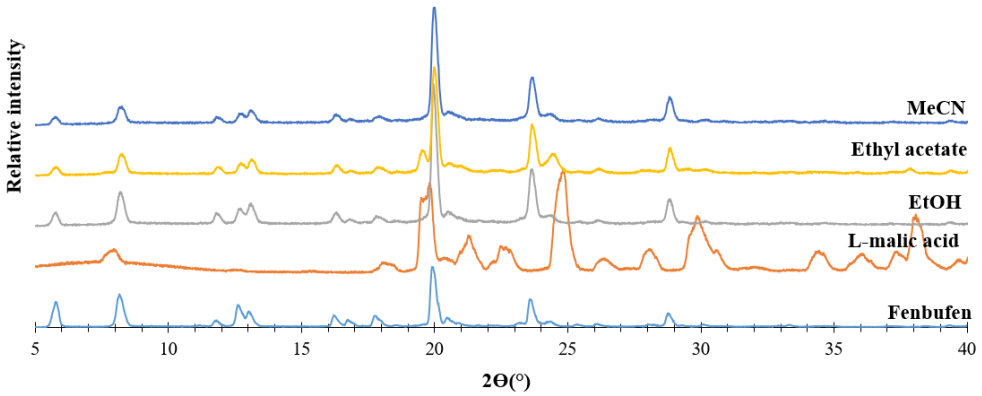

Figure 2.1.16: PXRD patterns of the starting materials FEN and L-malic acid and those of the products following LAG experiments using the solvents indicated.

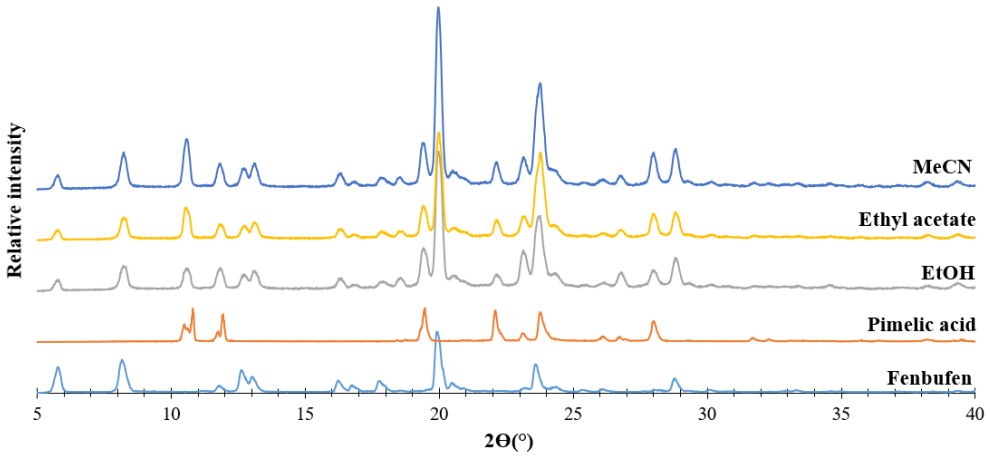

Figure 2.1.17: PXRD patterns of the starting materials FEN and pimelic acid and those of the products following LAG experiments using the solvents indicated.

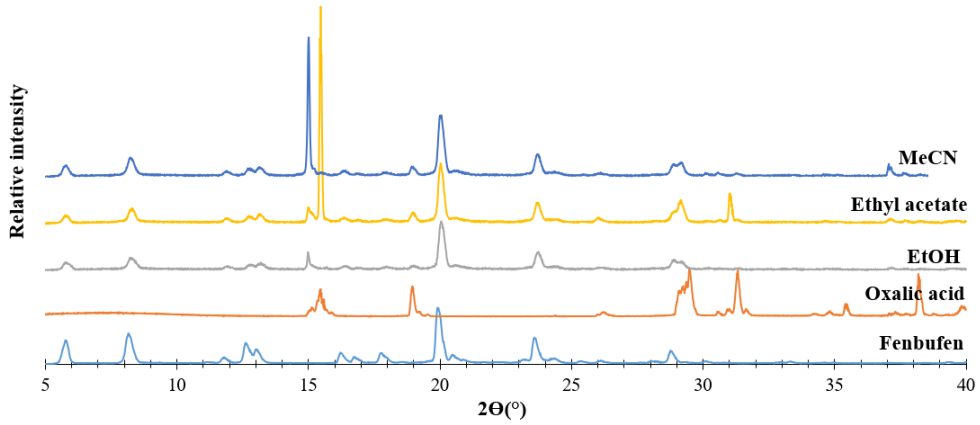

Figure 2.1.18: PXRD patterns of the starting materials FEN and oxalic acid and those of the products following LAG experiments using the solvents indicated.

2.2. Calculation of the number of water molecules in FEN-ISN:

$$0.0174 = \frac{18.016n}{18.016n + 2(122.12) + 121.11 + 254.27 + 253.26}$$

0.313n + 4.250 + 2.107 + 4.424 + 4.407 = 18.016n

17.703n = 15.188

n = 0.858

$$0.0170 = \frac{18.016n}{18.016n + 2(122.12) + 121.11 + 254.27 + 253.26}$$

0.306n + 4.152 + 2.059 + 4.323 + 4.305 = 18.016n

17.710n = 14.839

n = 0.838

0.85 ± 0.01

Section 3- Chapter 6

3.1. PXRD patterns of LAG and co-precipitation products of S-IBU and coformers.

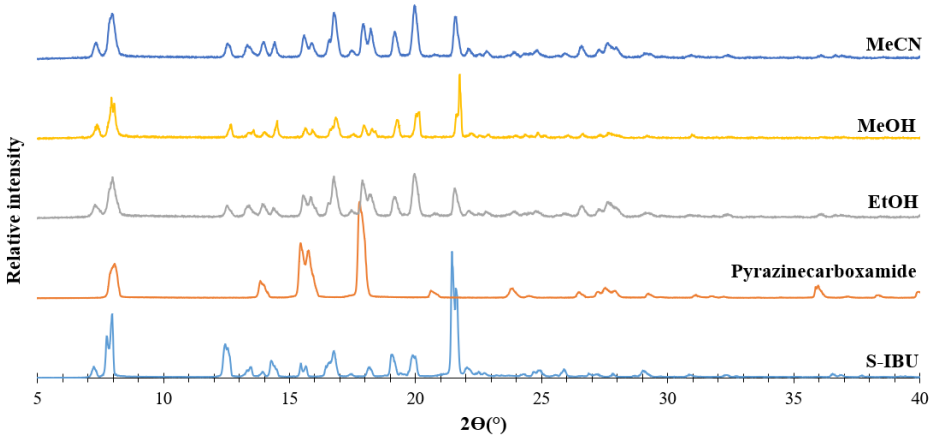

Figure 3.1.1: PXRD patterns of the starting materials S-IBU and pyrazinecarboxamide and those of the products following LAG experiments using the solvents indicated.

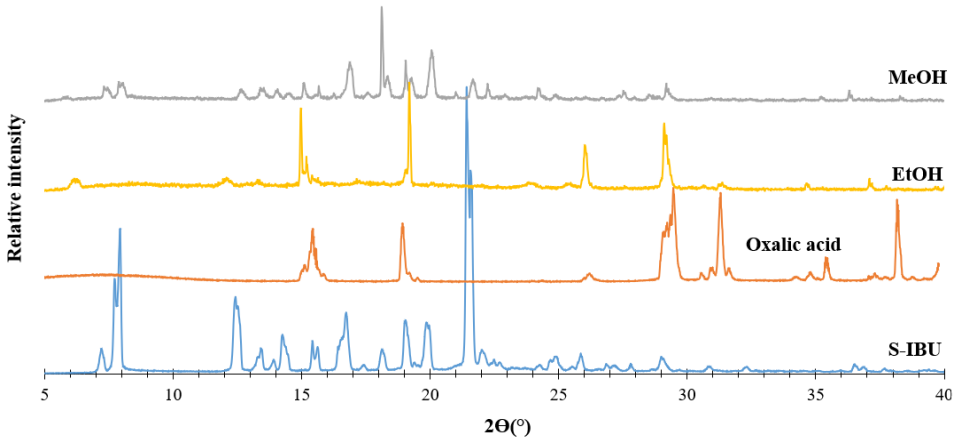

Figure 3.1.2: PXRD patterns of the starting materials S-IBU and oxalic acid and those of the products following LAG experiments using the solvents indicated.

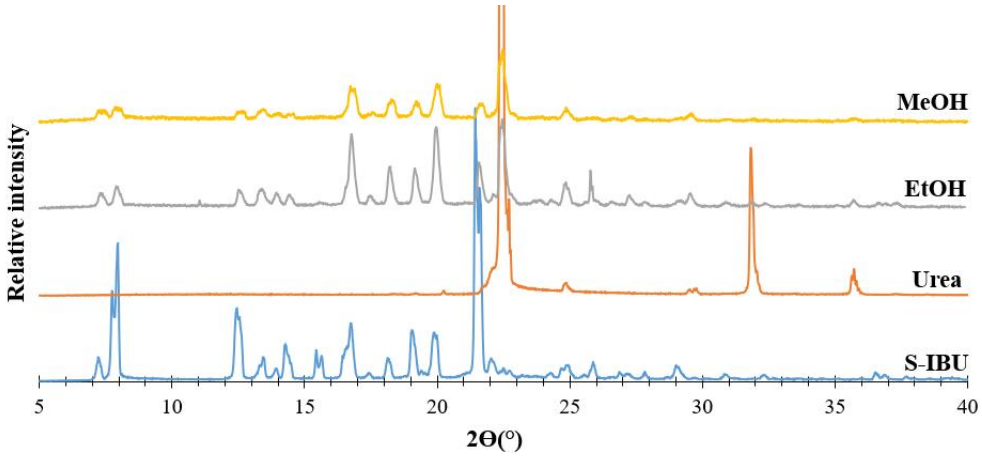

Figure 3.1.3: PXRD patterns of the starting materials S-IBU and urea and those of the products following LAG experiments using the solvents indicated.

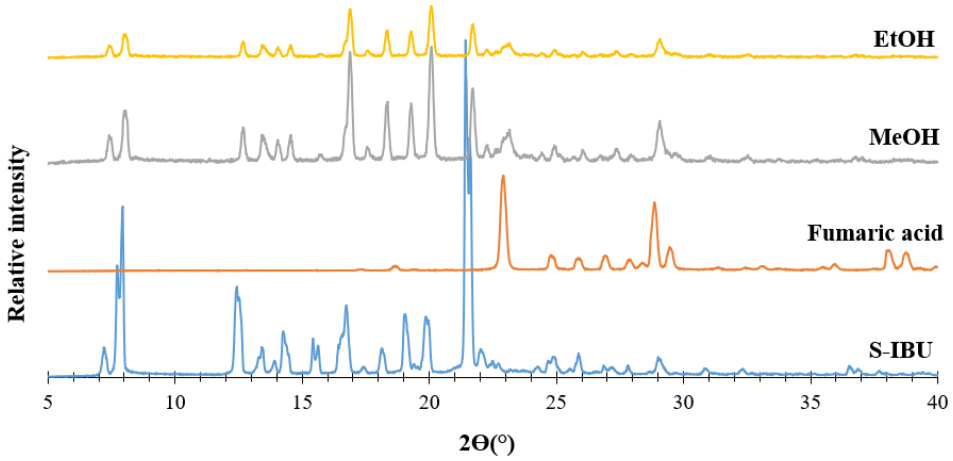

Figure 3.1.4: PXRD patterns of the starting materials S-IBU and fumaric acid and those of the products following LAG experiments using the solvents indicated.

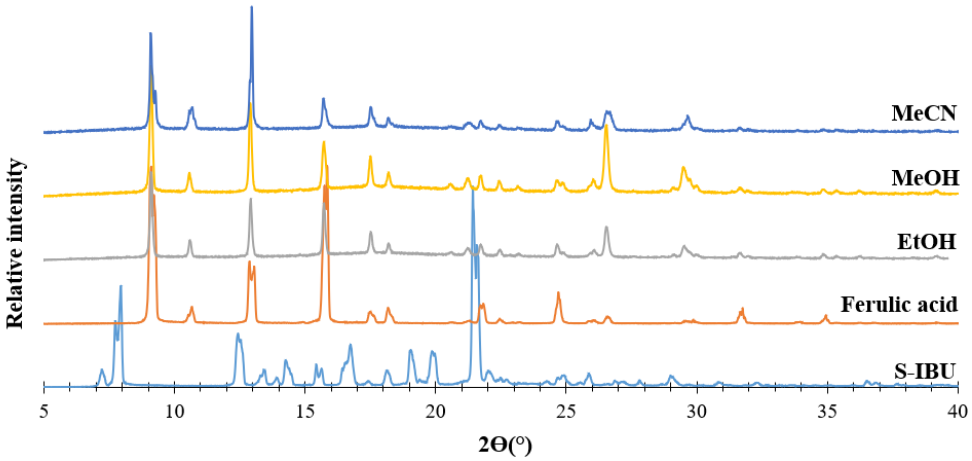

Figure 3.1.5: PXRD patterns of the starting materials S-IBU and ferulic acid and those of the products following LAG experiments using the solvents indicated.

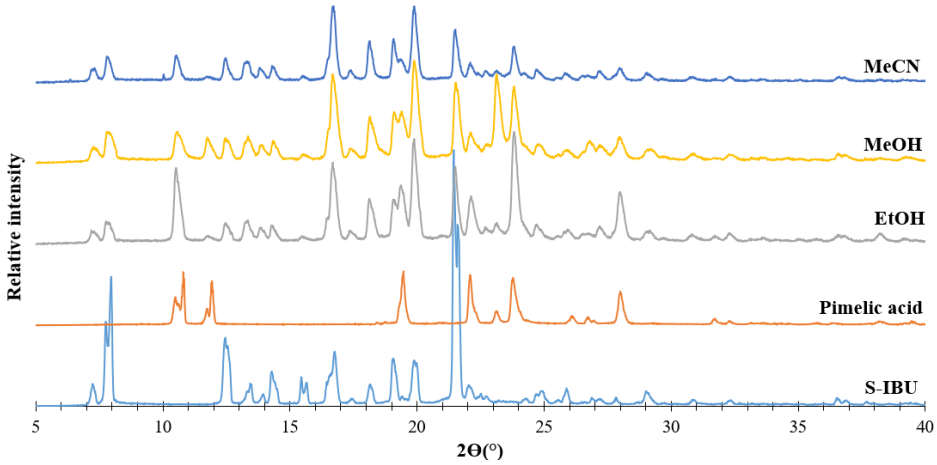

Figure 3.1.6: PXRD patterns of the starting materials S-IBU and pimelic acid and those of the products following LAG experiments using the solvents indicated.

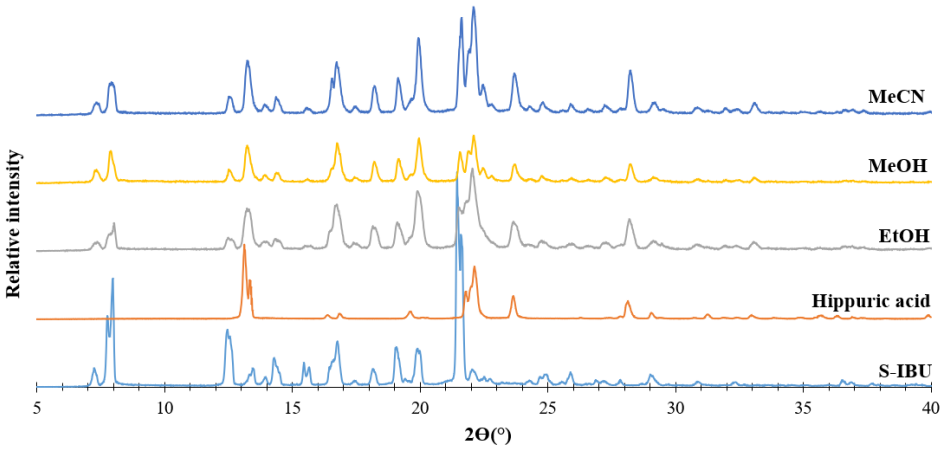

Figure 3.1.7: PXRD patterns of the starting materials S-IBU and hippuric acid and those of the products following LAG experiments using the solvents indicated.

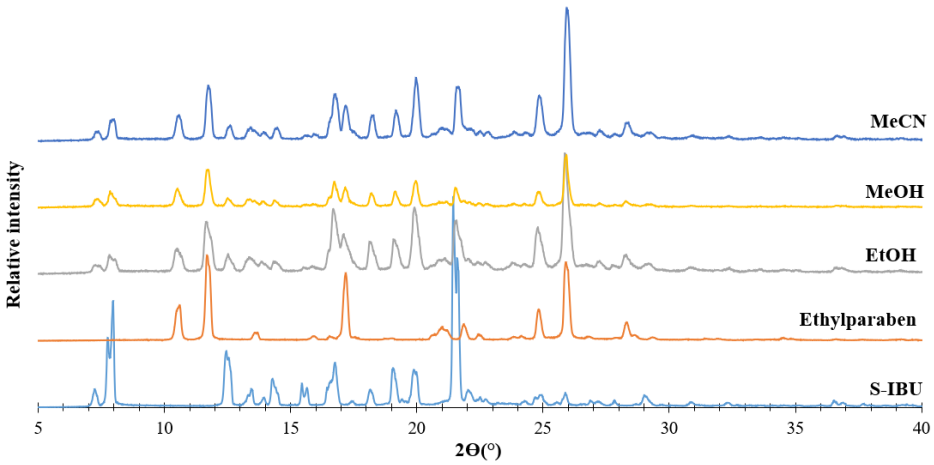

Figure 3.1.8: PXRD patterns of the starting materials S-IBU and ethylparaben and those of the products following LAG experiments using the solvents indicated.

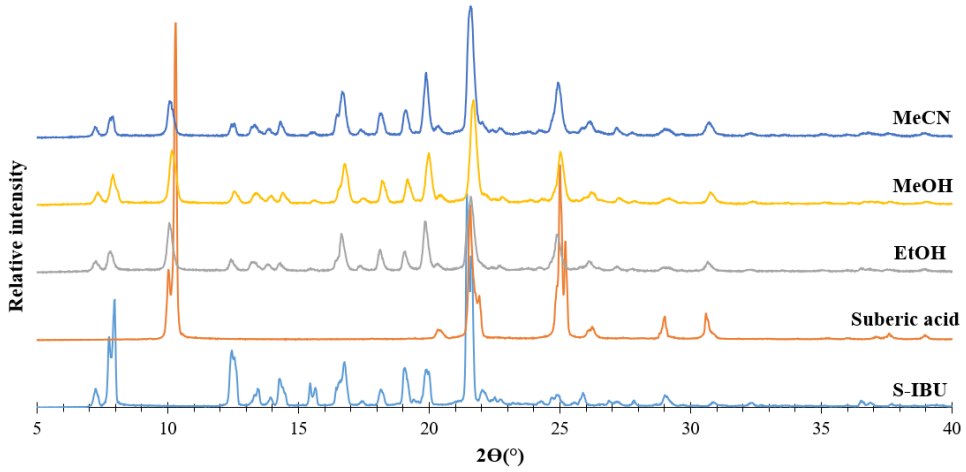

Figure 3.1.9: PXRD patterns of the starting materials S-IBU and suberic acid and those of the products following LAG experiments using the solvents indicated.

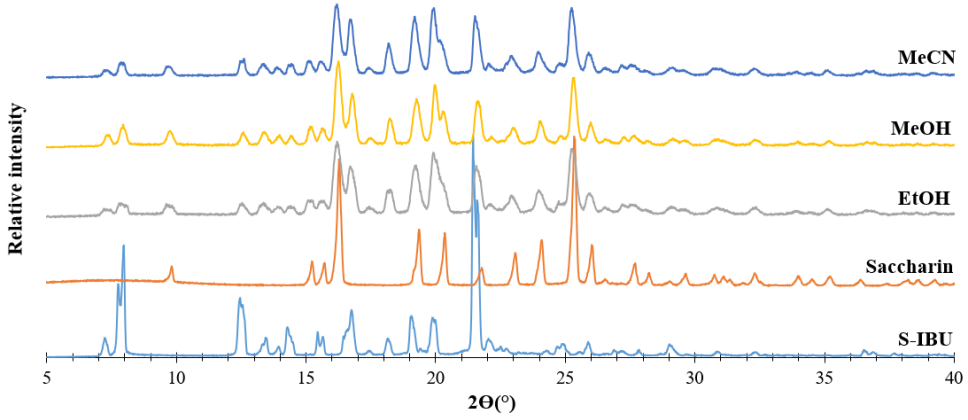

Figure 3.1.10: PXRD patterns of the starting materials S-IBU and saccharin and those of the products following LAG experiments using the solvents indicated.

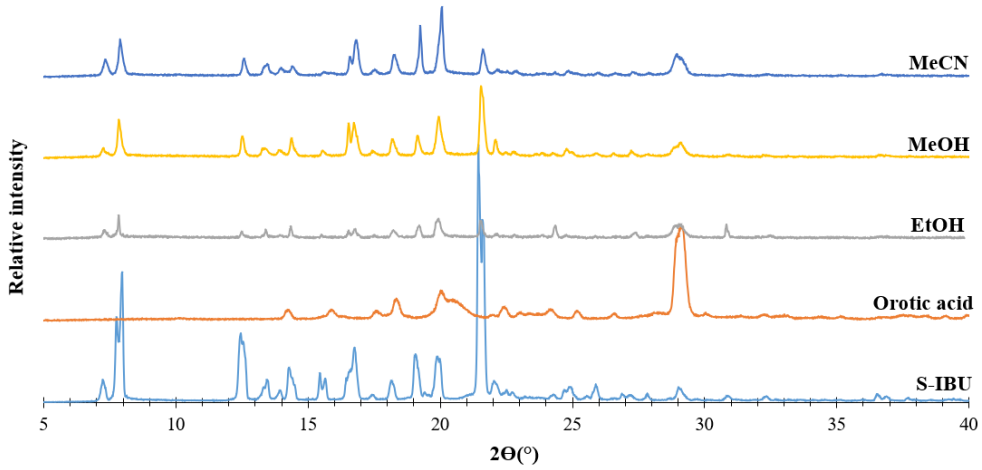

Figure 3.1.11: PXRD patterns of the starting materials S-IBU and orotic acid and those of the products following LAG experiments using the solvents indicated.

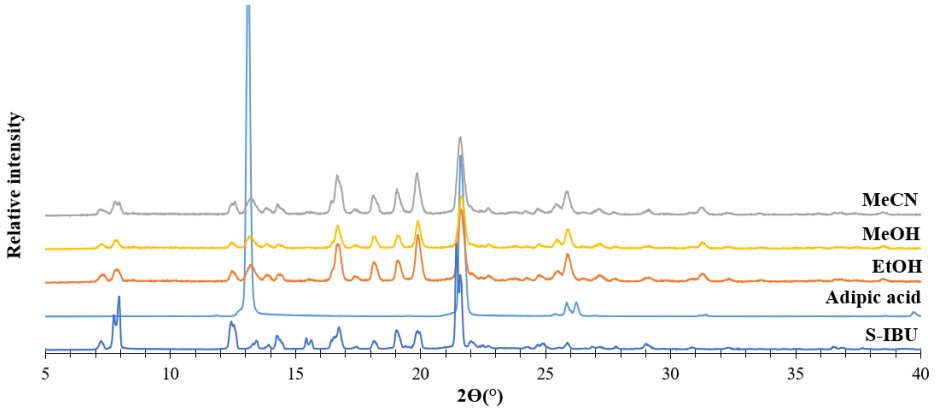

Figure 3.1.12: PXRD patterns of the starting materials S-IBU and adipic acid and those of the products following LAG experiments using the solvents indicated.

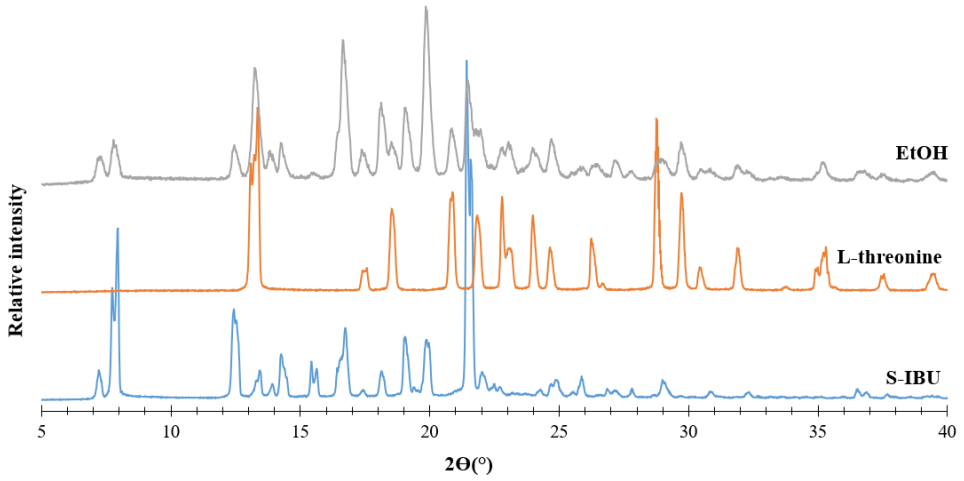

Figure 3.1.13: PXRD patterns of the starting materials S-IBU and L-threonine and that of the product following LAG experiment using EtOH.

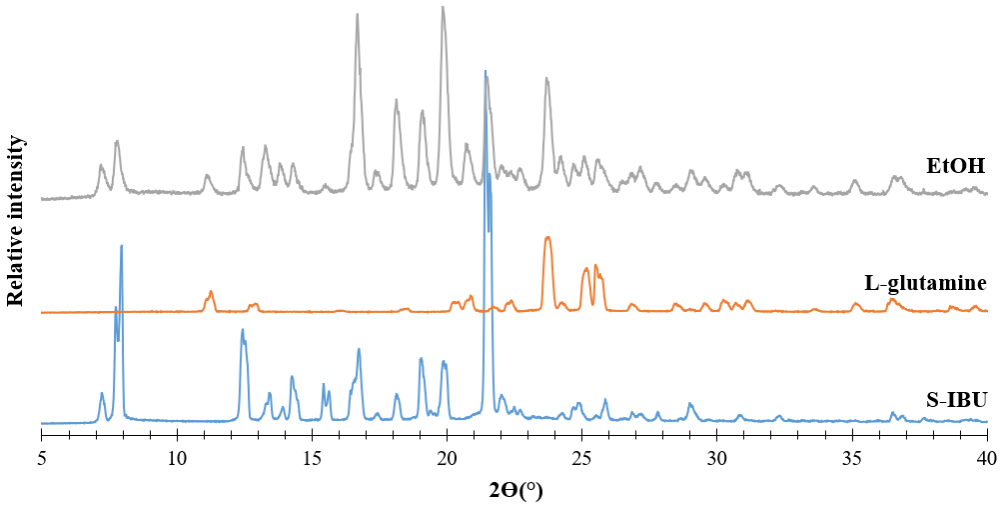

Figure 3.1.14: PXRD patterns of the starting materials S-IBU and L-glutamine and that of the product following LAG experiment using EtOH.

3.2. Standard solution and standard curve preparation

The S-IBU standard solution was prepared by dissolving a known accurately weighed sample of S-IBU in a known volume of phosphate buffer solution at pH 6.5. Using the standard solution, serial dilutions were prepared to produce a 10-point calibration curve (Figure 3.2.1). The concentration of S-IBU was quantified using UV-Vis spectroscopy, with absorbance measured at 265 nm.

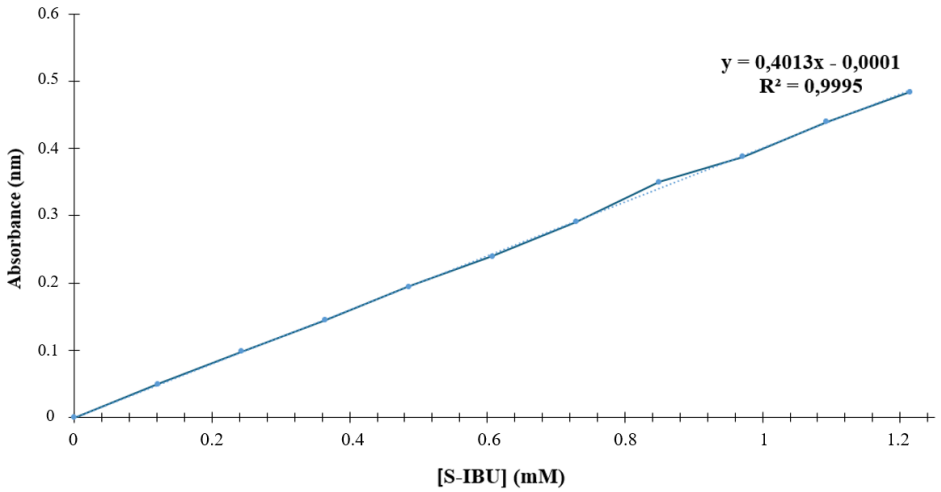

Figure 3.2.1: Standard curve produced by UV-Vis spectroscopy measured at 265 nm for the quantification of S-IBU in the dynamic solubility study.

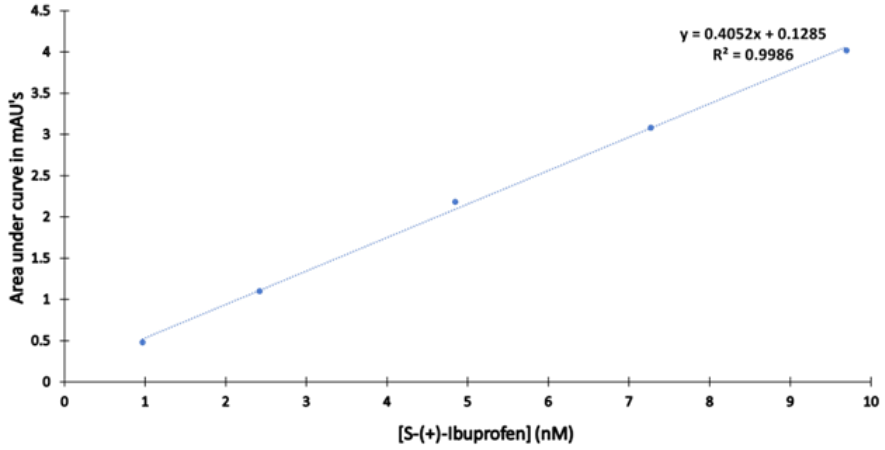

Figure 3.2.2: S-IBU calibration curve produced by HPLC used for the intrinsic solubility determination.

3.3. NMR spectra

3.3.1. ^{1}H NMR spectrum of $(S\text{-}IBU)^{-}(ACA)^{+}$ recorded in DMSO-d_6.

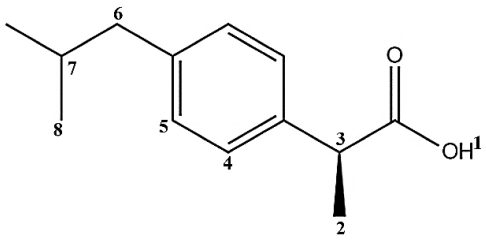

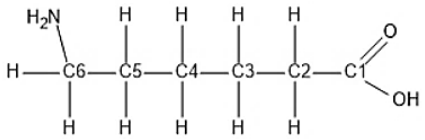

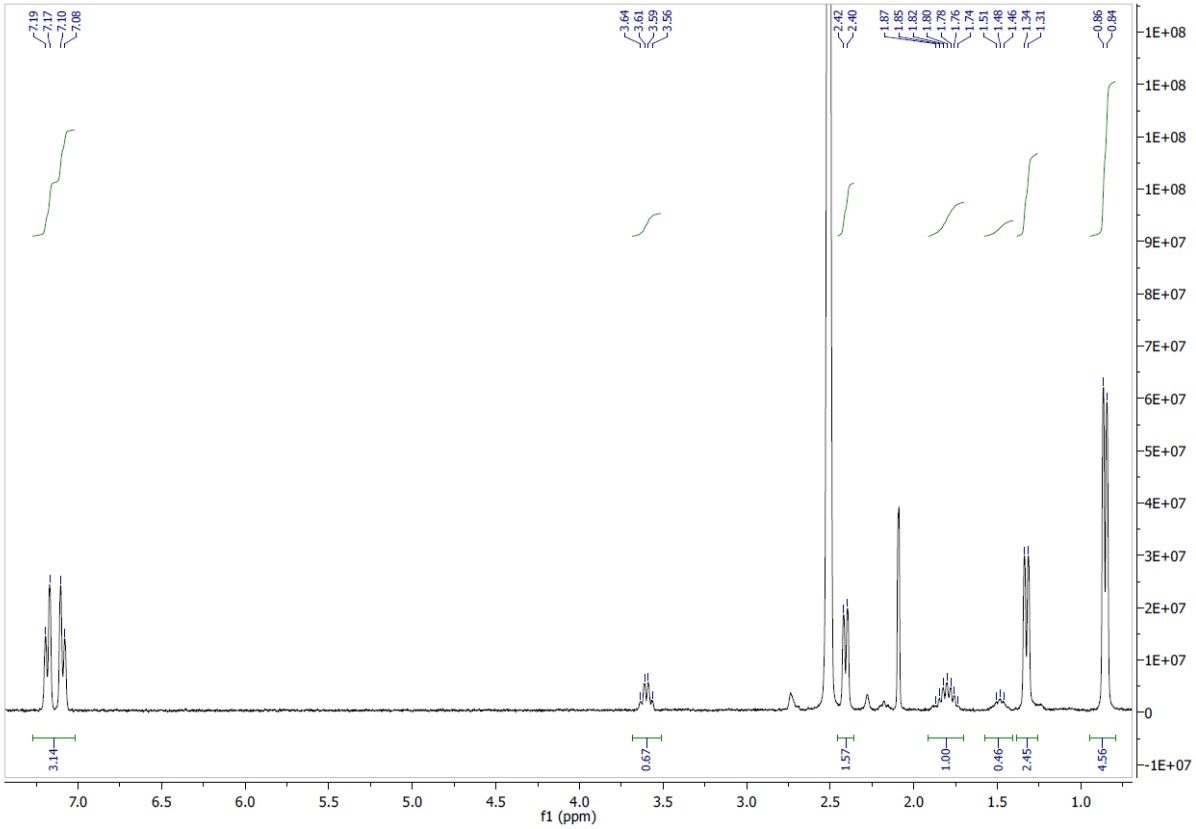

3.3.2. ^{1}H NMR spectrum of DMB·S-IBU recorded in DMSO-d_6.